Fabrication and Characterization of Hybrid Graphene Devices

Tesis doctoral presentada por
Andrés Black Morocoima

Para obtar al título de Doctor en Ciencias Físicas
Departamento de Física de la Materia Condensada
Universidad Autónoma de Madrid

Madrid, Junio de 2017

Tesis presentada para obtar al título de Doctor en Ciencias Físicas

Director de Tesis:

Prof. Amadeo López Vázquez de Parga

Universidad Autónoma de Madrid
Departamento de Física de la Materia Condensada

Instituto Madrileño de Estudios Avanzados
Nanociencia

Contents

Resumen

Han transcurrido más de diez años desde el descubrimiento del grafeno. En este tiempo, sus propiedades básicas se han explorado a fondo, y en gran medida, entendido. En los últimos años, los investigadores han empezado a explorar un número creciente de posibles aplicaciones para el grafeno, iniciando los pasos preliminares en el desarrollo de tecnologías útiles basadas en este extraordinario material. Muchas aplicaciones requieren sintonizar algunas de las propiedades del grafeno, o incluso conferirle propiedades extrínsecas. Ésto se puede conseguir combinando el grafeno con otras moléculas, compuestos químicos, películas delgadas o incluso otros tipos de materiales y estructuras de baja dimensionalidad. Esta forma de complementar las propiedades del grafeno es el tema principal de esta tesis. Los métodos y procesos empleados en esta tesis se llevaron a cabo tomando en cuenta posibles futuras aplicaciones tecnológicas. Por lo tanto, el grafeno empleado en este trabajo de tesis doctoral es de gran superficie ($>1\text{cm}^2$), crecido mediante un proceso industrialmente escalable, como es la deposición química en fase vapor, y todos los dispositivos se fabricaron usando técnicas de fotolitografía de alto rendimiento. El desarrollo de estos procesos tecnológicos, con el objetivo de producir dispositivos de grafeno de calidad, constituyen el primer resultado principal de esta tesis. Posteriormente, se exploraron métodos para modificar el dopaje de los dispositivos de grafeno, mediante funcionalización química en vapor. Como resultado, se obtuvieron dispositivos híbridos de grafeno con una molécula orgánica dopante tipo p o n. Con el fin de encapsular los dispositivos, de tal modo que los cambios en el dopaje fueran permanentes y constantes en el tiempo, se crecieron películas de óxido sobre los dispositivos funcionalizados mediante deposición de capa atómica y/o evaporación térmica. Se exploraron varios métodos para obtener películas de calidad sin comprometer excesivamente el dopaje químico. Un segundo tipo de dispositivo híbrido de grafeno se creó integrando al grafeno con películas fluorescentes de puntos cuánticos coloidales encapsulados (PCCE) en silica. Estas películas de PCCE se transfirieron a sustratos recubiertos en grafeno mediante el método Langmuir-Blodgett, técnica capaz de depositar películas de nanomateriales homogéneas y de gran superficie. Las heteroestructuras resultantes de grafeno/PCCE exhibieron varios procesos físicos interesantes, tales como la amplificación o reducción de la emisión fluorescente de los PCCEs en función a su entorno próximo (SiO_2, oro o grafeno). Los procesos de transferencia energética se han descartado como posible explicación de estas observaciones, y se proponen otros posibles mecanismos. Mediante un proceso optimizado de microfabricación, se realizaron dispositivos con las heteroestructuras. Medidas de transporte eléctrico mostraron que las películas de PCCE poseen propiedades aislantes excelentes, permitiendo su uso como capa dieléctrica en medidas eléctricas de efecto campo.

Además, se ha demostrado que los dispositivo híbridos fabricados mediante heteroestructuras grafeno/PCCE/grafeno son capaces de fotodetectar radicación en el rango del UV/Vis. Se propone un mecanismo de ganancia fotoconductiva mediado por atrapamiento de cargas en la película de PCCEs.

Abstract

More than ten years have passed since the discovery of graphene. Within this time, its basic properties have been thoroughly explored and largely understood. In the past few years, researchers have begun to explore an increasing number of possible applications for graphene, taking the first tentative steps in developing useful technologies based on this remarkable material. Many applications require controlled tuning of graphene's properties, which in many cases can be accomplished by combining graphene with molecules, chemical compounds, thin films, or even other classes of low dimensional materials and structures. This approach to complimenting graphene's capabilities is the subject of this thesis. The methods and processes employed in this work were carried out taking into account possible future technological applications. As such, the graphene used in all samples was large area ($>$1 cm^2), grown via an industrially scalable chemical vapor deposition process, with devices were fabricated using high throughput photolithography techniques. Developing these technological processes in order to consistently produce quality graphene devices constitutes the first main result of this thesis. Methods for modifying graphene's doping were then explored, using vapor phase chemical functionalization, resulting in hybrid devices consisting of graphene and an organic p or n dopant molecule. Oxide films were grown on these devices via atomic layer deposition (ALD) and thermal evaporation, in an attempt to encapsulate the devices and make them more resistant to environmental degradation. Several methods were explored for obtaining quality films without excessively compromising the chemical doping. A second type of hybrid graphene device was created by integrating graphene with films of fluorescent, silica encapsulated colloidal quantum dots (ECQDs). These films were transferred onto graphene covered substrates using the Langmuir-Blodgett method, a technique capable of depositing large area, homogeneous films of nanomaterials. The resulting graphene/ECQD heterostructures yielded several interesting physical phenomena, including fluorescence emission enhancement and quenching depending on the surrounding environment. Conventional energy transfer processes have been largely ruled out as explanations for these observations; possible alternative mechanisms are proposed. An optimized microfabrication process was used to realize devices from the heterostructures. Electron transport measurements revealed the ECQD films to have excellent insulating properties, permitting their use as a dielectric in electric field effect measurements. Moreover, graphene devices below the ECQD films were capable of photodetection in the UV/Vis range. This is likely due to trapping of excited carriers, producing a photoconductive gain mechanism.

List of Acronyms

AFM Atomic Force Microscopy

ALD Atomic Layer Deposition

C-AFM Conducting Atomic Force Microscopy

CVD Chemical Vapor Deposition

CQD Colloidal Quantum Dot

DMSO Dimethyl Sulfoxide

DP Dirac Point

ECQD Encapsulated Colloidal Quantum Dot

EDA Ethylenediamine

GFET Graphene Field Effect Transistor

LB Langmuir-Blodgett

PMMA Poly(methyl methacrylate)

SEM Scanning Electron Microscopy

TCNQ 7,7,8,8-tetracyano-quinodimethane

UFM Ultrasonic Force Microscopy

Description of Contents

Chapter 1 gives a brief introduction to graphene, starting with an overview of the most common production methods and a description of its lattice structure. The next section touches upon graphene's electronic bands, in particular its linear dispersion near the Dirac point, which give rise to graphene's remarkable electronic properties. Experimental factors limiting these properties are remarked upon, with emphasis on the ones most pertinent to the experiments in this thesis. The chapter concludes with a short overview of graphene's chemical properties and interactions with other compounds.

Chapter 2 describes the experimental details and methods used throughout this thesis, along with the most important characterization techniques. It begins with an overview of the sample fabrication process, introducing the chemical vapor deposition (CVD) furnace used for growing graphene on copper foils, the transfer method for transferring the graphene onto arbitrary substrates, and the lithographic techniques for fabricating devices. The second section describes characterization techniques, including electrical transport, Raman spectroscopy and optical measurements. Details on the instrumentation utilized are given. Where appropriate, theoretical background of a technique is included, emphasizing the particularities of the technique's application to graphene.

Chapter 3 details the technological processes, which had to be developed from scratch at IMDEA Nanoscience, for obtaining quality graphene devices. The challenges encountered and overcome at each particular step of the overall process are detailed. The starting point was optimization of the CVD growth recipe. Two particular recipes were developed, each yielding monolayer graphene suitable for different applications. This is followed by a description of the process for obtaining a clean transfer of large area (>1 cm^2), continuous graphene onto arbitrary substrates. The final step is the fabrication of devices via photolithography, particularly challenging due to the detrimental effects of photoresist. Several means of mitigating these effects are presented, along with electronic and Raman measurements to asses the quality of the final devices.

Chapter 4 introduces graphene hybrid devices. Chemical functionalization via vapor phase deposition is described, yielding p and n doped graphene, as confirmed via electronic and Raman measurements. The work in this chapter goes a step further, attempting to encapsulate the chemically functionalized graphene under an oxide film, with the aim of "sealing in" its doping properties, protecting them from environmental degradation. Ensuring adequate film growth while maintaining the desired properties proved to be particularly challenging, as demonstrated with a variety of characterization techniques. The last two chapters of this thesis deal with novel low dimensional heterostructures, combining graphene with silica encapsulated colloidal quantum dots (ECQDs).

Chapter 5 deals primarily with the assembly of the heterostructures. Using the Langmuir-Blodgett technique, compact, dense, homogeneous ECQD films were transferred onto graphene, previously deposited on a Si/SiO_2 substrate. In order to succesfully transfer a graphene sheet on top of the ECQD films, a new transfer process had to be developed and optimized. Various characterization techniques were used to gauge the quality of each layer of the graphene/ECQD/graphene heterostructure, including various scanning probe techniques, scanning electron microscopy, fluorescence measurements and Raman spectroscopy.

Chapter 6 describes the optical, electronic, and optoelectronic characterization of the ECQD heterostructures assembled in Chapter 5. A wide variety of physical phenomena are encountered, several of which are not fully understood at the moment of writing this dissertation. The ECQD film emission intensity is found to be highly sensitive to its environment, with strong enhancement in the vicinity of gold, and intense quenching beneath a graphene sheet. These observations are surprising considering that very low energy transfer rates are measured between the ECQDs and their surrounding environment, most likely due to the thick silica shell surrounding them. Possible mechanisms are discussed to explain the observed emission behavior, including the optical properties of the silica shells themselves. Electrical measurements demonstrate that the ECQD film can act as a quality electrical insulator, allowing field effect measurements to be made between the top graphene sheet and a graphene device beneath the ECQD film. The thesis concludes with preliminary photodetection measurements of a bottom graphene device. A photoconductive gain mechanism is observed, suspected to be caused by charge trapping by the silica shells of the ECQD.

The thesis concludes with two appendices, outlining in detail the CVD growth recipes, and graphene transfer process.

Chapter 1

Introduction

This chapter introduces concepts pertaining to graphene and its remarkable properties. Graphene's structure, including its atomic lattice, orbital hybridization and lattice boding is briefly discussed. A short summary of of graphene's various production methods follows, including mechanical and liquid exfoliation and chemical vapor deposition. An introduction to graphene's unique band structure is given, focusing on the low carrier density characteristics of the Dirac cone, charge carrier behavior and the effects of doping. Experimental aspects of graphene's electrical transport properties are touched upon, specifically the effect of impurities and defects on the maximum mobility and minimum conductivity. Finally, a brief the chemical functionalization mechanisms of graphene are summarized, including covalent and non-covalent bonding with other chemical species, as well as the mechanisms of chemical doping.

1.1 Structure and Production Methods

Graphene consists of a single sheet of carbon atoms arranged in a hexagonal honeycomb lattice. It can be considered a single sheet of graphite that has been isolated from the bulk. The honeycomb lattice is comprised of two triangular sublattices, as illustrated in Figure 1.1a. Graphene's unit cell consists of two atoms, one of each sublattice, with a lattice vector length of about 0.14 nm. Each atom in the graphene lattice is joined to its neighbors via three in plane σ bonds, resulting from an sp^2 hybridization of carbon's s, p_x and p_y orbitals. These σ bonds are responsible for graphene's (and graphite's) in plane mechanical strength. The remaining out of plane p_z obital forms a covalent π bond with its neighbors. The resulting π band, which is half filled with free moving electrons, is responsible for graphene's electronic properties [1].

Graphene was first isolated in 2004 through the mechanical cleavage of bulk graphite using scotch tape. The resulting graphene flakes were deposited onto a highly doped silicon wafer capped with an insulating SiO_2 layer. These samples resulted in the first field effect measurements of graphene devices, revealing the remarkable electronic properties of this material, and produced the seminal paper which sparked the enormous research effort to understand and utilize graphene and other 2-dimensional materials [2]. Today, mechanical exfoliation is still the preferred method for obtaning the highest electrical and optical quality samples. This method, however, is not scalable, and therefore cannot be used for industrial applications where mass production is necessary. Moreover, the flakes obtained from this

method are typically below 1 mm^2 in length, and more commonly below 100 μm^2. Liquid-phase exfoliation of graphene has proven to be a high yield, scalable method of producing graphene flakes [3]. Nonetheless, even under the best conditions, this method produces a large quantity of many small flakes, as opposed to a large area single sheet. The most promising method discovered thus far for industrial style production of large area, homogeneous graphene sheets is via chemical vapor deposition (CVD) growth on catalytic metallic substrates [4]. Indeed, graphene has been succesfully grown on many metals, including Ru, Ir, Pt, and Ni, amongst others. However, the most commonly used metal for graphene production, and the one used in this thesis, is copper, due to its easy accesibility, low price, and favorable properties for graphene growth, which will be covered in greater detail in the Graphene Technology chapter.

1.2 Electronic Properties

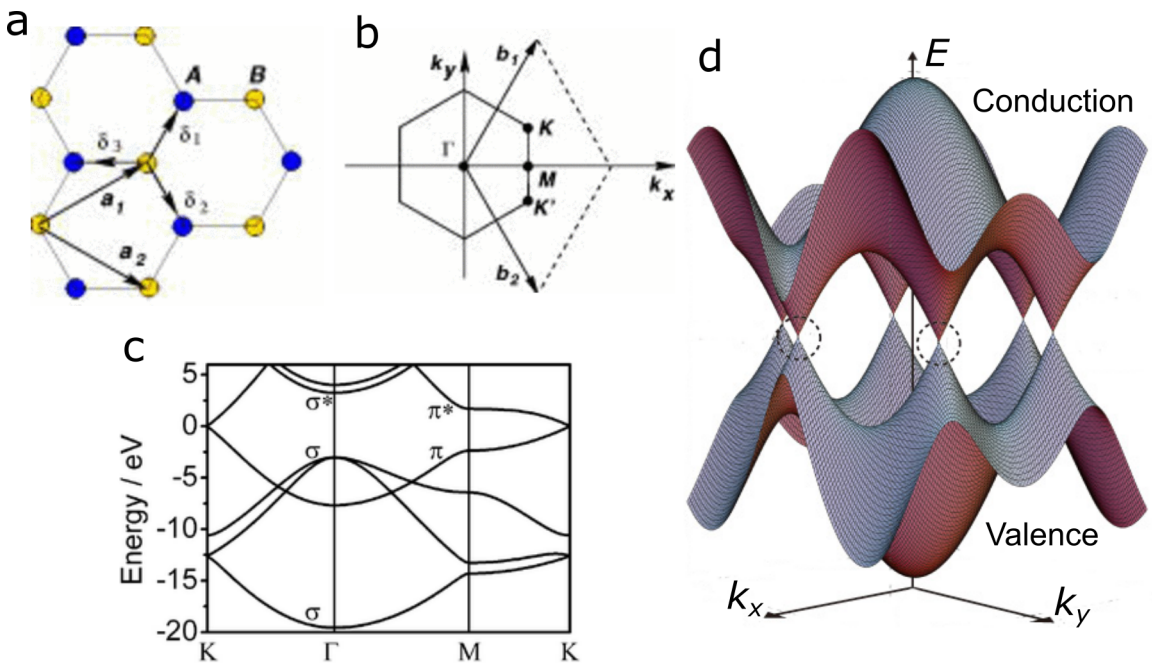

Figure 1.1: **a** Graphene crystal lattice, consisting of two triangular sub-lattices, depicted in blue and yellow. $\mathbf{a}_1$ and $\mathbf{a}_2$ are unit vectors. Adapted from [1]. **b** Graphene Brillouin zone. Adapted from [1]. **c** Full graphene band structure. Adapted from [5]. **d** Stylized graphene band structure, highlighting the Dirac points near the Fermi energy. Adapted from [6].

At the corner of graphene's Brillouin zone, shown in Figure 1.1b, are the inequivalent K and K' points, also known as the Dirac points. At these points, graphene's π bands intersect at the Fermi energy, and its σ bands are at much higher and lower energies, as shown in Figure 1.1c. Therefore, the π bands are responsible for graphene's electronic properties, which can be understood from the behavior of charge carriers close to the Dirac point. As such, the 2D momentum vector $\mathbf{q} = \mathbf{K} - \mathbf{k}$, defined with respect to the K momentum point,

is used to understand and describe graphene's band structure. A stylized band structure depicting this region of interest is shown in Figure 1.1d, showing the Dirac points at the intersection of the conduction and valence bands.

Tight binding calculations including contributions from nearest and next-nearest neighbors yield the band structure shown in Figure 1.1c [7]. In the vicinity of the K points ($|\mathbf{q}| \ll |\mathbf{k}| = k$) the energy dispersion is given by

$$E_{\pm} = \pm \hbar v_F |\mathbf{q}| \tag{1.1}$$

where the constant Fermi velocity $v_F \approx 10^6$ m/s does not depend on the energy or momentum. The linear relation between energy and momentum revealed by this equation, as well as the intersection of the valence and conduction bands at the Dirac points, gives rise to the Dirac cone representation of graphene's bands, shown in Figure 1.1d. Another important property depicted in this Figure is the vanishing density of states (DOS) at the Dirac points: graphene can therefore be described as a zero band-gap semiconductor, or a semi-metal with no band overlap. Graphene's linear energy-momentum relation implies massless charge transport particles, and a square root relation between their energy and the charge carrier density n, given by

$$E = \hbar v_F \sqrt{\pi n} \tag{1.2}$$

The charge carriers can thus be described as a two-dimensional gas of massless Dirac-like particles [1, 8].

Graphene is said to be intrinsic, i.e. undoped, when its Fermi energy is located at the Dirac point. When the Fermi energy is situated above or below the Dirac point, as shown in the insets in Figure 1.2d, the graphene is n or p-doped. Possible doping sources include the substrate the graphene sits upon, ambient contaminants such as oxygen and water vapor, structural defects, and impurity remnants from fabrication and transfer processes, among others. Chemical species can also be used to control graphene's doping level, as will be discussed in the next section.

The Fermi energy of graphene can also be modulated in a graphene field effect transistor (GFET), by applying a gate voltage to the device, which varies its charge density n, and measuring the resulting conductivity change, as shown in Figure 1.2a (GFET device technicalities will be discussed in greater detail in the next chapter). At the Dirac point, graphene's π bands intersect, with the density of states (DOS) going to zero, as seen in Figure 1.1. Therefore, when the Fermi energy is situated at the Dirac point, also known as the charge neutrality point (CNP), the conductivity will be at a minimum. The Fermi energy can be modulated to be above or below the CNP, resulting in carrier transport occurring via electrons or holes, respetively. As mentioned earlier, the intersecting valence and conduction bands at the Dirac points gives graphene a semi-metallic character. Although conductivity should tend towards zero at the Dirac point, due to the vanishing DOS, a minimum non-zero conductivity is always measured, due to the presence of electron-hole puddles arising from

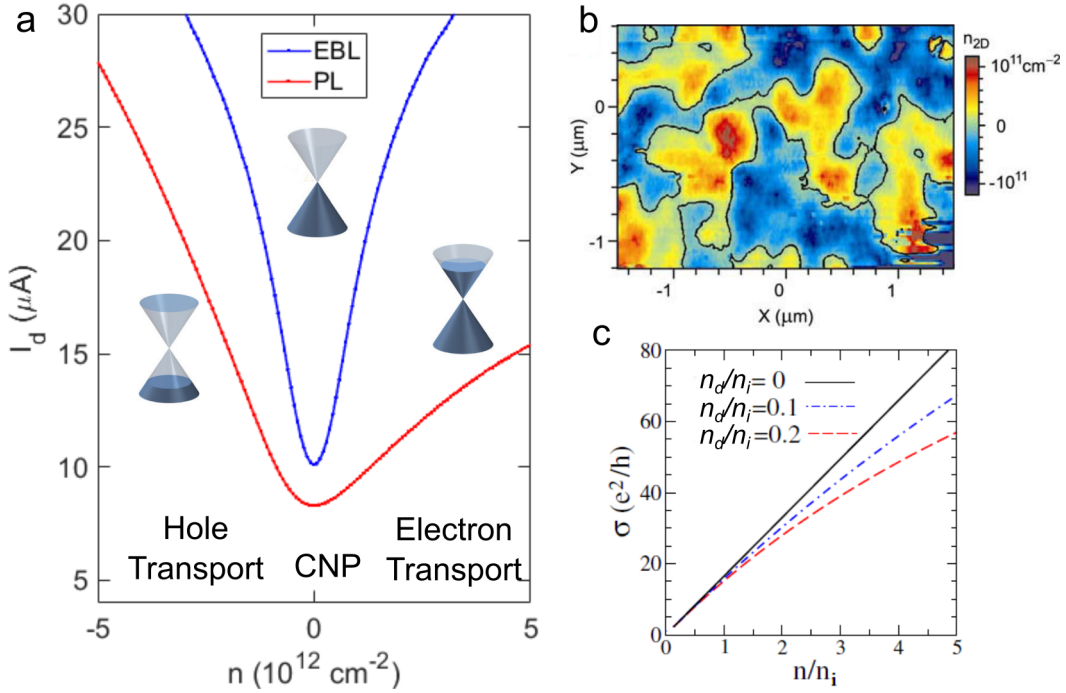

Figure 1.2: **a** Transport curves showing current versus charge density, in GFET devices fabricated during this thesis via electron beam lithography (EBL) and photolithography (PL). **b** Charged impurity electron-hole puddles measured in graphene on a SiO_2 substrate via scanning-single electron transistor. Adapted from [9]. **c** Calculations showing the effect of short and long range scattering center density (n_d and n_i, respectively) on the conductivity of graphene. Adapted from [10]

the substrate or intrinsic corrugations on the graphene. These puddles, imaged via scanning single-electron transistor, can be seen in Figure 1.2b [9], and are responsible for the transport behavior near the Dirac point [1, 8]. Unfortunately, graphene's finite conductivity minimum limits the ON/OFF ratio of GFETs [10, 11] (the ratio between the maximum and minimum conductivity), precluding it from being used for digital logic applications.

Extrinsic limits to graphene's mobility include impurity puddles, charged impurity centers (either between the graphene and the susbtrate or due to contaminants on the graphene surface), lattice disorder, and substrate surface phonons, which all contribute to the scattering of charge carriers. Under experimentally relevant conditions (including ultra high vacuum), phonon scattering, though more important at higher temperatures [12], is dwarfed by long range Coulomb scattering from charged impurities, which is the dominant scattering mechanism present in graphene [8]. Coulomb scattering is responsible for the linear dependence of conductivity vs. charge density away from the Dirac point (i.e. for n much larger than the density of charged impurities n_i). This linear dependence is seen in the black curve in Figure 1.2c, which has been calculated only taking into account long range Coulomb scattering. Short range scattering due to lattice defects and surface rippling, with a density

n_d, also play a role [8]. Calculations indicate that as the number of short range scattering centers due to disorder increases, the linear conductivity is flattened out for higher charge carrier densities, as seen in the blue and red curves of Figure 1.2c [10].

The blue curve in 1.2a, measured in a device fabricated using electron beam lithography (EBL), shows the aforementioned characteristics: a finite minimum conductivity at the Dirac point, with the linear conductivity starting to flatten out for increasing charge carrier densities. The red curve in Figure 1.2a shows the electrical characteristics of a graphene device measured after fabrication via photolithography. As will be discussed further in the Graphene Technology chapter, photoresist residues remaining from the fabrication process act as p-dopants, and introduce scattering centers in the device channel. The supression of conduction in the electron transport channel is due to the p-doping nature of the photoresist residues. In the model proposed by Farmer et al, chemical dopants such as the photoresist introduce a long range Coulomb scattering potential in the graphene channel [13]l. This potential results in a misalignment of the neutrality point at the electrode/graphene interface, forming a barrier to the injection of charge carriers. Dopants of p (n) type will therefore form a barrier against the injection of electrons (holes) [13]. Depending on the exact nature of the potential barrier introduced by the impurities, and their contribution to the overall charged impurity concentration n_i, the dopant chemical species may increase or decrease the mobility of the sample [14].

1.3 Chemical Properties

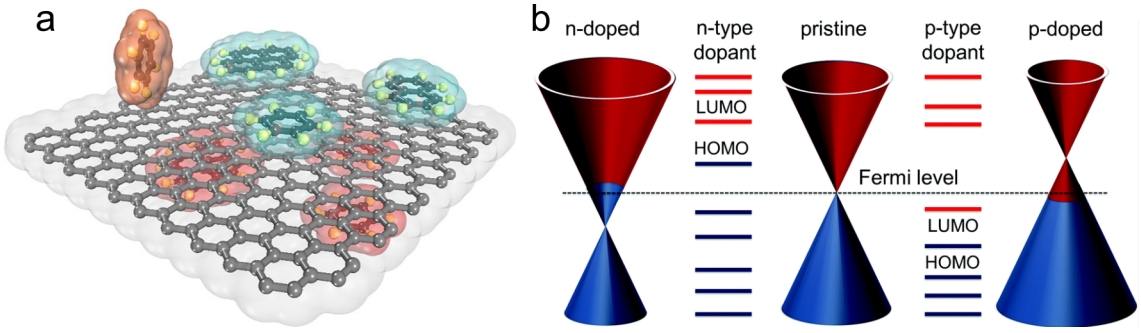

Figure 1.3: **a** Non-covalent $\pi-\pi$ and CH–π interactions between graphene and other molecules [15]. **b** Illustration showing the relationship between the dopant properties of molecules adsorbed on graphene and their HOMO-LUMO levels [16].

Chemical functionalization of graphene is of great interest, opening the possibility to the modification of graphene's properties, resulting in a slew of possible applications that would otherwise be impossible with pristine graphene. Graphene, whose π bonds are responsible for its chemical interactions, has been succesfully functionalized through both covalent and non-covalent means. Non-covalent interactions with graphene are governed by dispersive forces, such as $\pi-\pi$ interactions for molecules with a short to extended π system (i.e. aromatic molecules). Molecules with a hydrophobic character, on the other hand, will dispersively

interact with graphene's π orbitals via their CH bonds. Both of these types of non-covalent interactions are shown in Figure 1.3a. The dissociation energies of these interactions are relatively weak, below 50 kJ/mol (0.52 eV per C atom), and therefore are often reversible. Unlike the case of covalent bonding, none of the bonds within the graphene lattice are broken in non-covalent interactions, leaving graphene's mechanical and electrical properties largely intact [15]. Charge transfer between the graphene and other compounds can strengthen the non-covalent interactions. The position of graphene's Fermi energy E_F with respect to the highest occupied molecular orbital (HOMO) and lowest unoccupied molecular orbital (LUMO) of the adsorbed compound will determine the nature of the charge transfer and subsequent doping. If E_F is located below the dopant's HOMO, an electron will be transferred from the compound to the graphene, resulting in graphene n-doping. On the contrary, if the LUMO is below E_F, the dopant will accept an electron, p-doping the graphene [16]. This charge transfer relationship is schematically represented in Figure 1.3.

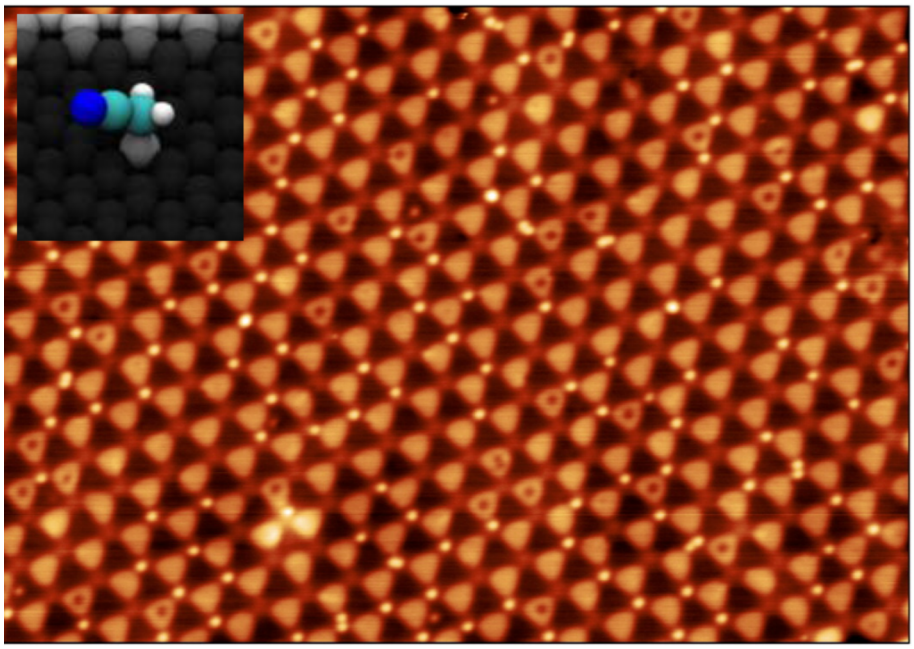

Figure 1.4: **a** STM image of epitaxial graphene on ruthenium functionalized with acetonitrile radicals, showing long range, ordered covalent patterning of graphene. Image size 66×40 nm. INSET: Schematic of acetonitrile radical covalently bonded to a carbon atom in the graphene lattice [17].

Covalent bonding in graphene, which generally proceeds via the reaction of its C=C bonds with free radicals of carbenes, nitrenes or arynes, is much stronger than the aforementioned non-covalent interactions. The formation of a covalent bond typically proceeds via the attack of the sp^2 hybridized carbon atom, resulting in the formation of a covalent bond with an sp^3 hybridization. This type of bonding, which can be detected via Raman spectroscopy, generally results in a decrease in the mobility of the graphene [16]. The

graphene substrate plays an important role in graphene's propensity to react and form covalent bonds. Wang et al. showed that substrates which produce larger electron-hole impurity puddle potentials will cause the graphene to be more reactive [18]. For example, relatively rough SiO_2 is more reactive than ultra-flat 2D hexagonal boron nitride [18]. The importance of the substrate on reactivity was also recently shown in the Gr/Ru system, in which a Moiré pattern is formed due to the lattice mismatch between the graphene and ruthenium. Consequently, a regular potential landscape is formed on the graphene surface, with the valleys of the Moiré pattern being particularly reactive to the formation of covalent bonds with acetonitrile free radicals, as shown in the inset of Figure 1.4. The resulting long-range, periodic, highly selective covalent functionalization of graphene is shown in the STM image of Figure 1.4c. Patterning of this sort has been predicted to be a possible method of opening a band gap in the graphene band structure [19].

Bibliography

[1] A.H. Castro Neto, F. Guinea, N.M.R. Peres, K.S. Novoselov, and A.K. Geim. The electronic properties of graphene. *Reviews of Modern Physics*, 81:109–162, 2009.

[2] K.S. Novoselov, A.K. Geim, S.V. Morozov, D. Jiang, Y. Zhang, S.V. Subonos, I.V. Grigorieva, and A.A. Firsov. Electric field effect in atomically thin carbon films. *Science*, 306:666–669, 2004.

[3] Y. Hernandez, V. Nicolosi, M. Lotya, F.M. Blighe, Z. Sun, S. De, I.T. MvGovern, B. Holland, M. Byrne, Y.K. Gun'ko, J.J Boland, P. Niraj, G. Duesberg, S. Krishnamurthy, R. Goodhue, J. Hutchison, V. Scardaci, A.C. Ferrari, and J.N. Coleman. High-yield production of graphene by liquid-phase exfoliation of graphite. *Nature Nanotechnology*, 3:563–568, 2008.

[4] S. Bae, H. Kim, Y. Lee, X. Xu, J. Park, Y. Zhen, J. Balakrishnan, T. Lei, H.R. Kim, Y.I. Song, Y. Kim, K.S. Kim, B. Özyilmaz, J. Ahn, B.H. Hong, and S. Ilijima. Roll-to-roll production of 30-inch graphene films for transparent electrodes. *Nature Nanotechnology*, 5:574–578, 2010.

[5] W. Li, M. Zhao, X. Zhao, Y. Xia, and Y. Mu. Hydrogen saturation stabilizes vacancy-induced ferromagnetic ordering in graphene. *Physical Chemistry Chemical Physics*, 12:13699–13706, 2010.

[6] T. Ando. The electronic properties of graphene and carbon nanotubes. *NPG Asia Materials*, 1:17–21, 2009.

[7] P.R. Wallace. The band theory of graphite. *Physical Review*, 71:622–634, 1947.

[8] S. Das Sarma, S. Adam, E. H. Hwang, and E. Rossi. Electronic transport in two-dimensional graphene. *Reviwes of Modern Physics*, 83:407–470, 2011.

[9] J. Martin, N. Akerman, G. Ulbricht, T. Lohmann, J.H. Smet, K. von Klitzing, and A. Yacoby. Observation of electron–hole puddles in graphene using a scanning single-electron transistor. *Nature Physics*, 4:144–148, 2008.

[10] E.H. Hwang, S. Adam, and S. Das Sarma. Charge transport in two-dimensional graphene layers. *Physical Review Letters*, 98:186806, 2007.

[11] Y.-W. Tan, Y. Zhang, K. Bolotin, Y. Zhao, S. Adam, E.H. Hwang, S. Das Sarma, H.L. Stormer, and P. Kim. Measurement of scattering rate and minimum conductivity in graphene. *Physical Review Letters*, 99:246803, 2007.

[12] J.-H. Chen, C. Jang, S. Xiao, M. Ishigami, and M. S. Fuhrer. Intrinsic and extrinsic performance limits of graphene devices on SiO_2. *Nature Nanotechnology*, 3:206–209, 2008.

[13] D.B. Farmer, R. Golizadeh-Mojarad, V. Perebeinos, Y-M. Lin, G.S. Tulevski, J.C. Tsang, and P. Avouris. Chemical doping and electron-hole conduction asymmetry in graphene devices. *Physical Review Letters*, 98:186806, 2009.

[14] E.H. Hwang, S. Adam, and S. Das Sarma. Transport in chemically doped graphene in the presence of adsorbed molecules. *Physical Review B*, 76:195421, 2007.

[15] V. Georgakilas, J.N. Tiwari, K.C. Kemp, J.A. Perman, A.B. Bourlinos, K.S. Kim, and R. Zboril. Noncovalent functionalization of graphene and graphene oxide for energy materials, biosensing, catalytic, and biomedical applications. *Chemical Reviews*, 116:5464–5519, 2016.

[16] K.S. Mali, J. Greenwood, J. Adisoejoso, R. Phillipson, and S. De Feyter. Nanostructuring graphene for controlled and reproducible functionalization. *Nanoscale*, 7:1566–1585, 2015.

[17] J.J. Navarro, S. Leret, F. Calleja, D. Stradi, A. Black, R. Bernardo-Gavito, M. Garnica, D. Granados, A.L. Vázquez de Parga, E. Pérez, and R. Miranda. Organic covalent patterning of nanostructured graphene with selectivity at the atomic level. *Nano Letters*, 16:355–361, 2016.

[18] Q.H. Wang, Z. Jin, K. K. Kim, A.J. Hilmer, G.L.C. Paulus, C.-J. Shih, M.-H. Ham, J.D. Sanchez-Yamagashi, K. Watanabe, T. Taniguchi, J. Kong, P. Jarillo-Herrero, and M.S. Strano. Understanding and controlling the substrate effect on graphene electron-transfer chemistry via reactivity imprint lithography. *Nature Chemistry*, 4:724–732, 2012.

[19] M. Dvorak, W. oswald, and Z. Wu. Bandgap opening by patterning graphene. *Scientific Reports*, 3:2289, 2013.

Chapter 2

Experiments and Methods

The experimental techniques, processes and machines used throughout this thesis to produce, fabricate and characterize samples are outlined in this chapter. Graphene growth via CVD and its transfer to arbitrary substrates is introduced, along with the main lithographic fabrication processes used for fabricating devices. Frequently used characterization techniques are subsequently explained, including electrical transport, Raman spectroscopy and optical measurements.

2.1 Graphene Production

2.1.1 CVD Growth

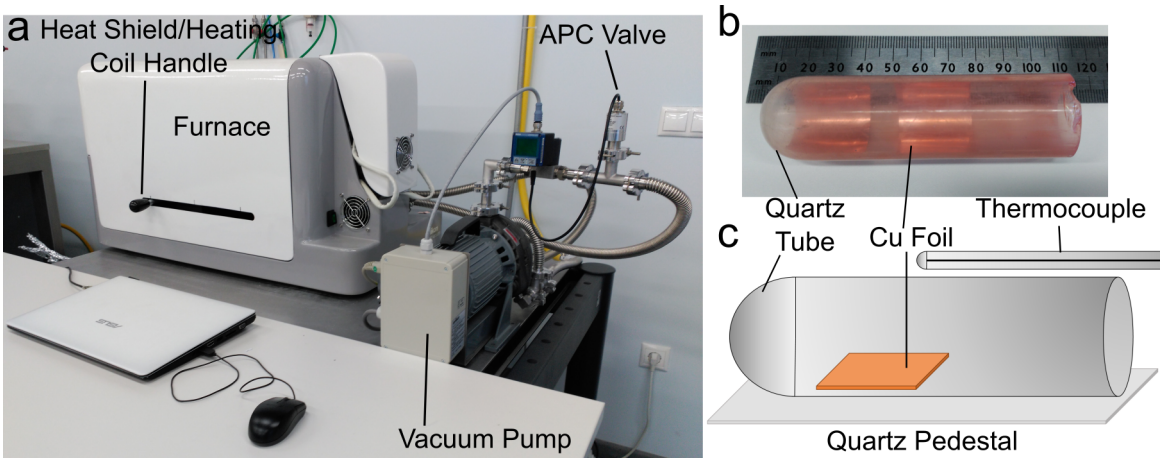

Figure 2.1: **a** CVD growth furnace showing heat shield/heating coil handle, along with rotary vacuum pump. An APC valve at the pump inlet is used to control the pressure within the furnace. **b** Quartz tube used to load the copper foils. **c** Schamatic showing quartz tube placed atop quartz pedestal table for loading into the furnace. The sample thermocouple is also visible.

A Nanoinnova Technologies CVD furnace is used to carry out the graphene growth process. The inside of the furnace consists of a 58 mm quartz tube surrounded by a moveable heat shield. Resistive heater coils line the inside of the heat shield, which can be manually moved using a handle protuding from the side of the furnace, as shown in Figure 2.1a. During growth, the heat shield is positioned so as to surround the quartz tube. Upon growth completion, the heat shield/heating coils are moved away from the quartz tube to

initiate a rapid cooling (greater than 200° C per minute) of the quartz tube and sample. The heater temperature is controlled by the user using a programmable logic controller (PLC) and specialized commercial computer software. Two thermocouples are present inside the furnace: one next to the heaters, used for controlling the temperature setpoint set by the user through the commercial software, and one in the middle of the quartz tube near the copper foil sample, as seen in Figure 2.1c. A scroll vacuum pump, which reaches a base pressure of about 3 mbar with no gases flowing into the furnace, is used to evacuate the quartz tube inside the furnace. An analog pressure controller (APC) valve at the entrance of the pump is used to regulate the pressure inside the furnace. Hydrogen, argon and methane gases can be simultaneously introduced into the furnace. Their flow rate is regulated by three mass flow controllers (MFCs), controlled via the previously mentioned software program.

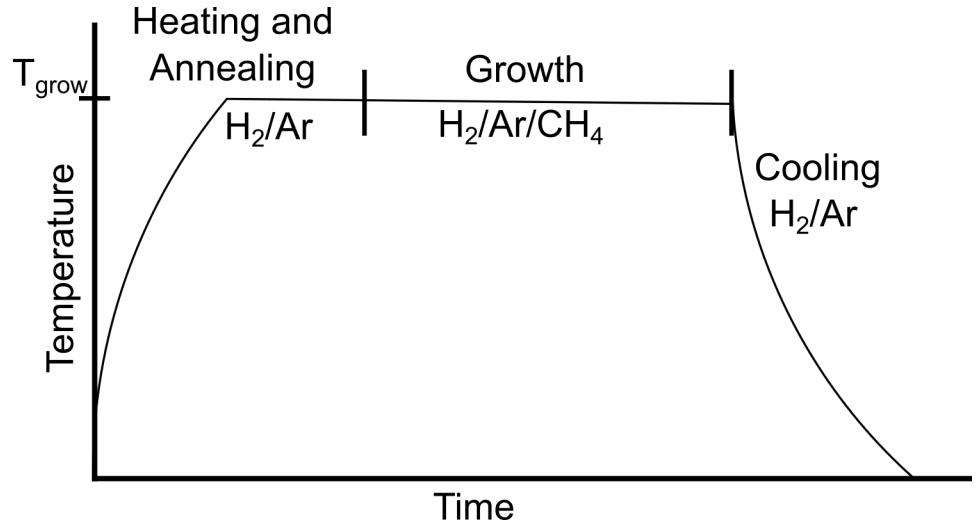

Figure 2.2: Schematic of CVD growth recipe, showing different stages of process.

Graphene growth is carried out on 99.8% purity 25 µm thick copper substrates (Goodfellow CU000340). Foils are cut to the appropriate size and placed inside a 22 mm inner diameter quartz tube (picture and schematic in Figure 2.1b and c, respectively). This 22 mm quartz tube is placed on a supporting quartz pedestal, next to the sample thermocouple (Figure 2.1c), and inserted into the furnace. After closing the furnace's stainless steel opening, which is sealed by a Kalrez o-ring, the furnace growth chamber can be evacuated. The basic growth process, depicted in Figure 2.2, begins with heating and annealing steps, in which the furnace temperature is raised to 1000° C in the presence of argon and/or hydrogen. During the subsequent growth stage, methane is introduced within a background atmosphere of hydrogen and argon. Having completed growth, the methane is turned off and the sample is cooled rapidly in argon or hydrogen. Typical growth recipes are presented in Appendix A; the physical mechanisms governing CVD graphene growth as well as the optimization of the growth recipes are presented in the Graphene Technology chapter.

2.1.2 Graphene Transfer

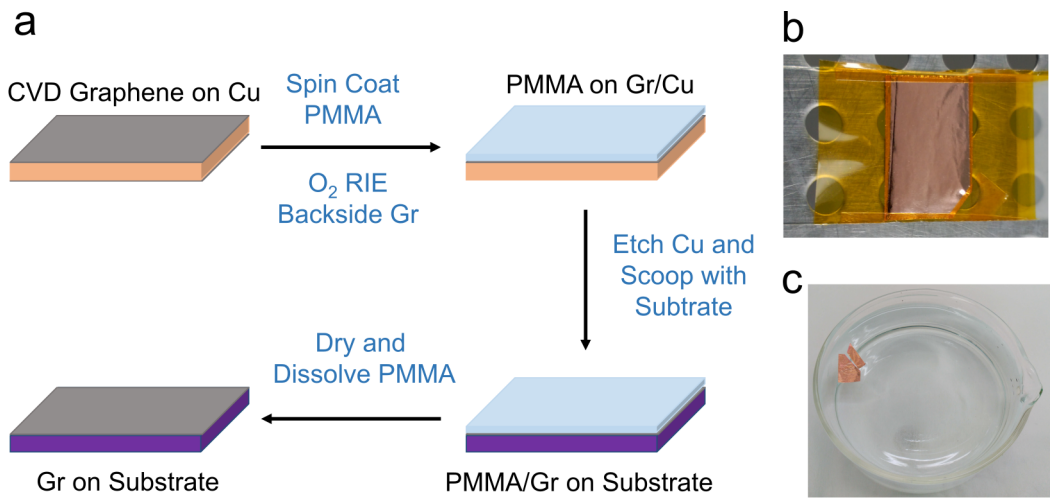

Figure 2.3: **a** Schematic of the basic PMMA mediated, wet chemical etching process for transferring CVD graphene onto arbitrary substrates. **b** Cu/Gr sample on glass slide held in place by Kapton frame. **c** Cu/Gr/PMMA stack floating atop ammonium persulfate etchant.

A poly(methyl methacrylate) (PMMA) mediated, wet chemical etching process is used to transfer the CVD graphene film onto the desired substrate [1]. A summary of the main steps of the process are presented in Figure 2.3a. The first step in the process consists in spinning a PMMA layer onto the Gr/Cu sample. In order to carry out this spin coating, the Gr/Cu is mounted onto a glass slide using Kapton tape (Figure 2.3b). To ensure a clean, residue free transfer, the graphene on the backside of the Cu/Gr sample is then removed in an oxygen plasma attack. In order to etch the copper substrate, the sample is floated in an ammonium persulfate wet etch, with the PMMA side facing up, as shown in Figure 2.3c. The sample is cleaned by transferring it to successive deionized water baths, prior to being scooped from the water surface with the desired substrate. After adequately drying the liquid present between the graphene and the substrate, the PMMA is dissolved in acetone, completing the transfer process. Great care must be taken in order to successfully complete the transfer process without damaging or contaminating the graphene. A more detailed description of the steps comprising an optimized transfer process is given in the Graphene Technology chapter and in Appendix B.

2.2 Fabrication

2.2.1 Photolithography

2.2.1.1 Instrumentation and Optics Basics

Photolithography, also known as optical lithography, is a microfabrication process in which light, typically ultraviolet, is used to project a pattern onto a substrate via a light sensitive

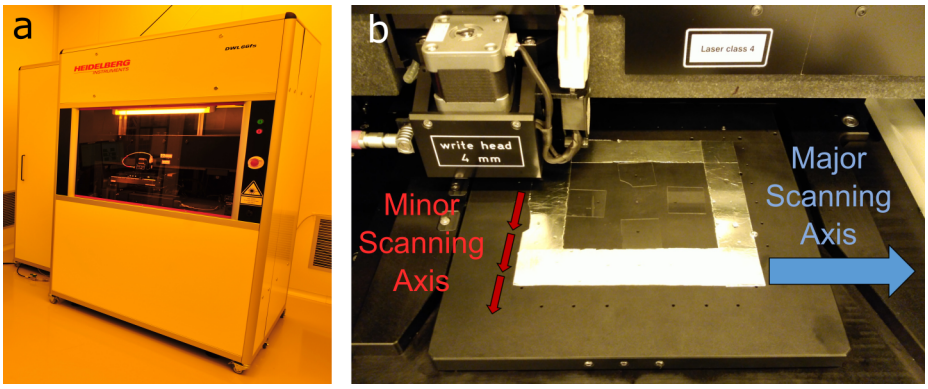

Figure 2.4: **a** Heidelberg DWL 66FS machine used for photolithography throughout this thesis. **b** Stage and writehead of Heidelberg DWL 66FS machine used for maskless laser writing photolithography, showing the major and minor raster scanning axes.

polymer, known as photoresist. By selectively removing parts of the photoresist, windows can be opened to expose the underlying substrate to other microfabrication processes, such as wet or dry etching, metallization and film deposition. Standard optical lithography uses masks, which project the desired pattern onto the photoresist through a selective spatial blocking of light. In this thesis, however, a maskless form of optical lithography was used, in which a laser was used to directly write the design pattern onto the photoresist. The machine used throughout this thesis is a Heidelberg DWL 66FS, shown in Figure 2.4a, with a laser excitation wavelength of 405 nm. The sample is placed on the machine stage, seen in Figure 2.4b, and the laser turned on and off selectively as the stage is moved below the laser in a raster scanning mode. The desired laser focus setting is maintained via a PID controlled optical focus or pneumatic pressure sensor.

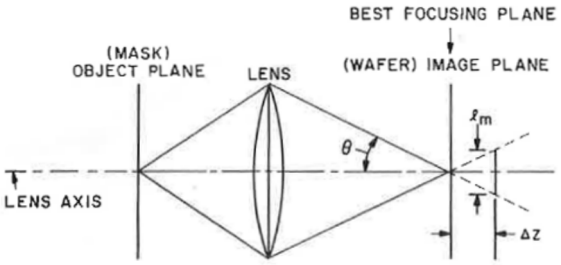

Figure 2.5: Basic schematic of optical setup for focusing laser beam. Adapted from [2].

The resolution, or the smallest feature size that can be projected onto the photoresist with a given optical system, is given by

$$l_m = k_1 \frac{\lambda}{NA} \tag{2.1}$$

where k_1 is an experimental parameter, on the order of 1, that depends on the lithography system and resist properties, λ is the exposure light wavelength and NA is the numerical aperture of the objective lens being used to focus the exposure light. A simplified schematic

of an optical setup used for photolithography is shown in Figure 2.5b. The numerical aperture is a function of the half angle θ, expressed as

$$NA = n \sin\theta, \tag{2.2}$$

where n is the index of refraction of the medium ($n = 1$ for air). The optical of focus δz can be expressed as

$$\delta z = \frac{\pm l_m}{2\tan\theta} \approx \frac{\pm l_m}{2\sin\theta} = \pm\frac{k_1 n\lambda}{2(NA)^2} \tag{2.3}$$

where the small angle approximation has been used for the $\tan\theta \approx \sin\theta$ approximation. Although an increase in the numerical aperture NA will improve the the resolution of the system (equation 2.1), it will also rapidly reduce the depth of focus (equation 2.3). Varying the focus is one of the parameters that can be used to achieve an adequate resist edge profile (as discussed below). However if the depth of focus is too small, the entire process will be overly sensitive upon difficult to control process parameters, such as small variations in the photoresist thickness. Reducing the exposure wavelength λ will also reduce the resolution, whilst having a smaller effect on the depth of focus than an increase in the numerical aperture [2].

2.2.1.2 Photoresists

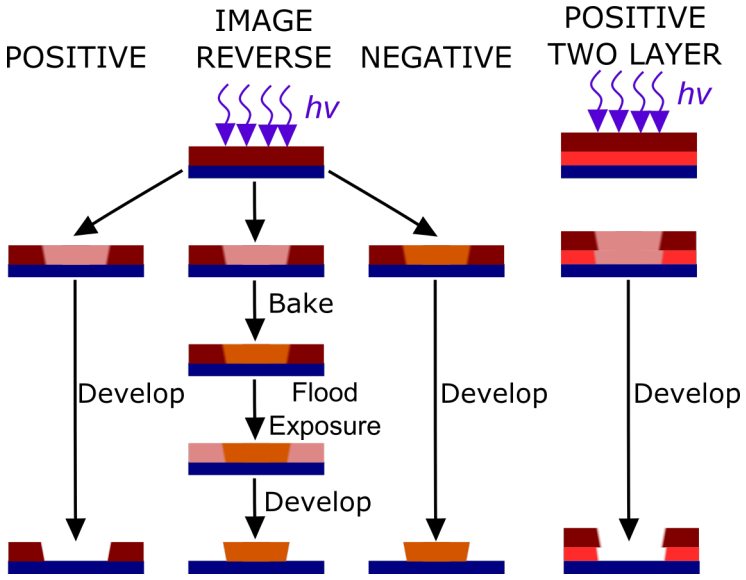

Figure 2.6: Basic flowchart showing the different characteristics and process steps for positive, negative, image reverse and positive two layer photoresists.

Photoresists are comprised of a polymer resin whose chain length, and proportional molecular weight, determine its solubility in certain solvents, known as developers. When a photoresist is exposed to a dose of UV light greater than a certain threshold value, a photoactive compound within the resist induces a change in the resin polymer chain length and

molecular weight, dramtically altering its solubility in developer. For positive photoresists, UV exposure above the threshold value causes chain scission, a process in which the resin chains are broken up into shorter components with lower molecular weight, resulting in increased developer solubility. Negative photoresists function in the opposite way: exposure to UV light beyond the threshold value causes the resin polymer chains to crosslink, increasing their molecular weight and reducing their solubility.

Photoresist is deposited onto substrates by spin coating, after which the organic solvent contained within the resist is evaporated by heating to temperatures around 100° C. In positive photoresists, areas exposed to UV light can be subsequently removed with appropriate developers. The photoactive compound in the positive photoresists used in this thesis (AZ 1512HS and AZ 1505 from MicroChemicals) is DiazoNaphtho-Quinone-sulphonates (DNQ), and the polymer resin is a phenol formaldehyde polymer known as Novolac. Upon exposure to UV light, the DNQ molecules transform into a carboxylic acid, inducing chain scission in the Novolac and increasing the solubility of the resist in alkaline developer solutions by several orders of magnitude. The transformation of DNQ into carboxylic acid requires the presence of water, thereby necessitating a minimum environmental humidity for water diffusion into the the resist within a reasonable timeframe. In addition, the reaction releases nitrogen gas, which can result in bubble formation within the resist for excessively high exposure doses. In image reversal resists, UV exposure also converts DNQ molecules into carboxylic acid and induces Novolac chain scission. However, a subsequent baking step causes crosslinking between carboxylic acid molecules and the Novolac, significantly reducing the resist solubility. Afterwards, a flood exposure of the entire substrate results in exposure of the non-crosslinked zones, which can then be removed by the developers [3]. This process is shown in Figure 2.6. The image reversal photoresist used in this thesis was AZ 5214, also from MicroChemicals.

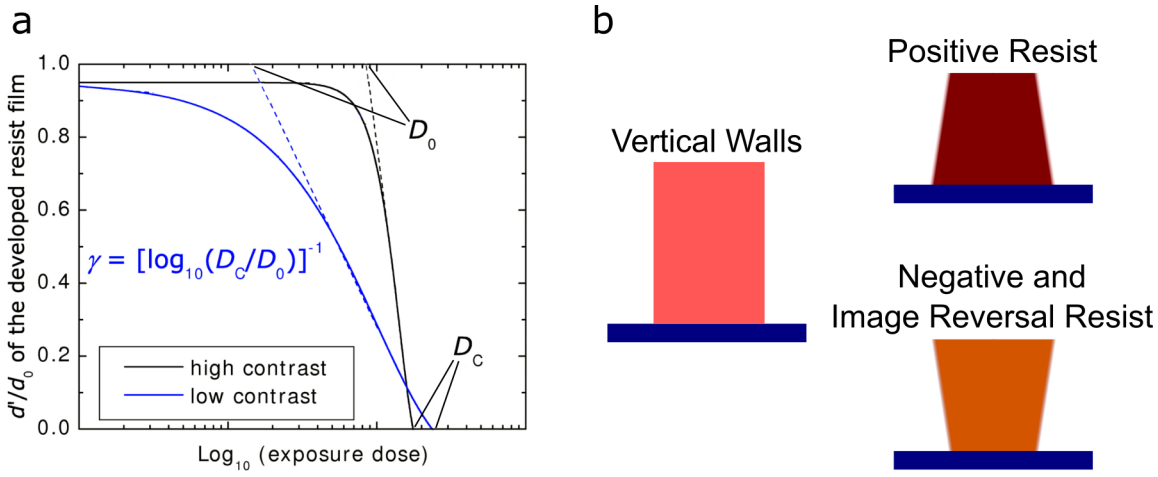

Figure 2.7: **a** Plot showing proportion of photoresist development vs. exposure dose, and the characteristics used to calculate the contrast. Adapted from [3]. **b** Vertical sidewalls compared to eroded sidewalls obtained using positive and negative or image reversal photoresists.

UV exposure of negative photoresists induces a crosslinking of the resist resin molecules. The crosslinked molecules are insoluble in the developer due to their high molecular weight. However, they are more prone to absoring water present in the developer, limiting their resolution [2]. Certain processes may necessitate two resist layers to be used (Figure 2.6). A highly sensitive resist is placed below the "normal" resist. UV light causes a large volume of the highly sensitive resist to become exposed, resulting in an undercut wall pattern.

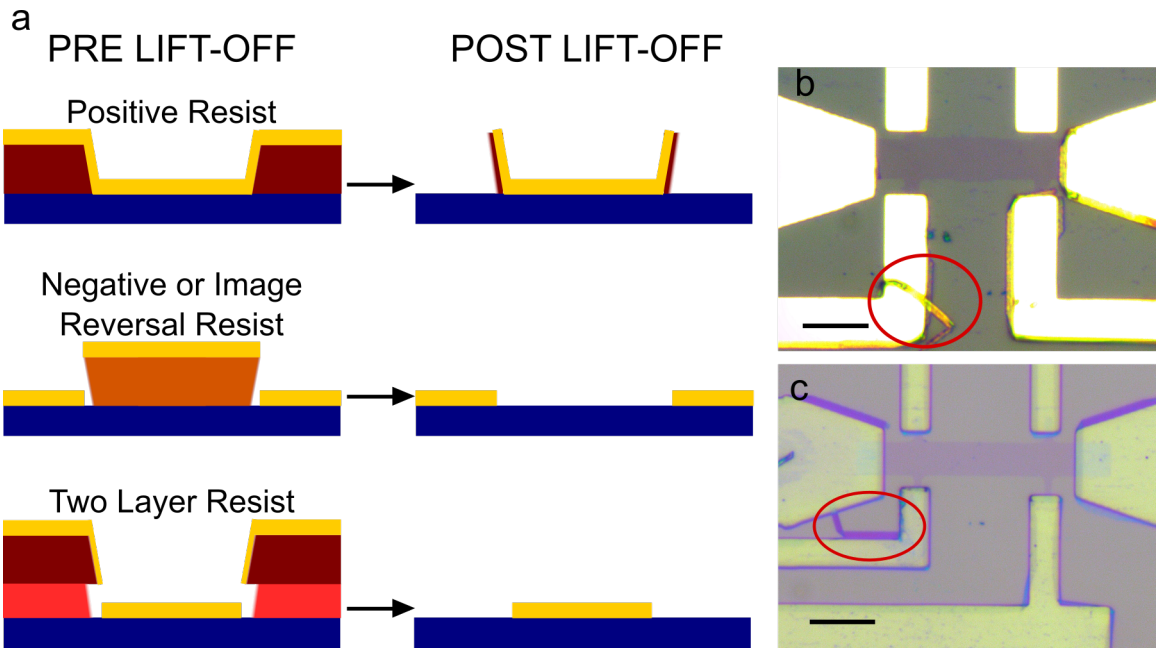

Figure 2.8: **a** Profiles and sidewalls obtained after metal evaporation for different types of photoresists, and the resulting lift-off process. **b** Graphene devices showing photoresist/metal wires peeling off from Cr/Au electrodes, highlighted in red circles. This is a result of a poor lift-off resulting from the use of a positive photoresist.

The three basic types of photoresist (positive, negative and image reversal) may be used to obtain different wall profiles, as depicted in Figure 2.7b, which may be desirable for specific fabrication processes. The likelihood of a resist to deviate from vertical sidewalls is characterized by its contrast. In a positive photoresist, the contrast is a measure of its ability to maintain its insolubility for low exposure doses, while rapidly achieving full solubility beyond a threshold exposure dose [2]. This characteristic is represented by the curves shown in Figure 2.7a, showing the proportion of developed exposed resist versus the exposure dose (on a logarithmic scale). The contrast is defined as

$$\gamma \equiv \left[\log_{10}\left(\frac{D_c}{D_0}\right)\right]^{-1} \tag{2.4}$$

where D_c is the exposure dose required for complete resist dissolution, and the threshold D_0 as the dose where the tangent to the curve at D_c intercepts 1. A high contrast resist is necessary in order to obtain the vertical sidewalls shown in Figure 2.7b. Otherwise, the

slanted sidewall profiles (known as erosion) seen in the figure will occur for positive and negative/image resist profiles [3]. Indeed, for high contrast resists such as the ones used throughout this thesis, a certain amount of erosion (dependent on the dose intensity, focus, resist age and resist moisture content) is inevitable.

Some resist wall erosion is not necessarily detrimental; indeed, certain processes, such as metal evaporation, may benefit from it. If a positive photoresist is used, even a small amount of erosion will cause metal to build up along the sidewalls. When the photoresist is removed using solvents such as acetone, in a process known as liftoff, the resist and metal deposited along the sidewalls will be especially difficult to remove, remaining stuck to the side of the metallic pads, as shown in Figure 2.8a. Sometimes these metal covered sidewalls may peel off like wires (Figure 2.8b), even causing short circuits between the metallic pads (Figure 2.8c).

2.2.2 Electron Beam Lithography

Electron beam lithography (EBL) uses a scanning focused electron beam to project the desired patterns onto an electron sensitive polymer resist. Condenser lenses are utilized to focus the electron beam down to a spot size on the order of nm. Many of the same attributes used to describe photoresists (resolution, positive/negative sensitivity, etc.) are also applicable to electron sensitive resists. The most common positive electron resist, and the one used in this thesis, is PMMA. Apart from being sensitive to electrons, PMMA is also sensitive to and can be patterned using deep ultraviolet (DUV) light, which technically also makes it a photoresist. DUV light sources, however, are not commonly utilized in academic research settings, and were not used throughout this thesis. As such, for the sake of argument and brevity, when photoresists are mentioned throughout this manuscript, it will refer to the UV sensistive photoresists, and not the electron and DUV sensistive resists such as PMMA. A double layer resist stack consisting of two types of PMMA with different sensitivities, of the kind seen in Figure 2.6, was also utilized for metallization processes requiring a lift-off. Apart from being a direct write method, like laser writing photolithography, the main advantage of EBL is the sub-10 nm resolution that can be obtained. Another advantage with regards to graphene devices is that the PMMA is a mild dopant and contaminant compared to the resists used in UV photolithography. The main disadvantage of EBL is the long writing times required. For the typical device geometries used in this thesis, the writing times were on the order of hours, compared to minutes for direct write laser photolithography. For this reason, the vast majority of the devices in this thesis were fabricated using this latter method.

The machine used in this thesis for EBL was a Zeiss Auriga Cross Beam Focused Ion Beam Scanning Electron Microscope. The pattern generator used for projecting the design pattern onto the PMMA via the electron beam is an Elphy Multibeam, with a 400 Hz digital signal processor and two 16-bit digital to analog converters.

2.3 Characterization

2.3.1 Electrical Transport

2.3.1.1 Instrumentation

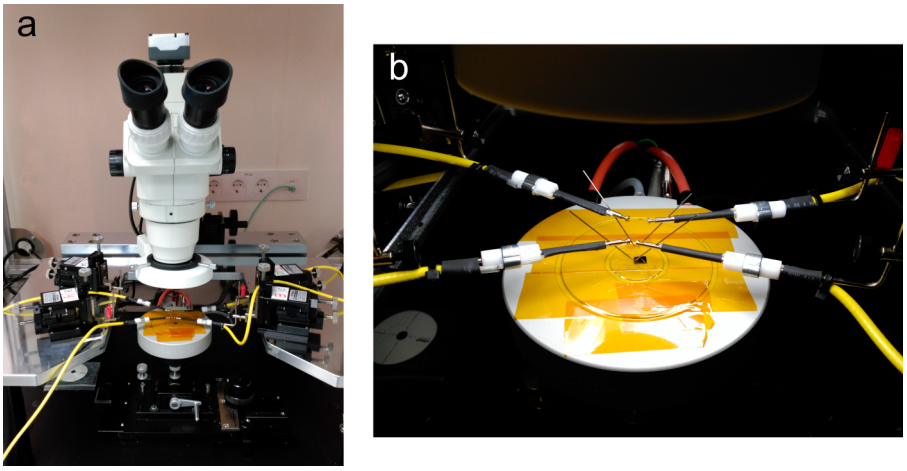

Figure 2.9: **a** Image of the probe station showing stereo zoom microscope and three-axis micrometer aligners for moving the probe needles. **b** Closeup of probe needles contacting a sample.

Most electrical transport measurements in this thesis were carried out under ambient conditions, using a Keithley 4200-SCS with four independent Source Measuring Units (SMUs). Each SMU is connected to a probe station needle, shown in Figure 2.9b. The sample is mounted on a stage, and up to four needles can be connected, each able to source current or voltage, and measure current and voltage simultaneously. The sample rests on a three axis moveable stage, and can be observed by using a mounted, moveable optical stereo zoom microscope (Figure 2.9a). Additionally, each probe station needle could be moved independently using three-axis micrometer aligners. Two point gated measurements were carried out using two probe needles contacted to the two device electrodes, plus another needle for the gate electrode. Four point gated measurements used the four needles on the four device electrodes (three connected to SMUs and one connected to common ground), and one additional gate electrode, connected to the last SMU, and contacted to the sample with conductive silver paint.

2.3.1.2 Graphene Field Effect Transistors

The charge accumulation of a field effect transistor can be modeled as a parallel plate capacitor. In this model, one of the capacitor plates is the metallic gate and the other plate is the device channel, in this case the graphene. For most of the measurements carried out in this thesis, a back gate configuration was used, where the graphene channel was separated from the bottom, degenerately doped silicon gate by a 285 nm SiO_2 layer. Although silicon

is a semiconductor, it can behave metallically when it is degenerately doped, i.e. doped to such a high concentration that its Fermi energy is either above the conduction band or below the valence band. Top gating can also be implemented, and is done so for the majority of metal-on-semiconductor field effect transistor (MOSFET) devices, with an oxide grown on top of the device channel, and a metallic gate electrode evaporated on top of the oxide.

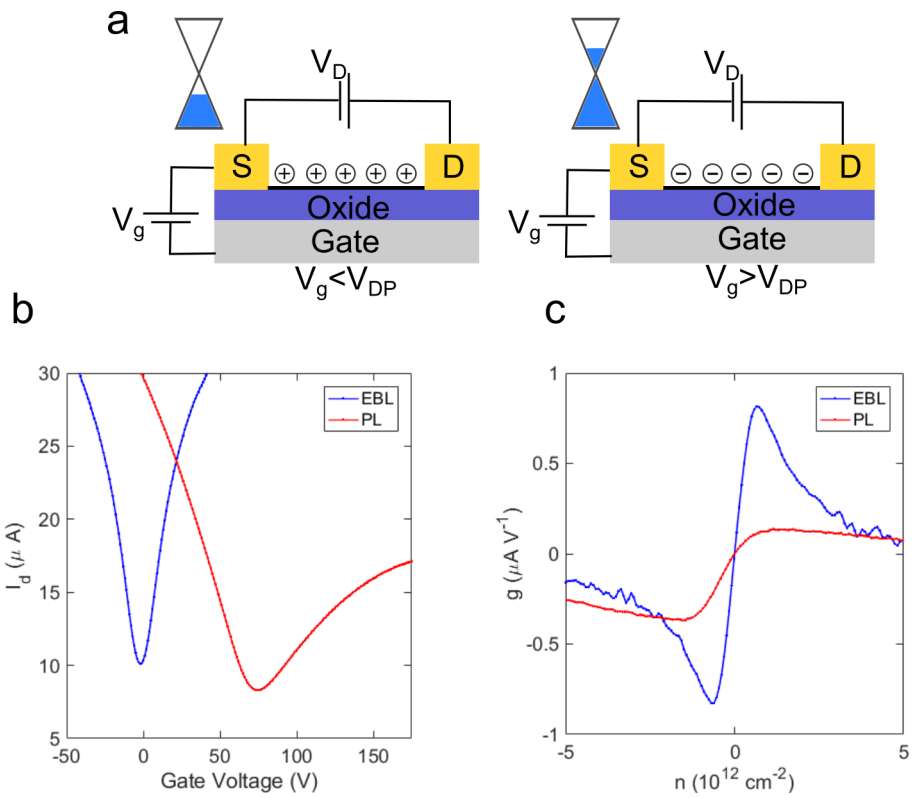

Figure 2.10: **a** Schematic of a graphene field effect transistor using a back-gate configuration. **b** Transfer curves showing GFET drain current versus gate voltage, for devices fabricated via electron beam lithography (EBL) and photolithography (PL). **c** Transconductance of the curves shown in **b**.

When a voltage is applied at the gate, charge carriers accumulate at the gate/oxide interface. These are then screened by charge carriers of the opposite polarity at the device channel. The carrier density n in a graphene field effect transistor (GFET) channel, expressed in cm^{-2}, induced by the gate voltage V_g, is given by

$$n = \frac{C_{ox}}{q}(V_{DP} - V_g) \tag{2.5}$$

where q is the elementary electron charge and V_{DP} is the Dirac point voltage of the device, which is indirectly a measure of its doping level, as will be shown below. The gate oxide capacitance per unit area, C_{ox}, is given by $C_{ox} = \varepsilon_r \varepsilon_0 / d$, where ε_0 is the permittivity of the vacuum, ε_r is the relative permittivity of the oxide (in the case of SiO_2, $\varepsilon_r = 3.9$), and d is the oxide thickness. As shown in Figure 2.10a, holes (electrons) will be induced in the

device channel for $V_g < V_{DP}$ ($V_g > V_{DP}$). By varying the charge density on the graphene device channel, one is effectively modulating the Fermi energy (see equation 1.2) via the gate voltage.

The doping concentration n_0 of the channel can be found by setting $V_g = 0$ in equation 2.5, obtaining

$$n_0 = \frac{C_{ox}}{q} V_{DP}. \tag{2.6}$$

As such, for $V_{DP} > 0$, $n_0 > 0$ and the graphene will be p-doped; likewise, for $V_{DP} < 0$, $n_0 < 0$ and the graphene will be n-doped. The blue curve in Figure 2.10b, showing the transport characteristics of a device fabricated via EBL, is very slightly n-doped, with a $V_{DP} = -1.8$ and intrinsic charge carrier density $n_0 = -1.34 \times 10^{11}$ cm^{-2}). The red curve, fabricated using photolithography, shows a $V_{DP} = 75$ ($n_0 = 5.57 \times 10^{12}$ cm^{-2}), and is very p-doped. One of graphene's unique features, and a consequence of its semi-metallic nature, is that it is ambipolar, i.e. it can conduct current using both electron and hole charge carriers. Most traditional semiconductors are unipolar, and transmit current through their majority charge carrier exclusively (unless the transistor is operating in inversion mode). In these devices, for gate voltages between the the threshold voltage and the inversion voltage, the FET is in depletion mode, with the Fermi level deep within the band gap, and practically no current flowing. This ability to turn current "on" and "off", 1 or 0, is what enables the use of semiconductor FETs for logic operations, a property which graphene is unfortunately lacking.

The conductivity of the channel is a function of its mobility μ

$$\sigma = qn\mu. \tag{2.7}$$

Note that due to graphene's 2D nature, the conductivity σ and charge density n are given in units of [Ω^{-1}] and [cm^{-2}], respectively, instead of the traditional [Ω^{-1} cm^{-1}] and [cm^{-3}]. The conductivity can be calculated directly from the drain current I_d and drain voltage V_d of the device

$$\sigma = \frac{L}{W}\frac{I_d}{V_d} \tag{2.8}$$

where W and L are the device width and length, respectively. Substituting equation 2.5 into 2.7 and equating with 2.8, one obtains the equation for drain current as a function of the gate voltage

$$I_d = \mu C_{ox}\frac{W}{L} V_d V_g. \tag{2.9}$$

Deriving with respect to V_g, one can define the transconductance g as

$$g \equiv \frac{dI_d}{dV_g} = \mu\frac{C_{ox}}{q}\frac{W}{L} V_d, \tag{2.10}$$

which can be rearranged to give the mobility as

$$\mu = \frac{q}{C_{ox}}\frac{L}{W}\frac{g}{V_d}. \tag{2.11}$$

In 4-point measurements, a constant current is passed through the device while a voltage drop ΔV is measured across the two center electrodes. In this case, the mobility is calculated using the conductance $G = I_d/\Delta V$, such that

$$\mu = \frac{q}{C_{ox}} \frac{L}{W} \frac{dG}{dV_g}. \tag{2.12}$$

In this equation, V_d substituted by the measured 4-point voltage.

A transfer curve, plotting I_d versus V_g, such as the one in Figure 2.10b, can be used to numerically calculate the transconductance, plotted in 2.10c. Using this method, the mobility can be calculated for both electron and hole charge carriers, by substituting the maximum absolute value of the transconductance for each carrier channel (i.e. for $n > 0$ and for $n < 0$) into equation 2.11. In doing so, the electron (hole) mobilities for the blue curve are found to be 2251 (2281) $\mathrm{cm^2\,V^{-1}\,s^{-1}}$. For the red curves, a stark difference is seen in the two conduction channels, with the electron mobility (415 $\mathrm{cm^2\,V^{-1}\,s^{-1}}$) being much lower than the hole mobility (1127 $\mathrm{cm^2\,V^{-1}\,s^{-1}}$). This difference is due to p-doping impurities presenting a barrier to the injection of electrons at the electrode/channel interface, as was discussed in Chapter 1.

2.3.2 Raman Spectroscopy

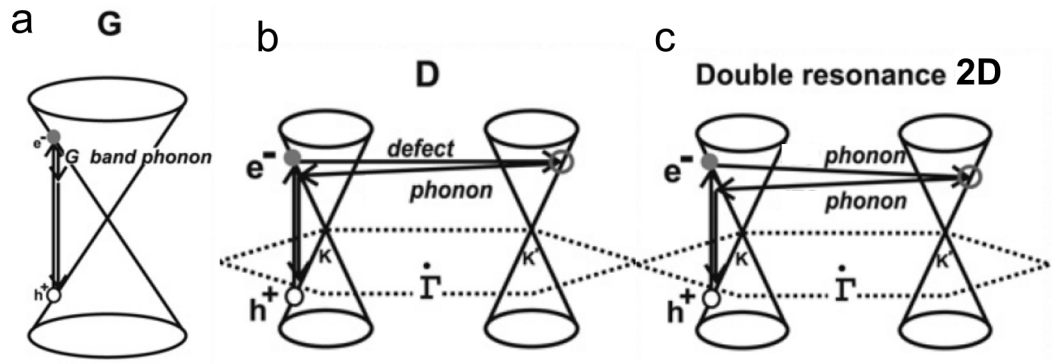

Figure 2.11: Phonon processes involved in creating the graphene **a** G, **b** D, and **c** 2D peaks. Adapted from [4].

Raman spectroscopy is an optical technique which uses the inelastic scattering of light to probe the changes in the vibrational, rotational or electronic energy of a material. Raman spectroscopy is widely used to provide a unique fingerprint, or identification, of a specific molecule or material. A monochromatic light source in the UV, visible, or near infrared is typically used. When an inelastic scattering event occurs, a photon is released, which can have an energy higher or lower than the incident photon. The experimental setups used throughout this thesis are only able to detect scattered photons with energies lower than that of the incident photon. The Raman shift produced by inelastic scattering of light, $\tilde{\nu}$, given in $\mathrm{cm^{-1}}$, is defined as

$$\tilde{\nu} = \frac{1}{\lambda_{ex}} - \frac{1}{\lambda_{sc}} \tag{2.13}$$

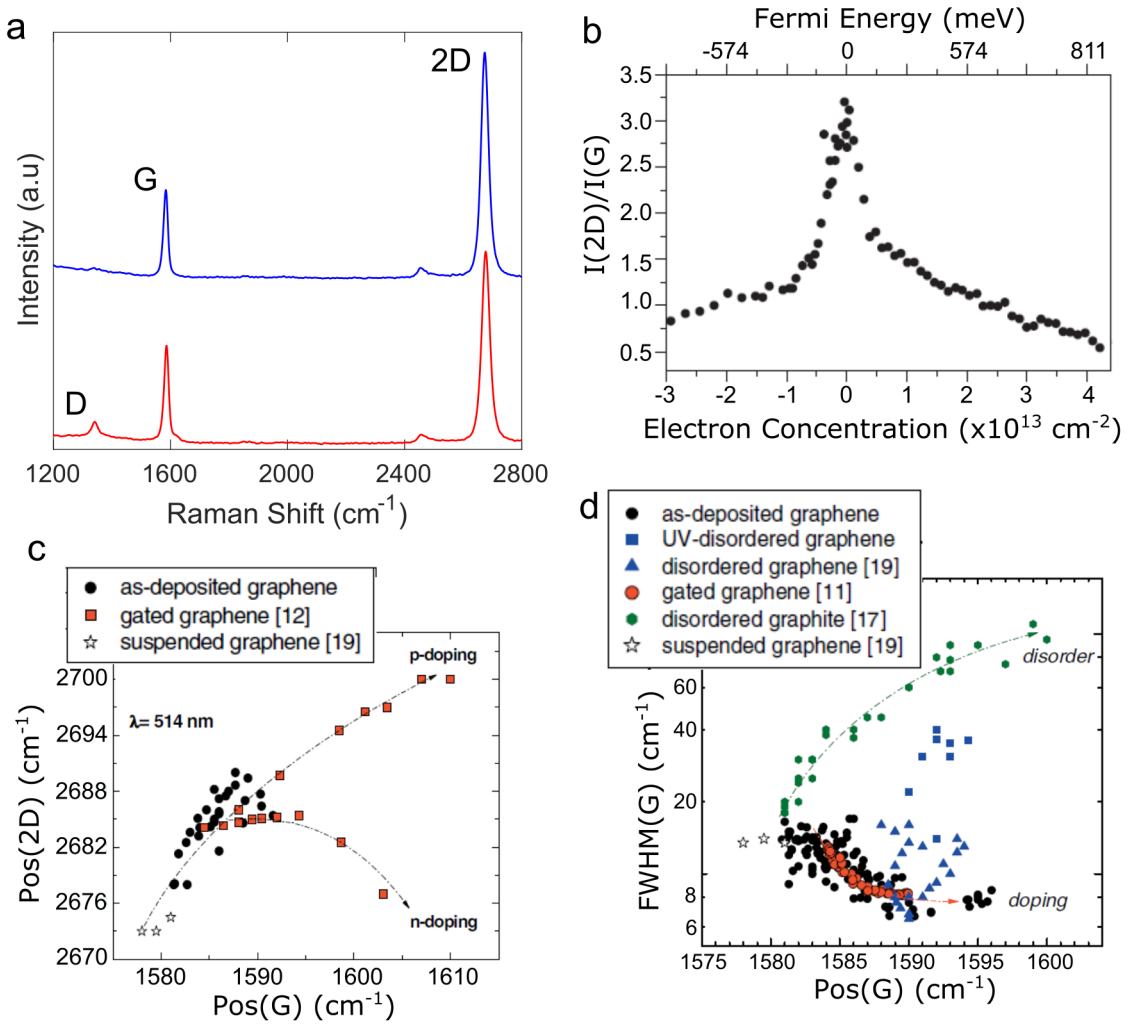

Figure 2.12: **a** Raman spectra of two different monolayer graphene samples produced in this thesis, with $\lambda_{ex} = 532$ nm. **b** I_{2D}/I_G vs. Electron concentration and Fermi Energy for top gated graphene sample. Adapted from [5]. **c** Pos(2D) vs. Pos (G) for exfoliated graphene samples. Adapted from [6]. **d** FWHM(G) vs. Pos(G) for exfoliated graphene samples. Adapted from [6].

where λ_{ex} and λ_{sc} are the wavelengths of the excitation and scattered photons.

Graphene's Raman spectrum consists of three main peaks, as labeled in Figure 2.11: 2D, G and D, each centered around 2700, 1585 and 1350 cm^{-1}. The phonon processes involved in each of these peaks are depicted in Figure 2.12. The G peak involves a simple intraband transition, resulting from bond stretching of sp^2 atom pairs in the carbon ring, and is the only first order Raman process peak observed in graphene [4, 7]. The inelastic scattering event resulting in a D peak requires the excitation of an e-h pair, its inelastic scattering by a phonon, followed by a second scattering by a defect to finally result in recombination [8]. The 2D peak is the overtone of the D peak, and also an inter-valley, double resonance scattering process between two Dirac cones. However, being a scattering event which does

not require defects (merely two phonons with opposite momenta),the 2D peak is always present [8]. Both the D and 2D peaks are strongly dispersive, with their peak position increasing with laser excitation energy [4, 7]. Additionally, the intensity of the 2D peak is particularly dependent on the excitation energy and graphene doping level [8].

Figure 2.11 b-d show the important relationship between Raman peak parameters, such as the full width half maximum (FWHM), intensity and position, and the graphene sample characteristics such as the doping level and disorder. The G peak position is seen to increase with both p and n type doping. Disorder in the graphene increases both the G peak position and FWHM. Doping alters the 2D peak position, with p-doping (n-doping) increasing (decreasing) the peak position [6]. The intensity of the 2D peak is also seen to be maximum when the graphene is undoped, as shown in Figure 2.11c [5]. The ratio of the intensities of the 2D and G peaks, I_{2D}/I_G, is often used heuristically to characterize the number of graphene layers, with a value of I_{2D}/I_G greater than 1 often arbitrarily designated in the literature as single-layer graphene. Figure 2.11c shows, however, that this measure is also significantly dependent on the doping level present in the graphene, and that a monolayer sample (such as those studied to generate Figure 2.11c) may have quite low I_{2D}/I_G values when intensely doped. The D peak is an indicator of the overall disorder and defect density in the graphene. Its presence is also used as an indicator of covalent bonding in graphene, due to the appearance of sp^3 orbitals breaking the graphene lattice to form covalent bonds with other molecules [9, 10].

Raman measurements were carried out on a Bruker Senterra machine, or in the optical setup shown in the following section.

2.3.3 Optical Measurements

Optical measurements were carried in the free space setup shown in Figure 2.13a. The excitation sources were a 488 nm Ar laser, and a supercontinuum laser source (Fianium SC400-4) with its output coupled to a tunneable bandpass fillter (SuperChrome) with 400-2400nm wavelength output and bandwidth selectivity between 0 and 100nm with respect to the central wavelength selection. The repetition rate of this light source is 40 MHz. Emission spectra were collected by a Peltier cooled, electron multiplied, silicon CCD detector (Andor Newton EM), passing through a 0.5 m diffraction spectrometer. The light beam is directed into an inverted scanning optical microscope stage, with $<$1 µm spatial resolution, shown in Figure 2.13b, which allows for the acquisition of photoluminescene and Raman spectrocopy maps. A schematic of the free space optical setup, optimized for measuring emission with 488 nm laser excitation light, is shown in Figure 2.13c. Laser light first passes through a line filter (Semrock MaxLine Laser Line Filter LL01-488-25), intended to narrow the spectral width of the emitted light narrower about 488 nm, as well as eliminating lower and higher spurious wavelength plasma emission lines. The light is reflected off a dichroic filter with a cutoff at 488 nm (Semrock RazorEdge Dichroic LPD02-488RU), and onto the sample. The emitted light, of longer wavelength than the excitation light, will pass through the

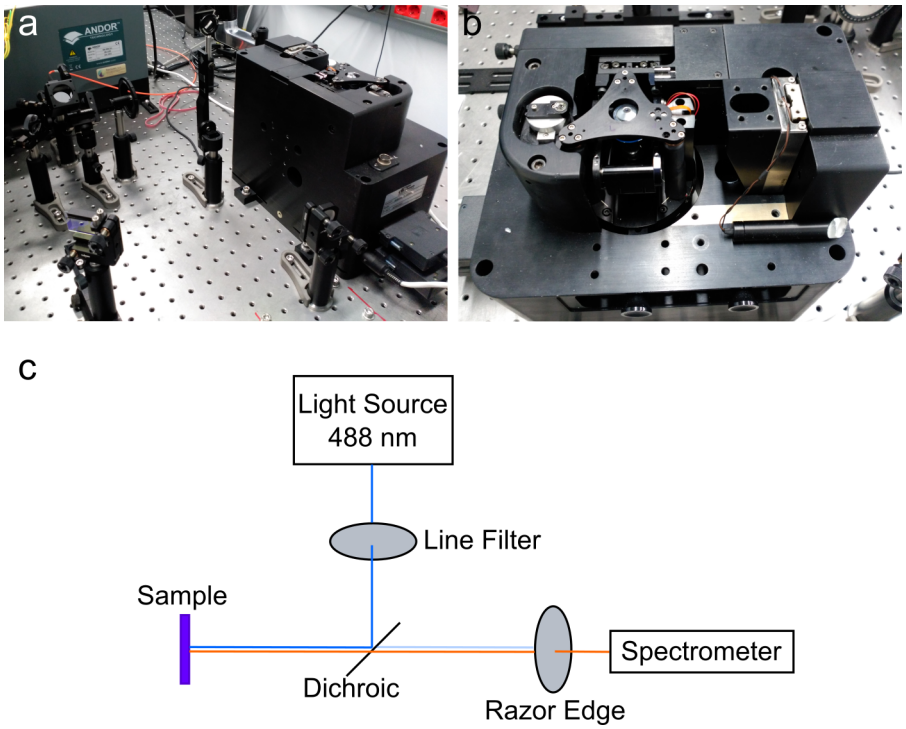

Figure 2.13: **a** Free-space optical setup, showing scanning stage towards the right of the image. **b** Scanning stage for acquiring photoluminescence and Raman spectroscopy maps. **c** Schematic of free space optical setup and components.

dichroic filter. A final razor edge filter (Semrock RazorEdge LP02-488RU) sits before the spectrometer, intended to filter the small amount of Rayleigh scattering light reflected off of the sample and transmitted through the dichroic filter.

Bibliography

[1] J.W. Suk, A. Kitt, C.W. Magnuson, Y. Hao, S. Afmed, J. An, A.K. Swan, B.B. Goldberg, and R. Ruoff. Transfer of CVD-grown monolayer graphene onto arbitrary substrates. *ACS Nano*, 5:6916–6924, 2011.

[2] S.M. Sze. Lithography and etching. In *Semiconductor Devices: Physics and Technology*, chapter 11, pages 428–467. Wiley, 2004.

[3] MicroChemicals. *Photolithography: Theory and Application of Photoresists, Etchants and Solvents*, 2012.

[4] L.M. Malard, M.A. Pimenta, G. Dresselhaus, and M.S. Dresselhaus. Raman spectroscopy in graphene. *Physics Reports*, 473:51–87, 2009.

[5] A. Das, S. Pisana, B. Chakraborty, S. Piscanec, S.K. Saha, U.V. Waghmare, K.S. Novoselov, H.R. Krishnamurthy, A.K. Geim, A.C. Ferrari, and A.K. Sood. Monitoring dopants by raman scatering in an electrochemically top-gated graphene transistor. *Nature Nanotechnology*, 3:210–215, 2008.

[6] C. Casiraghi. Probing disorder and charged impurities in graphene by raman spectroscopy. *Physica Status Solidi RRL*, 3:175–179, 2009.

[7] A.C. Ferrari. Raman spectroscopy of graphene and graphite: Disorder, electron–phonon coupling, doping and nonadiabatic effects. *Solid State Communications*, 143:47–57, 2007.

[8] A.C. Ferrari and D. M. Basko. Raman spectroscopy as a versatile tool for studying the properties of graphene. *Nature Nanotechnology*, 8:235–246, 2013.

[9] Q.H. Wang, Z. Jin, K. K. Kim, A.J. Hilmer, G.L.C. Paulus, C.-J. Shih, M.-H. Ham, J.D. Sanchez-Yamagashi, K. Watanabe, T. Taniguchi, J. Kong, P. Jarillo-Herrero, and M.S. Strano. Understanding and controlling the substrate effect on graphene electron-transfer chemistry via reactivity imprint lithography. *Nature Chemistry*, 4:724–732, 2012.

[10] S. Niyogi, E. Bekyarova, M.E. Itkis, H. Zhang, K. Shepperd, J. Hicks, M. Sprinkle, C. Berger, C.N. Lau, W.A. deHeer, E.H. Conrad, and R.C. Haddon. Spectroscopy of covalently functionalized graphene. *Nano Letters*, 10:4061–4066, 2010.

Chapter 3

Graphene Technology Development

3.1 Introduction

The fabrication of devices from graphene grown by chemical vapor deposition (CVD) necessitates the optimization of various processes; namely, the CVD growth itself, the transfer of the graphene from the growth substrate to a substrate suitable for characterization and experimentation, and the fabrication of graphene devices via standard microfabrication techniques. Each of these processes is comprised of a multitude of interconnected parameters, which must be fine-tuned within a narrow margin of error to produce a quality final device. This chapter outlines the optimization of the aforementioned processes, with the acquired technological know-how serving as a basis for all further studies presented in the subsequent chapters of this thesis. The ultimate goal of this knowledge is to transform graphene from a scientifically remarkable, highly researched laboratory material into a massively scalable, industrially viable, and application-worthy one.

3.2 Graphene Growth via Chemical Vapor Deposition

3.2.1 Growth Mechanism

Chemical vapor deposition (CVD) growth of graphene on metals has become the preferred method for obtaining large area, high quality graphene films. Limited only by the size of the metallic substrate and growth furnace, these films can often be transferred relatively easily to another substrate for subsequent characterization and/or fabrication [1]. Growth is initiated by heating the metallic substrate to high temperatures and introducing a hydrocarbon precursor gas, such as methane. Interaction between the gas and the metallic substrate causes some or all of the hydrogen atoms in the gas to dissociate from the carbon atoms, leaving the carbon species free to diffuse about the surface of the substrate. Graphene growth on transition metals is characterized by the solubility of carbon in the bulk of the metal [2]. In metals such as Ni or Ru, carbon species on the surface are able to diffuse into the bulk due to the high C solubility of the metal. Upon cooling, the dissolved carbon segregates out onto the surface of the metal and can proceed to nucleate and form graphene sheets. In low solubility metals such as copper, this bulk dissolution/segregation process does not occur, and all processes occur on the surface. The interaction energy between graphene and low carbon solubility transition metals is a relatively weak van der Waals interaction, below

0.1 eV per C atom [2]. For both high and low solubility metals, nucleation is typically heterogeneous, occurring at surface defects, kinks or impurities [2]. Once the initial graphene site is formed, adsorbed carbon species diffusing about the surface can become incorporated into the growing graphene lattice by forming C-C σ bonds. In this simplified growth model, depicted schematically in Figure 3.1, graphene nucleation and growth depends on the concentration of nucleation sites and carbon species present on the surface. As such, the origin of the carbon species (segregation from bulk metal or from gaseous precursor in high and low solubility metals, respectively) is unimportant [2].

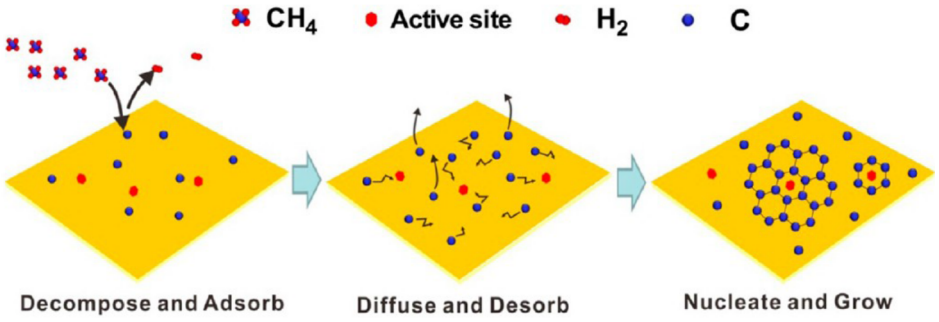

Figure 3.1: a Schematic of CVD growth process [3].

Growth of a single monolayer sheet is especially challenging in metals with high solubilities, since segregation, and as such, graphene nucleation and growth, will continue as long as dissolved carbon is present in the bulk. For this reason, along with its easy accesibility and low cost, low solubility copper has become the substrate metal of choice for large area CVD graphene production. Its use for the growth of monolayer CVD graphene was first reported in 2009 by the group of professor Rodney Ruoff [4].

3.2.2 Growth Optimization on Copper

Initial attempts in this thesis at growing graphene on copper foils resulted in very inhomogeneous graphene over the substrate surface, with some areas being mostly monolayer, while other areas were almost completely multilayer, as shown in Figure 3.2a and b, respectively. These images also indicate that very small grains were obtained, less than 5 µm in size. It was clear that the nucleation density first needed to be homogenized over the copper foil surface area, and subsequently reduced in order to achieve larger graphene grains and fewer detrimental grain boundaries. Several methods have been investigated to reduce the surface roughness of the copper substrate, and thereby the number of nucleation sites, including *in situ* high temperature and pressure annealing [3], and polishing of the copper substrate prior to growth [5], both with the aim of reducing the surface roughness. Another complementary method of reducing the nucleation density is by changing the growth environment, namely by lowering the methane partial pressure, which reduces the likelihood of surpassing the initial energy barrier required for nucleation. This approach is constrained, however, by the vacuum pump used during the growth, and by the minimum achievable methane flow

rate. The lowest pressure reached by the scroll pump used in this thesis is a few mbar at typical gas flow rates, which is relatively high compared to values in the literature used to grow milimeter size graphene grains. Another method that has been successfully explored for changing the growth environment is creating an enclosure or pocket from the copper foil used as a growth substrate. This creates a quasi-static flow environment, as well as lowering the methane partial pressure [6]. It has also been reported that the enclosed areas in the pocket supress the high temperature sublimation of the copper substrate, resulting in lower surface roughness [7].

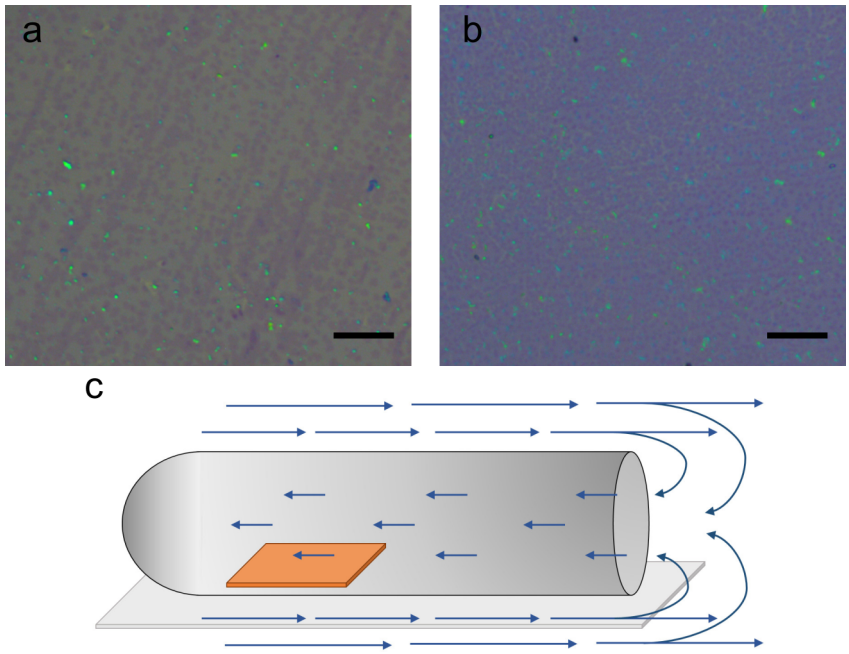

Figure 3.2: **a** and **b** Optical images of graphene transferred onto SiO_2 substrate, showing different regions of the same sample. Sample was grown prior to the implementation of the inner quartz tube. The region in **b** shows a few multilayer islands on a monolayer background, whereas the region in **b** shows almost complete multilayer coverage. Scale bar in **a** and **b** 15 µm **c** Schematic of small quartz tube during growth process, showing fast, convective gas flow on the outside and slow, diffusive gas flow on the inside.

An alternative to using copper foil enclosures was reported by Wang et al., in which they observed significantly reduced nucleation density by placing a small quartz tube within the larger quartz tube chamber, with the mouth of the small quartz tube facing away from the direction of flowing gases [8]. This same approach was also utilized in this thesis (Figure 2.1 of the previous chapter). By placing the copper substrate within this smaller quartz tube, the velocity of the flowing gases in contact with the copper foil is significantly reduced, as shown in the schematic of Figure 3.2c. Within the quartz tube, gaseous flow transport is expected to be dominated by diffusion, as opposed to convection outside of the tube. This quasi-static growth environment avoids the large pressure and methane concentration gradients present on the outside of the quartz tube.

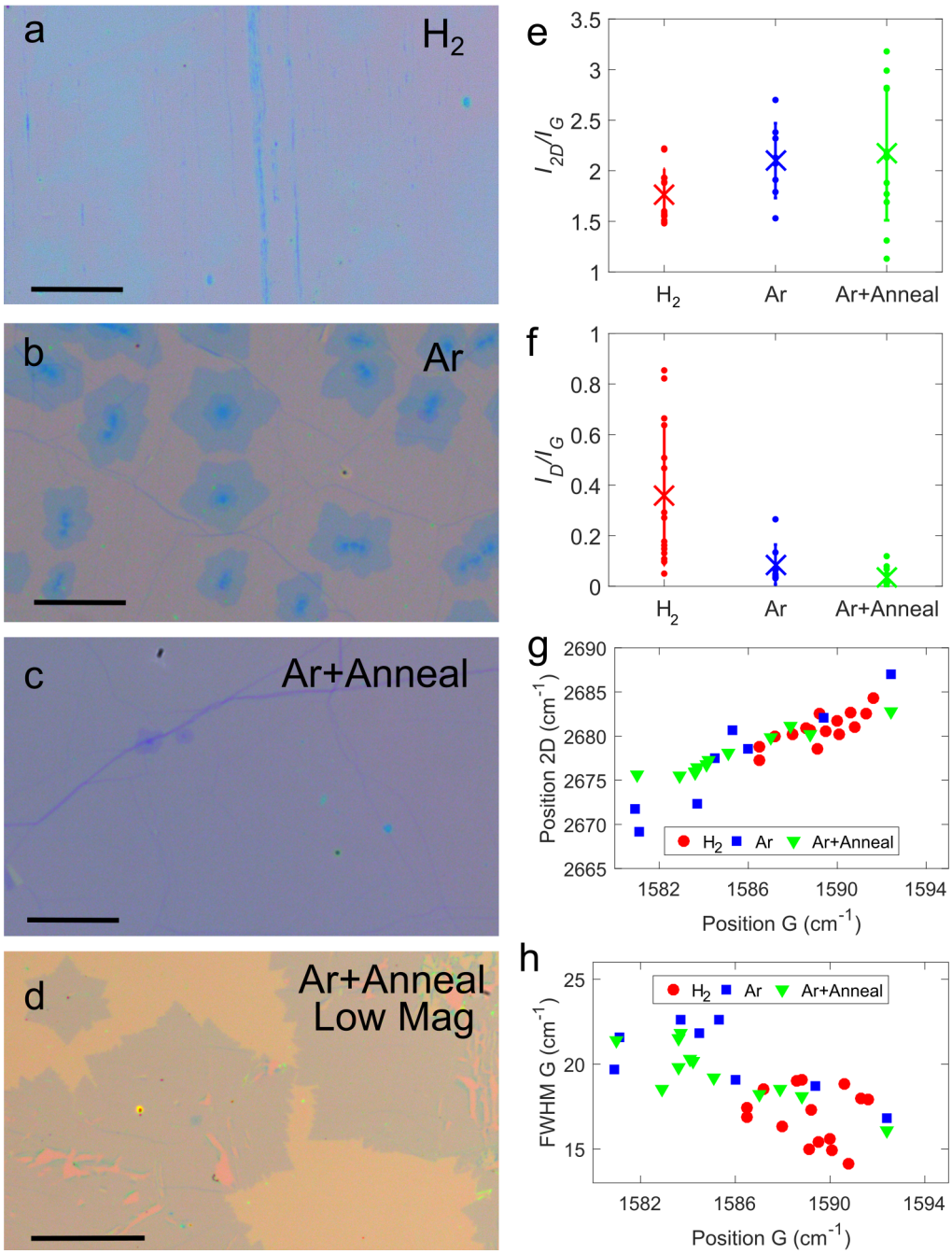

Figure 3.3: **a-d** Optical images of graphene transferred to SiO_2 substrate for different CVD growth recipes, as indicated in the labels within the images. Scale bar 20 µm for **a-d**, 75 µm for **d**. **e-h** Raman spectra statistics ($\lambda = 532$ nm). Histograms of **e** I_{2D}/I_G and **f** I_D/I_G values for the different growth recipes. **g** 2D vs G peak positions and **h** G peak FWHM versus position.

After employing the quartz tube in the growth process, a much more homogeneous nucleation density was achieved throughout the copper foil, resulting in almost fully monolayer growth throughout the entire sample area, as seen in Figure 3.3a. The sample in that image

was grown using only hydrogen during all process phases (and methane during the growth phase, obviously), with no argon introduced into the chamber (see Appendix A for recipe). This recipe results in I_{2D}/I_G values between 1.5 and 2, confirming that the graphene is monolayer (3.3e). However, high I_D/I_G peak values are observed, as seen in the histogram of Figure 3.3f, indicating a high defect density. Both the high defect density and monolayer character of the graphene likely stem from hydrogen's role as an etchant during growth. Not only does the hydrogen help to suppress the formation of multilayers [9], it can also result in anisotropic etching of the graphene film [10]. Excessive etching of the graphene may lead to the formation of defects, especially for smaller graphene grain sizes with their high density of grain boundaries, which are preferential hydrogen etching sites. The high number of broken bonds along the grain boundaries may help to explain the high defect density observed in Raman measurements of growths using only hydrogen.

Following this logic, one can surmise that by increasing the graphene grain size, the defect density can be reduced by reducing the density of grain boundaries. In the past years, one of the most effective ways of reducing the nucleation density in CVD growth of graphene on copper has been to maintain the native layer of copper oxide (CuO_2) on the surface of the substrate, as opposed to fully reducing the copper surface in hydrogen prior to growth. One possible explanation for the observed reduced nucleation density is that CuO_2 presents reduced catalytic activity with respect to the breaking of hydrocarbon CH bonds [11], and thus increases the energy barrier for nucleation to occur, although this explanation is not unanimously agreed upon [12]. Another proposed mechanism is that the oxygen released at high temperature from the CuO_2 layer reacts with and eliminates organic residues and impurities present on the copper foil surface. The resulting ultra-clean surface presents fewer nucleation sites, reducing overall nucleation density and increasing grain size [13, 14]. Regardless of the exact explanation, very low nucleation densities and large graphene grains have been achieved by avoiding the reduction of the CuO_2 surface on the copper substrate, generally by heating and annealing the substrate in argon instead of reducing hydrogen.

By replacing the hydrogen in the heat up and annealing phase with argon, and adding argon to the hydrogen background atmosphere during the growth phase (see Appendix A for recipe), several changes were observed in the resulting graphene. Flower-like, multilayer graphene islands appeared on a monolayer background, as shown in Figure 3.3b. The flower-like shape of the graphene grains has been reported elsewhere, and is most likely a result of the presence of oxygen on the copper surface, which shifts the growth kinetics from edge-attachment limited to diffusion limited, a growth mode which is known to favor dendritic, flower-like grain shapes over compact ones [15]. The presence of multilayer islands may seem puzzling at first, considering the large monolayer grains obtained by other researchers. One possible explanation is that these multilayer islands result from the formation of copper nanoparticles on the substrate surface, observed to form during the heating of copper in an argon atmosphere [16]. These nanoparticles, which are observed in much lower densities

when heating in hydrogen atmosphere, have been shown to act as nucleation centers, and may possibly be responsible for the multilayer islands seen in Figure 3.3b. Another important observation from this growth is that the grain size has increased, with a typical lateral size of about 20 µm, if one assumes that the center of the multilayer islands are the nucleation sites. This indicates that the nucleation density has indeed been reduced by replacing the hydrogen for argon during the annealing phase. Additionally, the multilayer graphene streaks (seen as vertical lines in Figure 3.3a), which result from directional roughness on the copper substrate, have been largely eliminated by switching from hydrogen to argon.

Raman measurements taken *between* the multilayer islands of the argon grown sample confirm that the graphene background is monolayer, with a mean I_{2D}/I_G ratio greater than 2. Moreover, the defect density has been reduced, as evidenced by the I_D/I_G ratio below 0.2 for almost all points sampled. Nonetheless, a higher dispersion is observed in the positions of the G and 2D peaks, as well as in the G peak FWHM (Figure 3.3g and h) compared to the sample grown in hydrogen.

In order to reduce the presence of multilayer islands and further increase the graphene grain size, a long annealing in argon (3 h) was employed prior to the growth stage. A similar annealing process was shown to eliminate the copper surface nanoparticles formed during the heating in an argon atmosphere [16]. Indeed, annealing processes are commonly used to increase the graphene domain size, presumably by reducing surface roughness and concomitantly the nucleation center density [1, 3]. Figure 3.3c shows that by incorporating a long annealing into the growth process, the number of multilayer islands are reduced, and the graphene is much more homogeneous, as seen in Figure 3.3c. Moreover, the grain size has been drastically increased, with the low magnification image in Figure 3.3d showing grain sizes on the order of 100 µm. A very small I_D/I_G ratio indicates few defects are present, and the average I_{2D}/I_G ratio measured for these samples has been increased. Nevertheless, a large dispersion is observed, and is also evident for the peak positions and G peak FWHM. This may indicate that the sample is inhomogeneously doped, possibly due to remnants of water trapped beneath the graphene and substrate. Indeed, the large grain Ar+Anneal grown samples required a longer period in vacuum to achieve adequate graphene/substrate adhesion, indicating that longer time periods are required for the trapped water to fully evacuate from underneath the graphene. The lower density of grain boundaries in these samples compared to the small grain H_2 grown samples may result in the water taking a longer time to escape from beneath the graphene, resulting in inhomogeneous doping over the sample area.

3.3 Graphene Transfer

Initial attempts to transfer graphene were hampered by large amounts of debris that remained on the surface, shown in Figure 3.4a and b. The low magnification image (a) shows that this debris follows the contours of the copper foil. Upon magnification, the debris is revealed to have a rolled up, scroll-like shape. Indeed, it was discovered that these scrolls are

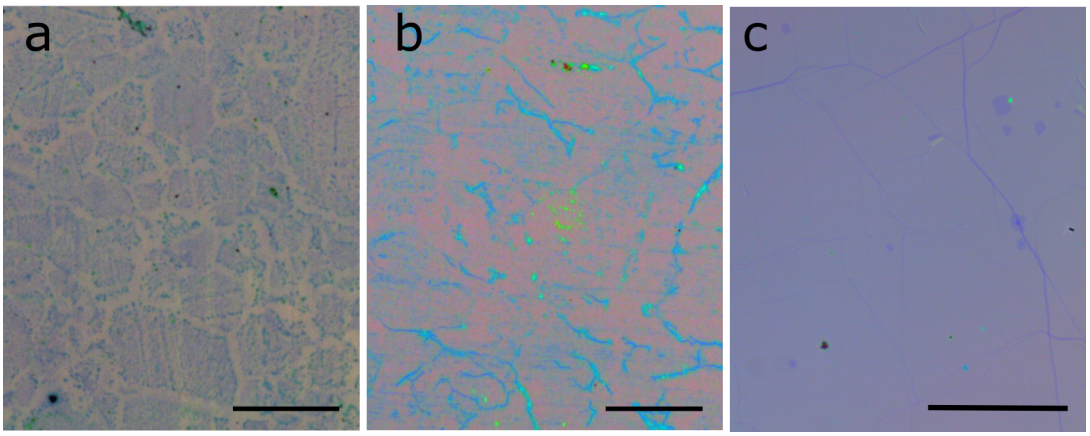

Figure 3.4: Optical images of graphene on SiO_2 substrate with inadequate backside graphene etching. **a** Low magnification, showing how graphene debris follow the copper grain contours. Scale bar 250 µm. **b** High magnification, clearly showing graphene scrolls. Scale bar 50 µm. **c** High magnification image of clean, continous graphene. Scale bar 50 µm.

rolled up remnants of graphene from the underside of the copper foil used for growth. This face of the foil, which is not covered in PMMA, is in contact with the copper wet etchant. The graphene film covering this face is damaged during the etching process, and rolls up into scrolls due to graphene's hydrophobic nature, sticking to the underside of the top, PMMA covered graphene film. When the PMMA/graphene stack is transferred to a substrate, the broken remnants of the underside graphene film are also transferred. In order to avoid this problem, it was necessary to eliminate the underside graphene film prior to the wet etching step. Initially, an oxygen plasma etching was employed, although this resulted in inadequate removal of the backside graphene. By switching to a stronger oxygen plasma in a reactive ion etching (RIE) chamber, the backside graphene was fully eliminated, resulting in a clean graphene transer (Figure 3.4c).

Apart from the removal of the backside copper substrate graphene, two seemingly unrelated problems that were encountered during the graphene transfer process, upon closer examination, had similar origins: the appearance of stains in the graphene sheet, and poorly adhered graphene that tore upon the removal of the PMMA film in acetone. These stains are visible in Figure 3.5a and b, and reveal either a greenish or bluish coloration, depending on the optical microscope acquisition settings. The stained zones showed a very distorted Raman spectrum (Figure 3.5d), with an enormous D peak and practically nonexistent 2D peak. Clearly, these stains consisted of some other material that was severely altering graphene's Raman spectrum. In regions where stains were present, the graphene was largely continuous, showing few rips. On the other hand, regions showing few stains showed significant ripping of the graphene sheet, as seen in Figure 3.5c.

This led to the present discovery that the stains were due to water trapped between the substrate and the graphene sheet. This trapped water inhibited proper adhesion between

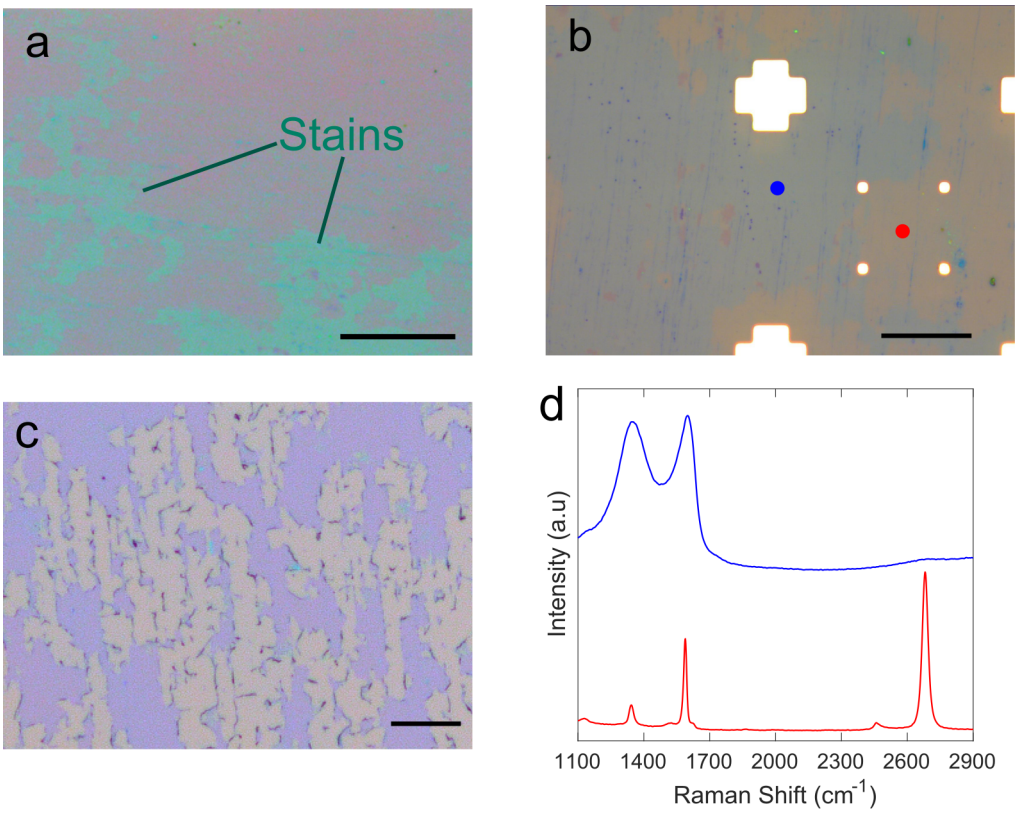

Figure 3.5: **a-c** Optical images of graphene on SiO_2 taken with different acquisition settings. **a** Greenish stains from trapped water. Scale bar 50 µm. **b** Bluish stains from trapped water. Scale bar 25 µm. **c** Ripped graphene, a result of poor adhesion due to water trapped between graphene/substrate. Scale bar 100 µm. **d** Raman spectra ($\lambda = 532$ nm), with colors corresponding to the same color points in **b**, showing severe graphene distortion in stained region.

the graphene and the substrate, which could cause the graphene to rip when the PMMA was removed in acetone. For this reason no stains were seen in regions of ripped graphene: the trapped water which caused the stains also caused the ripping of the graphene. Two process steps were optimized in order to achieve better graphene/substrate adhesion and eliminate stains and graphene ripping. First, the sample was stored in vacuum overnight (or at least for a few hours), prior to removing the PMMA. This ensured enough time for all of the water to diffuse out from under the graphene sheet. Storage in a sealed dessicator with silica gel pellets for moisture removal was also shown to be an adequate form of removing water. Second, the oxygen plasma cleaning of the substrate immediately prior to graphene transfer was eliminated. Oxygen plasma cleaning is used for removing organic substances and residues from the surface of the substrate. When this process is carried out on a SiO_2 substrate, however, it also increases the density of silanol (Si-OH) terminated groups on the surface, reducing the concentration of Si-O-Si bonds. This results in a much more hydrophilic SiO_2 surface, which is readily wetted by a water film [17], and favors the trapping of water between the SiO_2 substrate and the graphene. By carrying out the oxygen plasma

cleaning hours or days before the transfer (being careful, of course, to not contaminate the substrate after cleaning), the substrate has time to revert back to its normal hydrophobic state, ensuring better graphene adhesion and reducing the appearance of stains and ripping.

3.4 Graphene Fabrication with Photolithography

Fabrication of graphene transistors using photolithography is particularly difficult, due to the fact that UV sensitive photoresists leaves residues on the graphene surface, which act as defects, long range scattering centers, and are generally p-dopants [18, 19]. UV sensitive photoresists are much more contaminating and damaging to graphene than the PMMA used in electron beam lithography (EBL). Photolithography, a much faster, higher throughput method than EBL, is the preferred lithographic mehtod in industry. Significant efforts have therefore been undertaken to mitigate the negative effects of photoresists on graphene, with varying levels of success. This section outlines some of the methods explored throughout this thesis to succesfully fabricate quality graphene transistors via photolithography.

3.4.1 Fabrication with Al Film Buffer

One of the fabrication strategies adopted to prevent contact between graphene and the photoresist layer is to first evaporate a metallic or oxide film onto the graphene prior to fabrication. In this way, the film acts as a buffer, preventing contact between the graphene and the photoresist, and is sacrificially etched to open windows for graphene patterning and contact evaporation. Both metallic [20, 21] and oxide films have been used in this way [22]. Throughout this thesis, an Al film, subsequently oxidized under ambient conditions into aluminum oxide (abbreviated here as AlOx, notAl_2O_3, due to its amorphous and likely non-stoichiometric composition) has been utilized as a buffer layer for several reasons. Firstly, AlOx can be easily etched in the alkaline solutions used for developing photoresists. Consequently, this eliminates one step of the fabrication process, by combining the resist development and susbequent etching step needed to remove the buffer film and expose the underlying graphene. Secondly, the AlOx film can be used as a seeding layer to grow oxide films via atomic layer deposition (ALD), as will be discussed in the next chapter. Finally, the AlOx film is transparent in the visible light range, allowing for optical and Raman spectroscopy characterizations of the underlying graphene.

The basic device fabrication process flow using an Al film buffer is outlined in Figure 3.6a and was inspired by Hsu et al [22]. In theory, since the graphene is never in direct contact with the photoresist, it should not leave any contaminating residues. Consequently, very low contact resitances have been reported [22], since no photoresist residues remain between the graphene and contacting metal. These residues can be removed via a mild plasma treatment prior to the evaporation, at the cost, however, of producing defects within the graphene contact area.

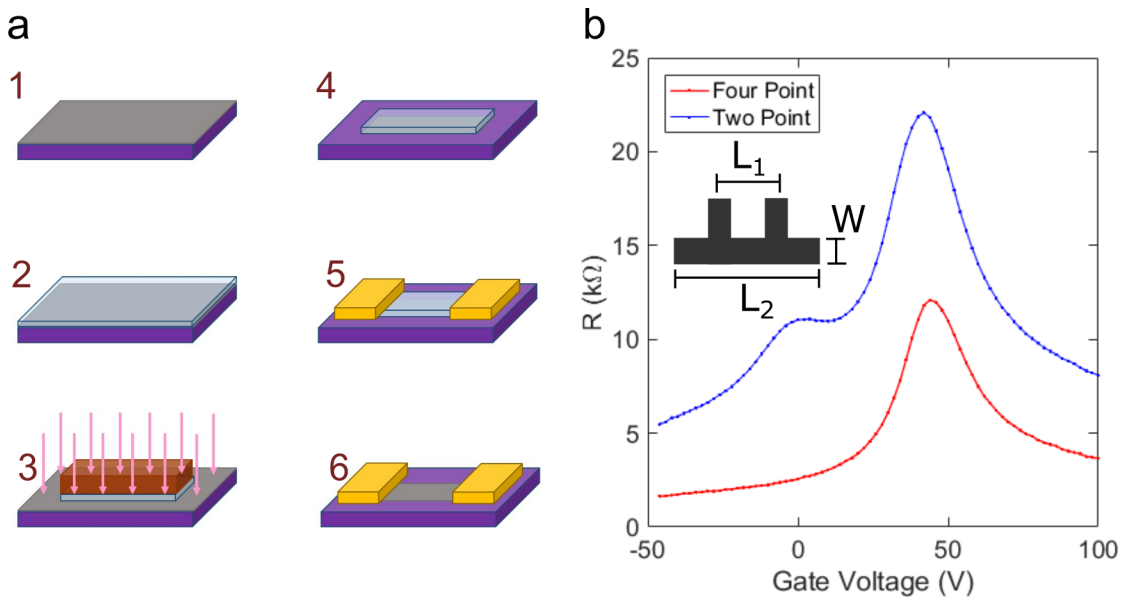

Figure 3.6: **a** Process flow for device fabrication using an Al film buffer: 1. Graphene sheet on substrate. 2. Evaporation of approximately 4 nm Al film, which oxidizes in ambient. 3. Patterning of device area with photoresist, with developer solution etching the AlOx film, followed by oxygen plasma etching of exposed graphene. 4. Isolated graphene/AlOx in device shape, onto which another photoresist layer is spun and patterned into metal contact shape. 5. Evaporation of metal contacts and removal of photoresist. 6. Removal of remaining AlOx film. **b** Transfer curves of succesfully fabricated device using Al film buffer, showing simultaneous 2 and 4-point measurement curves. Inset shows a schematic of the measured figure, with L_1 corresponding to the 4-point measurement curve and L_2 to the 2-point measurement curve.

Figure 3.6b shows simultaneously acquired 2 and 4-point transport curves for a device fabricated using an Al film buffer. These measurements were obtained by sourcing constant currents between the two outer electrodes separated by $L_2 = 30.9\,\mu\text{m}$ and measuring the voltage between the two inner electrodes, separated by $L_1 = 19.5\,\mu\text{m}$, as depicted in the schematic inset of Figure 3.6b. The Dirac point for both curves is located at a gate voltage of 45 V, corresponding to a p-doped intrinsic carrier concentration of 3.34×10^{12}. Most devices fabricated via photolithography in an unoptimized process exhibit much more severe p-doping, with the Dirac point not visible within the gate sweeping range. The measured 4-point resistance R_1 can be used to calculate the sheet resistance $R_{sh} = R_1 W/L$ of the graphene sample ($W = 5.7\,\mu\text{m}$), corresponding to the resistance of a square of graphene. The 4-point measurements yield a minimal and maximum sheet resistance of 0.48 and 3.52 kΩ, yielding an ON/OFF ratio of 7.3. The contact resistance of the outer electrodes is then calculated as $R_c = (R_2 - R_{sh}L_2/W)/2$, and is usually given by normalizing for the device width, as $R_c W$. The duly normalized contact resistances obtained for the minimal and maximum sheet resistances are 8.2 and $8.4\,\text{k}\Omega\,\mu\text{m}$, which are quite high compared to the values obtained in [22] and elsewhere. This high contact resistance, along with the

anomalous resistance maximum in the 2-point measurement around 0 gate voltage indicate that the contact between the graphene and Cr/Au electrode is poor. This may be due to poor bonding between the Cr and graphene, slightly oxidized Cr from residual oxygen in the evaporation chamber, or even AlOx cluster remnants that were inadequately removed during the photoresist development [23].

Despite the poor contact resistance values, the mobility values calculated are quite good, especially considering that the sample was measured in ambient conditions. The hole and electron mobilities for the 2-point measurement are 1092 and 883 $cm^2\,V^{-1}\,s^{-1}$, and for the 4-point measurement are 2652 and 1354 $cm^2\,V^{-1}\,s^{-1}$. The significantly higher mobilities in 4-point mode are due to removing the effect of contact resistance. The comparatively lower electron mobilities, relative to the hole mobilities, are most likely due to p-doping contaminants suppressing electron conduction in the graphene channel, through the formation of an energy barrier at the graphene/electrode interface, as discussed in the Graphene Basics chapter.

Despite the high quality of the device discussed above, most devices fabricated with an Al film buffer showed relatively poor quality, with very high doping and low mobilities, almost as if the Al film buffer were not present. Indeed, the sample in Figure 3.6 belonged to a batch in which it was the only working device out of 8 fabricated. This may be due to inhomogeneous film deposition over the sample surface, possibly due to wrinkles or rips in the graphene, as well as residues leftover from the PMMA. An inhomogeneous, porous, cracked or pinhole-containing AlOx film may allow photoresist to permeate and seep underneath it, contaminating the underlying graphene. Moreover, recent studies have shown that the amount of residual oxygen in the chamber during evaporation has a significant impact on the overall oxidation state of the Al film, with important consequences on the final quality of the resulting graphene devices [24].

3.4.2 Optimized Fabrication

The inconsistent results and low yields obtained for devices fabricated using an Al film buffer, necessitated the optimization of a device fabrication process in which the photoresist is in direct contact with the graphene. One simple way of reducing graphene's contact with photoresists, which has been used throughout this thesis, is by transferring it onto subtrates with pre-patterned contacts. In this way, one less lithography step has to be carried out on the graphene, namely the patterning of windows for the evaporation of metal contacts. In addition, with this method of graphene/electrode contacting, there are no contact-resistance enhancing photoresist residues present between the graphene and the metal.

After transferring the graphene sheet onto the pre-patterned contacts, it is patterned into the desired device shape via photolithography and dry etching, using either an oxygen plasma or oxygen RIE. Devices fabricted using these two dry etching methods are shown in Figure 3.7. It is evident that for the devices etched via a RIE process, a greenish photoresist film remains on top of the graphene channel. This film is not present in the oxygen plasma

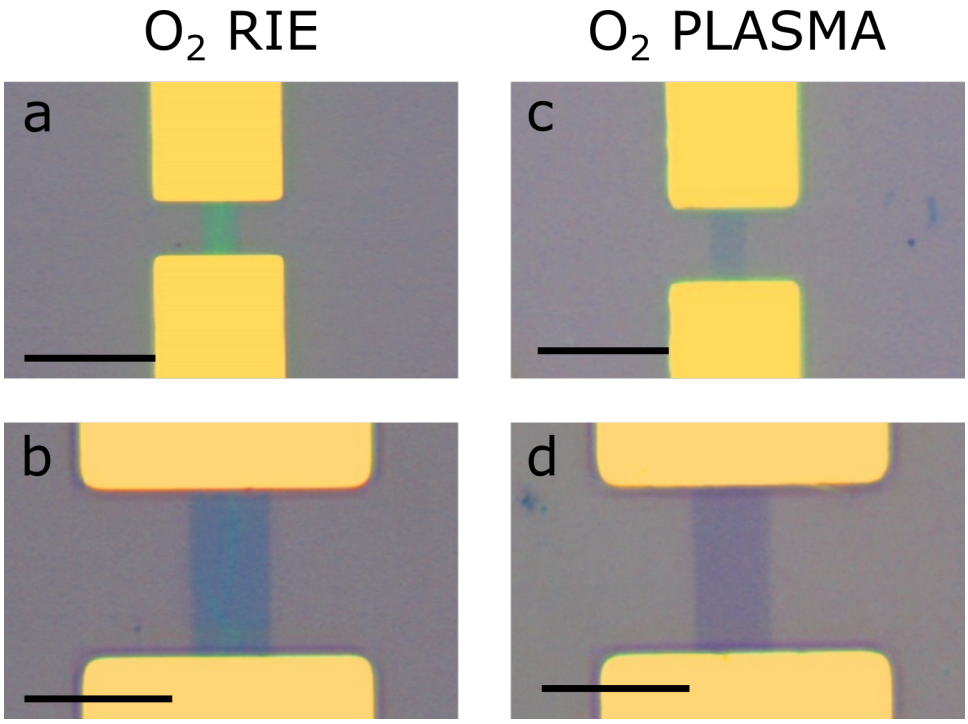

Figure 3.7: Optical microscopy images of graphene devices, fabricated via photolithography, on SiO_2 substrate. Graphene patterning was carried out via O_2 RIE (**a** and **b**), O_2 plasma (**c** and **d**). Scale bars 20 µm (**a** and **c**), 10 µm (**a** and **c**).

etched devices. Indeed, even in the RIE etched devices, the film is only present in the graphene channels, not in the large area graphene regions. This indicates that the RIE process thermally crosslinked the photoresist film by reaching high local temperatures in the device area [25], whereas in the zones of large area graphene, the generated heat is more easily dissipated. The reason RIE reaches such high local temperatures, leading to photoresist crosslinking, and plasma does not, has to do with the nature of the etching mechanism behind each of these processes. Plasma etching occurs at pressures of around 1 to 10 Torr. The generated plasma creates a relatively high density of charged ions and atomic radicals. As a result, the mean free path of the charged particles following the eletric field lines present within the plasma is relatively short; they quickly bump into some other particle, changing their trajectory and robbing them of kinetic energy. Moreover, the plasma machine used throughout this thesis is set up so that the sample is electrically floated, and lacks a defined voltage. Therefore, there are no well defined electric field lines between the sample and the RF generator, making the acceleration of charged particles onto the sample surface nearly impossible. The short particle mean free path and lack of a guiding electric field result in an isotropic, chemical etching process that is dominated by uncharged atomic radicals diffusing onto the sample surface.

The RIE differs from the plasma in two important ways. Firstly, the pressures used in the RIE are much lower, on the order of 100 mT. The resulting particle mean free path is much

longer, with particles accelerated to much higher kinetic energies before encountering another particle. Secondly, the sample in the RIE machine is DC isolated from earth a capacitor, and reaches a well defined voltage bias (known as the DC Bias) with respect to the RF generator. As a result, high energy charged particles follow the electric field lines emanating from the sample, crashing onto its surface and physically removing material. Etching via this physical mechanism is anisotropic, following the electric field lines. In a RIE process, both the physical and chemical etching mechanism described in the previous paragraph are present; as the pressure is lowered, the physical mechanism becomes increasingly dominant [26]. The high kinetic energy of the charged ions slamming into the substrate increase its surface temperature. In areas where the generated heat is poorly dissipated, such as the graphene device channel, the increased temperature causes the photoresist to crosslink and makes its removal extremely difficult.

After graphene patterning via oxygen plasma etching, the photoresist can be removed with N-methyl-2-pyrrolidone (NMP), a powerful solvent often used in photolithography due to its high boiling point, which allows it to be heated up to 80° C, and low vapor pressure, which prevents the formation of streaks and striations on the sample surface. NMP is often used as a solvent for exfoliating graphene from bulk graphite, since its surface tension is ideal for overcoming the surface energy of graphite sheets (about 0.17 $\mathrm{J\,m^{-2}}$) [27]). The adhesion energy between graphene and SiO_2 has been measured to be 0.45 $\mathrm{J\,m^{-2}}$ [28], with calculations confirming this value [29]. These values can be significantly lower, however, under non-ideal conditions, such as for a hydroxylated SiO_2 surface (which occurs after an oxygen plasma), or for a thin film of water molecules being present between the graphene and SiO_2. The adhesion energy approaches 0.2 $\mathrm{J\,m^{-2}}$ for these conditions, similar to the adhesion energy between sheets of graphite [30]. Therefore it follows that if NMP is able to exfoliate sheets of graphite, it should be able to exfoliate graphene that is poorly adhered to a SiO_2 substrate.

Indeed, such behavior is observed, with NMP exfoliating or ripping large area graphene sheets, resulting in samples similar to those observed in Figure 3.5c. Once again, this underscores the importance of having graphene adequately adhered to the substrate. It is possible that the NMP intercalation occurs in small regions of poorly adhered graphene, and is able to exfoliate and rip a fairly large area around these regions. As a result, even a fairly small concentration of poorly adhered points in the graphene can cause large area damage to the sheet. This exfoliation mechanism could also help to explain why the vast majority of devices survive the hot NMP dip: if the small area devices do not contain any points of weak adhesion, then the NMP will not intercalate and exfoliate the device.

Apart from the use of strong solvents such as NMP, thermal annealing is a commonly used method in microelectronics for ridding samples, including graphene and other 2D materials, of organic residue. Annealing can be carried out in vacuum [31] or using a mixture of gases including argon, nitrogen and hydrogen. Annealing does not always improve graphene device properties, and can, in fact, be detrimental, particularly for graphene devices fabricated

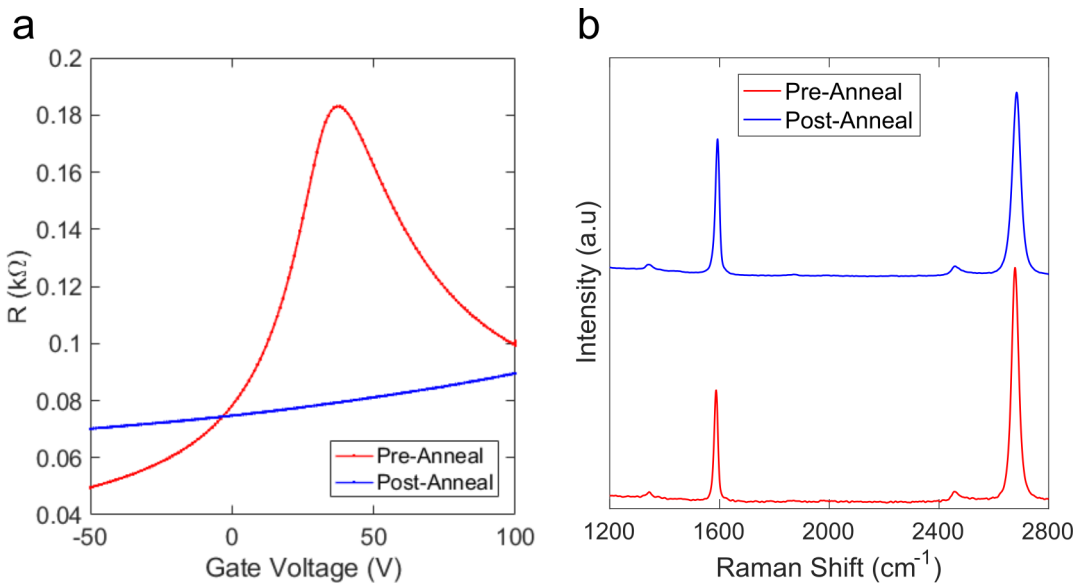

Figure 3.8: **a** Transfer curves and **b** Raman spectra ($\lambda = 532$ nm) showing the effect of thermal annealing on a graphene sheet transferred onto an SiO_2 substrate with pre-patterned contacts, with no subsequent fabrication steps.

using photoresits [19, 20]. Figure 3.8 shows the effect of a 3 hour annealing at 300° C in 96/4% Ar/H_2. The transfer curve shows that the Dirac peak has completely disappeared, possibly due to heavy substrate induced doping. In addition, a significant reduction of the resistance versus gate voltage slope is observed (i.e. the transconductance), indicating that the mobility has been reduced.

	Pre-Anneal	**Post-Anneal**
I_{2D}/I_G	2.11	1.37
FWHM 2D (cm^{-1})	29.8	36
Position 2D (cm^{-1})	2677.6	2682.5
FWHM G (cm^{-1})	14.8	16.1
Position G (cm^{-1})	1587.2	1592.2

Table 3.1: Effect of long annealing on Raman properties of device processed via photolithography.

The Raman spectra of the same sample taken before and after annealing (Figure 3.8b) also indicate that the graphene quality has been diminished, as outlined in Table 3.1. The FWHM values of both the G and 2D peaks are increased. Both peaks are also blueshifted, increasing their Raman frequency, and the I_{2D}/I_G ratio is decreased, results which were also observed by Jang et al [19], and which they attribute to possible hole doping by O_2 from the SiO_2 substrate, or from residual O_2 in the furnace chamber. This type of long annealing, which was repeated several times in rapid thermal processing (RTP) and CVD furnaces, was found to be detrimental for the samples used in this thesis. Moreover, the long

annealing had a negative effect on devices fabricated using photoresists, PMMA or even on graphene sheets transferred onto pre-patterned substrates with no subsequent fabrication steps, such as the samples shown in Figure 3.8. In order to improve its effectiveness, the annealing process was adapted according to the process published by Jang et al [19], by changing several parameters: 1. Lowering the annealing temperature from 300° C to 250° C; 2. reducing annealing time from 3 hours to 10 minutes; 3. Increasing the heating ramp speed so that the annealing temperature was reached in less than one minute as opposed to around 30 minutes; 4. Eliminating hydrogen, and using only argon throughout the process. With these modifications, significantly better results were obtained, as will be discussed below.

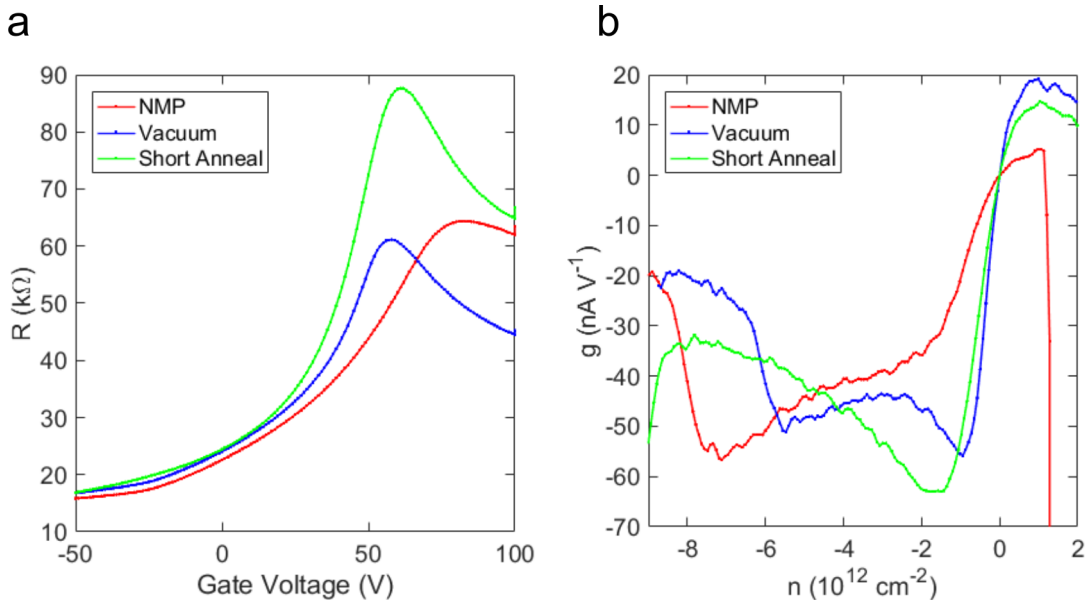

Figure 3.9: **a** Transfer and **b** transconductance curves of graphene device processed via photolithography using an optimized fabrication technique. After fabrication, the samples were first dipped in hot NMP, followed by overnight storage in vacuum, and finally a short annealing process.

Three transport curves are seen in Figure 3.9a, measured in two point configuration, depicting the evolution of the same sample under an optimized photolithography fabrication process. The initial curve of the as-processed device, just after finishing the photoresist removal, is not shown. This curve, however, reveals a heavily p-doped device, with the Dirac point not visible within the gate sweeping range. By dipping the device in 80° C NMP for 10 minutes, the Dirac point is brought back into the measuring range (at a gate voltage of 83), with a measured concentration p-dopant charge carriers of 6.15×10^{12}, as shown in table 3.2. The transconductance curve of the NMP dipped sample, shown in Figure 3.9b, does not follow its habitual shape of having a minimum/maximum for hole/electron conduction on either side of the Dirac point. Indeed, the transconductance minimum is obtained at a carrier density of -7.05×10^{12}, very far away from the Dirac point, corresponding to a hole

mobility of 307 $\mathrm{cm^2\,V^{-1}\,s^{-1}}$. The electron conduction branch appears to show the same tendencies on the other side of the Dirac point, and exhibits very low mobilities.

Sample	V_{DP} (V)	n_0 (10^{12} $\mathrm{cm^{-2}}$)	μ_h/μ_e ($\mathrm{cm^2\,V^{-1}\,s^{-1}}$)
NMP	82.8	6.15	309/-
Vacuum	57.7	4.29	305/105
Short Anneall	61.2	4.55	344/80
Al Film Buffer	45.0	3.34	1092/883

Table 3.2: Transport properties for the curves shown in Figures 3.9 and 3.6. All measurements taken in two point configuration.

By storing the sample in vacuum overnight, the p-doping is further reduced, with the Dirac point at a gate voltage of 58 V, and charge carrier concentration of 4.3×10^{12} $\mathrm{cm^2}$. In addition, the transconductance curve now exhibits its maxima and minima on either side of the Dirac point, with measured electron and hole mobilities of 301 and 103 $\mathrm{cm^2\,V^{-1}\,s^{-1}}$. The vacuum cleaned sample retains two properties from the solely NMP dipped curve: electron branch conduction supression and concomitant low electron mobility, and an anomalous, unexplained local transconductance minimum at a charge density of -5.0 $\mathrm{cm^2}$. The decreased p-doping and improved transconductance curve indicates that the overnight storage in vacuum had a significant effect on the device properties. Most likely, the vacuum was able to desorb and/or eliminate residual water residue on top of the graphene device, or trapped between the susbtrate and the device. These measurements also underscore the high sensitivity of graphene to its surrounding environment.

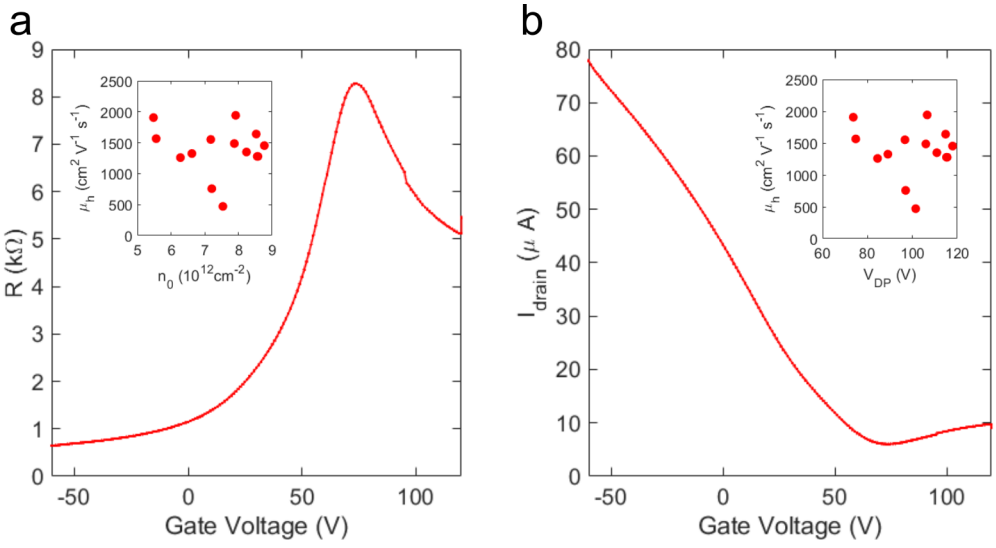

Figure 3.10: Significant improvement in device quality using optimized fabrication process and graphene grown with Ar+Anneal recipe. Transfer curves showing **a** resistance and **b** drain current. Insets: Device hole mobilities as a function of intrinsic doping, shown versus **a** n_0 and **b** V_{DP}.

The last post-fabrication step carried out on the device, after the dip in hot NMP and storage in vacuum overnight, was a short annealing in an RTP furnace, at 250° C in an argon atmosphere for 10 minutes, according to the annealing process discussed above [19]. The resulting transport curve shows that the p-doping increased slightly, with the Dirac point located at 61 V. The hole mobility increased to 344 $cm^2\,V^{-1}\,s^{-1}$, whereas the electron mobility was reduced to 80 $cm^2\,V^{-1}\,s^{-1}$. Although the electron conduction branch is still significantly suppressed, the transconductance curves shows that the anomalous local minimum around -5.0 cm^2 has disappeared, possibly indicating the elimination of some contaminant. The measured properties for this device fabricated with photolithography are not as good as the device fabricated with an Al film buffer, as evidenced in Table 3.2. However, the yield of usable devices with Dirac points within the measured gate voltage range and mobilities in the 100's of $cm^2\,V^{-1}\,s^{-1}$ present a significant advantage.

All of the transport curves presented thus far in this chapter are taken from devices fabricated with small grain graphene grown using the H_2 growth recipe. Figure 3.10 shows transfer curves taken from devices grown with Ar+Anneal recipe, and fabricated using the optimized process outlined in this section. The much larger grain sizes in this graphene result in higher device hole mobilities (the majority in the range between 1000 and 2000 $cm^2\,V^{-1}\,s^{-1}$), due to the lack of charge scattering grain boundaries [32]. In addition, the hole mobilities do not depend on the doping levels, as seen in the insets of the curves. Despite these improvements, significant electron branch conduction suppression is still observed (3.10b), with electron mobility values in the 100's of $cm^2\,V^{-1}\,s^{-1}$, most likely due to the p-doping nature of the photoresist residues.

3.5 Conclusion

This chapter has outlined the steps taken throughout this thesis to optimize the various processes needed to fabricate graphene devices. The quality of the CVD grown graphene was shown to be highly sensistive to the process environment within the chamber. Maintaining a static atmosphere during growth was found to be critical for obtaining homogeneous graphene over the sample area. In order to reduce nucleation density, increase graphene grain size and reduce disorder and defect density, the hydrogen atmosphere during the heating phase was replaced with an argon atmosphere, which prevented the reduction of the native CuO_2 surface into copper. A long annealing stage in argon was employed prior to the growth stage, to smooth the substrate surface and reduce the density of nucleation sites, resulting in large grained, high quality, graphene with very few multilayer regions. A succesful graphene transfer required the elimination of the graphene on the backside of the copper foil, which was accomplished by using an oxygen RIE. In addition, the graphene adhesion to the substrate was found to be critically important for eliminating water trapped between the substrate and the graphene. This is achieved by eliminating the oxygen plasma cleaning of the substrate just prior to the transfer, and by thoroughly drying the transferred graphene in vacuum prior to removing the PMMA in acetone. The final optimized process was device fabrication

via photolithography. By employing an Al buffer film, very good device characteristics could be obtained, due to the oxidized Al film preventing contact between the graphene and photoresist. Despite these promising results, the yield of usable devices was very low and the measured device properties inconsistent between devices. This is possibly due to a non-optimal Al film allowing photoresist to come into contact with the graphene through cracks and pinholes. Better device yields were obtained by fabricating with the photoresist in direct contact with the graphene sheet, and optimizing the post-fabrication process by using strong solvents, vacuum cleaning and adequate thermal annealings. Significantly higher mobilities were obtained by using large grain graphene, due to the elimination of charge scattering grain boundaries. Nevertheless, electron branch supression due to photoresist p-dopants remains limit the electron mobilities to values below 1000 $\mathrm{cm^2\,V^{-1}\,s^{-1}}$). The optimized processes and the explanations behind them presented in this chapter, are by no means exhaustive or comprehensive, as significantly more in depth studies have been conducted by many groups into each particular process. Nonetheless, it cannot be denied that significant improvements have been achieved in the overall development of graphene technology within the scope of this thesis.

Bibliography

[1] H. Ago, Y. Ogawa, M. Tsuji, S. Mizuno, and H. Hibino. Catalytic growth of graphene: Toward large-area single-crystalline graphene. *The Journal of Physical Chemistry Letters*, 3:2228–2236, 2012.

[2] N.C. Bartelt and K.F. McCarthy. Graphene growth on metal surfaces. *MRS Bulletin*, 37:1158–1165, 2012.

[3] Z. Yan, J. Lin, Z. Peng, Y. Sun, Z. Zhu, L. Li, C. Xiang, E.L. Samuel, C. Kittrell, and J.M. Tour. Toward the synthesis of wafer-scale single crystal graphene on copper foils. *ACS Nano*, 6:9110–9117, 2012.

[4] X. Li, W. Cai, J. An, S. Kim, J. Nah, D. Yang, R. Piner, A. Velamakanni, I. jung, E. Tutuc, S.K. Banerjee, L. Colombo, and R Ruoff. Large-area synthesis of high quality and uniform graphene films on copper foils. *Science*, 324:1312–1314, 2009.

[5] Z. Luo, Y. Lu, D.W. Singer, M.E. Berck, L.A. Somers, B.R. Goldsmith, and A.T.C. Johnson. Effect of substrate roughness and feedstock concentration on growth of wafer-scale graphene at atmospheric pressure. *Chemistry of Materials*, 23:1441–1447, 2011.

[6] X. Li, C.W. Magnuson, A. Venugopal, R.M. Tromp, J.B. Hannon, E.M. Vogel, L. Colombo, and R. Ruoff. Large-area graphene single crystals grown by low-pressure chemical vapor deposition of methane on copper. *Journal of the American Chemical Society*, 133:2816–2819, 2011.

[7] S. Chen, H. Ji, H. Chou, Q. Li, H. Li, J.W. Suk, R. Piner, L. Liao, W. Cai, and R.S. Ruoff. Milimeter-size single crystal graphene by supressing evaporative loss of Cu during low pressure chemical vapor deposition. *Advanced Materials*, 25:2062–2065, 2013.

[8] C. Wang, W. Chen, C. Hang, G. Wang, B. Tang, C. Tang, Y. Wang, W. Zou, X Zhang, S. Qin, S. Chang, and L. Wang. Growth of milimeter-size single crystal graphene on Cu foils by circumfluence chemical vapor deposition. *Scientific Reports*, 4:4537, 2014.

[9] I. Vlassiouk, M. Regmi, P. Fulvio, S. Dai, P. Datskos, G. Eres, and S. Smirnov. Role of hydrogen in chemical vapor deposition growth of large single-crystal graphene. *ACS Nano*, 5:6069–6076, 2011.

[10] Y. Zhang, Z. Li, P. Kim, L. Zhang, and C. Zhou. Anisotropic hydrogen etching of chemical vapor deposited graphene. *ACS Nano*, 6:126–132, 2012.

[11] H. Zhou, W.J. Yu, L. Riu, R. Cheng, Y. Chen, X. Huang, Y. Liu, Y. Wang, Y. Huang, and X. Duan. Chemical vapour deposition growth of large single crystals of monolayer and bilayer graphene. *Nature Communications*, 4:2096, 2013.

[12] S. Gottardi, K. Müller, L. Bignardi, J.C. Moreno-López, T.A. Pham, O. Ivashenko, M. Yablonskikh, A. Barinov, J. Björk, P. Rudolf, and M. Stöhr. Comparing graphene growth on Cu(111) versus oxidized Cu(111). *Nano Letters*, 15:917–922, 2015.

[13] J. Pang, A. Bachmatiuk, L. Fu, C. Yan, M. Zeng, J. Wang, B. Trzebicka, T. Gemming, J. Eckert, and M.H. Rummeli. Oxidation as a means to remove surface contaminants on Cu foil prior to graphene growth by chemical vapor deposition. *The Journal of Physical Chemistry C*, 119:13363–13368, 2015.

[14] C.W. Magnuson, X. Kong, H. Hi, C. Tan, H. Li, R. Piner, C.A. Ventrice, and R.S. Ruoff. Copper oxide as a self-cleaning substrate for graphene growth. *Journal of Materials Research*, 29:403–409, 2014.

[15] Y. Hao, M.S. Bharathi, L. Wang, Y. Liu, H. Chen, S. Nie, X. Wang, H. Chou, C. Tan, B. Fallahazad, H. Ramanarayan, C.W. Magnuson, E. Tutuc, B.I. Yakobson, K.F. McCarty, Y.W. Zhang, P. Kim, J. Hone, L. Colombo, and R.S. Ruoff. The role of surface oxygen in the growth of large single-crystal graphene on copper. *Science*, 342:720–723, 2013.

[16] L. Gan and Z. Luo. Turning off hydrogen to realize seeded growth of subcentimeter single-crystal graphene grains on copper. *ACS Nano*, 7:2096, 2013.

[17] T. Suni, K. Hentinnen, I. Suni, and J. Mäkinen. Effect of plasma activation on hydrophilic bonding of Si and SiO_2. *Journal of the Electrochemical Society*, 149:G348–G351, 2002.

[18] J. Fan, J.M. Michalik, L. Casado, S. Roddaro, M.R. Ibarra, and J.M. De Teresa. Investigation of the influence on graphene by using electron-beam and photo-lithography. *Solid State Communications*, 151:1574–1578, 2011.

[19] C.W. Jang, J.H. Kim, J.M. Kim, D.H. Shin, S. Kim, and S.-H. Choi. Rapid-thermal-annealing surface treatment for restoring the intrinsic properties of graphene field-effect transistors. *Nanotechnology*, 24:405301, 2013.

[20] P. Ahlberg, M. Hinnemo, M. Song, X. Gao, J. Olsson, S.-L. Zhang, and Z.-B. Zhang. A two-in-one processo for reliable graphene transistors processed with photo-lithography. *Applied Physics Letters*, 107:203104, 2015.

[21] J. Choi, H. Kim, J. Park, M.W. Iqbal, M.Z. Iqbal, J. Eom, and J. Jung. Enhanced performance of graphene by using gold film for transfer and masking process. *Current Applied Physics*, 14:1045–1050, 2014.

[22] A. Hsu, H. Wang, K.K. Kim, G. Kong, and T. Palacios. Impact of graphene interface quality on contact resistance and RF device performance. *IEEE Electron Device Letters*, 32:1008–1010, 2011.

[23] F.A. Chaves, D. Jiménez, A.A. Sagade, W. Kim, J. Riikonen, H. Lipsanen, and D. Neumaier. A physics-based model of gate tunable metal-graphene contact resistance benchmarked against experimental data. *2D Materials*, 2:025006, 2015.

[24] A.A. Sagade, D. Neumaier, D. Schall, M. Otto, A. Pesquera, A. Centeno, A.Z. Elorza, and H. Kurz. Highly air stable passivation of graphene based field effect devices. *Nanoscale*, 7:3558–3564, 2015.

[25] MicroChemicals. *Photolithography: Theory and Application of Photoresists, Etchants and Solvents*, 2012.

[26] K.A. Jackson. Plasmas. In *Kinetic Processes: Crystal Growth, Diffusion and Phase Transitions in Materials*, chapter 18, pages 241–258. Wiley, 2004.

[27] M.-F. Yu, T. Kowalewski, and R. Ruoff. Structural analysis of collapse, and twisted and collapsed, multiwalled carbon nanotubes by atomic force microscopy. *Physical Review Letters*, 86:87–90, 2000.

[28] S.P. Koenig, N.G. Boddeti, M.K. Dunn, and J.S. Bunch. Ultrastrong adhesion of graphene membranes. *Nature Nanotechnology*, 6:543–546, 2011.

[29] W. Gao and R. Huang. Effect of surface roughness on adhesion of graphene membranes. *Journal of Physics D: Applied Physics*, 44:452001, 2011.

[30] W. Gao, P. Xiao, G. Henkelman, K.M. Liechti, and R. Huang. Interfacial adhesion between graphene and silicon dioxide by density functional theory with van der Waals corrections. *Journal of Physics D: Applied Physics*, 47:255301, 2014.

[31] J. Chan, A. Venugopal, A. Pirkle, S. McDonnell, D. Hinojos, R.S. Magnuson, C.W. adn Ruoff, L. Colombo, R.M. Wallace, and E.M. Vogel. Reducing extrinsic performance limiting factors in graphene grown by chemical vapor deposition. *ACS Nano*, 6:3224–3229, 2012.

[32] Q. Yu, L.A. Jauregui, W. Wu, R. Colby, J. Tian, Z. Su, H. Cao, Z. Liu, D. Pandey, D. Wei, T.F. Chung, P. Peng, N.P. Guisinger, E.A. Stach, J. Bao, S.-S. Pei, and Y.P. Chen. Control and characterization of individual grains and grain boundaries in graphene grown by chemical vapour deposition. *Nature Materials*, 10:443–449, 2011.

Chapter 4

Graphene Chemical Functionalization and Encapsulation

Chemical functionalization of graphene could pave the way for favorably modifying this material's already remarkable properties. To this end, organic molecules have been utilized in various studies to alter graphene's structural, chemical, electrical, optical and even magnetic properties. One of the most pressing requirements for graphene's incorporation into practical electronic devices is control of its dopin. This entails customizing its Fermi level, and thus its charge carrier type and density, work function and conductivity, ideally without compromising its superior carrier mobility. Non-covalent chemical functionalization using organic molecules could provide a path to achieving this goal. To this end, two organic molecules, 7,7,8,8-tetracyano-quinodimethane (TCNQ) and ethylenediamine (EDA), have been investigated in this thesis to achieve p and n-doped graphene, respectively. Subsequently, encapsulating Al_2O_3 films were grown via atomic layer deposition (ALD) on the functionalized graphene, with the goal of protecting its chemical doping from environmental contamination and degradation.

4.1 Introduction

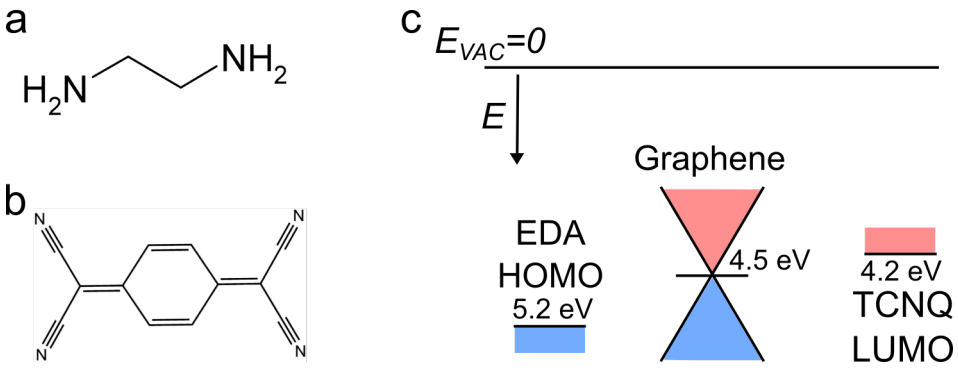

Figure 4.1: Schematics of **a** EDA and **b** TCNQ molecules. **c** Graphene Dirac Point [1], gas phase EDA (TCNQ) [2] HOMO (LUMO) [3] energy levels.

Graphene n and p doping has been investigated by using the organic molecules EDA and TCNQ, shown schematically in Figure 4.1. EDA is a liquid at room temperature, whereas TCNQ is a solid powder. The four cyano groups surrounding TCNQ's central carbon ring

endow it with strong electron accepting capabilities, whereas EDA's two amine groups make it an electron donor. Figure 4.3c shows the energy levels, relative to the vacuum level E_{vac}, of graphene's Dirac point (DP) [1], TCNQ's lowest unoccupied molecular orbital (LUMO) [3] and EDA's highest occupied molecular orbital (HOMO) [2]. The energy levels of the molecules were calculated in gas phase, while graphene's work function was measured via scanning Kelvin probe microscopy. Upon adsorption on the graphene surface, the precise locations of the energy levels changes due to interaction between the molecular and graphene orbitals. The strength of these interactions determines the magnitude and orientation of the induced surface dipole at the substrate/molecule interface, altering the energy levels of the graphene and adsorbed molecules by up to 1 eV or more, and determining the nature of the substrate-adsorbate charge transfer characteristics [4]. As will be shown throughout the rest of the chapter, electron transfer occurs from the EDA to the graphene, resulting in graphene n-doping, whereas TCNQ accepts an electron from the graphene (equivalent to saying that TCNQ transfers a hole to the graphene), resulting in graphene p-doping.

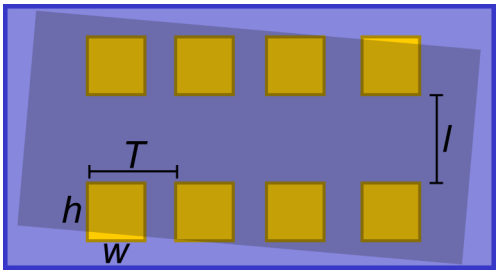

Figure 4.2: Schematic of graphene sheet transferred onto SiO_2 substrate with prepatterned contacts. Typical contact dimensions are $w = h = 400$ µm, with spacing $T = l = 500$ µm, although these varied slightly between samples.

To investigate the effects of molecular doping on the electrical properties of graphene, transport measurements were often carried out on graphene sheets transferred onto substrates with pre-patterned contacts (Figure 4.2) and subsequently chemically functionalized. No fabrication steps were carried out on the graphene, ensuring that no contaminants other than those present in the ambient came into contact with the functionalized graphene substrate, allowing for the controlled study of the effects of the doping molecule. Since there is no defined channel geometry for the graphene sheet transistors, mobility values cannot be calculated directly. However, transfer curves from the same sample can be compared to gauge the *relative* change in mobility between curves. This was done by comparing the values of the derivatives of the conductance with respect to gate voltage, dG/dV_g. The transconductance $g = dI_d/dV_g$ was not used since not all curves were taken with the same drain voltage, and therefore the magnitude of the drain current values I_d are not directly comparable. This approach is similar to the one used to calculate mobility in 4-point probe measurements (discussed in Chapter 2), in which the current is held constant and $g = 0$ by definition. Once the effect of chemical functionalization on a pristine graphene sheet was understood, devices were fabricated from pristine graphene using standard photolithography,

followed by molecular functionalization. All electrical transport measurements were taken in ambient conditions in two point configuration.

4.2 TCNQ Functionalization

TCNQ has been previously utilized to produce highly p-doped graphene, resulting in the opening of an electrical bandgap in bilayer graphene [5], and for use as a conductive anode in graphene organic solar cells [6]. Studies carried out in ultra-high vacuum have found that TCNQ deposited onto graphene grown epitaxially on ruthenium is able to form extended spin-split electronic bands resulting in long range magnetic order [7]. X-ray photoemission spectroscopy (XPS) and scanning tunneling microscopy (STM) measurements confirmed that charge transfer from the ruthenium substrate to the TCNQ, modulated by the graphene layer in between, caused the molecules to develop a magnetic moment [8, 9].

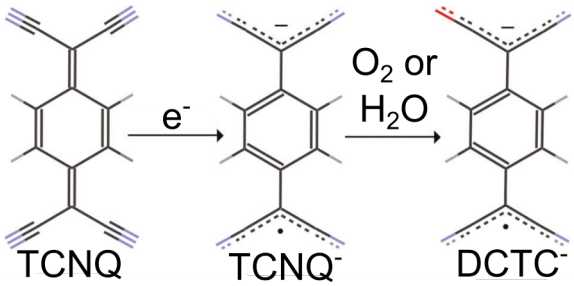

Figure 4.3: Schematic showing the formation of DCTC from TCNQ. Carbon, oxygen, nitrogen and hydrogen atoms are represented by black, red, blue and grey, respectively. Adapted from [10]

.

TCNQ and its salts have been studied extensively by Raman spectroscopy, confirming their strong electron accepting capabilities for both films and crystals synthesized by evaporation or from solution [11–15]. Depending on the substrate used and the TCNQ deposition conditions, the oxidation product of $TCNQ^{-}$, α,α-dicyano-p-toluoylcyanide (DCTC) is often detected. The formation of this molecule proceeds as depicted in Figure 4.3, with the TCNQ first accepting an electron and subsequently becoming oxidized by an oxygen or water molecule, resulting in a cyano group being substituted by a carbonyl group [10]. DCTC was detected for thin films of TCNQ evaporated onto Ag, suggesting that the TCNQ layers closes to the Ag substrates were being ionized and oxidized. As the TCNQ film thickness increased, DCTC was no longer detected, indicating that the upper layers of the film were comprised of neutral TCNQ [16]. XPS measurements of 2,3,5,6-Tetrafluoro-7,7,8,8-tetracyanoquinodimethane (F4-TCNQ) molecules deposited on epitaxial graphene on SiC showed similar behavior: electron transfer from the graphene to the first few layers of adsorbed F4-TCNQ resulted in graphene p-doping [17]. For CVD graphene transferred to an insulating substrate, DCTC was also detected for low TCNQ coverage, whereas for higher

coverages only TCNQ was detected, suggesting a similar mechanism of electron charge transfer from the graphene substrate to the first few TCNQ layers adjacent to it [10].

The investigations carried out in this study sought to understand the growth process and morphology of TCNQ evaporated onto CVD graphene supported by a SiO_2/Si substrate. Understanding the growth mechanism of TCNQ on graphene is necessary for the further development of devices utilizing graphene/TCNQ structures, with the hope of exploiting the unique properties of each material. In paritcular, TCNQ's strong doping capabilities make it a candidate for reducing graphene's sheet resistance and modulating its work function, a requirement for graphene to be integrated as a transparent electrode in organic solar cells and optical display devices [6]. Different growth regimes were explored by varying the TCNQ evaporation temperature, the graphene substrate temperature, and the location of the substrate within the growth chamber. By varying these parameters, TCNQ structures ranging from thin films to pure crystals were obtained on the graphene. Electron charge transfer from the graphene to the TCNQ and subsequent oxidation to DCTC, as previously seen by Qi et al [10], was confirmed by Raman spectroscopy and electrical transport measurements.

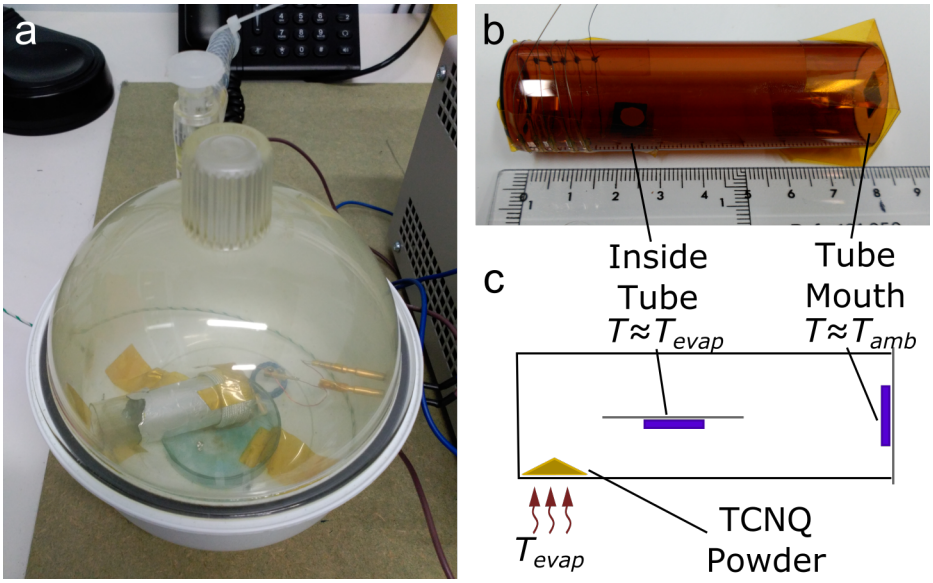

Figure 4.4: **a** Vacum dessicator **b** and large tube for TCNQ evaporation. **c** Schematic of large tube for TCNQ evaporation. The small tube setup is the same, but only has the substrate mounted on the mouth of the tube.

TCNQ evaporation was carried out in a quartz tube placed inside a vacuum desiccator (Figure 4.4a), at a pressure of 600 mbar. Each growth was carried out in either a small (3.5 cm long, 1.8 cm diameter) or a large (8 cm long, 2.3 cm diameter) quartz tube shown. The large quartz tube is shown in Figure 4.4b. The lower region of the tubes was heated resistively, by coiling tungsten wire around the exterior of the tubes. 100 mg TCNQ powder (Sigma Aldrich 157635) was placed inside the bottom of the tube. In order to achieve more

homogeneous heating, aluminum foil was also wrapped around the bottom 2 cm of the tubes. An *in situ* thermocouple was used to calibrate the relation between the power dissipated in the resistive coil (usually between 2 and 10 W) and the temperature at the bottom of the tube; subsequent evaporations were carried out without the thermocouple. The quartz tubes were sealed at their mouth openings with a glass slide, with the graphene/SiO_2 samples mounted on the glass slide facing the TCNQ powder inside the tube. In the case of the large evaporator, samples were mounted at the tube mouth and also inside the quartz tube 2 cm away from the tube bottom, facing the TCNQ powder, as shown in the picture and schematic in Figure 4.4b and c, respectively.

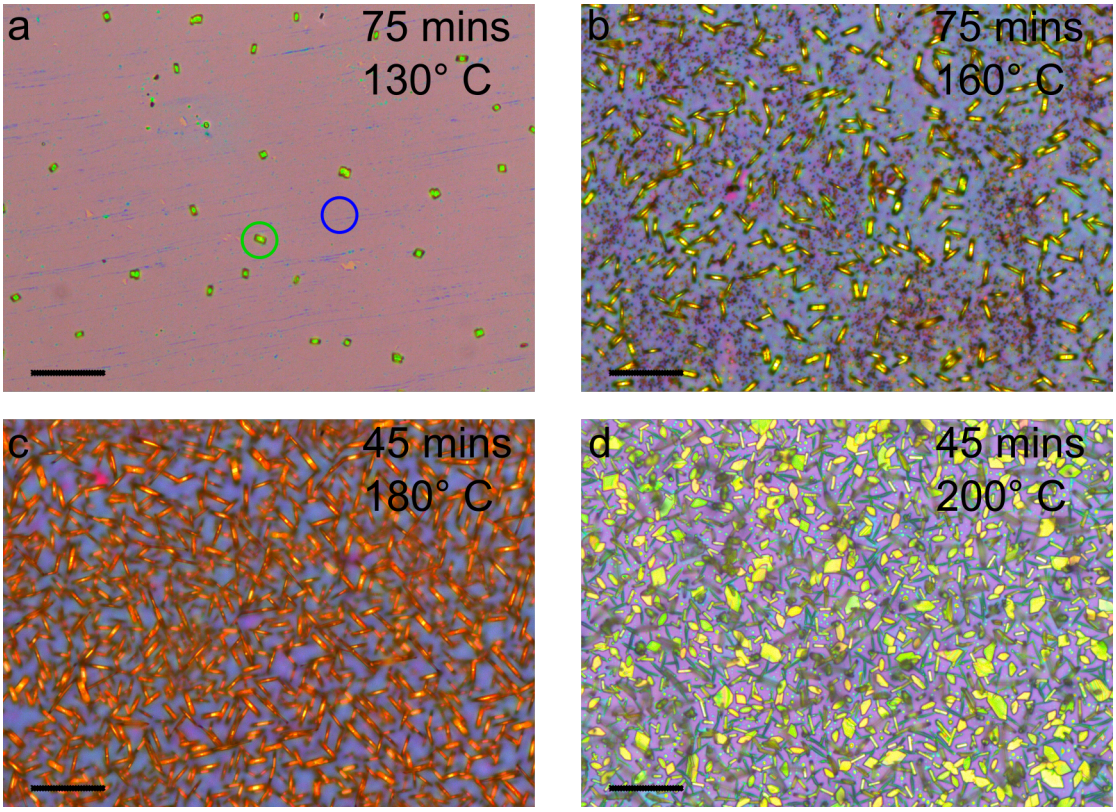

Figure 4.5: White light reflection images of TCNQ evaporated onto CVD graphene in small tube evaporator with the following conditions: **a** 75 minutes at 130° C, **b** 75 minutes at 160° C, **c** 45 minutes at 180° C and **d** 45 minutes at 200° C. All scale bars 25 µm. Circles in **a** correspond to location of Raman spectra in Figure 4.7a.

Figure 4.5 shows white light reflection optical images of TCNQ evaporated onto graphene in the small tube evaporator, for different sublimation temperatures and growth times. As seen in Figure 4.5a, a growth temperature of 130° C for 75 minutes results in the formation of pellet-like crystals on the surface of the graphene, with lateral dimensions on the order of 5 µm. Crystal separation of a few dozen microns indicates that TCNQ molecules on the graphene surface are able to diffuse a relatively large distance until they encounter a growing TCNQ crystal and become adsorbed onto it. Increasing the growth temperature

to 160° C and maintaining the same growth time clearly changes the growth regime, as shown in Figure 4.5b. The graphene substrate is no longer visible and seems to have been covered by a thick film. The morphology of the crystals on the surface has also changed, from pellets to needles with a typical length on the order of 10 µm, and width of about 2 µm. The needles are packed more closely together on the surface than the pellets. The increase in sublimation temperature substantially modifies the density of TCNQ molecules on the surface. In this growth regime, the molecules are no longer able to reach the initial condensation points; on the contrary, the TCNQ molecules self-assemble, probably via H-bonds or π-π interactions, forming a full layer that reduces the effective diffusion length of the incoming molecules and as consequence increases the density of 3D island pellets. From this temperature the growth mode remains unchanged and further increasing the growth temperature to 180° C completely saturates the graphene surface with TCNQ needles, as shown in Figure 4.5c, despite a reduction in the evaporation time from 75 to 45 minutes. Evaporating at the highest temperature obtainable in the small tube evaporator, 200° C, for 45 minutes, maintains the high crystal density on the surface but results in a change in the structure of the crystals, as seen in Figure 4.5d. Apart from needles, many plaque-shaped crystals are seen on the surface, with a typical size of 5 to 10 µm.

The large tube evaporator can accommodate two samples simultaneously, one at the tube mouth, where the sample remains close to room temperature, and another one inside the tube close to the resistive heating coils, where the sample is heated along with the TCNQ powder (see Figure 4.4c). Using this configuration, substrates close to the resistive heating coils will remain at temperatures close to the evaporation temperature, whereas substrates at the tube mouth will remain close to ambient temperature. Figure 4.6 shows optical images of TCNQ evaporated onto graphene for different growth conditions in the large tube evaporator. Figure 4.6a and b show the images corresponding to the substrate placed at the mouth of the tube, where it remains close to room temperature. Evaporating at 120° C for 60 minutes results in the formation of TCNQ crystal pellets, as seen in Figure 4.6a. Figure 4.6b shows that increasing the growth temperature to 170° C favors the formation of a high concentration of short needles on the graphene surface, with a typical length of 2 to 3 µm. The comparison with images in Figure 4.5a and b reveals a similar morphology for for similar growth conditions in both the small and large tubes. When the substrate remains close to room temperature, the main findings can summarized as follows: for lower sublimation temperatures the growth of pellet-like TCNQ crystals occurs, whereas for higher sublimation temperatures, the growth regime changes, and a high density of TCNQ crystal needles form.

For samples placed on the inside of the large tube, where the substrate is heated during the evaporation, TCNQ films were formed for all growth conditions. For low TCNQ coverage, like that shown in Figure 4.6c, practically no changes are noticeable on the graphene surface when compared to pristine graphene. By increasing the evaporation temperature from 120° C to 170° C, a change is observed in the coloration of the graphene, which becomes slightly

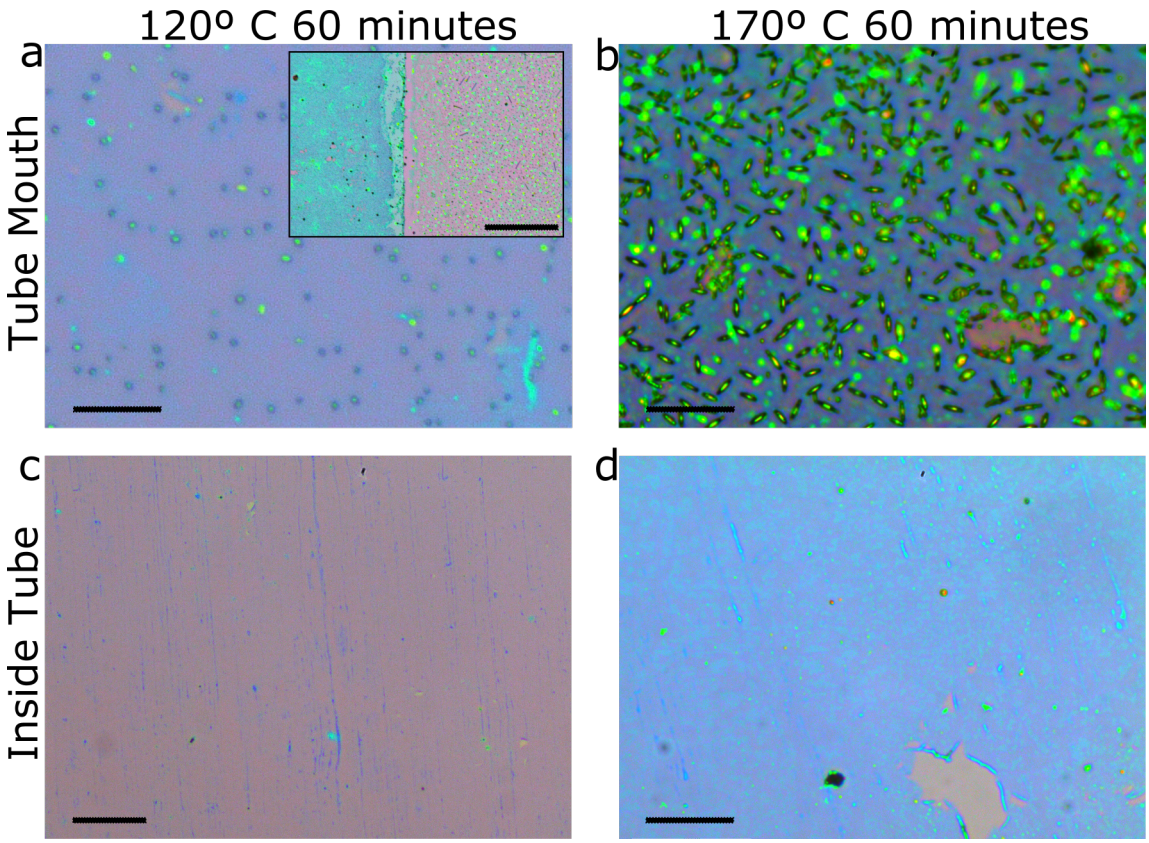

Figure 4.6: White light reflection images of TCNQ evaporated onto graphene substrate in large tube evaporator with the conditision outlined on the margins of the images. Scale bar in **c** is 40 µm, in **a**, **b**, and **d** 15 µm. INSET: Same sample as in **a**, showing the boundary between graphene (left) and bare SiO_2 (right). TCNQ crystals can be seen on both sides of the boundary. Scale bar 250 µm.

bluer as seen in Figure 4.6d (note that in all of these images, the white balance has been adjusted to make bare SiO_2 background equal). More interestingly, blue patches and spots are visible within the purple background, covering almost half of the surface area, with a typical size of 15 to 20 µm.

From these results it is clear that the growth mechanism on both the large and small tube evaporator is the same for the substrates held close to ambient temperature, and leads to the formation of TCNQ crystals. When the substrate is held at elevated temperatures during evaporation the TCNQ deposition produces a uniform thin molecular film on the graphene substrate. The change from crystals to films at higher substrate temperatures may be due to two different mechanisms. First, an elevated substrate temperature increases desorption, reducing the overall sticking coefficient of the TCNQ molecules present on the graphene surface. Second, TCNQ molecules on a hotter substrate will have more thermal energy to diffuse about the surface, making it less likely they will remain stuck to previously formed TCNQ clusters they encounter, thereby limiting the formation of large crystals. It is interesting to note that at low evaporation temperatures, TCNQ crystals grow in a

similar fashion on both the graphene and the bare SiO_2 substrate, as shown in the inset of Figure 4.6. At elevated substrate temperatures, however, no TCNQ is detected on the SiO_2 either via optical inspection or Raman spectroscopy, indicating that under these conditions the sticking coefficient approaches zero. This confirms that desorption is a much more pronounced mechanism at higher temperatures. Under these growth conditions, TCNQ films form only on the graphene due to more favorable adhesion conditions, most likely a result of π-π interactions and dispersion forces between TCNQ and graphene's honeycomb lattice.

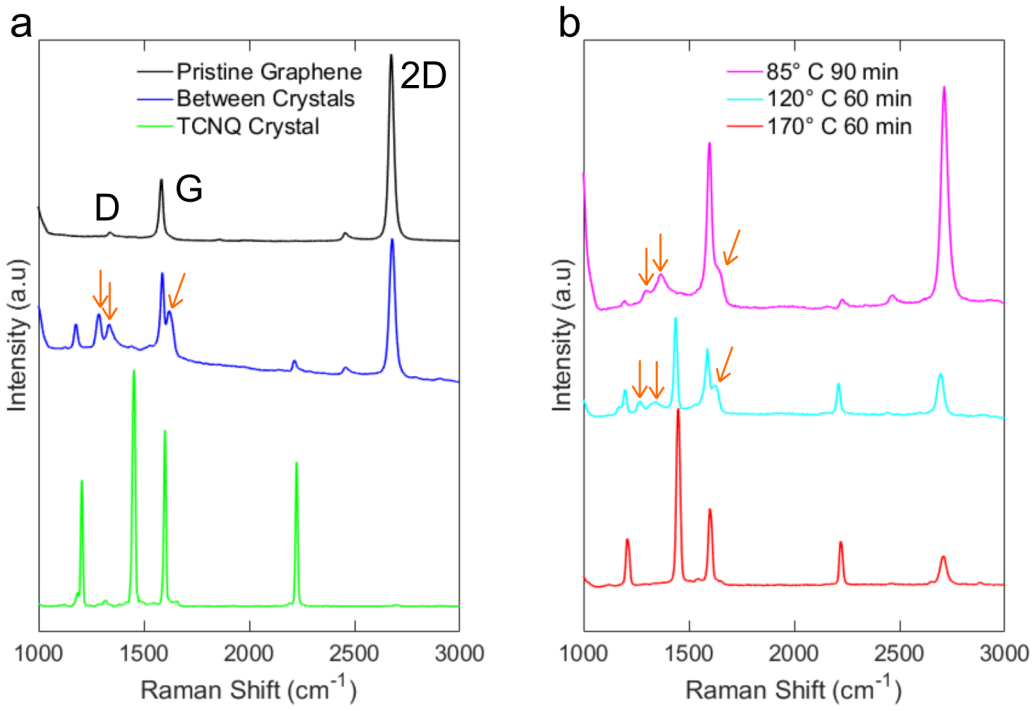

Figure 4.7: Raman spectra of TCNQ functionalized graphene. Blue and green spectra in **a** were carried out on the sample in Figure 4.5a, grown in the small tube, in the locations indicated by the colored circles. **b** Raman spectra of different TCNQ films grown in the large tube near the heating coils. Evaporation temperature indicated in the legend. Peaks corresponding to DCTC are pointed out with orange arrows in both figures.

Raman spectroscopy measurements were carried out on the TCNQ/graphene structures, with spectra from growths in the small tube shown in Figure 4.7a, and spectra from films grown in the large tube shown in Figure 4.7b. A reference spectrum of pristine graphene on SiO_2 is also shown in Figure 4.7a. The low intensity of the D peak, and high I_{2D}/I_G ratios confirm that the graphene is almost defect free and monolayer, with little intrinsic doping. For all of the TCNQ functionalized samples, a diminishing I_{2D}/I_G ratio was interpreted as an indication of graphene doping, as confirmed experimentally in multiple studies [18, 19]. The theoretical description behind this phenomenon is based on a model in which electron-electron scattering increases with doping, thereby decreasing the recombination

of photoexcited electron-hole pairs [20]. Within this model, the 2D peak intensity I_{2D} is inversely proportional to the square of the total scattering rate γ of the photoexcited electron-hole pair: $I_{2D} \propto \gamma^{-2} = (\gamma_{e-ph} + \gamma_{e-e})^{-2}$, where γ_{e-ph} and γ_{e-e} are the electron-phonon and electron-electron scattering rate. In the limit of low doping (for $|E_F|$ below 0.3 to 0.4 eV, well within the achievable doping range in these experiments), the scattering rate is dominated by small momentum transfer collisions, where $\gamma_{e-e} = c|E_F|$, with $c \sim$ 0.5 - 1 determined by the dielectric environment. Therefore, as doping $|E_F|$ increases, the 2D peak intensity I_{2D} will decrease [20]. Given that the G peak intensity is practically constant at low doping levels, a decreased I_{2D}/I_G ratio, as seen in Figure 4.7 for TCNQ functionalization, is a telltale sign of increased graphene doping.

The blue curve in Figure 4.7a was taken between the crystals on the surface of the sample from Figure 4.5a. The reduction in I_{2D}/I_G is clear, indicating that the graphene is doped. The peaks observed at 1179, 1288 and 1621 cm^{-1} are associated with the presence of DCTC, the oxidation product of TCNQ, replicating the measurements made by Qi et al [10]. DCTC associated peaks are pointed out with orange arrows for all spectra in Figure 4.7. The presence of TCNQ on the graphene surface is confirmed from the peaks at 1204, 1446, and 2218 cm^{-1} [11, 14]. The peak located at 1592 cm^{-1} results from a combination of the graphene G peak and a TCNQ peak at 1598 cm^{-1}. An increase in the graphene D peak is also observed, suggesting that the TCNQ is increasing the disorder in the graphene, possibly due to lattice strain. Along with the diminished I_{2D}/I_G ratio, the presence of DCTC confirms that electron charge transfer is occurring from the graphene to the TCNQ, as explained in the schematic in Figure 4.3. The green spectrum in Figure 4.7a shows Raman spectra taken on top of the crystals from Figure 4.5a. Strong, pure TCNQ peaks are detected, with no sign of graphene or DCTC; identical results obtained whenever Raman spectra were taken on top of needle or pellet-like crystals.

Raman spectra taken of TCNQ films evaporated on the inside of the large tube, where the substrate is heated during growth, are shown in Figure 4.7b. TCNQ and DCTC are detected over the entire surface for evaporation temperatures as low as 85° C. At this low temperature, the graphene peaks are quite strong, and weak peaks corresponding mostly to DCTC are identifiable in the range between 1150 and 1600 cm^{-1}, as well as a TCNQ peak at 2220 cm^{-1}. A slight increase in the graphene D peak is also observed. Increasing the evaporation temperature to 120° C, corresponding to the sample shown in Figure 4.6c, intensifies both the TCNQ and DCTC peaks with respect to the graphene peaks, although an increase in the D peak intensity is also observed. For the highest achievable evaporation temperature in the large tube evaporator, 170° C, corresponding to the sample shown in Figure 4.6d, only TCNQ and graphene peaks are detectable, with no sign of DCTC. It would seem that for these high coverages, the bulk TCNQ film is thick enough that it overwhelms any signal that may be coming from the oxidized layers of DCTC adjacent to the graphene, where charge transfer is occurring. The measured G peak frequency is seen to increase from around 1585 cm^{-1} in pristine graphene towards 1600 cm^{-1} for samples grown in both the

large and small evaporator. This is another indication that there is charge transfer from the graphene to the TCNQ molecules, resulting in graphene p-doping [18, 21]. Apart from the charge transfer, part of this apparent shift in the graphene G peak may also be due to its merging with the TCNQ peak situated at 1600 cm^{-1}.

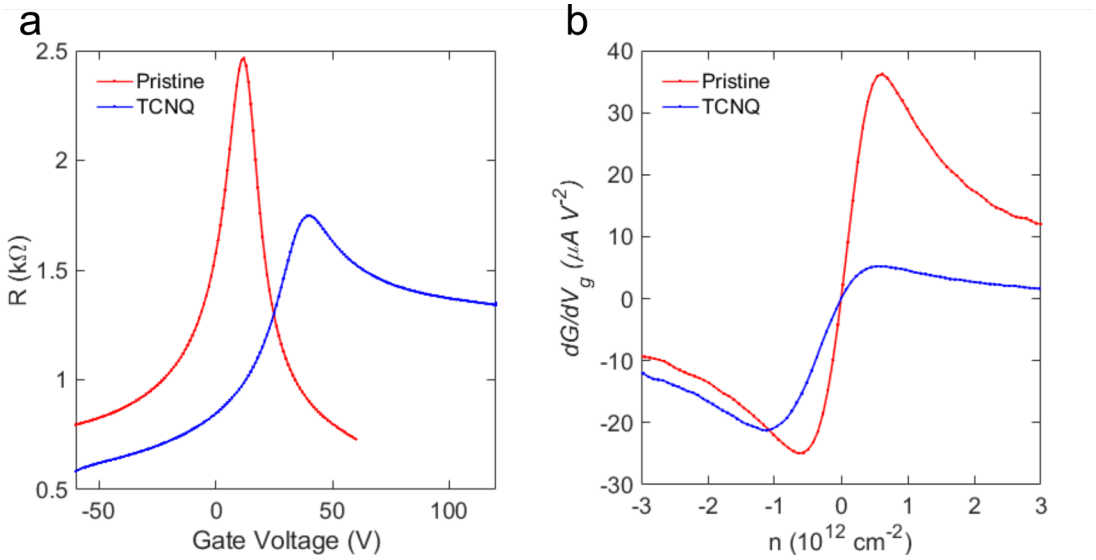

Figure 4.8: Transfer curves (**a** resistance and **b** dG/dV_g) showing the evolution of the transport behavior of pristine graphene upon TCNQ functionalization. Measurement taken on graphene sheet with no subsequent fabrication steps.

Transport measurements carried out on graphene sheets before and after TCNQ functionalization (with no subsequent microfabrication), are shown in Figure 4.8. The transfer curves further confirm the p-doping properties of TCNQ. The initial pristine graphene curve exhibits the typical shape, with slight p-doping and electron mobility nearly twice as large as hole mobility, as evidenced by the peak minimum and maximum values of dG/dV_g 4.8b. After TCNQ film evaporation, significant p-doping is observed, accompanied by a drastic decrease in the electron mobility. Similar to photoresist residues, the p-doping TCNQ molecules act as long range Coulomb scattering centers for electrons, suppressing their conduction due to band misalignment at the graphene/electrode interface. The hole mobility, on the other hand, is much less affected, with the resistance of the entire hole conduction branch reduced (a reduction of 25% was measured for a gate voltage of -50 V). Reducing graphene's sheet resistance is an important requirement for its implementation as a viable transparent electrode, and as such, low resitance TCNQ doped graphene has been utilized as a transparent anode in an organic solar cell [6].

AFM measurements, shown in Figure 4.9, indicate that increasing TCNQ functionalization leads to significant rippling and wrinkling of the graphene sheet. Although the pristine graphene surface is mostly clean (Figure 4.9a), it shows several folds with typical heights of 2-3 nm, and a few much larger PMMA clusters, with heights varying between 20 and 30 nm. Evaporating TCNQ at 120° C for 60 minutes produces an obvious change on the graphene

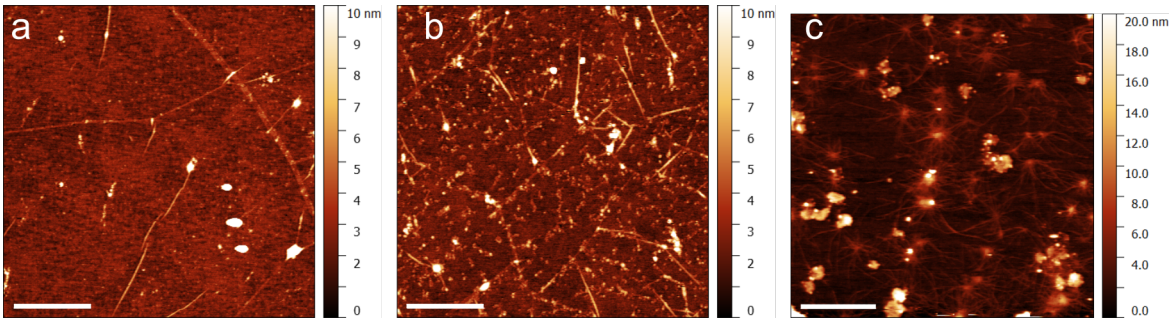

Figure 4.9: AFM topography images of pristine graphene with various degrees of TCNQ functionalization: **a** Pristine, **b** 60 min 120° C, **c** 120 min 170° C. Scale bars 1 µm.

surface, as seen in Figure 4.9b, with the appearance of randomly distributed TCNQ/DCTC clusters, with a typical size of 50-200 nm and heights of 2-3 nm. At very high TCNQ coverage, shown in Figure 4.9c, very large clusters have formed, with heights ranging between 10 and 20 nm, and several hundred nm in lateral size. In addition, a sort of filament-like feature can be seen to extend from cluster to cluster, with a typical height of 1.5–2.5 nm. These filaments may be folds or wrinkles caused by the TCNQ clusters straining the graphene surface, or even by the intercalation of TCNQ between the graphene and SiO_2 substrate. These folds and ripples could be responsible for the increased defect/disorder related D peak intensity observed in highly functionlized graphene-TCNQ samples, as well as acting as short range scattering centers, reducing charge carrier mobility [22].

4.3 Ethylenediamine Functionalization

Functionalization with EDA was used to n dope graphene, complimenting the p-doping capabilities of TCNQ. EDA's strong electron donating capabilities make it an effective agent for the reduction of graphene oxide, as well as functioning as a surface modifier and linker between reduced graphene oxide flakes [23]. EDA, along with other related ethyl amine molecules such as diethylene triamine (DETA) and triethylene tetramine (TETA), have been previously used as effective graphene n-dopants [24]. One significant advantage of using these molecules is that they physisorb to graphene without altering its lattice or orbital structure, and therefore have a relatively small effect on the carrier mobility. TCNQ also physisorbs to graphene, however, as observed in the last section, with increasing coverage it forms increasingly large clusters which wrinkle and ripple the graphene, and likely act as mobility reducing charge scattering centers. AFM images of EDA functionalized graphene shown by Kim et al [24] indicate that EDA forms small islands on the graphene surface, without causing any visible straining or distortion of the graphene. EDA physisorption is in stark contrast to n-doping via covalent functionalization, which has been achieved by substituting C atoms for N atoms within the graphene lattice [25]. In that study, the strong increase in the D peak Raman intensity indicated that the atomic substitution severely distorted the graphene lattice. Despite this drawback, one important advantage of covalent modification

is its superior stability compared to non-covalent functionalization methods, since mildly physisorbed molecules have a tendency to desorb with time or with increased temperature. This section presents the results of chemically functionalizing graphene with EDA via vapor phase deposition. Highly effective n-doping is demonstrated, with a relatively small effect on carrier mobility. The stability of this functionalization is also explored, with doping shown to decrease with time and immersion in iso-propyl alcohol (IPA), while being largely resistant to immersion in acetone and temperatures up to 100°.

Vapor phase EDA functionalization was carried out using a method similar to that presented in [24]. Cleanroom tissue paper was placed on a quartz petri dish and wetted with EDA (usually between 0.1 and 0.8 mL). The graphene substrate was placed next to the cleanroom paper on the petri dish, which was then placed on a hotplate at 70° C and covered with a quartz glass. The process was completed after about 30 minutes, when the EDA had fully evaporated from the tissue paper. In this configuration, the graphene substrate and the EDA soaked tissue paper are heated to the same temperature. This prevented condensation of EDA droplets on the graphene substrate. The doping intensity could be modulated by varying the amount of EDA used: larger volumes of EDA required longer time to fully evaporate, increasing the exposure dose.

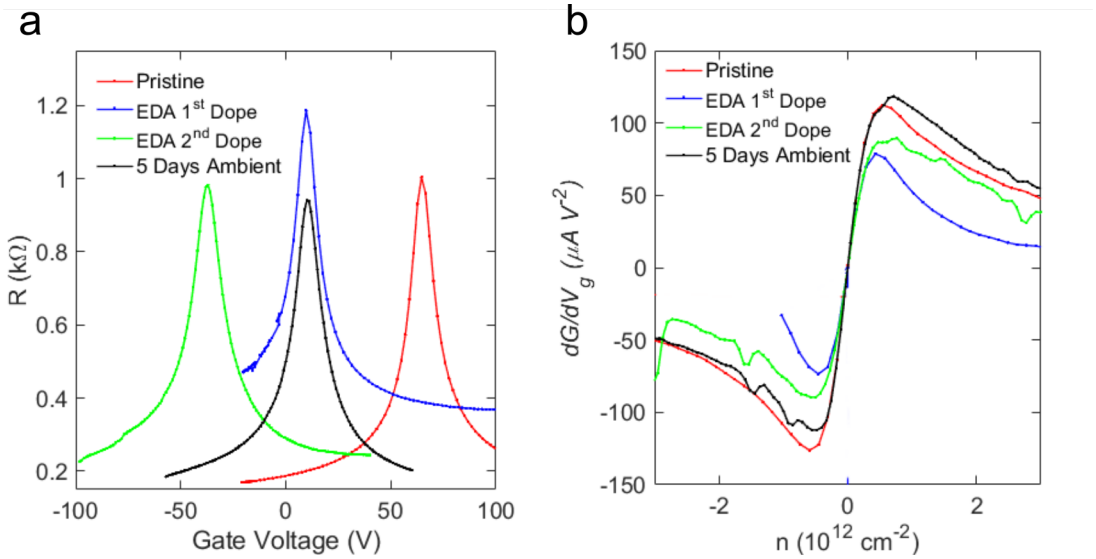

Figure 4.10: Transfer curves of EDA functionalized graphene, showing **a** resistance and **b** dG/dV_g. Measurements were carried out in two point configuration on a graphene sheet transferred onto a substrate with pre-patterned contacts, with no subsequent fabrication steps.

Figure 4.10 shows the effect of EDA doping on graphene sheets with no subsequent fabrication. The electrical parameters of each curve presented in Table 4.1. The pristine curve shows that the graphene is intrinsically p-doped, likely due to a combination of PMMA residues from the transfer process, substrate effects, and environmental contaminants such as water and oxygen. The ratio between its hole and electron mobilities is close to unity,

Sample	V_{DP} (V)	n_0 (10^{12} cm^{-2})	μ_h/μ_e	$\mu_{h,pristine}$
Pristine	64.9	4.82	1.12	-
EDA Dope 1	9.9	0.74	0.93	0.58
EDA Dope 2	-37.3	-2.77	1.00	0.71
Ambient 5 Days	10.4	7.73	0.95	0.89

Table 4.1: Transport properties of the curves shown in Figure 4.10, showing the Dirac point V_{DP}, intrinsic doping n_0, ratio of hole to electron mobilities mu_h/mu_e and ratio of each sample's hole mobility to that of the pristine graphene, $\mu_{h,pristine}$.

in contrast to devices fabricated with photoresist, which exhibit a hole to electron mobility ratio ranging from 3 to 5. The sample was chemically functionalized by exposing it to 0.2 mL EDA for 30 minutes, resulting in a a nearly intrinsic, undoped graphene with a very low charge carrier density. This confirms that the n-doping EDA is compensating for the p-doping contaminants in the pristine graphene. The overall resistance is increased by about 25%, resulting decrease in overall mobility, as seen in the dG/dV_g curves and in the last column of Table 4.1, showing the ratio of the hole mobility to the hole mobility of the original pristine sample. Other experiments carried out under similar conditions indicate that this resistance increase effect is anomalous and not a result of the EDA doping, but due to poor contact between the probe tips and electrodes during this particular measurement. Repeating the same functionalization process results in further n-doping of the graphene, similar in magnitude to the first doping, indicating that the process is cumulative. Although the measured resistance is close to that of the pristine graphene, the mobility has been reduced by about 30%. The reduced mobility may be an indication that the high concentration of adsorbed EDA molecules may be acting as scattering centers for the charge carriers. Leaving the doped substrate in ambient for five days results in slight p-doping of the graphene. In addition, the absolute mobility has recovered to 89% of its pristine value. The p-doping and mobility recuperation most likely result from desorption of some of the EDA molecules over time. It is interesting to note that in all of the measured curves, the hole to electron mobility ratio remains close to unity. This indicates that unlike photoresist residues or TCNQ molecules, the EDA is not acting as a preferential scattering center for one type of charge carrier, although the precise reasons behind this phenomenon remain unclear.

The results of testing the effect of solvents commonly used during microfabrication on the EDA functionalization can be seen in Figure 4.11. Acetone had little effect, as shown in the resistance and dG/dV_g curves. These results, along with sustained doping even after 5 days in ambient (Figure 4.10), indicate that even though the EDA is physisorbed to the graphene, it is not so weakly bound as to be easily removable. Due to EDA's solubility in alcohols and water, immersing the functionalized sample in iso-propyl alcohol (IPA) results in a much more effective reversal of the doping, as seen in Figure 4.10c. After one hour in IPA, the n-doping has been almost completely reversed, although the absolute mobility values remain practically constant, as evidenced by the peak maximum and minimum values

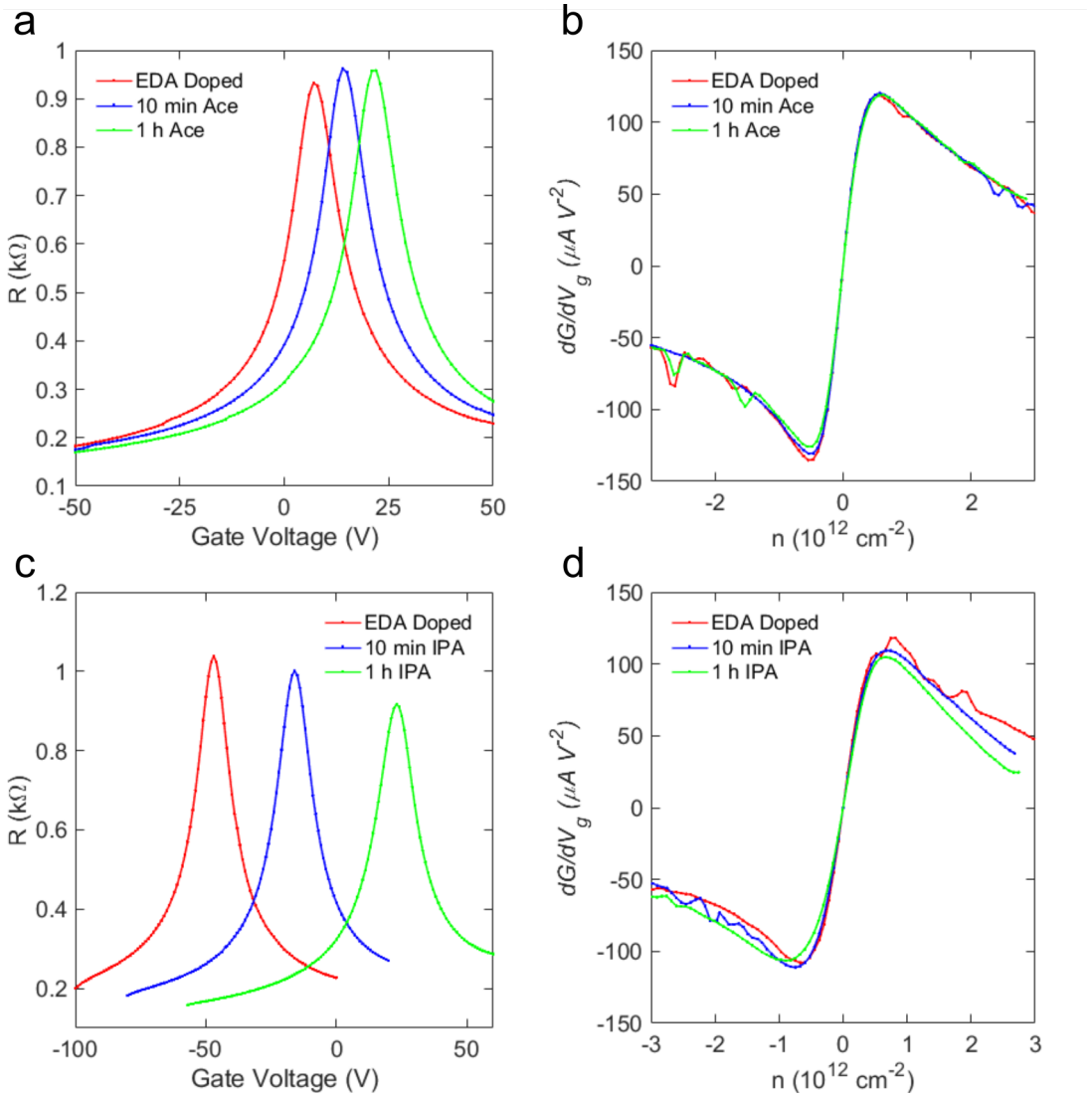

Figure 4.11: Transfer curves of EDA functionalized graphene, demonstrating the effects of different commonly used solvents on the doping. **a** and **b** acetone, **c** and **d** IPA.

of the dG/dV_g curve in Figure 4.11d. Overall, the mobility values of graphene seem to be much less affected by EDA doping compared to TCNQ doping. This is especially true for electron mobility, which is drastically suppressed with TCNQ functionalization. It is possible that TCNQ cluster and filaments, resulting in graphene wrinkles and ripples seen in the AFM images of Figure 4.9, may be strong electron scattering centers. EDA doping has not been reported to cause such large strains on the graphene, which probably account for its much less pronounced effect on the absolute mobility values.

4.4 Al_2O_3 Atomic Layer Deposition on Graphene

In order for graphene and other 2D materials to become suitable for scalable mass production, techniques and processes must be developed to effectively protect and passivate them from contamination and degradation. For chemically doped graphene, this entails preventing the desorption of the doping molecules and their reaction with compounds present in the ambient environment. With this goal in mind, encapsulating Al_2O_3 films were grown via ALD on graphene chemically doped with EDA and TCNQ. ALD grown films are commonly used in the microelectronics industry, serving as top gate dielectric in field effect transistors, tunneling barriers in memory devices, and as protective encapsulating layers in optical displays. With so many important functions, it is clear that the growth of such films on graphene, and specifically on chemically functionalized graphene, is a stepping stone for the full scale incorporation of graphene into the microelectronics fabrication line.

ALD is a thin film deposition technique, unique in its ability to coat complex three dimensional geometries in a conformal way. The resulting film covers all surfaces of the shape, even within high aspect ratio zones, with minimal variations in properties and thickness. ALD film growth is based on a chemical reaction between gaseous precursors sequentially deposited on a substrate. Under ideal conditions, the gaseous precursors react with the surface of the material in a self-limiting gas-solid reaction. By repeating sequential precursor cycles, a thin film of the desired material is deposited. Al_2O_3 is one of the materials most commonly deposited via ALD, as well as one of the most studied and well understood. Trimethylaluminum (TMA) and water are the most often used gaseous precursors for ALD deposition of Al_2O_3 [26]. Figure 4.12 shows the sequential steps comprising one growth cycle of the ALD process. The first step consists of the introduction of TMA into the growth chamber, carried by an inert gas such as argon at at pressures between 1 and 10 Torr. The TMA chemically reacts with functional groups on the surface of the substrate, such as the hydroxyl OH groups shown in the Figure 4.12, producing methane as a gaseous byproduct. Ideally this reaction is self-terminating, resulting in bonding between all the functional groups on the surface and the Al atom on the TMA. As shown in the Figure, the reaction does not necessarily proceed in a completely homogeneous fashion. Some TMA molecules may bond to only one oxygen atom, whereas others may bond to two; some hydroxyl groups may be left unreacted. The likelihood of these scenarios depend on the density and homogeneity of functional groups on the substrate surface, as well as the growth conditions. At lower temperatures, these sort of inhomogeneities are more likely to occur and accumulate during growth [27]. A purging step evacuates the remaning unreacted TMA and gaseous byproducts from the chamber, prior to the introduction of the water gaseous precursor in Step 2. By chemically reacting with the water molecules, the aluminum is oxidized, replacing the CH_3 groups with hydroxyls, once again producing methane as a byproduct. After another purge, the cycle can be repeated sequentially to result in the growth of an Al_2O_3 film [26, 28]. Similar to step 1, the oxidation of the surface with water is not necessarily a homogeneous reaction, especially at lower temperatures [27].

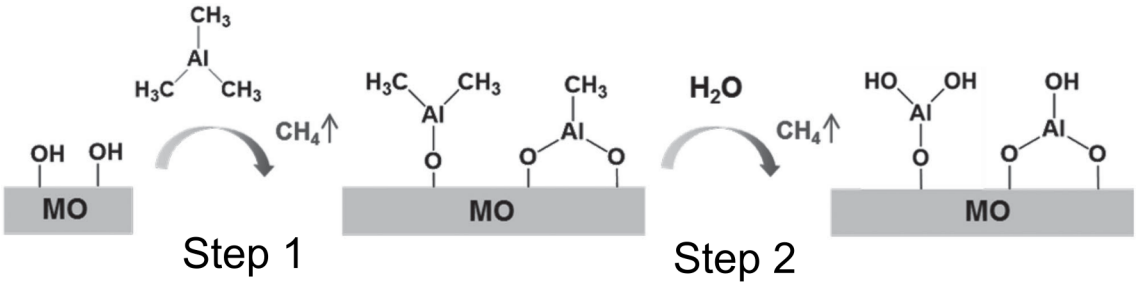

Figure 4.12: Sequential steps for the deposition of Al_2O_3 via ALD using TMA and water as precursors. Adapted from [28].

Self-limiting growth of Al_2O_3 has been achieved in temperatures ranging from ambient up to 350° C [27]. Growth at low temperature, particularly below 100° C, is of particular interest, since it allows for film deposition on organic and/or biological materials without degrading them. This growth regime, however, presents several challenges. At low temperatures, the precursors are more likely to physisorb on the surface in a reversible way, as opposed to irreversible chemisorption with the substrate functional groups (as shown in Figure 4.12. Unreacted functional groups and physisorbed precursors remaining on the surface prevent the chemical reaction from being self-limiting. Due to slow desorption at low temperatures, longer purge times are required to fully evacuate the unreacted precursors to avoid the mixing of reactants in the chamber. A consequence of these conditions is that Al_2O_3 films grown at low temperatures tend to be more amorphous and porous, with higher hydrogen and carbon concentration, most likely due to the presence of unreacted precursors within the film.

Graphene's relatively inert character in the out of plane direction, due to the lack of any functional groups or reactive dangling bonds suitable for precursor chemisorption, make the growth of oxide layers via ALD particularly challenging. Various techniques have been implemented to circumvent this limitation. One way of growing conformal ALD films is by chemically functionalizing or seeding the graphene with a molecular monolayer prior to the ALD growth. Carboxylate groups which can become easily deprotonated offer ideal functional sites for the chemisorption of the TMA/water precursors. As such, both 3,4,9,10-perylene tetracarboxylic acid (PTCA) [29] and perylene-3,4,9,10-tetracarboxylic dianhydride (PTCDA) [30] have been effectively used as a graphene functionalization layer to grow continuous Al_2O_3 films. In addition, the planar, conjugated ring structure of these molecules allow for π-π dispersion interactions between them and the graphene. Mild plasma treatments with oxygen [31] and hydrogen [32] prior to ALD film growth have also been used to make graphene more reactive to precursors. These plasma based methods, however, alter the graphene lattice by creating defects and bonds between carbon and plasma radical atoms. Furthermore, the harsh plasma would damage any functionalizing molecules present on the graphene surface. An analogous approach replaces the oxidizing precursor water with ozone during ALD growth [33]. The highly reactive ozone, much like a plasma, is prone to

damaging the graphene and any organic molecule on the surface, and thus ALD growths using ozone should be carried out at low temperatures to limit damage [34].

Instead of functionalizing with organic molecules, metal oxide seeding layers can be used as a base upon which to grow ALD oxide films. Thin metal films, generally below 5 nm, are evaporated onto the graphene and allowed to naturally oxidize in ambient conditions to form the seeding layer. For example, to grow Al_2O_3 via ALD, a thin layer of Al is evaporated and oxidized into AlOx. This approach has been succefully used to fabricate graphene field effect transistors (GFETs) with top gates [35], although reductions in the intrinsic mobility of the graphene along with slight n-doping have been observed [36]. Better results have been obtained by directly depositing an oxide layer through physical vapor deposition, instead of allowing a metal film to naturally oxidize [37]. The importance of the metal oxidation process was explored by Sagade et al [38]. In their study, oxygen was introduced into the chamber during metal seed evaporation, resulting in *in situ* oxidation of the Al seed layer. After a subsequent ALD growth, the doping of the GFET devices was found to be highly sensistive to the oxygen partial pressure in the chamber; large n-doping was found for growths without any *in situ* oxygen, whereas excessive oxygen partial pressure resulted in p-doped devices with large hysteresis. Obtaining fully passivated, hysteresis free devices has proved difficult, requiring thick (at least 90 nm) films [34, 38] to overcome their porous nature, preventing ambient contaminants such as oxygen and water from settling on the graphene devices [39].

The small process window and high sensitivity of the oxidized metal seeding layer approach has spurred various research groups to re-examine the direct growth of ALD films on graphene. The basic idea behind these efforts is to increase the concentration of precursors on the graphene film, thereby increasing the nucleation density of Al_2O_3. One way of achieving this is by drastically reducing the process temperature, thereby encouraging the physisorption of precursors on the graphene surface [40]. By growing at 50° C, and adequately adjusting the precursor purge times, thin (<5 nm) Al_2O_3 films with high quality dielectric properties were obtained [40]. An alternative method for increasing the precursor concentration on the graphene is to simply increase their residence time within the ALD chamber, allowing more molecules to settle on the graphene surface and react with the previous layer of precursors [34]. This method requires special attention to the purge times between pulses, to prevent reactions between leftover precursors in the chamber or on the graphene surface. A variation of this method involves the "seeding" of the graphene surface with precursors: by repeatedly dosing the graphene with just one type of precursor, a layer of precursor molecule is formed, similar to the seeding layers of PTCA and PTCDA mentioned previously. After the initial seeding step, direct growth of Al_2O_3 can proceed as normal [34, 41]. This method has been used to successfully encapsulate graphene beneath a 90 nm Al_2O_3 film, with the GFET devices showing minimal hysteresis and doping, while retaining their pre-encapsulation mobilities.

Building upon these advances, one of the obvious next steps that needs to be explored is the growth of oxide films on chemically doped graphene, which may be critical if graphene

is ever to become a practical material for microelectronic device applications. This work explores the growth of Al_2O_3 films on graphene functionalized with TCNQ and EDA molecules, and characterized by Raman spectroscopy, AFM and SEM. GFET devices were also fabricated to explore the electronic properties of these functionalized system. Despite the chemical functionalization of the graphene surface, direct growth of ALD films was found to be exceptionally difficult. Moreover, when GFET devices incorporating these films were fabricated, they were found to inadequately protect the chemical functionalization of the graphene from the microfabrication process. By combining a thermally evaporated AlOx seeding film with Al_2O_3 growth, better quality results were obtained. For the TCNQ functionalized graphene, a strong n-doping and mobility reduction was observed after thermal/ALD film growth, even though the presence of TCNQ was detected below the Al_2O_3 film. The EDA functionalized graphene, on the other hand, was found to maintain its n-doping qualities after film deposition. Moreover, the devices were shown to preserve their doping even after a week of exposure to ambient conditions.

TCNQ functionalization for all ALD growth experiments was carried out on the inside of the small tube, resulting in TCNQ film growth, at 150° C. Likewise, EDA functionalization for ALD film growth was carried out using the habitual hotplate method, heating the EDA and sample to 70° C. The EDA quantities used varied from 0.3 to 0.8 mL.

4.4.1 Direct Al_2O_3 ALD Growth

Initially, direct growth of ALD Al_2O_3 films on chemically functionalized graphene was attempted, based on the logic that the molecules on the graphene surface might serve as nucleation centers and yield a continuous film. An optical microscopy examination comparing directly grown ALD Al_2O_3 shows a much more continuous film on TCNQ functionalized graphene compared to pristine graphene (Figure 4.13a and b). Pink areas in the pristine graphene image are regions of higher Al_2O_3 nuleation density. These regions show clearly defined boundaries, which correspond to the grains of the copper substrate upon which the graphene was grown. This distribution may be due to differences in the graphene grain size and nucleation density on different copper grains, a result of the different nucleation activation energies for varying copper surface orientations [42]. Another possible explanation is that substrate effects may be favoring Al_2O_3 nucleation in certain regions. Different surface adsorption energies are observed for graphene depending on the substrate, resulting in different nucleation densities and growth modes for directly grown ALD films [43]. The variations in film density observed in Figure 4.13 could thus partly be explained by inhomogeneous trapping of water between the graphene sheet and SiO_2 substrate. The film grown on the TCNQ functionalized graphene, shown in Figure 4.13b, is much more homogeneous than that grown on the pristine graphene, indicating that the TCNQ molecules and clusters serve as effective nucleation sites for Al_2O_3. Upon closer inspection, however, scanning electron microscopy (SEM) images reveal that the film is discontinuous. Al_2O_3 clusters are shown to have a characteristic length distribution of 10-50 nm, with similar interspacing between

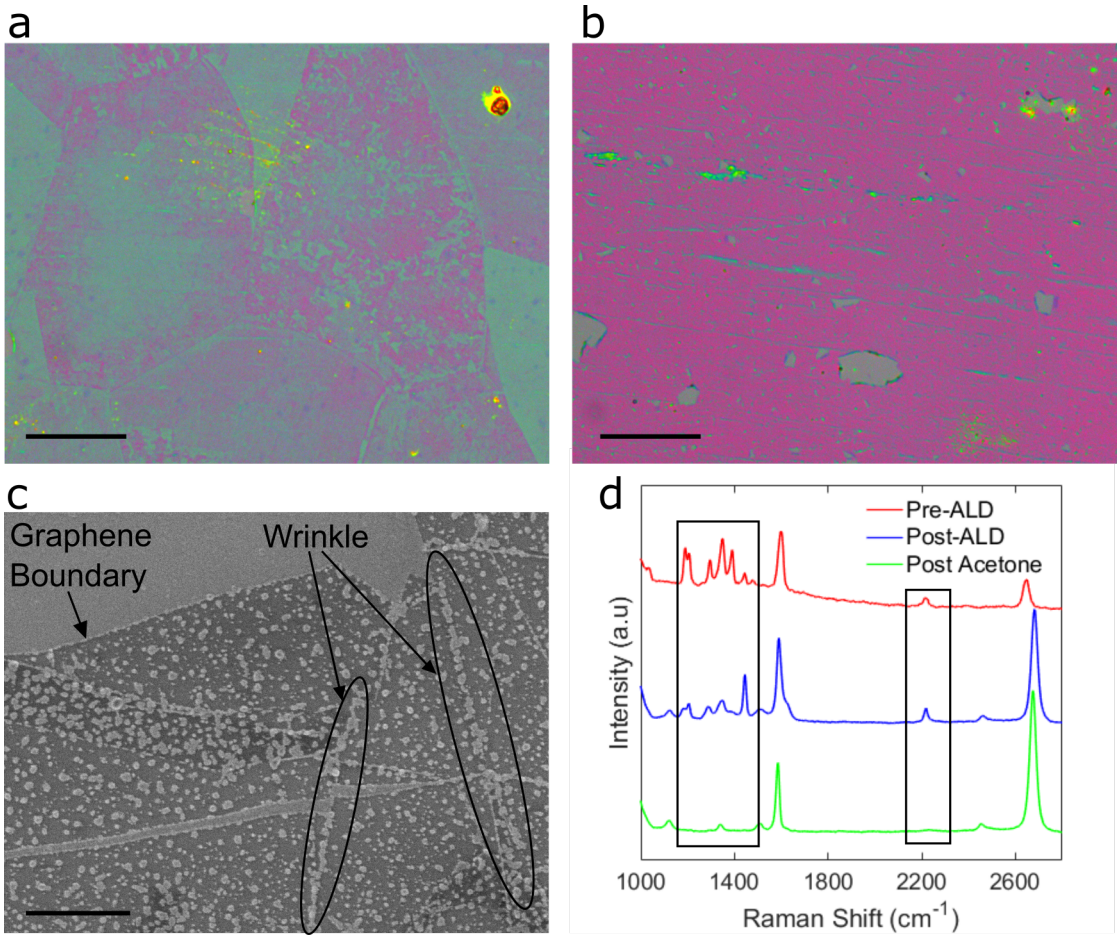

Figure 4.13: **a** Optical images of Al_2O_3 grown directly onto **a** pristine and **b** TCNQ functionalized graphene. Scale bars 25 µm. ALD film grown at 100° C, with a nominal thickness of 20 nm. **c** SEM image of Al_2O_3 grown directly onto functionalized graphene. Scale bar 500 nm. **d** Raman spectra of TCNQ functionalized graphene before and after ALD growth of Al_2O_3. TCNQ and DCTC peaks are highlighted with black boxes. After dipping in acetone, the TCNQ related peaks have disappeared, indicating that the incomplete ALD film is unable to protect the TCNQ molecules. Excitation wavelength 532 nm.

them. Clusters are only observed on the graphene, with continuous film growth on the bare SiO_2 substrate. Moreover, graphene wrinkles are seen to be favorable nucleation sites. Upon immersing the sample in acetone, the discontinuous Al_2O_3 film was unable to protect the TCNQ functionalization, as confirmed by the Raman spectra shown in Figure 4.13d. Before and after ALD film growth, TCNQ and DCTC peaks are observed (highlighted in the Figure with black boxes). However, after briefly dipping the sample in acetone and rinsing in IPA, these peaks are no longer detected, indicating that the solvent has washed away the TCNQ chemical functionalization, and would not survive the microfabrication process.

GFET devices were fabricated to test the ability of directly grown ALD Al_2O_3 films and oxidized, thermally evaporated Al films to protect the graphene chemical functionalization from the fabrication process. Graphene sheets on SiO_2 substrates were chemically function-

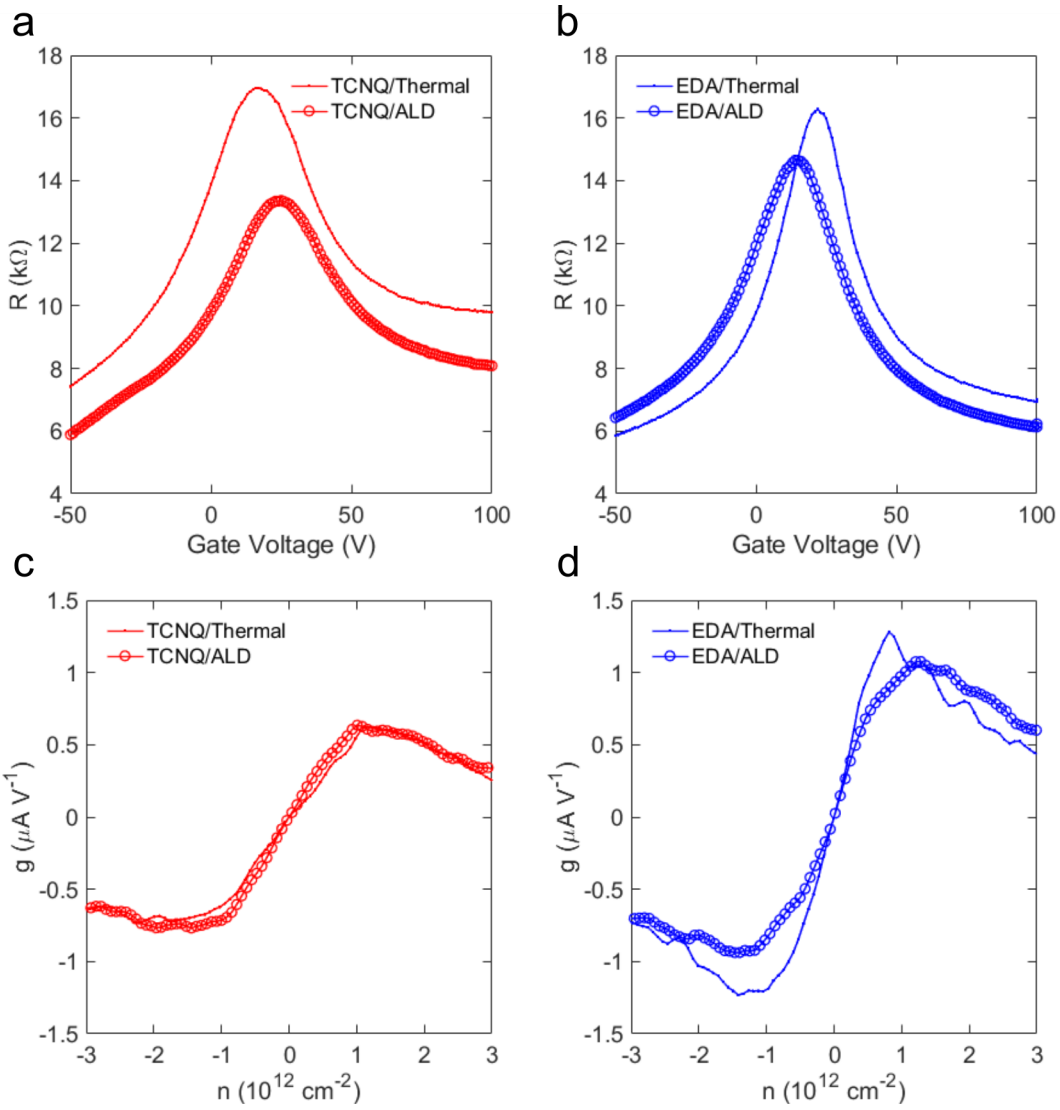

Figure 4.14: Transfer curves of TCNQ (**a** and **c**) and EDA (**b** and **d**) functionalized graphene devices, covered with either an ALD Al_2O_3 or thermally evaporated AlOx film. ALD films grown at 120° C, with nominal thickness of 5 nm.

Sample	V_{DP} (V)	n_0 (10^{12} cm^{-2})	μ_h/μ_e (cm^2 V^{-1} s^{-1})
TCNQ/Thermal	16.6	1.24	225/193
TCNQ/ALD	24.5	1.82	301/199
EDA/Thermal	21.9	1.63	374/396
EDA/ALD	14.7	1.10	288/334

Table 4.2: Transport properties for the curves shown in Figure 4.14.

alized with EDA or TCNQ, followed by film growth of 20 nm of ALD Al_2O_3 at 120° C or 5 nm of thermally evaporated Al, allowed to oxidize in ambient. Devices were then fabricated via the standard photolithography process, with the alkaline photoresist developer used to

etch the Al_2O_3 and AlOx films. The only solvents used in the process were acetone and IPA, and no post-fabrication annealing was carried out. The transfer curves and transport properties of the resulting devices are shown in Figure 4.14 and Table 4.2. The intrinsic doping levels of all devices falls within a relatively narrow range, between 1.10 and 1.82×10^{12} cm^{-2}. This indicates that neither the ALD or thermal film is fully protecting the graphene's chemically induced doping. If this were the case, negative intrinsic doping would be expected from the EDA devices. When the mobilities are compared, however, a difference is noted between the TCNQ and EDA functionalized devices. The former show the habitual electron branch suppression observed for devies fabricated via photolithography, with electron mobilities lower than hole mobilities. The EDA functionalized devices, on the other hand, show higher electron mobilities. This would indicate that there are fewer positively charged, long range electron scattering centers due to the EDA functionalization. Residual EDA doping still present in the graphene, in particular near the Cr/Au electrodes, could result in a more favorable alignment of the graphene neutrality point at the electrode/graphene interface, resulting in more efficient injection of electron charge carriers [44], as discussed earlier in this section and in previous chapters. Despite the indications that there are some remaining EDA molecules which may be enhancing the electron mobility in the devices, it is not large enough to ensure n-doping in the graphene device. It should be noted that these devices were fabricated using graphene grown using H_2 CVD recipe (see Graphene Technology chapter), with small grains and many grain boundaries, which most likely accounts for the relatively low mobility values.

4.4.2 Combined Thermal/ALD Al_2O_3 Growth

In an attempt to better protect the chemical functionalization and doping of the graphene devices during the device fabrication process, a combined film growth method was adopted, in which an Al seeding film was thermally evaporated and allowed to oxidize to AlOx in ambient, followed by ALD growth of Al_2O_3 on top of the AlOx film. Atomic Force Microscopy (AFM) showing the topography of these films can be seen in Figure 4.15. The white clusters seen in all of the images, with heights up to 80 nm, are most likely PMMA remnants from the graphene transfer process, or photoresist residues. The directly grown ALD films are patchy and discontinuous, particularly for the EDA doped sample. For the TCNQ doped sample, the directly grown ALD film is thicker and seems to follow a template laid out by the TCNQ molecules, resulting in greater Al_2O_3 nucleation, with merging of the clusters seen in the SEM image in Figure 4.13. The streaks or lines seen in the AFM image probably correspond to wrinkles in the graphene where TCNQ molecules accumulated (as seen in Figure 4.9), favoring Al_2O_3 nucleation. The TCNQ films were all grown at 150° C, although the ones in Figure 4.15 were grown for 45 minutes, whereas those in Figure 4.13 were grown for 20 minutes. This was done in the hope of densifying the TCNQ film and therefore increasing the nucleation density of Al_2O_3 clusters. Despite these efforts, the AFM images reveal that there are still significant bare patches in the direct growth Al_2O_3 films. The thermal/ALD

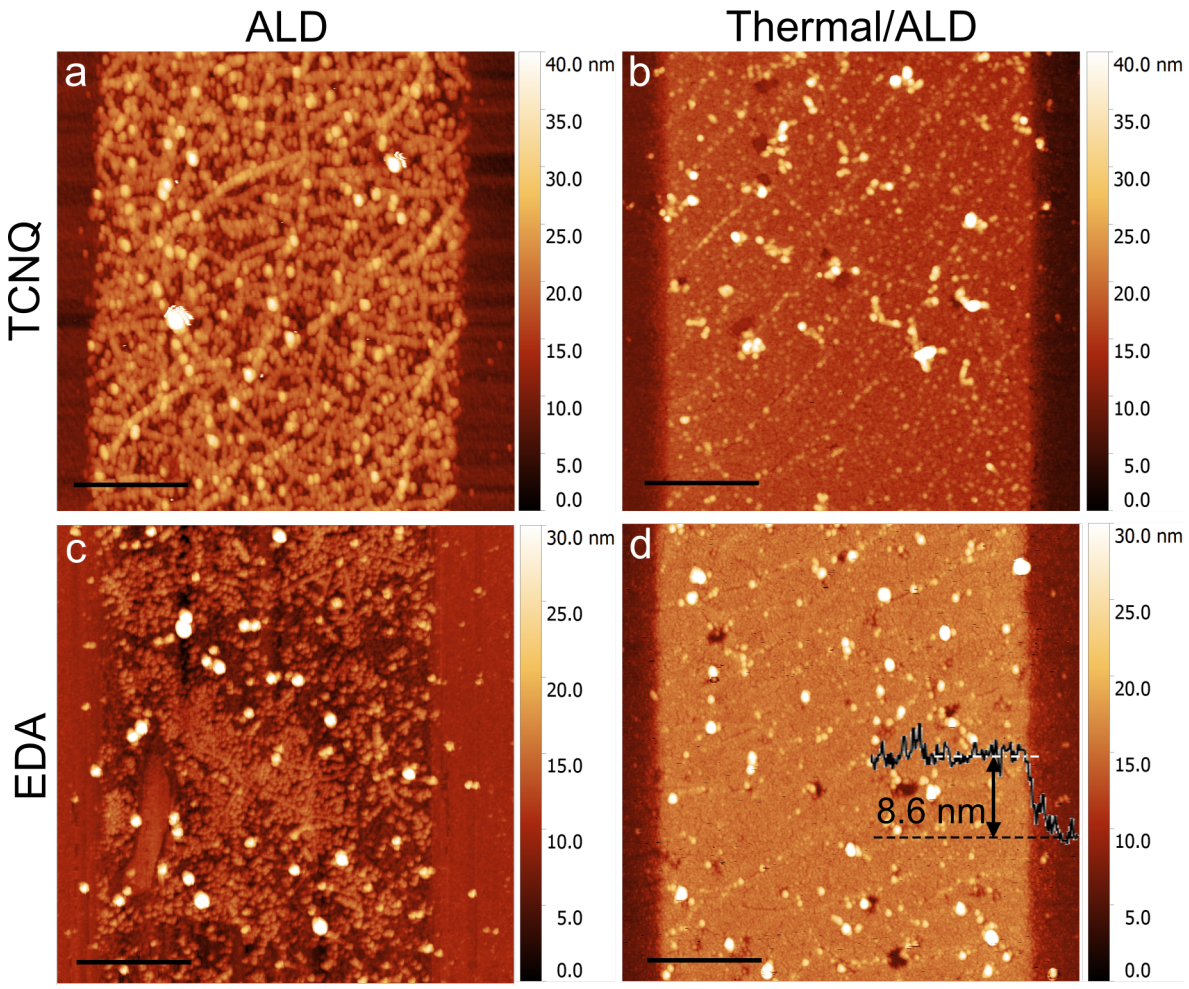

Figure 4.15: AFM images of TCNQ (**a** and **b**) and EDA (**c** and **d**) functionalized graphene strips with ALD (**a** and **c**) and thermal/ALD (**b** and **d**) Al_2O_3 films. Scale bars 500 nm. ALD films grown at 120° C, for both direct and thermal/ALD growth, with nominal thickness of 10 nm.

films, on the other hand, are seen to be much more continuous, compact and homogeneous, with heights of about 8.6 nm measured for both EDA and TCNQ functionalization.

Sample	V_{DP} (V)	n_0 (10^{12} cm^{-2})	μ_h/μ_e	$\mu_h/\mu_{h,pristine}$
Pristine	13	0.96	0.69	-
TCNQ	39.9	2.97	4.08	0.85
TCNQ/Th/ALD	-28.3	-2.10	0.81	0.38

Table 4.3: Transport properties of the curves shown in Figure 4.16.

To test the effect of thermal/ALD Al_2O_3 growth on the electrical properties of functionalized graphene, transport measurements were carried out on graphene sheets with no subsequent fabrication tests. The results of these tests on TCNQ functionalized graphene

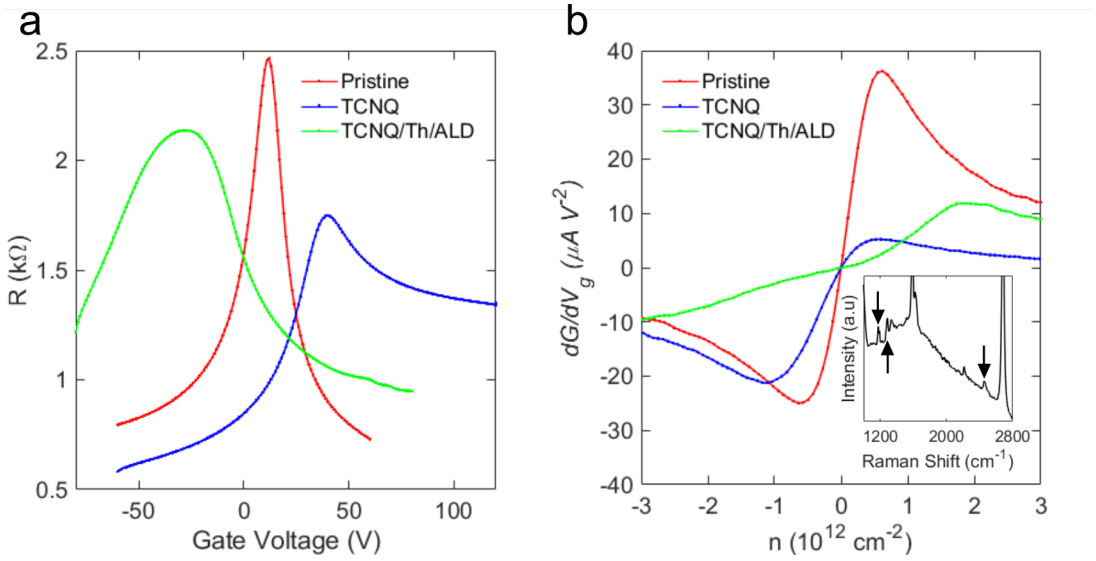

Figure 4.16: Transfer curves showing the evolution of the transport behavior of graphene, from pristine to TCNQ functionalized, followed by growth of thermal/ALD Al_2O_3 film. Measurements taken on graphene sheet with no subsequent fabrication steps. INSET: Raman spectrum of TCNQ/Th/ALD graphene, showing the presence of weak TCNQ peaks (highlighted with arrows). ALD films grown at 120° C, with nominal thickness of 10 nm.

can be seen in the transfer curves of Figure 4.16, and are summarized in Table 4.3. The initial pristine graphene curve has the typical shape, with slight p-doping and electron mobility nearly twice as large as hole mobility. After TCNQ film evaporation, significant p-doping is observed, accompanied by a drastic decrease in the electron mobility (as discussed for the same curves, shown in Figure 4.8). Upon growing a combined thermal/10 nm ALD Al_2O_3 film, the graphene becomes significantly n-doped, which agrees with previously obtained results [36, 38], and would seem to indicate that there is no longer efficient electron transfer from the graphene to the TCNQ. In previous studies, the n-doping has been attributed to the desorption of oxygen and water species during metallic film evaporation and ALD deposition, rippling caused by seed film oxidation [37–39], and the passivation of charge traps present in the SiO_2 substrate [34]. Moreover, the TCNQ/Th/ALD curve shows an ill defined hole branch transconductance, while the electron mobility is slightly increased, indicating that the TCNQ molecules are less efficient electron scattering centers than prior to thermal/ALD film growth. These observations seem to indicate that while the TCNQ is still present, at least in small amounts (Raman spectrum inset of Figure 4.16), it is somehow decoupled from the graphene. TCNQ molecules were already shown to be highly mobile at temperatures comparable to the ALD growth temperature (see TCNQ Functionalization section), indicating that they are weakly adsorbed on the graphene. Molecular desorption of the TCNQ molecules may therefore be playing a role. Another possibility is that due to their weak adhesion, Al_2O_3 clusters may be intercalating and decoupling the TCNQ from the graphene. Lowering the ALD growth temperature may offer a solution to these problems,

by maintaining the TCNQ more strongly adhered to the graphene.

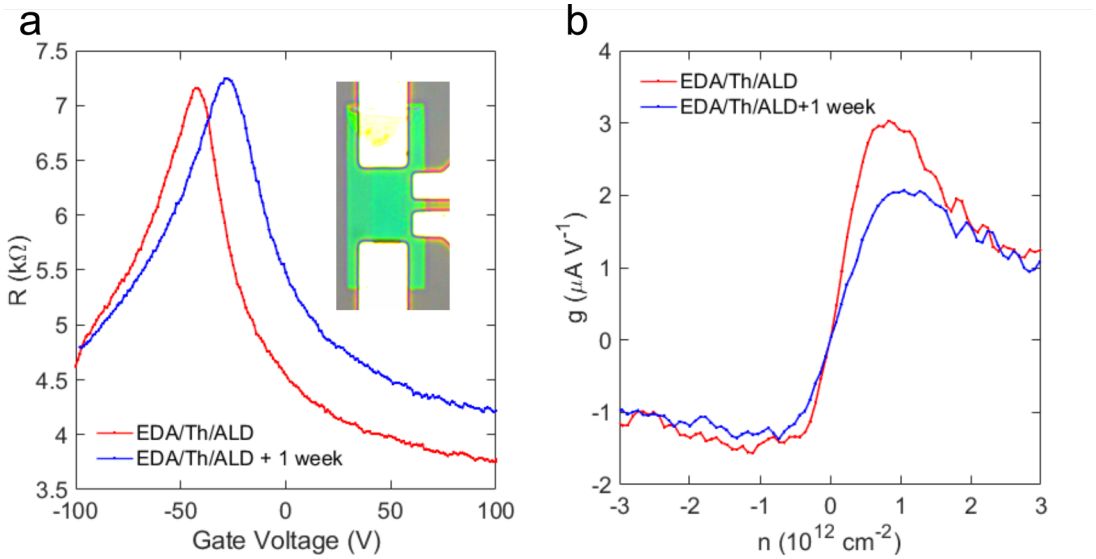

Figure 4.17: Transfer curves (**a** resistance and **b** transconductance) of window EDA/Th/ALD devices, taken in four point configuration. ALD films grown at 120° C, with nominal thickness of 10 nm. INSET: Optical image of window device.

Sample	V_{DP} (V)	n_0 (10^{12} cm^{-2})	μ_h/μ_e (cm^2 V^{-1} s^{-1})
EDA/Th/ALD	-42.4	-3.15	186/339
+1 Week	-27.9	-2.07	168/237

Table 4.4: Transport properties for the curves shown in Figure 4.17.

More encouraging results were obtained when growing thermal/ALD films on EDA functionalized graphene. GFET devices were first fabricated using the standard photolithography procedure. Windows were then opened around the devices, using PMMA and electron beam lithography (EBL), to avoid further p-doping with photoresist. Functionalization of the exposed GFETs followed, with subsequent growth of a thermal/ALD Al_2O_3 film of 20 nm nominal thickness at 120° C. Finally, the PMMA was removed in acetone. An optical image of the final device structure can be seen in the inset of Figure 4.17a. The transfer curves indicate that the n-doping afforded by the EDA molecules is maintained after the film growth, along with an electron mobility larger than the hole mobility. Moreover, the devices were shown to maintain their doping even after a week of being left out in ambient conditions, although a reduction in the electron mobility was observed. This indicates that the thermal/ALD film is indeed encapsulating the functionalized graphene, and significantly slowing the desorption of EDA molecules. The low mobilities are most likely due to the use of small grain graphene for these devices; higher values are expected by using large grain graphene from the optimized CVD growth recipe.

4.5 Conclusion

Effective p and n-doping of graphene has been demonstrated by vapor phase functionalization with TCNQ and EDA molecules. Various growth conditions were explored for the TCNQ molecules. When the substrate was maintained close to ambient temperatures, TCNQ crystals formed on the graphene, with increasing size and density for higher evaporation temperatures and longer growth times. When the substrate temperature was elevated during growth, TCNQ films were formed on the graphene. Raman spectroscopy measurements confirmed that electron charge transfer occurred from the graphene to the TCNQ films, in agreement with previous studies, resulting in graphene p-doping. This was also confirmed by electrical transport measurements, which also showed that the TCNQ molecules acted as charge scattering centers for electrons, reducing electron mobility. TCNQ clusters caused rippling and wrinkling of the graphene, which also contributed to charge carrier scattering. EDA proved to be a robust n-dopant, which could be reversed through immersion in IPA, with a much milder effect on graphene's mobility. Interestingly, it did not suppress either electron or hole mobility preferentially, a phenomenon which has yet to be explained.

Encapsulation of the functionalized graphene was carried out through the growth of Al_2O_3 films. Direct ALD growth on functionalized graphene yielded discontinuous, inhomogeneous films, which were unable to protect the dopant molecules from the device microfabrication process. Much more compact, homogeneous films were obtained when a seeding AlOx layer was evaporated prior to the ALD process. TCNQ functionalization did not survive the thermal/ALD growth, possibly due to desorption and/or intercalation of Al_2O_3 between the TCNQ and graphene. It may be possible to obtain better results by growing films at lower temperatures. Thermal/ALD films grown on EDA functionalized graphene exhibited promising results, yielding n-doped graphene devices with enhanced electron mobility, and significantly reduced EDA desorption times.

Several possibilities exist for improving the chemical doping of graphene. Stable p-doping has been achieved using nitric acid, with little damage to the graphene lattice, a relatively small reduction in the mobility, and a significant reduction of the sheet resistance [45]. Carefully selected p-doping self assembled monolayer molecules may also be a suitable option, especially considering that they tend to form relatively organized films which could act as a seeding layer for subsequent ALD encapsulation. Increased understanding of the conditions necessary for the growth of optimized protective ALD films on graphene will most likely spur the adoption of direct growth techniques, without the use of an oxidized metallic seeding layer. Two immediately foreseeable benefits come to mind from the direct growth of ALD films on chemically functionalized graphene. First, the deleterious impact of the oxide layer on graphene's doping and mobility would be eliminated. Second, lower temperatures would reduce surface diffusion and desorption of the chemical species, a phenomenon observed for the TCNQ functionalized graphene. These routes need to be further explored and developed in order for graphene to become a technologically viable material.

Bibliography

[1] Y.J. Yu, Y. Zhao, S. Ryu, L.E. Brus, K.S. Kim, and P. Kim. Tuning the graphene work function by electric field effect. *Nano Letters*, 9:3430–3434, 2009.

[2] A. Liu, X. Ren, B. Wang, J. Zhang, P. Yang, J. Zhang, and M. An. Complexing agent study via computational chemistry for environmentally friendly silver electrodeposition and the application of a silver deposit. *RSC Advances*, 4:40930–40940, 2014.

[3] R. Precht, R. Hausbrand, and W. Jaegermann. Electronic structure and electrode properties of tetracyanoquinodimethane (TCNQ): a surface science investigation of lithium intercalation into TCNQ. *Phys. Chem. Chem. Phys.*, 17:6588–6596, 2015.

[4] R. Otero, A.L. Vázquez de Parga, and J.M. Gallego. Electronic, structural and chemical effects of charge-transfer at organic/inorganic interfaces. *Surface Science Reports*, 72:105 – 145, 2017.

[5] W. Zhang, C.-T. Lin, K.-K. Liu, T. Tite, C.-Y. Su, C.-H. Chang, Y.-H. Lee, C.-W. Chu, K.-H. Wei, J.-L. Kuo, and L.-J. Li. Opening an electrical bandgap of bilayer graphene with molecular doping. *ACS Nano*, 5:7517–7524, 2011.

[6] C.-L. Hsu, C.-T. Lin, J.-H. Huang, C.-W. Chu, K.-H. Wei, and L.-J. Li. Layer-by-layer graphene/TCNQ stacked films as conducting anodes for organic solar cells. *ACS Nano*, 6:5031–5039, 2012.

[7] M. Garnica, D. Stradi, S. Barja, F. Calleja, C. Díaz, M. Alcamí, N. Martín, A.L. Vázques de Parga, F. Martín, and R. Miranda. Long-range magnetic order in a purely organic 2D layer adsorbed on epitaxial graphene. *Nature Physics*, 9:368–374, 2013.

[8] M. Garnica, D. Stradi, F. Calleja, S. Barja, C. Díaz, M. Alcamí, A. Arnau, A.L. Vázquez de Parga, F. Martín, and R. Miranda. Probing the site-dependent Kondo response of nanostructure graphene with organic molecules. *Nano Letters*, 14:4560–4567, 2014.

[9] D. Maccariello, M. Garnica, M.A. Niño, C. Navío, P. Perna, S. Barja, A.L. Vázquez de Parga, and R. Miranda. Spatially resolved, site-dependent charge transfer and induced magnetic moment in TCNQ adsorbed on graphene. *Chemistry of Materials*, 26:2883–2890, 2014.

[10] Y. Qi, U. Mazur, and K.W. Hipps. Charge transfer induced chemical reaction of tetracyano-p-quinodimethane adsorbed on graphene. *RSC Advances*, 2:10579–10584, 2012.

[11] M. Harris, J.J. Hoagland, U. Mazur, and K.W. Hipps. Raman and infrared spectra of metal salts of α,α-dicyano-p-toluoylcyanide: Non-resonant raman scattering in tetracyano-p-quinodimethanide. *Vibrational Spectroscopy*, 9:273–277, 1995.

[12] A. Pawlukojc, I. Natkaniec, G. Bator, L. Sobczyk, and E. Grech. Inelastic neutron scattering (ins) spectrum of tetracyanoquinodimethane (TCNQ). *Chemical Physics Letters*, 378:665–672, 2003.

[13] X. Jiang, Z. Li, C. Sun, and X. Zhang. Study of electron transfer process of TCNQ under external electric field. *Journal of the Physical Sciences*, 7:901–905, 2012.

[14] D.L. Jeanmaire and R.P. Van Duyne. Resonance raman spectroelectrochemistry. 2. scattering spectroscopy acoompanying excitation of the lowest $^2B_{1u}$ excited state of the tetracyanoquinodimethane anion radical. *Journal of the American Chemical Society*, 98:4029–4033, 2012.

[15] H.-H. Tseng, M. Serri, N.M. Harrison, and S. Heutz. Thin film properties of tetracyanoquinodimethane (TCNQ) with novel templating effects. *Journal of Materials Chemistry C*, 3:8694–8699, 2015.

[16] M. Yoshikawa, S. Nakashima, and A. Mitsuishi. Raman spectra of thin TCNQ films deposited on silver films. *Journal of Raman Spectroscopy*, 17:369–371, 1986.

[17] W. Chen, S. Chen, D.C. Qi, X.Y. Gao, and A.T.S. Wee. Surface transfer of p-type doping of epitaxial graphene. *Journal of the American Chemical Society*, 129:10418–10422, 2007.

[18] A. Das, S. Pisana, B. Chakraborty, S. Piscanec, S.K. Saha, U.V. Waghmare, K.S. Novoselov, H.R. Krishnamurthy, A.K. Geim, A.C. Ferrari, and A.K. Sood. Monitoring dopants by raman scatering in an electrochemically top-gated graphene transistor. *Nature Nanotechnology*, 3:210–215, 2008.

[19] C. Casiraghi. Doping dependence of the Raman peaks intensity of graphene close to the Dirac point. *Physical Review B*, 80:233407, 2009.

[20] D. M. Basko, S. Piscanec, and A. C. Ferrari. Electron-electron interactions and doping dependence of the two-phonon Raman intensity in graphene. *Physical Review B*, 80:165413, 2009.

[21] C. Casiraghi. Probing disorder and charged impurities in graphene by Raman spectroscopy. *Physica Status Solidi RRL*, 3:175–179, 2009.

[22] S. Das Sarma, S. Adam, E. H. Hwang, and E. Rossi. Electronic transport in two-dimensional graphene. *Reviwes of Modern Physics*, 83:407–470, 2011.

[23] N.H. Kim, T. Kuila, and J.H. Lee. Simultaneous reduction, functionalization and stitching of graphene oxide with ethylenediamine for composites application. *Journal Materials Chemistry A*, 1:1349–1358, 2013.

[24] Y. Kim, J. Ryu, M. Park, E.U. Kim, J.M. Yoo, J. Park, J.H. Kang, and B.H. Hong. Vapor-phase molecular doping of graphene for high-performance transparent electrodes. *ACS Nano*, 8:868–874, 2014.

[25] L. Zhao, R. He, K.T. Rim, T. Schiros, K.S. Kim, H. Zhou, C. Gutiérrez, S.P. Chockalingam, C.J. Arguello, L. Pálová, D. Nordlund, M.S. Hybertsen, D.R. Reichmann, T.F. Heinz, P. Kim, A. Pinczuk, G.W. Flynn, and A.N. Pasupathy. Visualizing individual nitrogen dopants in monolayer graphene. *Science*, 333:999–1003, 2011.

[26] R.L. Puurunen. Surface chemistry of atomic layer deposition: A case study for the trimethylaluminum/water process. *Journal of Applied Physics*, 97:121301, 2005.

[27] M.D. Groner, F.H. Fabreguette, J.W. Elam, and S.M. George. Low-temperature Al_2O_3 atomic layer deposition. *Chemistry of Materials*, 16:639–645, 2004.

[28] Y.H. Lee, M.-K. Son, P. Gao, K.T. Cho, J. Seo, S.M. Zakeeruddin, M. Grätzel, and M.K. Nazeeruddin. Enhanced charge collection with passivation layers in perovskite solar cells. *Journal of Applied Physics*, 28:3966–3972, 2016.

[29] X. Wang, S.M. Tabakman, and H. Dai. Atomic layer deposition of metal oxides on pristine and functionalized graphene. *Journal of the American Chemical Society*, 130:8152–8153, 2008.

[30] J.M. Alaboson, Q.H. Wang, J.D. Emery, A.L. Lipson, M.J. Bedzyk, J.W. Elam, M.J. Pellin, and M.C. Hersam. Seeding atomic layer deposition of high-k dielectrics on epitaxial graphene with organic self-assembled monolayers. *ACS Nano*, 5:5223–5232, 2011.

[31] P. Zhou, S. Yang, Q. Sun, L. Chen, P. Wang, S. Ding, and D.W. Zhang. Direct deposition of uniform high-κ dielectrics on graphene. *Scientific Reports*, 4:6648, 2014.

[32] R.H. Vervuurt, B. Karasalu, M.A. Verheijen, W.M.M. Kessels, and A.A. Bol. Uniform atomic layer deposition of Al_2O_3 on graphene by reversible hydrogen plasma functionalization. *Chemistry of Materials*, 29:2090–2100, 2017.

[33] M.-B. VMartin, B. Dlubak, R.S. Weatherup, H. Yang, C. Deranlot, K. Bouzehouane, F. Petroff, A. Anane, S. Hofmann, J. Robertson, A. Fert, and P. Seneor. Sub-nanometer atomic layer deposition for spintronics in magnetic tunnel junctions based on graphene spin-filtering membranes. *ACS Nano*, 8:7890–7895, 2014.

[34] A.I. Aria, K. Nakanishi, L. Xiao, P. Braeuninger-Weimer, A.A. Sagade, J.A. Alexander-Webber, and S. Hofmann. Parameter space of atomic layer deposition of ultrathin oxides on graphene. *ACS Applied Materials and Interfaces*, 8:30564–60575, 2016.

[35] D.B. Farmer, H.-Y. Chiu, Y.-M. Lin, K.A. Jenkins, F. Xia, and P. Avouris. Utilization of a buffered dielectric to achieve high field-effect carrier mobility in graphene transistors. *Nano Letters*, 9:4474–4478, 2009.

[36] J.A. Robinson, M. LaBella III, K.A. Trumbull, X. Weng, R. Cavelero, T. Daniels, Z. Hughes, M. Hollander, M. Fanton, and D. Snyder. Epitaxial graphene materials integration: Effects of dielectric overlayers on structural and electronic properties. *ACS Nano*, 4:2667–2672, 2010.

[37] M.J. Hollander, M. LaBella, Z.R. Hughes, M. Zhu, K.A. Trumbull, R. Cavalero, D.W. Snyder, X. Wang, E. Hwang, S. Dataa, and J.A. Robinson. Enhanced transport and transistor performance with oxide seeded high-κ gate dielectrics on wafer-scale epitaxial graphene. *Nano Letters*, 11:3601–3607, 2011.

[38] A.A. Sagade, D. Neumaier, D. Schall, M. Otto, A. Pesquera, A. Centeno, A.Z. Elorza, and H. Kurz. Highly air stable passivation of graphene based field effect devices. *Nanoscale*, 7:3558–3564, 2015.

[39] C.G. Kang, Y.G. Lee, S.K. Lee, E. Park, C. Cho, S.K. Lim, H.J. Hwang, and B.H. Lee. Mechanism of the effects of low temperature Al_2O_3 passivation on graphene field effect transistors. *Carbon*, 53:182–187, 2013.

[40] D.B. Farmer, H.-Y. Chiu, Y.-M. Lin, K.A. Jenkins, F. Xia, and P. Avouris. Physisorbed-precursor-assisted atomic layer deposition of reliable ultrathin dielectric films on inert graphene surfaces for low-power electronics. *2D Materials*, 3:035027, 2016.

[41] L. Zheng, X. Cheng, D. Cao, G. Wang, Z. Wang, D. Xu, C. Xia, L. Shen, Y. Yu, and D. Shen. Improvement of Al_2O_3 films on graphene grown by atomic layer deposition with pre-H_2O treatment. *ACS Applied Materials and Interfaces*, 6:7014–7019, 2010.

[42] J.D. Wood, S.W. Schmucker, A.S. Lyons, E. Pop, and J.W. Lyding. Effects of polycrystalline Cu substrate on graphene growth by chemical vapor deposition. *Nano Letters*, 11:4547–4554, 2011.

[43] B. Dlubak, P.R. Kidambi, R.S. Weatherup, S. Hofmann, and J. Robertson. Substrate assisted nucleation of ultra-thin dielectric layers on graphene by atomic layer deposition. *Applied Physics Letters*, 100:173113, 2012.

[44] D.B. Farmer, R. Golizadeh-Mojarad, V. Perebeinos, Y-M. Lin, G.S. Tulevski, J.C. Tsang, and P. Avouris. Chemical doping and electron-hole conduction asymmetry in graphene devices. *Physical Review Letters*, 98:186806, 2009.

[45] L. D'Arsie, S. Esconjauregui, R.S. Weatherup, X. Wu, W.E. Arter, H. Sugime, C. Cepek, and J. Robertson. Stable, efficient p-type doping of graphene by nitric acid. *RSC Adv.*, 6:113185–113192, 2016.

Chapter 5

Assembly and Characterization of Graphene and Encapsulated Colloidal Quantum Dot Heterostructures

In the past few decades, prior to the discovery of graphene and its 2D cousins, other low dimensional structures had already attracted much attention due to their remarkable properties, arising from quantum confinement in one or more dimensions. One such class of structures are 0-dimensional semiconducting colloidal quantum dots (CQDs), also known as semiconducting nanocrystals [1, 2]. The electronic and optical properties of CQDs can be tuned by varying the size, shape, and composition of their semiconducting core. Moreover, the interaction of a CQD with its environment is mediated by the materials surrounding its core, which can be organic, dielectric or metallic [1, 2]. Increased scientific understanding of low dimensional materials–along with technological advancements in their synthesis, production, and device fabrication–has spurred the demand for their integration into hybrid quantum systems that combine the unique properties of their material components.

Hetrostructures combining CQDs and graphene are a prime example of this system, with numerous studies carried out in the past few years. Energy and charge transfer dynamics between these two materials have been explored and exploited to fabricate optoelectronic devices [3–6]. In all of these studies, the interaction between the graphene and the CQDs has been mediated by the organic or inorganic ligands surrounding the CQD semiconducting core. Interaction between graphene and SiO_2 encapsulated semiconducing CQDs has not yet been invetigated, and is the subject of the last two chapters of this thesis. These encapsulated colloidal quantum dots (ECQDs) have garnered attention due to their interesting properties, including increased functionality for biological applications and decreased toxicity [7].

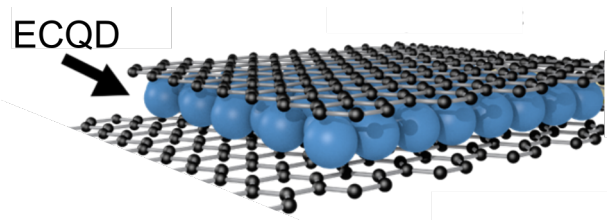

Figure 5.1: Schematic of ECQD film sandwiched between two graphene layers.

The work presented in the last two chapters of this thesis explores the assembly, fabrication and characterization of heterostructures based on graphene and ECQDs. Specifically, these hereostructures are comprised of an ECQD film sandwiched between two graphene sheets, as shown in Figure 5.1. Ever mindful of possible technological applications, the methods used for growing graphene and transferring the ECQD films onto the substrate, CVD and Langmuir-BLodgett, are scalable, and suited for producing numerous devices or samples on a large area substrate. Indeed, the Gr/ECQD/Gr heterostructures produced in this study could span areas on the order of 10 cm^2. This chapter explores two main topics relating to these Gr/ECQD/Gr heterostructures. The first is their assembly, namely, the deposition of a continuous ECQD film via the Langmuir-Blodgett method onto graphene covered substrates, followed by the transfer of a top graphene sheet onto the ECQD film. Second, characterization of the structural and spectroscopic properties of these heterostructures via scanning probe methods, SEM and Raman spectroscopy. Electrical and optical characteristics of the heterostructures are briefly commented upon; however, a deeper exploration of these properties is reserved for the next and final chapter of this thesis.

5.1 Introduction

Before delving into the details of the assembly and characterization of the heterostructures, a very brief introduction to semiconducting CQDs is given, followed by a description of the specific CQDs used in this thesis, namely CdSeZnS alloyed, silica encapsulated CQDs. This section concludes with a short description of the Langmuir-Blodgett film deposition technique.

5.1.1 Semiconducting Colloidal Quantum Dots

Semiconducting CQDs are an important class of inorganic, solution processed material, with many possible optoelectronic applications, including light emitting diodes, solar cells, field effect transistors, photodectors and even memory storage devices [1, 2]. Recently, they have also been utilized by Samsung in televisions. In a bulk semiconductor, the large number of atoms gives rise to state filled bands that are continuous in energy. In semiconducting CQDs, the small number of atoms (hundreds to thousands) and reduced crystal size (typically 2-20 nm) give rise to discrete states at specific energies due. The resulting electron and hole orbital confinement within the crystal give rise to the optical and electronics properties of CQDs [1]. In a bulk semiconductor, the range of forbidden energies between the top of the valence band and bottom of the conduction band is known as the band gap. In a semiconducting CQD, the band gap is located between the highest hole and lowest electron states, S_h and S_e, as shown in Figure 5.2. The S, P, D and F labels for the energy levels are due to the hydrogen-like states of spherical CQDs, reminiscent of the s, p, d and f orbitals in a hydrogen molecule [8].

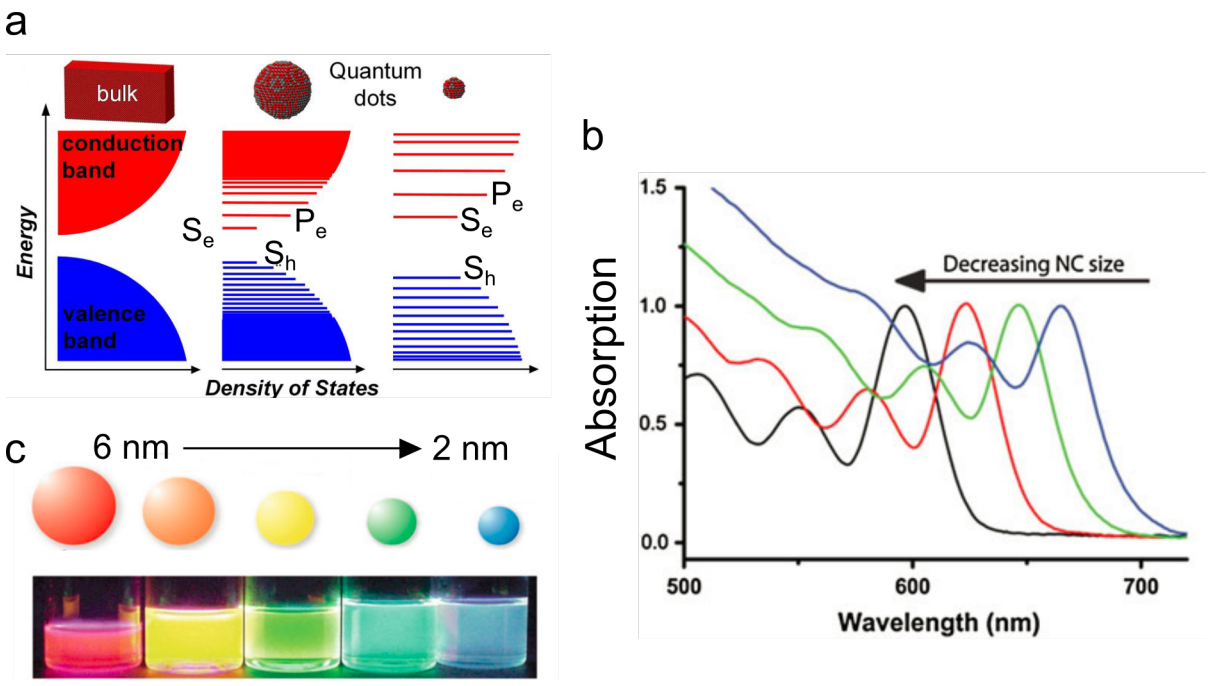

Figure 5.2: **a** Confinement of energy levels in bulk semiconductor and semiconductor CQD. As quantum dot size decreases, energy levels become more widely spaced, shifting the main absorption peak (**b**) and the emission color **c** towards higher energies. **a** adapted from [1], **b** and **c** adapted from [8]

.

Electrons in CQDs, as in bulk semiconductors, can be excited by absorbing a photon with energy greater than or equal to the difference between S_h and S_e. The resulting electron-hole pair is known as an exciton. Optical selection rules require a net dipole to be created when a photon is absorbed, and this can only occur in a semiconducting CQD between electron and hole levels with the same orbital type (i.e. S_h to S_e, P_h to P_e and so on), and thus these transitions are much more likely than transitions between orbitals of different types [8]. Thus the peaks in the absorption spectra shown in Figure 5.2b correspond to the allowed transitions between discrete energy levels, known as excitonic transitions, with the most intense peak corresponding to the lowest energy S_h to S_e excitonic transition [8]. Decreasing the core size of semiconducting CQDs further confines the electrons, causing the discrete energy steps to be spaced farther apart. This results in a larger energy difference between states, as visualized in Figure 5.2a. Optically, this manifests itself as a shift in the absorption and emission peaks towards higher energies. The main excitonic absorption peak is seen to shift towards shorter wavelengths in Figure 5.2b, while the emission spectrum behaves in the same way, as seen in the striking visual display of the emitted colors in Figure 5.2c [8].

As explained above, photon absorption in the semiconducting CQD creates an exciton, depicted with an X in the Excitation and Relaxation schematic of Figure 5.3. If the photon energy is greater than the $S_e - S_h$ energy difference, the resulting electron (hole) will be excited to states above (below) the S_e (S_h) ground states. The electron and hole will very

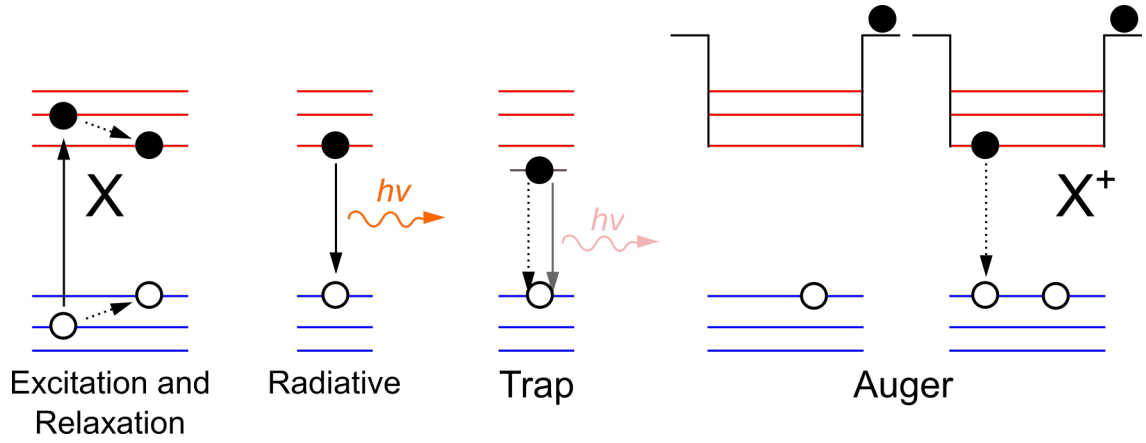

Figure 5.3: Recombination processes in a CQD. Excitation of an electron to a higher energy results in the formation of an exciton. Upon relaxing to the lowest energy level, the exciton can recombine via radiative, trap mediated, or Auger processes. In the Auger process, a charge carrier is expelled from the CQD core, leaving it electrically charged. When another electron-hole pair is excited within this charged core, a charged exciton X^+ will form, which recombines nonradiatively.

quickly (<1ps) relax to the ground states [8]. Upon reaching the ground state, several processes exist for the electron and hole to recombine, as depicted in the remaining schematics of Figure 5.3. In radiative recombination, a photon is released, resulting in a narrow emission peak, slightly redshifted from the lowest energy absorption transition. An ensemble of CQDs with a certain size distribution will therefore show a broadened emission spectrum [8]. Another recombination process involves the trapping (localization) of one of the charge carriers within a surface state, which decreases the overlap between the electron and hole wave functions, making radiative recombination much less likely. The trapped charge carrier usually recombines by coupling with localized vibrations (phonons) [1]. Trap state radiative decay is generally very inefficient, with a quantum yield generally below 5% [8]. When the charge carrier *does* decay radiatively, its emission will be redshifted with respect to the normal radiative decay emission. Since the vast majority of trap states arise from surface defects, it is critically important to engineer the properties of the semiconducting CQD surface to ensure large radiative recombination rates [1].

The Auger process is a very fast (about 100 ps), and therefore efficient, nonradiative recombination mechanism [2]. It is generally accepted that this process occurs within electrically charged CQDs, in which a charge separation event ejects a charge carrier from the luminescent region of the semiconducting core [9]. The resulting lone charge generates very large electric fields within the luminescent core (tens of MV cm^{-}1). An exciton created while the CQD is in this charged state (a charged exciton X^+, as seen in the schematic of Figure 5.3) will recombine nonradiatively. In this process, known as Auger recombination, the unpaired extra charge withdraws the energy from the excited electron-hole pair, preventing its radiative recombination [9]. The mechanism by which the initial charge separation occurs,

resulting in a charged luminescent core, is still a subject of debate, although non-resonant Auger ionization is the most widely accepted explanation. In this bi- or multi-excitonic process, one exciton transfers its energy to another exciton within the core, ejecting one of the charge carriers [9]. The long duration of the charged state (up to tens or even hundreds of seconds) can cause the characteristic "blinking" behavior of CQDs, where they may persist in a nonradiative state until charge neutrality is re-established [9].

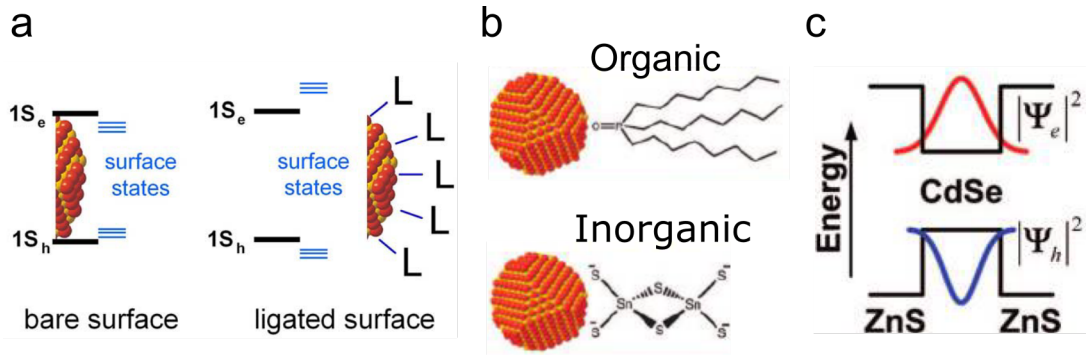

Figure 5.4: **a** Broken bonds at the surface of the CQD semiconducting core give rise to states within the bandgap. By choosing adequate surface ligand molecules, the surface states can be passivated and pushed outside of the bandgap. **b** Schematic of organic and inorganic ligands capping a CQD, used to passivate surface states, stabilize it in solution, and mediate its interaction with the environment. **a** and **b** adapted from [1]. **c** Band structure schematic of a CdSe/ZnS core/shell CQD. Electron (hole) radial probability distribution function shown in red (blue). Adapted from [2]

.

Dangling bonds at the surface of the CQD core result in surface states within the bandgap which act as traps, introducing nonradiative excitonic decay paths which drastically reduce CQD emission [1]. One way of passivating these surface states is by coordinating the semiconducting surface with ligands, significantly reducing the density of traps and pushing their energy level outside of the bandgap, as shown in Figure 5.4a [1]. Ligands can be either inorganic or organic in nature (Figure 5.4b). Inorganic ligands, such as metal/chalcogenide complexes, facilitate charge transfer between CQDs due to their short length and availability of empty states [2]. Longer organic ligands are typically composed of a head group for attachment to the semiconducting surface, and a carbon chain tail. Such ligands provide stability during the synthesis process, and allow the CQDs to be dissolved in various nonpolar solvents [2]. Apart from the ligands surrounding the CQD core, heterostructures can be synthesized to engineer the band energies within the core itself. CdSe/ZnS core/shell CQDs, shown in Figure 5.4c, are a type I heterostructure, in which the bandgap of the core material lies totally within the bandgap of the shell material. This band energy alignment confines the excitonic electron and hole functions within the inner CdSe layer of the core [1], inhibiting both charge transfer from the core to the outside environment as well as interaction with surface state traps. By significantly diminishing the importance of these

nonradiative decay channels, high photoluminescent quantum yields are obtained in type I heterostructure CQDs [8].

5.1.2 Silica Encapsulated Alloyed Semiconducting Colloidal Quantum Dots

The semiconducting ECQDs used throughout this thesis have two unique characteristics setting them apart from the most widely employed and studied CQDs: a smoothly varying composition gradient in the semiconducting core, comprised of a CdSe rich center transitioning to a ZnS rich outer edge, and a silica shell surrounding the core. The bandgap of this alloyed core follows the smooth stoichiometric composition gradient, as shown in the schematic of Figure 5.5a. This CdSeZnS alloy is in contrast to the more widespread structure of a CdSe core surrounded by a ZnS shell. One of the advantages of the alloyed composition gradient is that it reduces lattice mismatches which are normally present at the CdSe/ZnS interface [7]. This mismatch can introduce trap states in the bandgap, and also help to facilitate multicarrier Auger processes, both of which increase the rate of non-radiative recombination processes [9, 10]. The main drawback of alloyed CQDs is due to the difficulty of controlling the precise composition gradient during synthesis, resulting in batch to batch variations in CQD properties with slightly different precursor concentrations [11].

Dodecanethiol (DDT) ligands, used to stabilize the CQDs in solution and maintain optical properties after silica encapsulation, bond to the semiconducting core via metal-sulfur bonds. Oleic acid (OA) and stearic acid (SA) ligands are interdigitated between the DDT, and play a critical role in the nucleation of the encapsulating silica shell surrounding the entire core/ligand structure [11]. The silica shell in ECQDs give rise to several attractive properties, including increased functionality for further applications, reduced seepage of toxic heavy metals to the environment, and solubility in water [7], all while maintaining the superior optical properties of the semiconducting core [11].

A schematic of the entire ECQD structure, including semiconducting core, organic ligands and surrounding silica shell is seen in Figure 5.5b. Two batches of ECQDs were used in this thesis, both having a semiconducting core size of about 4.7 nm. The total mean diameter of each batch, including the silica core, was 44 and 71 nm. Both batches had a nearly identical emission spectrum, due to having the same core size, as seen in Figure 5.5c. The ECQDs were dissolved in ethanol solution. This is possible because of the hydrophilic nature of the silica shell, which allows for dispersion in polar solvents, in contrast to unencapsulated CQDs, which require nonpolar solvents due to their hydrophobic organic ligands. Transmission electron microscopy (TEM) images (Figure 5.5d) of the ECQDs in solution clearly show their core and silica shell structure. The upper left corner of the image shows a clump of unencapsulated CQDs, indicating that the process for growing the silica shell is not 100% efficient. These CQDs tend to agglomerate because they are insoluble in ethanol, due to their organic ligand covering. The ECQDs used throughout this thesis were synthesized by Maria Acebrón in the Hybrid Systems Based on Semiconductor Nanoparticles group, headed by Dr. Beatriz Hernández Juárez. They and their collaborators developed

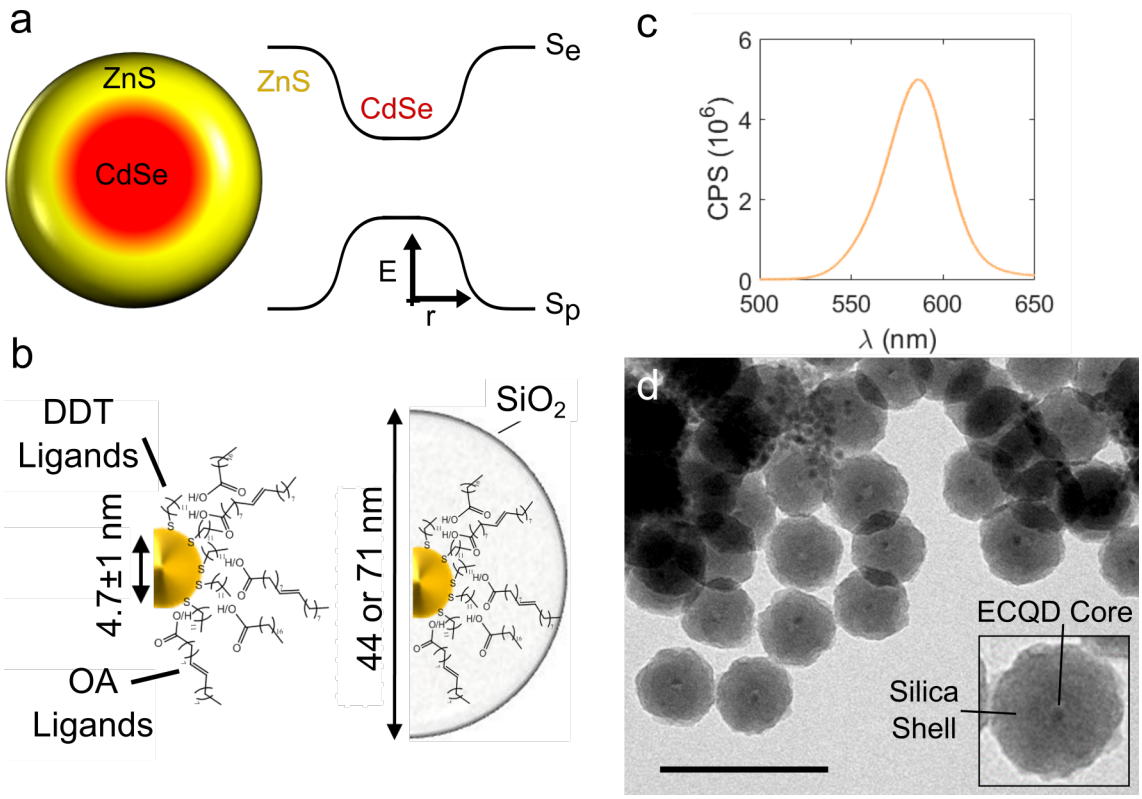

Figure 5.5: **a** Schematic of CdSeZSnS alloyed CQD semiconducting core, showing radial gradient transition from CdSe center to ZnS outer edge. Also shown is a depiction of the band structure in the CQD, with a smoothly varying bandgap. **b** Structure of alloyed CQD shown in **a**, along with stabilizing OA ligands and DDT ligands, which are crucial for ensuring successful growth of the surrounding silica shell. **c** Fluorescence spectrum of ECQDs in solution, showing peak at 586 nm. **d** TEM image of the ECQDs, with mean total diameter of 44 nm. Note that in the upper left corner, an agglomeration of unencapsulated CQDs is visible. Scale bar 100 nm. INSET: Closeup (53×53 µm) of single ECQD showing the silica shell and EQD core.

the process for for synthesizing both the alloyed CQDs and the growth of the silica shell, with the methods and results of presented in [11].

5.1.3 Langmuir-Blodgett Film Transfer Technique

The Langmuir-Blodgett method is a classical technique suited for coating substrates with mono or few layer films of different nanomaterials, including molecules, nanoparticles, CQDs and even flakes of 2D materials [12, 13]. A schematic of the necessary components for an LB deposition are shown in Figure 5.6a. A shallow trough is filled with a liquid, known as a subphase, most commonly water. The nanomaterial to be deposited is dispersed onto the subphase, in theory at the air/liquid interface, between two solid barriers. At this stage, the individual nanomaterial particles are spaced far apart and do not interact with each other, as shown in the "gas" schematic of Figure 5.6b. The surface tension of the liquid

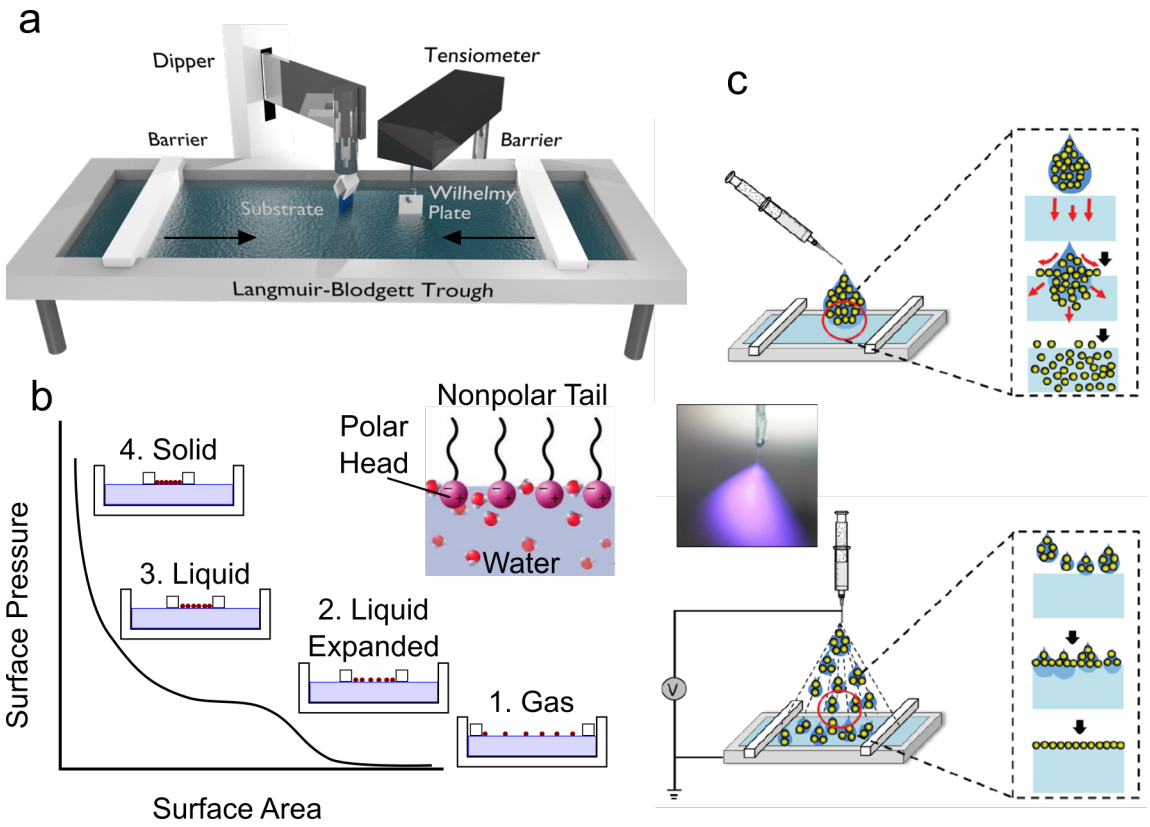

Figure 5.6: **a** Schematic showing a Langmuir-Blodgett trough. **b** Schematic of an idealized P-A isotherm, showing phase changes, numbered in progressing order, experienced by nanomaterial dispersed at the air/subphase surface as the LB trough barriers are compressed. **c** Conventional and electrospray dispersion of nanomaterial on the subphase surface [12]. INSET: Picture of an illuminated electrosprayed stream of ECQDs.

subphase is monitored by a Wilhelmy plate, usually a strip of metal or paper, connected to a tensiometer. As the mechanical barriers are slowly compressed, the increasing density of the nanomaterial film increases the subphase surface tension, which is plotted versus the surface area contained between the barriers to obtain the surface pressure versus surface area (P-A) isotherm, shown schematically in Figure 5.6b. The nanomaterial particles begin to interact with each other as the barriers compress, reducing the available surface area and producing an increase in surface pressure. Initially, the particles form a disorganized "liquid expanded" phase, where individual particles feel the presence of other particles, but do not yet touch any of their neighbors [14]. The "liquid compressed", or simply liquid, phase is reached as the particles come into contact with their neighbors, while still having a small amount of room to move between their nearest neighbors. The transition between the liquid expanded and liquid compressed phase is often characterized by a plateau in the PA isotherm, whereas the full liquid phase is characterized by a steadily increasing isotherm slope. Further area reduction immobilizes the particles into a tightly packed film, the "solid phase", which sometimes exhibits long range order, and is characterized by a

nearly vertical P-A isotherm. It should be noted that the distinction between phases is not always clear, with the transition between liquid expanded and compressed phases being especially ill-defined, as there is often no plateau region to identify it [13, 14]. One of the main advantages of the LB method is that the size of the deposited films are only limited by the size of the trough, making the LB method a technique especially suited for coating large area substrates easily.

The LB technique is especially suited for depositing films of amphiphilic molecules comprised of a polar head, such as an alcohol with large R group, and nonpolar tail, such as an alkane chain, on a water subphase. Upon dispersion, these molecules are able to sit on the surface because the polar head of the molecules are attracted to the polar water molecules, whereas the nonpolar chains are repelled, as shown in the inset of Figure 5.6b. Traditionally, nanomaterials dissolved in solution are dispersed using a syringe (Figure 5.6c). Dispersion is particularly difficult for nanomaterials that do not exhibit any sort of orientation of their surface chemistry to favor flotation on the subphase, such as the polar/nonpolar head/tails in amphiphiles. Nanomaterials that require dissolution in polar solvents are also challenging, since solution droplets from the syringe will tend to mix in with the polar subphase, resulting in substantial losses, as shown at the top of Figure 5.6c [12]. Spherical ECQDs dissolved in ethanol posses both of these properties, resulting in extremely inefficient dispersal with a syringe. Nie et al [12] recently proposed dispersal via electrospray to circumvent these problems,and successfully deposited LB films of several traditionally challenging materials. The micron-sized droplets produced by the electrospray quickly evaporate upon reaching the subphase surface, preventing excessive solvent/subphase mixing and consequent material loss [12]. For these reasons, the electrospray method was used to disperse the ECQDs studied in this thesis onto the LB subphase surface.

LB depositions were carried out at the Lancaster University physics department, under the supervision of Professor Robert Young and Lecturer Dr. Benjamin Robinson. The LB trough utilized was a KSV Nima KN 2003 Large model, equipped with a Brewster angle microscope (BAM) for imaging film formation on the surface of the trough. In this technique, p-polarized light is launched at the subphase/water surface at an angle (the Brewster angle) such that no light is reflected. This angle depends on the refractive index of the subphase. When a condensed phase with a different index intercepts, such as a film on the surface, intersects the light beam, a large change in reflection can be measured. Thus high contrast images can be obtained using this technique [15]. Depositions were carried out on two different subphases: water and dimethyl sulfoxide (DMSO). ECQD solution in ethanol (6 mmol concentration, 0.4-0.8 mL for water subphase, 1-2 mL for DMSO subphase) was loaded into a plastic syringe barrel with a stainless steel needle tip (8 mm long, 0.2 mm aperture). The syringe was placed 3-6 cm vertically above the subphase surface and an electrical bias was applied, usually between 2.5 and 5 kV. The electrical bias was varied to maintain a spray rate of about 1 mL/h. Once all solution was sprayed, the LB trough barriers were compressed at a rate of 10 mm/min, and the surface pressure monitored using a paper Wilhelmy plate

immersed in the subphase. Once the barriers were fully compressed, or upon reaching the desired surface pressure, the substrate, initially immersed in the subphase normal to its surface prior to spraying the solution, was withdrawn at a rate of 1 mm/min. ECQD film structure and homogeneity was found to be largely independent of the withdrawal speed, from 0.1 mm/min to 5 mm/min. After LB transfer, samples were dried in vacuum overnight.

5.2 Heterostructure Assembly and Characterization

5.2.1 ECQD Film Transfer and Resulting Properties

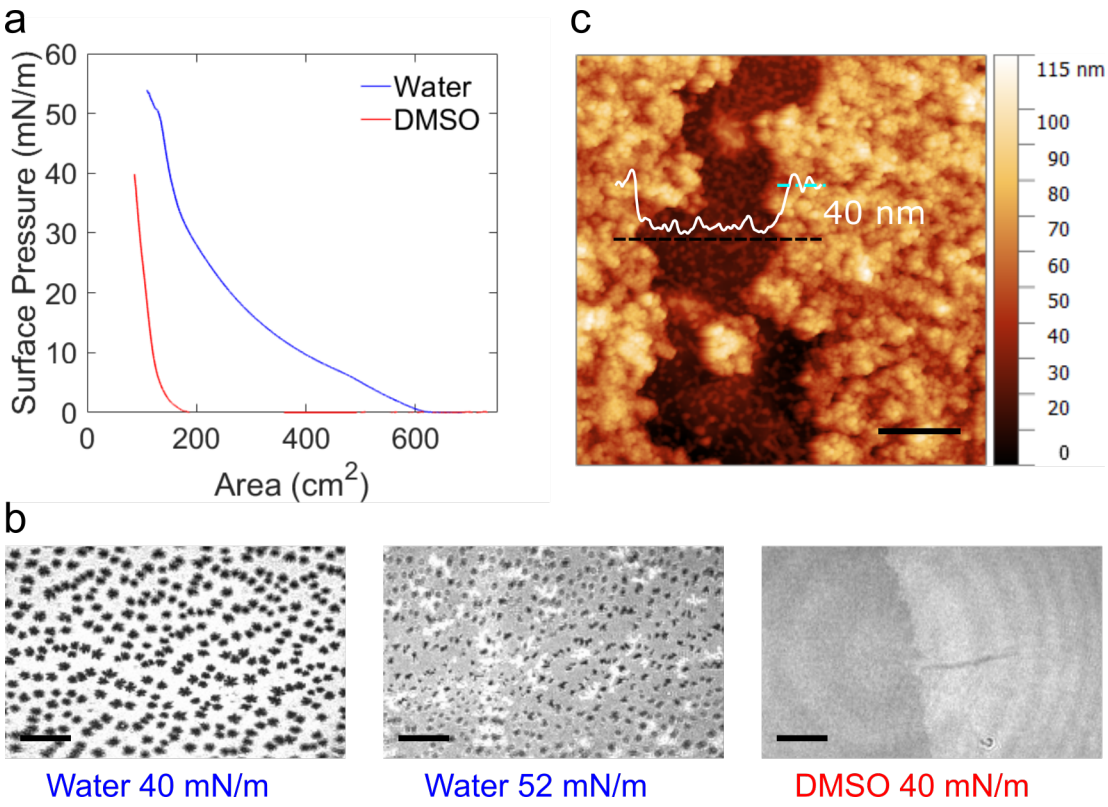

Figure 5.7: **a** P-A isotherm of LB compression of ECQDs on water and DMSO subphases. 0.8 (2) mL solution used for film deposition on water (DMSO). **b** Brewster angle microscopy images of ECQDs on water and DMSO surface at different surface pressures. Scale bars 200 µm. **c** AFM image of a gap in water transferred ECQD film, showing unencapsulated CQDs littering the underlying graphene.

Figure 5.7a shows clear differences in the P-A isotherms of ECQD films transferred using water and DMSO subphases. The water isotherm shows an almost immediate increase in surface pressure upon barrier compression. The isotherm slope steadily increases as the ECQD film passes through a liquid phase prior to reaching a solid phase characterized by a nearly vertical slope. The kink in the water curve at around 50 mN/m indicates the initiation of collapse and buckling of the solid film. Figure 5.7b shows BAM images of the film on the

water surface during the solid film phase, at 40 mN/m, and just after the initiation of film collapse at 52 mN/m. In both of the water images, black areas correspond to gaps in the film, tens of microns in size. Although compressing the film beyond the solid phase to the point of collapse reduces the size of the gaps, it does not eliminate them. The DMSO P-A isotherm and BAM image is markedly different than the water one. The surface pressure does not begin to rise until the barriers are close to full compression (due to the trough geometry, the minimum surface area achievable by barrier compression is about 80 cm^2). Once the pressure begins to rise, however, it passes to the solid phase almost immediately. In order to achieve film formation using a DMSO subphase, a significantly larger volume of ECQD solution was needed; the curves in Figure 5.7b were obtained using 0.8 and 2 mL solution for the water and DMSO subphases, respectively. The BAM images indicate that the ECQDs form dense, compact plaques when compressed on a DMSO subphase, as seen in the rightmost image of Figure 5.7b, with the ECQD plaque appearing on the right half of the image. Unlike the film on water, which is full of holes but covers the entire surface, the film on DMSO is free of holes but only covers part of the liquid surface.

The different film formation behavior observed on the two subphases can be attributed to the presence of unencapsulated CQDs on the water surface. As seen in the TEM images (Figure 5.5a), these CQDs agglomerate in the ethanol (relative polarity compared to water 0.654), due to interaction between their nonpolar hydrophobic ligands and the polar solvent, although they remain suspended in the liquid. Water, having a high polarity and surface tension (72 mN/m), is thus able to keep these agglomerated CQD clusters afloat on its surface, allowing them to form islands within the ECQD film. DMSO has a much lower polarity (0.44) and surface tension (43 mN/m) than water, which facilitates the dispersal into the subphase of the unencapsulated CQD clusters, eliminating the gaps in the ECQD film. Figure 5.7c shows an AFM topography image of two ECQD islands separated by a graphene patch riddled with a large concentration of unencapsulated CQDs. Similar CQD/subphase interactions were reported by Aleksandrova et al upon attempting to transfer Co/Pt CQDs covered by organic ligands via the LB method [16]. Using water as a subphase led to poor film formation, with almost no CQDs transferred onto the substrate, which they attributed to agglomeration and sinking due to the interaction between the hydrophobic surface ligands and water. Homogeneous monolayer films were obtained by switching to a less polar (0.71) diethylene glycol subphase [16].

ECQD films were transferred onto the standard highly doped Si/SiO_2 wafers, with different zones covered in monolayer graphene and gold, while some areas were left uncovered. For both subphases, practically no variations are seen in film morphology or distribution upon transfer to bare SiO_2, graphene covered SiO_2 and gold. Figure 5.8a and the inset in c show ECQD films transferred onto these substrates on water and DMSO subphases, respectively. These images replicate the BAM observations, confirming that the ECQD film is conformally transferred from the liquid/air interface onto the substrate. The blue regions in the dark field image of Figure 5.8a corresponds to ECQDs, while the dark islands are

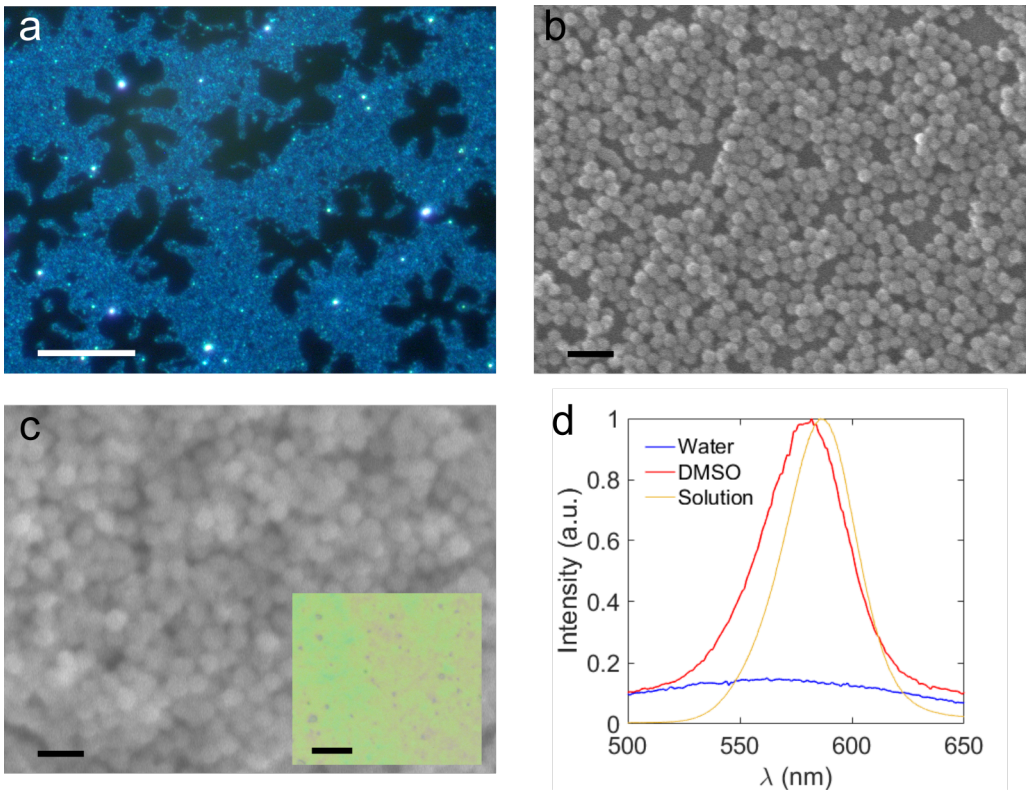

Figure 5.8: **a** Dark field optical image of water deposited ECQD film, at 30 mN/m. Blue areas correspond to ECQDs, while dark areas are gaps in the film. Within these gaps there are many unencapsulated CQDs present. Scale bar 10 µm. **b** SEM image of water transferred ECQD film. Scale bar 100 nm. **c** SEM image of DMSO transferred ECQD film. Scale bar 100 nm. INSET: Optical image of DMSO deposited ECQD film. Scale bar 10 µm. **d** Photoluminescence spectra of water and DMSO deposited ECQD films, taken using a spectroflourometer. Original spectrum in solution is also shown. Excitation wavelength in solution 450 nm, on substrate 300 nm.

gaps in the film having the same size and shape as the gaps seen in the BAM images. The DMSO film, on the other hand is compact, gap free and homogeneous, as seen in the optical image inset of Figure 5.8c. High magnification SEM images of the ECQD film transferred onto graphene on water and DMSO are shown in Figure 5.8b and c, respectively. Neither film shows any sort of long range order. The water transferred film shows a relatively large amount of small gaps, tens of nm in size, exposing the underlying graphene, as well as areas of multilayer stacking. In contrast, the DMSO transferred film is free of gaps and the underlying graphene is not visible, with increased multilayer stacking and bunching of the ECQDs observed. Thus the water transferred films displayed gaps on both the nano and micro scale, whereas the DMSO film is homogeneous and compact on all length scales. For electrical applications, a gap free film is critical to prevent short circuits between the top and bottom graphene sheets, as will be discussed in the next chapter.

Photoluminescence (PL) spectra of ECQD films are shown in Figure 5.8d. The DMSO

deposited film shows that it retains its flourescence properties, although its emission peak is slightly blue-shifted from 586 nm in solution to 581 nm on the higly doped Si/SiO_2 substrate. We refrain from speculating on the origin of this peak shift, since the measurements were taken months apart using different optical setups and different wavelength excitations. The solution spectrum is included to show that the overall emission spectrum characteristics remain the same before and after LB transfer. Water deposited films, however, result in a complete quenching of the emission properties. Pietra et al have observed similar quenching of silica coated CdSe nanorods upon exposure to ambient oxygen in a water solution, observing an immediate decrease in the quantum yield of the solution, with complete quenching occurring over the span of two weeks [17]. This quenching may be caused by radicals originating at the water/silica interface, as observed experimentally [18] and predicted theoretically [19], which subsequently oxidize or damage the ECQD semiconducting core. The observed extreme, super rapid quenching of the ECQDs occurred only at the air/water interface of the LB trough. ECQDs deposited onto a Si/SiO_2 substrate, both by LB film transfer and by simple drop casting, and left overnight immersed in water suffered only a slight reduction in their emission intensity. In conclusion, the PL, SEM and optical microscopy measurements confirm that for optical and electronic studies and applications, ECQD films cannot be deposited on a water subphase, due to the resulting gaps in film coverage and emission quenching. Transfer on DMSO, however, is succesfull, resulting in dense, compact, homogeneous films exhibiting strong light emission.

5.2.2 Graphene Transfer onto ECQD Films

Having transferred the ECQD film onto the substrate, the following step in heterostructure assembly is the transfer of a top graphene sheet onto the ECQD film. The material below the ECQD film (graphene, gold or bare SiO_2) was found to be unimportant for the tranfer of the top graphene sheet. The LB deposition subphase, however, was found to be critically important. Transferring the top graphene onto the water transferred ECQD film was relatively straightforward, with no changes made to the habitual PMMA mediated transfer process for CVD graphene. In contrast, graphene adhesion on the DMSO transferred ECQD films proved to be particularly challenging. There may be several reasons for this. First, the gaps in the water transferred film expose the underlying smooth substrate, which act as strong adhesion points for the top graphene sheet. Second, DMSO has a strong affinity for graphene, and is used as a solvent and exfoliant for graphene sheets in solution, much like N-methyl pyrrolidone [20]. Thus its presence on the surface of the ECQD silica shell will hinder graphene adhesion. It should be noted that the graphene used in the heterostructures was grown using the H_2 based CVD growth recipe (see Chapter 2 and Appendix A). The higher density of grain boundaries produced by this recipe enhanced adhesion to surfaces, and was thus utilized throughout this study for both the top and bottom graphene sheets.

In order to overcome these challenges, the graphene transfer process had to be modified in two specific ways. First, as much DMSO residue as possible was removed from the surface

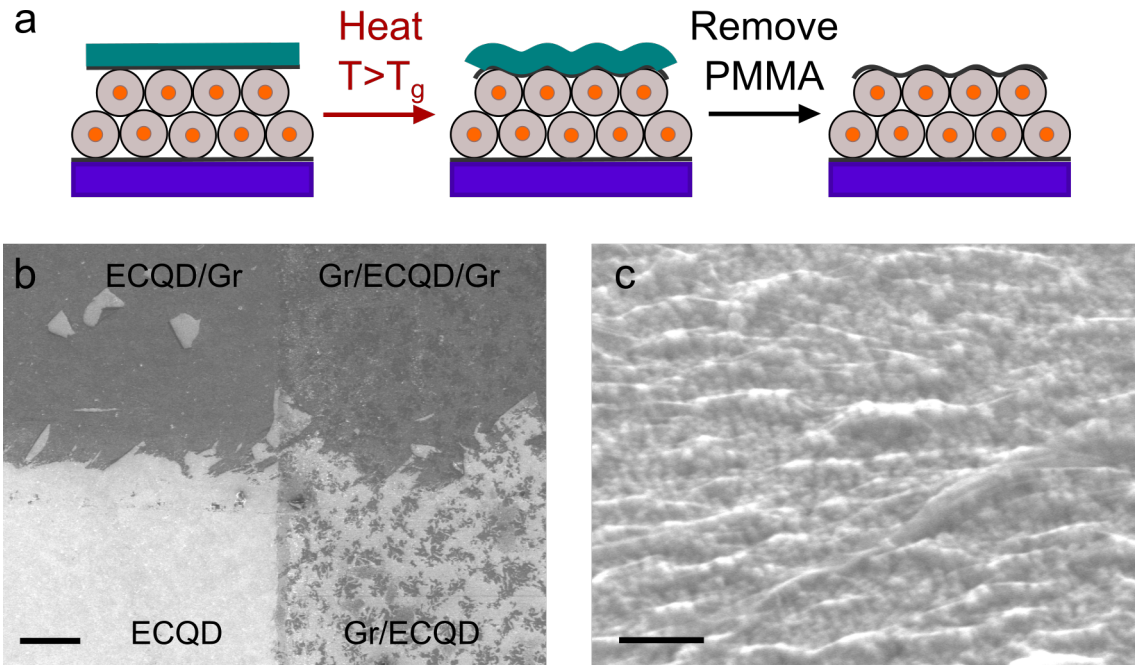

Figure 5.9: **a** Schematic depicting process for transferring top graphene sheet onto ECQD film. Stacking order, from top to bottom starting with the substrate SiO_2 substrate, is SiO_2/Gr/ECQD/Gr/PMMA. **b** SEM image showing all layers of the heterostructure. The bottom graphene sheet covers the right half of the image, while the top graphene sheet covers the top half of the image. Labels depict layer order from bottom to top, so Gr/ECQD region region consists of bottom graphene sheet covered in ECQD film. Scale bar 100 µm. **c** Angled SEM image in Gr/ECQD/Gr region, showing the top graphene sheet rippling on top of the ECQD film. Scale bar 200 nm.

of the ECQDs. This was done by washing the samples in a strong acetone jet for 30 s, prior to placing them in a vacuum (about 100 mT) at 80° C for four hours. The temperature was kept below 100° C to avoid denaturing the organic ligands within the ECQD shell. Otherwise, previously passivated surface traps would be exposed, reducing the luminescent quantum yield of the ECQDs. Second, and most critical for adequate adhesion of the top graphene sheet, is heating of the sample to a temperature greater than PMMA's glass transition temperature ($T_g \approx 180°$ C) prior to removing the PMMA. This ensures that the PMMA is able to release mechanical tensions and conform to the underlying ECQD film [21], allowing the graphene to conform to the silica surface of the ECQDs (see schematic in Figure 5.9a). Otherwise, upon PMMA removal with acetone, the graphene sheet was repelled from the ECQD film, tearing and rolling up into scrolls. The heating step was carried out by placing the sample on a hotplate at 200° C for 12 minutes. Initial attempts to transfer the top graphene sheet avoided this heating step (and were ultimately unsucceful) because luminescence quenching was expected, due to ligand denaturing and oxidation due to ambient oxygen [22]. Despite the prolonged high temperatures, ECQD film luminescence was maintained, as will be shown in the next chapter. This is most likely due to the

robustness of the silica shell, insulating the organic ligands while locking them in a fixed position. Moreover, the graphene top sheet may also have acted as a barrier preventing the diffusion of oxygen into the CdSeZnS core [22].

Figure 5.9b reveals each layer of the graphene/ECQD/graphene heterostructure, taken in a low magnification SEM image. The insulating ECQDs appear bright, whereas the conductive graphene is dark. The gaps in the ECQD film, visible as dark patches in the lower right hand corner of the figure, are due to its transfer on a water subphase. The high magnification, angled SEM image in Figure 5.9c clearly shows the top graphene sheet of the heterostructure rippling on top of the ECQD film.

5.2.3 Heterostructure Characterization

An AFM topography image of a film comprised of 71 nm diameter ECQDs, shown in Figure 5.10a, reveals the same features as seen in the SEM images, with few gaps in the coverage and various ECQD stacking heights. Analysis of various similar AFM images revealed a typical film height of 105 nm, corresponding to 1.48 monolayers, and a root mean square roughness of 35 nm. Figures 5.10b through d show simultaneously acquired AFM topography, ultrasonic force microscopy (UFM) and conducting AFM (C-AFM) images. In UFM measurements, a piezoelectric transducer is used to vibrate the sample at ultrasonic frequencies (tens to hundres of MHz)with an amplitude of about a nanometer, resulting in contact between the nanoscale measuring tip and the sample for about half of the vibration period [23, 24]. This technique is capable of measuring the mechanical stiffness of the materal beneath the tip; a larger (smaller) measured signal corresponds to a stiffer (softer) material. A voltage biased condutive tip, which comes into contact with the sample whilst current is recorded, is utilized to carry out the C-AFM measurements [25]. By electrically contacting the bottom graphene sheet and measuring the transmitted current, the vertical resistance in the vicinity of the C-AFM tip is probed. The images show the edge of a DMSO transferred ECQD film, sandwiched between a top and bottom graphene sheet. The Gr/ECQD/Gr and Gr/Gr regions can be clearly distinguished, and are marked on the images for clarity (Figure 5.10b-d). The ECQD spheres in these images have a diamter of 44 nm. A topographic line profile taken in the AFM image shows the stacking of two ECQD spheres, as shown in the schematic of Figure 5.10b. Comparing with Figure 5.10a, individual ECQDs are not resolved nearly as well, most likely due to the presence of the top graphene sheet, which may be suspended in small regions between ECQD spheres. Faint wrinkles visible in the Gr/Gr region, 2-4 nm in height, are most likely grain boundaries from the CVD growth process or from the graphene transfer process. The amorphous shapes in the Gr/Gr region are unencapsulated CQDs.

UFM measurements (Figure 5.10c) in the Gr/Gr region display a large measured signal, due to the stiffness of the underlying SiO_2 substrate [26]. In contrast, a much lower signal is measured in the Gr/ECQD/Gr region, indicating that it is much softer. This could be attributed to the organic ligands present in the silica shell endowing the ECQDs with a certain elasticity, or the porous nature of the silica shell reducing its mechanical stiffness [27]. The

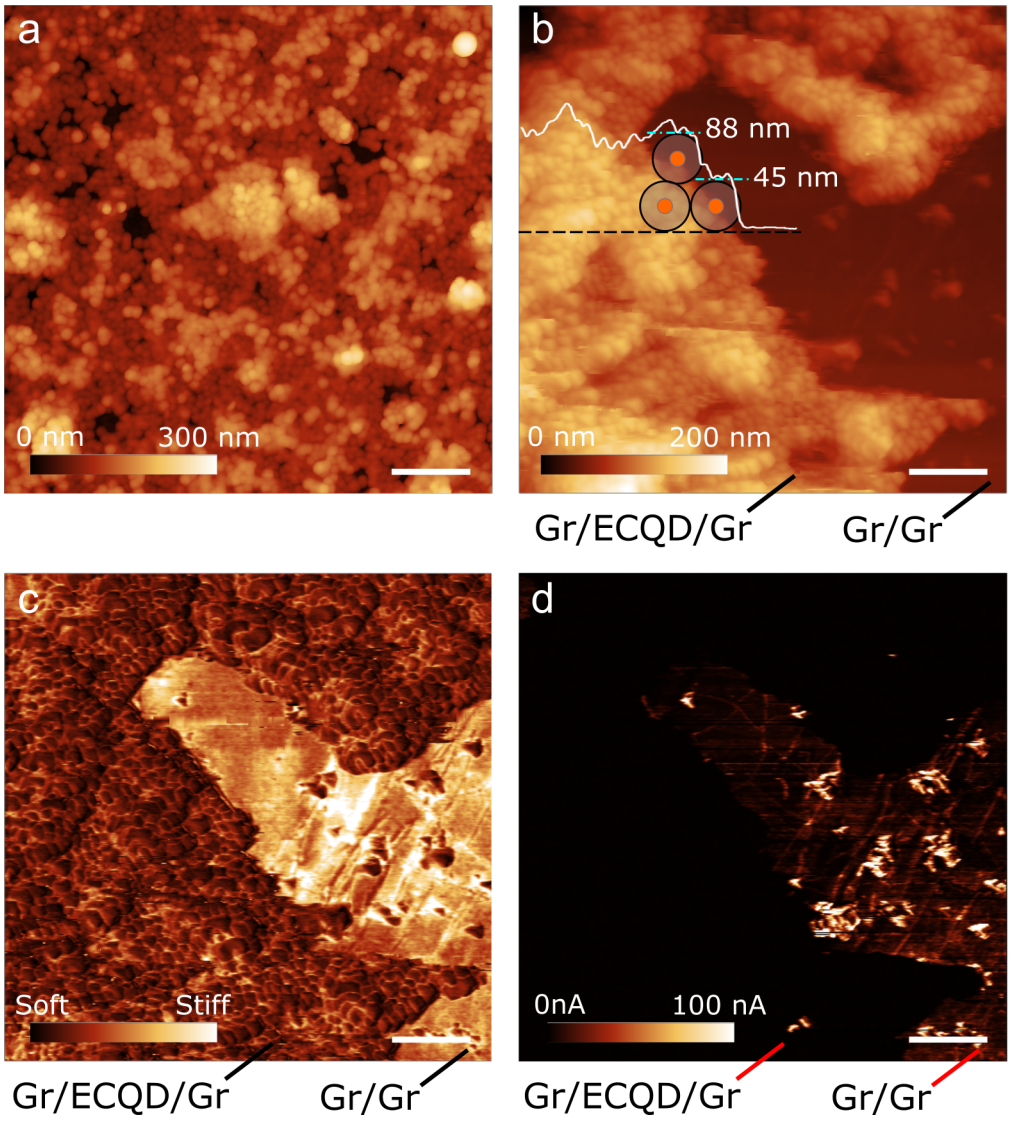

Figure 5.10: **a** AFM topography image of DMSO transferred, 44 nm diameter ECQD film. Scale bar 800 nm. Image taken by Dr. S. Casado at IMDEA Nanoscience. Images **b** through **d** correspond to simultaneously acquired topography, UFM and C-AFM images of Gr/ECQD/Gr heterostructure. ECQD film (71 nm diameter) was transferred on DMSO. Scale bars 400 nm. Images taken by G. Alsharif at Lancaster University.

graphene is seen to conform well to the ECQD silica shell surface, and no large suspended graphene regions, which are known to have low contact stiffness in UFM measurements, are observed [28], although there may be small suspended regions with sizes below the resolution of the probe tip. In the C-AFM image (Figure 5.10d), the Gr/ECQD/Gr region is measured to be completely insulating, indicating that no current is able to penetrate the insulating silica shells surrounding the ECQD cores. Measurements of various samples of DMSO transferred films all showed that the ECQD films were mechanically soft compared to the substrate, and completely insulating. The small conducting spot within the Gr/ECQD/Gr

region, seen at the bottom of Figure 5.10d, is most likely due to an agglomeration of unencapsulated CQDs within the ECQD film. These small, isolated spots of conduction, akin to point-defects or pin-holes in a dielectric film, were observed very infrequently within the ECQD film area.

The Gr/Gr region clearly conducts electricity, with the thicker wrinkles being more conductive [25, 29]. The unencapsulated CQDs trapped within the Gr/Gr region are quite soft, due to their organic ligand covering. Their relatively high conductance is harder to understand; it is possible that due to their elasticity, a better electrical contact is formed between the probe tip and CQDs.

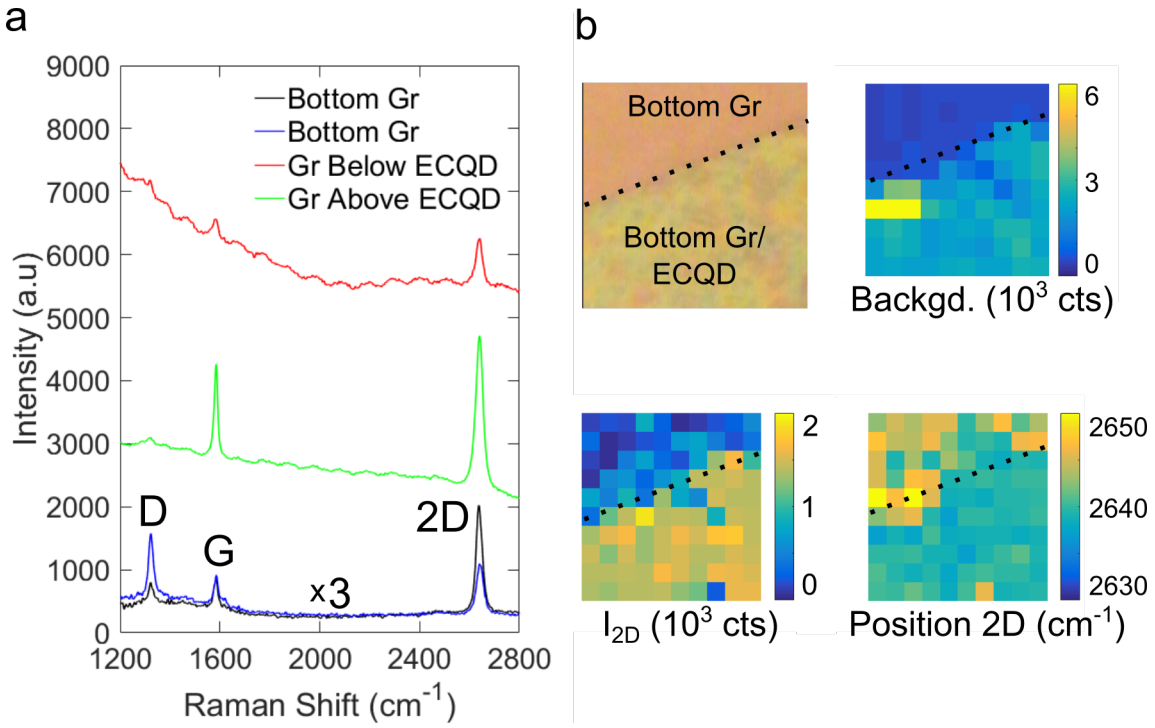

Figure 5.11: **a** Raman spectra of graphene on SiO_2 substrate, as well as above and below DMSO transferred ECQD film. The intensity of the two graphene on substrate spectra have been multiplied by 3 for clarity, while maintaining their background noise level fixed. **b** Optical image and Raman maps of a bottom graphene sheet, partially covered by an ECQD film. Scanning region 30×30 µm. Excitation wavelength 633 nm.

Raman spectra and maps of each layer of the Gr/ECQD/Gr heterostructure are shown in Figure 5.11a. The excitation wavelength was set to 633 nm to reduce the PL signal from the DMSO transferred ECQD films, which ave an emission peak centered around 586 nm with a full width half maximum of about 20 nm. Spectra taken on the bottom graphene sheet, with no ECQD film on top, shows significant variation in the 2D and D peak intensities in different locations. One spectrum shows a large 2D peak and small D peak, while this situation is reversed in the other peak. Both spectra show a constant G peak height. The variation of D peak intensity is typical for graphene grown using the H_2

based CVD recipe. The decreased I_{2D}/I_G peak ratio at constant I_G is indicative of graphene doping, due to an increased electron-electron scattering rate reducing 2D peak electron-hole recombination efficiency (this is discussed in greater detail in Chapter 4) [30]. This doping is most likely caused by DMSO solvent residues or loose CQDs present on the graphene susbtrate. Defected graphene, characterized by a high D peak intensity, will tend to attract dopants due to the availability of broken bonds in the lattice, explaining the simultaneous detection of high I_D and low I_{2D}/I_G throughout the spectra.

In order to more clearly observe the bottom sheet graphene spectra, their intensity was re-normalized by a factor of 3. This simply makes the spectra more easily visible in the figure, while leaving their original background noise unchaged. In the presence of an ECQD film, both the graphene Raman spectrum intensity and background noise are enhanced, with the greatest intensity (background noise) augmentation for graphene above (below) the ECQD film, as shown by the red and green spectra in Figure 5.11a. The high intensity peaks of the top graphene sheet could be a result of small suspended graphene regions between the nanoparticles, which are known to give more intense Raman peaks than substrate supported graphene [31]. Scanning Raman maps of a bottom graphene sheet, taken at the edge of a ECQD film, also show enhancement effects. The results of fitting the 2D peak are shown in Figure 5.11b (the D and G peaks were not fitted since they were affected by the PL tail of the ECQD film). Comparing parameters inside and outside of the ECQD film revealed I_{2D} enhancement factors of the bottom graphene sheet as high as 8, while the background noise level increased by a more homogeneous factor of about 4.2. These observations indicate that the ECQD film is somehow increasing the efficiency of the laser's excitation, or the the light collection of the microscope objective, topics that will be discussed in greater detail in the next chapter. In addition, the 2D peak position is shifted to lower frequencies in the presence of the ECQD film. If this effect is not a consequence of light scattering from the ECQD film, it could indicate that graphene's doping changes in the presence of the ECQD film [30].

5.3 Conclusion

Large area heterosturctures consisting of ECQD films sandwiched between CVD graphene sheets were successfully assembled by utilizing a LB film transfer technique. The subphase used for the transfer was found to be critically important to the final quality of the film. Whereas DMSO transferred films were homogeneous, compact, free of holes, with approximately 1.5 monolayers in coverage, water transferred films had significant gaps in coverage, both on the nano and micro scale, due to the presence of unencapsulated CQDs at the air/water interface. In addition, the luminescence of water transferred films was completely quenched, precluding these heterostructures from being useful for optical and electronic studies and applications. Adhering a top graphene sheet to the DMSO transferred films necessitated a high temperature baking step, in order for the graphene to conform to the underlying silica spheres. Scanning probe measurements of the completed heterostructures

showed that the ECQD films were mechanically elastic and completely insulating. Raman spectroscopy revealed that the films enhanced the efficiency of collected light, increasing both the spectrum intensity and background noise, while shifts in the 2D peak position hinted that the graphene was being doped by the ECQDs. This new type of low dimensional heterostructure, and the methods used to assemble it, suggest the possibility of exciting new scientific discoveries and technological applications, as will be shown in the next chapter.

Bibliography

[1] Cherie R. Kagan, Efrat Lifshitz, Edward H. Sargent, and Dmitri V. Talapin. Building devices from colloidal quantum dots. *Science*, 353:aac5523, 2016.

[2] Dmitri V. Talapin, Jong-Soo Lee, Maksym V. Kovalenko, and Elena V. Shevchenko. Prospects of colloidal nanocrystals for electronic and optoelectronic applications. *Chemical Reviews*, 110:389–458, 2010.

[3] Z. Chen, S. Berciaud, C. Nuckolls, T.F. Heinz, and L.E. Brus. Energy transfer from individual semiconductor nanocrystals to graphene. *ACS Nano*, 4:2964–2968, 2010.

[4] O. A. Ajayi, N. C. Anderson, M. Cotlet, N. Petrone, T. Gu, A. Wolcott, F. Gesuele, J. Hone, J. S. Owen, and C. W. Wong. Time-resolved energy transfer from single chloride-terminated nanocrystals to graphene. *Applied Physics Letters*, 104:171101, 2014.

[5] G. Konstantatos, M. Badioli, L. Gaudreau, J. Osmond, M. Bernechea, F.P.G. Garcia de Aquer, F. Gatti, and F.H.L. Koppens. Hybrid graphene-quantum dot phototransistors with ultrahigh gain. *Nature Nanotechnology*, 7:363–368, 2012.

[6] Z. Sun, Z. Liu, J. Li, G. Tai, S.-P. Lau, and F. Yan. Infrared photodetectors based on CVD-grown graphene and PbS quantum dots with ultrahigh responsivity. *Advanced Materials*, 24:5878–5883, 2012.

[7] Celso de Mello Donega. Synthesis and properties of colloidal heteronanocrystals. *Chemical Society Reviews*, 40:1512–1546, 2011.

[8] R. Koole, E. Groeneveld, D. Vanmaekelbergh, A. Meijerink, and C. de Mello Donegá. Size effects of semiconductor nanoparticles. In C. de Mello Donegá, editor, *Nanoparticles: Workhorses of Nanoscience*, chapter 2. Springer-Verglag, 2014.

[9] A.L. Efros and D.J. Nesbitt. Origin and control of blinking in quantum dots. *Nature Nanotechnology*, 11:661–671, 2017.

[10] W.K. Bae, L.A. Padilha, Y.-S. Park, H. McDaniel, I. Robel, J.M. Pietryga, and V.I. Klimov. Controlled alloying of the core–shell interface in CdSe/CdS quantum dots for suppression of auger recombination. *ACS Nano*, 7:3411–3419, 2013.

[11] M. Acebrón, J.F. Galisteo-López, D. Granados, J. López-Ogalla, J.M. Gallego, R. Otero, C. López, and B.H. Juárez. Protective ligand shells for luminescent SiO_2-coated alloyed semiconductor nanocrystals. *ACS Applied Materials & Interfaces*, 7:6935–6945, 2015.

[12] H.L. Nie, X. Dou, Z. Tang, H.D. Jang, and J. Huang. High-yield spreading of water-miscible solvents on water for Langmuir-Blodgett assembly. *Journal of the American Chemical Society*, 137:10683–10688, 2015.

[13] K. Ariga, Y. Yamauchi, T. Mori, and J.P. Hill. 25th anniversary article: What can be done with the Langmuir-Blodgett method? recent developments and its critical role in materials science. *Advanced Materials*, 25:6477–6512, 2013.

[14] D.R. Talham. Conducting and magnetic Langmuir-Blodgett films. *Chemical Reviews*, 104:5479–5502, 2004.

[15] KSV NIMA. *KSV NIMA MicroBAM Manual*, 2014.

[16] V. Aleksandrovic, D. Greshnykh, I. Randjelovic, A. Frömsdorf, A. Kornowski, S.V. Roth, C. Klinke, and H. Weller. Preparation and electrical properties of cobalt-platinum nanoparticle monolayers deposited by the Langmuir-Blodgett technique. *ACS Nano*, 2:1123–1130, 2008.

[17] F. Pietra, R.J.A. van Dijk Moes, X. Ke, S. Bals, G. Van Tendeloo, C. de Mello Donega, and D. Vanmaekelbergh. Synthesis of highly luminescent silica-coated CdSe/CdS nanorods. *Chemistry of Materials*, 25:3427–3434, 2013.

[18] H. Zhang, D.R. Dunphy, X. Jiang, H. Meng, B. Sun, D. Tarn, M. Xue, X. Wang, S. Lin, Z. Ji, R. Li, F.L. Garcia, J. Yang, M.L. Kirk, T. Xia, J.I. Zink, A. Nel, and C.J. Brinker. Processing pathway dependence of amorphous silica nanoparticle toxicity: Colloidal vs pyrolytic. *Journal of the American Chemical Society*, 134:15790–15804, 2012.

[19] J. Narayanasamy and J.D. Kubicki. Mechanism of hydroxyl radical generation from a silica surface: Molecular orbital calculations. *The Journal of Physical Chemistry B*, 109:21796–21807, 2005.

[20] David W. Johnson, Ben P. Dobson, and Karl S. Coleman. A manufacturing perspective on graphene dispersions. *Current Opinion in Colloid and Interface Science*, 20:367 – 382, 2015.

[21] J.W. Suk, A. Kitt, C.W. Magnuson, Y. Hao, S. Afmed, J. An, A.K. Swan, B.B. Goldberg, and R. Ruoff. Transfer of CVD-grown monolayer graphene onto arbitrary substrates. *ACS Nano*, 5:6916–6924, 2011.

[22] D. Zhang, D.Z.-R. Wang, R. Creswell, C. Lu, J. Liou, and I.P. Herman. Passivation of CdSe quantum dots by graphene and MoS2 monolayer encapsulation. *Chemistry of Materials*, 27:5032–5039, 2015.

[23] F. Dinelli, H. E. Assender, N. Takeda, G. A. D. Briggs, and O. V. Kolosov. Elastic mapping of heterogeneous nanostructures with ultrasonic force microscopy (UFM). *Surface and Interface Analysis*, 27, 1999.

[24] F. Dinelli, M. R. Castell, D. A. Ritchie, N. J. Mason, G. A. D. Briggs, and O. V. Kolosov. Mapping surface elastic properties of stiff and compliant materials on the nanoscale using ultrasonic force microscopy. *Philosophical Magazine A*, 80:2299–2323, 2000.

[25] J.M. Mativetsky, Y.-L. Loo, and P. Samori. Elucidating the nanoscale origins of organic electronic function by conductive atomic force microscopy. *Journal of Materials Chemistry C*, 2:3118–3128, 2014.

[26] B.J. Robinson and O.V. Kolosov. Probing nanoscale graphene-liquid interfacial interactions via ultrasonic force spectroscopy. *Nanoscale*, 6, 2014.

[27] M. Darbandi, G. Urban, and M. Krüger. A facile synthesis method to silica coated CdSe/ZnS nanocomposites with tuneable size and optical properties. *Journal of Colloid and Interface Science*, 351:30 – 34, 2010.

[28] B.J. Robinson, C. Rabot, R. Mazzocco, A. Delamoreanu, A. Zenasni, and O.V. Kolosov. Nanomechanical mapping of graphene layers and interfaces in suspended graphene nanostructures grown via carbon diffusion. *Thin Solid Films*, 550:472 – 479, 2014.

[29] M. Ahmad, S.A. Han, D.H. Tien, J. Jung, and Y. Seo. Local conductance measurement of graphene layer using conductive atomic force microscopy. *Journal of Applied Physics*, 110:054307, 2011.

[30] D. M. Basko, S. Piscanec, and A. C. Ferrari. Electron-electron interactions and doping dependence of the two-phonon Raman intensity in graphene. *Physical Review B*, 80:165413, 2009.

[31] S. Berciaud, S. Ryu, L.E. Brus, and T.F. Heinz. Probing the intrinsic properties of exfoliated graphene: Raman spectroscopy of free-standing monolayers. *Nano Letters*, 9:346–352, 2009.

Chapter 6

Electrical and Optical Properties of Encapsulated Colloidal Quantum Dot Heterostructures

This chapter describes the investigation of the electrical and optical properties of the ECQD heterostructures introduced in the previous chapter. The optical properties, examined in detail herein on the micro and nano scale, and which arise from quantum phenomena, are nonetheless observable at macroscopic length scales with the naked eye, as is so clearly displayed in Figure 6.1. The image on the left shows a white light picture of an ECQD film on top of a Si/SiO_2 substrate, in which some areas are covered with gold electrodes and graphene devices. A top graphene sheet, which covers part of the ECQD film, is barely discernible, due to graphene's small, constant absorption value of 2.29% for visible wavelengths. When the sample is illuminated with UV light, however, the presence of the top graphene sheet is clearly revealed, as it blocks the orange light emitted from the ECQD film. In contrast, emission from the ECQD film on top of the gold electrodes is enhanced with respect to the emission in the SiO_2 region. The origin of these physical behaviors will be investigated in this chapter.

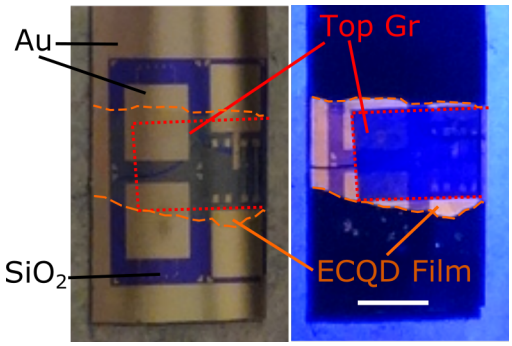

Figure 6.1: Picture of ECQD heterostructure under white light (left) and UV light (right) illumination, showing the ECQD film's fluorescence. Under UV illumination, two distinctive features are observed: strong emission enhancement on Au regions, and strong emission quenching on regions covered by top graphene sheet. In the white light picture, the Au regions correspond to yellow areas, and SiO_2 regions to dark blue/purple areas, as pointed out in the image. Scale bar 5 mm.

Transport measurements of graphene devices below the ECQD film revealed that it is

electrically insulating, allowing the top graphene sheet to be used as a top gate, with minimal leakage current (< 1 nA), and a capacitance value similar to the underlying SiO_2 substrate. Preliminary optoelectronic measurements revealed that the bottom sheet graphene devices are capable of photodetection in the UV/Visible range. Although these measurements are preliminary, important qualitative conclusions can nonetheless be drawn.

The ECQD heterostructures present a plethora of physical phenomena occurring simultaneously within one system. As such, disentangling one process from another, and discerning the delicate interplay between them, is a complex undertaking. The complexity of the system and time limitations therefore left many unanswered questions. This chapter concludes with a list of possible experiments and modeling that could be performed to better understand the the observations which still lack a full explanation.

6.1 Introduction: Fluorescence on the Nanoscale

This section presents a brief introduction to the physics of fluorescence on the nanoscale, and considers the most relevant topics for understanding the results obtained from the optical characterization of the ECQD heterostructures. To start off, basic definitions are given of the parameters that can be related to the measured physical observables in a fluorescence experiment. The physics of a fluorophore, defined as an atom, molecule, or structure which emits light when excited with light, is then touched upon. Classical and quantum approaches for calculating its decay rate are compared, by modeling the fluorpphore as a radiating dipole. The next sections cover the interaction between a fluorophore and its surrounding environment, in particular interactions with plane, semi-infinite surfaces. Special cases of the latter are then described more deeply, due to their relevance to our system: fluorophore energy transfer to i) plasmons on metallic surfaces and ii) graphene. For these two latter cases, the current state of the art scientific knowledge is reviewed, with particular emphasis on experiments involving semiconducting CQDs.

This section aims to present the most important physical aspects relevant to the problem at hand. Therefore, the basic equations used to model the nanoscale fluorophore are presented, along with the principal results, while skipping the intermediate mathematical details. Although no modeling or simulations were carried out to describe the experimental results, the physical equations nonetheless serve as a useful backdrop for understanding the most relevant physical processes present in the interaction of the ECQD film with its surrounding.

6.1.1 Basic Definitions

The recombination of excited electron-hole pairs in a fluorophore can occur via different mechanisms, as described in the previous chapter. Each of these mechanisms is characterized by a frequency or rate of occurrence. Recombination via faster processes is therefore more likely than by slower processes. The fluorescence quantum yield or quantum efficiency

Q is typically defined as the probability that an excited fluorophore will produce a fluorescence photon. The intrinsic quantum yield Q_0 of a fluorophore is defined in terms of the recombination rates of each of these processes, as

$$Q_0 = \frac{\Gamma_r}{\Gamma_r + \Gamma_{nr}} = \frac{\Gamma_r}{\Gamma_0} \tag{6.1}$$

where Γ_r and Γ_{nr} are the radiative and non-radiative decay rates. For semiconducting CQDs, the main non-radiative decay rates are trap mediated and Auger proceses (see previous chapter). The intrinsic lifetime that a fluorophore remains in an excited state is given by the inverse of the intrinsic decay rate, $\tau_0 = \Gamma_0^{-1}$. Ideally, Q_0 and τ_0 are measured with the fluorophore in a homogeneous, transparent medium, with which it has no electromagnetic interaction [1, 2]. Typically this is done by measuring the fluorophore in solution. More generally, the fluorophore may be in a non-homogeneous medium, with which it may interact through electromagnetic energy transfer processes. In these cases the quantum yield is given by

$$Q = \frac{\Gamma_r}{\Gamma_r + \Gamma_{ET} + \Gamma_{nr}} = \frac{\Gamma_r}{\Gamma} \tag{6.2}$$

where Γ_{ET} is the rate of the energy transfer processes, which are non-radiative. The measured lifetime is given by $\tau = \Gamma^{-1}$. Changing the environment around a fluorophore may increase or decrease its quantum yield Q (which measures the efficiency of radiative processes), as well as its lifetime τ. These two values are not correlated: an increased lifetime (decreased Γ) may result in increased Q if the radiative relaxation rate Γ_r is increased. Likewise, increased lifetime may reduce Q if the energy transfer relaxation rate Γ_{ET} increased. To a first approximation, the intrinsic non-radiative decay channels included in Γ_{nr} (Auger and trap-mediated recombination, primarily) are not affected by the surrounding electromagnetic environment [1]. They may, however, be affected by experimental processing steps, such as film assembly or heating, as will be discussed later on.

The intensity of detected emitted photons, I_{det}, is proportional to the rate of excitation of the fluorophores Γ_{exc}, the quantum yield, and the collection efficiency CE:

$$I_{det} \propto \Gamma_{exc} \times Q \times \mathrm{CE} = \Gamma_{exc} \times \frac{\Gamma_r}{\tau} \times \mathrm{CE}. \tag{6.3}$$

All of the terms in this equation are sensitive to the environment surrounding the fluorophore. For example, surface plasmons may increase the local excitation electric field and thus increase Γ_{exc}, while at the same time modifying the directional dependence of the radiatively emitted waves, which directly affects CE [2].

6.1.2 Calculating Flourescence Decay Rates

Flourescence is a spontaneous emission process in which the emitter fluorophore is initially assumed to be in an excited state. Spontaneous emission results from the emitter decaying to a lower energy state [3]. The spontaneous decay rate of a fluorophore in a homogeneous,

transparent medium may be solved following either classical or quantum-mechanical approaches. The classical approach models the fluorophore as a dipole oscillating at frequency ω_0, where the dipole is much smaller than the emitted wavelength $\lambda_0 = 2\pi c/\omega_0$ (and thus the electric field is assumed constant over the dipole's volume), where c is the speed of light, and the decay rate Γ_0 is much smaller than ω_0. The equation for a classically oscillating dipole $\boldsymbol{\mu}$ of mass m is

$$\frac{\mathrm{d}^2}{\mathrm{d}t^2}\boldsymbol{\mu}(t) + \Gamma_0 \frac{\mathrm{d}}{\mathrm{d}t}\boldsymbol{\mu}(t) + \omega_0^2 \boldsymbol{\mu}(t) = \frac{q^2}{m}\mathbf{E_s}(t), \tag{6.4}$$

where q is the elementary charge. The scattered electric field $\mathbf{E_s}(t)$ is a driving force for the dipole, and is the result of the dipole's electromagnetic interaction with the surrounding environment. In a homogeneous, transparent environment, $\mathbf{E_s} = \mathbf{0}$, and the dipole does not interact with its environment. For these conditions, the decay rate Γ_0 can be found by calculating the power dissipated by the radiating, undriven dipole, and then applying energy conservation conditions, yielding

$$\Gamma_0 = \frac{1}{Q_0}\frac{q^2\omega_0^2}{6\pi m \varepsilon_0 c^3}, \tag{6.5}$$

where ε_0 is the vacuum permittivity [1, 2]. The intrinsic quantum yield is included in this equation to account for the fact that there will be energy losses to non-radiative decay channels.

The quantum approach calculates the decay rate in a system with two energy levels separated by $\hbar\omega$ by using Fermi's golden rule. In this case, the decay rate is a function of the photonic mode density, or local density of optical states $\rho_{\boldsymbol{\mu}}$, available for the photon to decay into. The photon is initially in an excited state i, and decays to a final ground state f:

$$\Gamma_0 = \frac{2\pi}{\hbar^2}\sum_f \left|\langle f|\hat{H}_i|i\rangle\right|^2 \delta(\omega_i - \omega_f) = \frac{2\omega_0}{3\hbar\varepsilon_0}\left|\hat{\boldsymbol{\mu}}\right|^2 \rho_{\boldsymbol{\mu}}, \tag{6.6}$$

with the interaction Hamiltonian $\hat{H}_i = -\hat{\boldsymbol{\mu}}\cdot\hat{\mathbf{E}}$, where $\hat{\boldsymbol{\mu}}$ and $\hat{\mathbf{E}}$ are the dipole and electric field operators, and $\boldsymbol{\mu} = \langle g|\hat{\boldsymbol{\mu}}|e\rangle$ is the transition dipole matrix between the ground and excited state. The right hand side of the equation also introduced the photonic mode density, or local density of optical states, $\rho_{\boldsymbol{\mu}}$. This latter quantity is used to describe the surroundings of the fluorophore [1]. For a quantum system with no fixed dipole axis in free space, the decay rate can be averaged over all orientations, yielding

$$\Gamma_0 = \frac{1}{Q_0}\frac{\omega_0^3\left|\boldsymbol{\mu}\right|^2}{3\pi\varepsilon_0\hbar c^3}. \tag{6.7}$$

This expression differs from the classical decay rate given in equation 6.5, and is generally more accurate. However, both models give identical results when used to calculate the effect of changing the environment surrounding a fluorophore, and therefore give equal value for the relative change in decay rate Γ/Γ_0 [1].

In 1946, Purcell was the first to consider that the spontaneous decay rate of a fluorophore could be altered by its surrounding environment, due to its modifying the local density of optical states [4]. When considering an inhomogeneous system, such as a fluorophore in a transparent medium in front of a metallic surface, the electric field $\mathbf{E_s}$ scattered off the surrounding environment must be considered in equation 6.4, yielding new decay and emission rates Γ and ω. The general solution is thus

$$\frac{\Gamma}{\Gamma_0} = 1 + Q_0 \frac{6\pi\varepsilon_0 c^3}{\omega^3} \mathrm{Im}\{\mathbf{n}_\mu \cdot \mathbf{S} \cdot \mathbf{n}_\mu\} \tag{6.8}$$

where $\mathbf{n}_\mu$ is the unit vector in the dipole direction. The electric field susceptibility, given by $\mathbf{E_s} = \mathbf{S} \cdot \boldsymbol{\mu}$, contains the information about the dipole's interaction with its surroundings. The frequency shift is generally very small, and is usually approximated as $\omega = \omega_0$.

6.1.3 Dipole-Surface Interaction

Chance, Prock and Silbey introduced a model to calculate the decay rate of a fluorophore in front of a flat interface [5]. The model, sometimes called the CPS model, is based on the classical radiative decay of a dipole accounting for excitations from a scattered electric field, as presented in equation 6.8. The dipole is assumed to be in a transparent, lossless medium with dielectric constant ε_1 (real dielectric constant at wavelengths of interest), in front of another material with dielectric constant ε_2, which may be complex. Within this framework, an in plane wave vector $u = k_x/k_1$ is defined, representing the component of the wave vector in the surface plane normalized to the far-field wave vector k_1 of the dipole radiation in medium 1 (for a characteristic oscillation rate ω, $k1 = \sqrt{\varepsilon_1}\omega/c$) [2, 3]. The decay rate is found as a function of the distance d of the fluorophore from the surface of medium 2 by integrating the power dissipated by dipole over all in plane wavevectors u. In order to evaluate this integral, it is convenient to define several parameters: $r_p = (\varepsilon_1 l_2 - \varepsilon_2 l_1)/(\varepsilon_1 l_2 + \varepsilon_2 l_1)$ and $r_s = (l_1 - l_2)/(l_1 + l_2)$ are the Fresnel reflection coefficients for p and s polarized light; $l_i = -i(\varepsilon_i/\varepsilon_1 - u^2)^{-1/2}$ is the normalization component normal to the surface; $\Delta\varphi_1 = -2k_1 l_1 d$ is the phase shift of the incoming wave associated with the reflection on the interface 1-2. The decay rates for dipoles perpendicular and parallel to the surface are thus

$$\begin{aligned} \frac{\Gamma_\perp}{\Gamma_0} &= 1 - \frac{3}{2} Q_0 \,\mathrm{Im} \int_0^\infty r_p e^{-\Delta\varphi_1 d} \frac{u^3}{l_1} \mathrm{d}u \\ \frac{\Gamma_\parallel}{\Gamma_0} &= 1 + \frac{3}{4} Q_0 \,\mathrm{Im} \int_0^\infty \left[(1-u^2) r_p + r_s\right] e^{-\Delta\varphi_1 d} \frac{u}{l_1} \mathrm{d}u. \end{aligned} \tag{6.9}$$

These equations contain all the information necessary to calculate the power dissipated to the near and far field for a dipole in front of any material with a smooth surface [2].

Figure 6.2a shows the dissipated dipole power calculated using equations 6.9 for different fluorophore distances d in front of a silver surface. In the far field region, plane light waves are fully developed and the dipole's energy is dissipated radiatively. If the fluorophore is

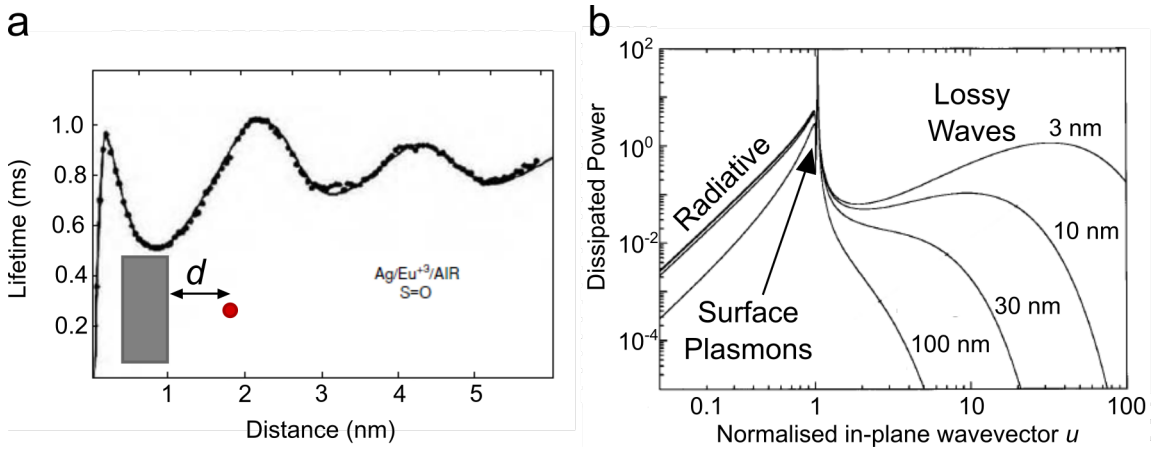

Figure 6.2: **a** Lifetime of Eu^{3+} ions in front of a Ag mirror separated a distance d by variable length fatty acid spacers, as shown in inset. Fitted line was calculated taking the isotropic average of equations 6.9. Adapted from [5]. **b** Dissipated power (integrand of equation 6.9) for isotropic dipole distribution in front of a Ag surface as a function of normalized in-plane wave vector u. Various distances d (as shown in inset in **a**) between the fluorophore and the silver surface have been calculated. The fluorophore is set to have an emission wavelength of 614 nm, and the silver dielectric constant is $\varepsilon_{Ag} = -16 + 0.6i$. Adapted from [3].

in front of a reflective surface, the reflected light couples with the emitter; if the coupling is in phase the dipole is driven harder, enhancing emission, whereas out of phase coupling results in reduced emission. The phase is a function of the distance d, and this explains the oscillation in decay rate with distance evident in Figure 6.2a. The amplitude of oscillations decreases with distance, since the field strength emitted by the dipole and thus reflected from the interface also decreases with distance [3]. As the distance between the fluorophore and the reflective surface is reduced, the rate of nonradiative energy transfer processes goes up drastically, quenching the emission and reducing the measured the decay lifetime. Figure 6.2b shows the dissipated dipole power as a function of the normalized wave vector u, calculated using equations 6.9 for an isotropic dipole distribution in front of a reflective silver surface. The far field region, where energy is dissipated radiatively, corresponds to $u < 1$. A strong spike is seen for values of u just above 1, due to near field coupling of the dipole to the silver surface plasmons. This spike arises from poles in the integrand of equation 6.9. Since plasmons are non-radiative, emission is strongly quenched by their excitation, although some of this energy may be recovered under adequate conditions. Energy transfer to surface plasmons is competitive for fluorophore/metal separations typically below 200 nm [3]. As the surface/dipole distance is further decreased ($u \gg 1$), additional non-radiative decay routes appear, normally called lossy surface waves. These are associated with the excitation of electron-hole pairs at the metal surface, which dissipate by scattering in the substrate bulk, and show a distance dependence of d^{-4} [2, 3]. Non-radiative lossy energy transfer is typically dominant for $d < 20$ nm [3].

6.1.4 Dipole Coupling to Surface Plasmons

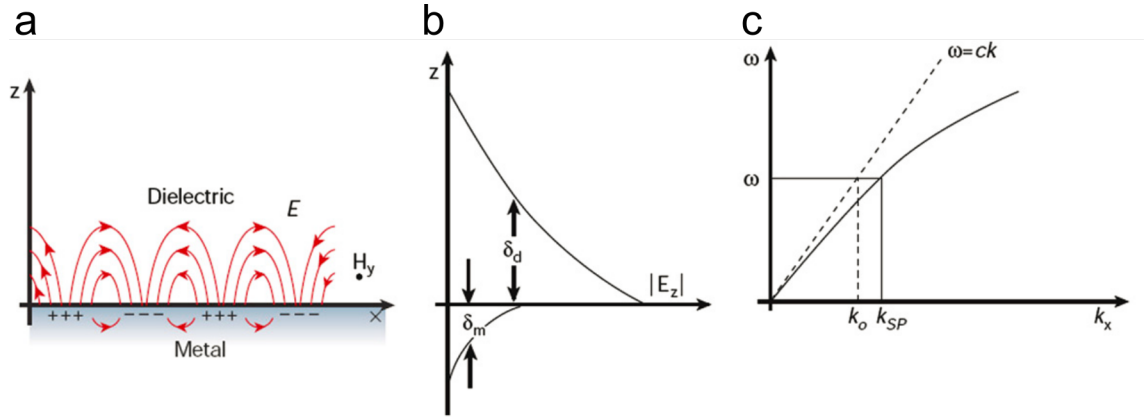

Figure 6.3: Schematics showing physical characteristics of surface plasmons. **a** Surface plasmon propagating along a metal/dielectric interface. With +/- representing regions of high/low electron density. Note that the electric field is normal to the surface, and the magnetic field transverse parallel. **b** Evanescent electric field intensity normal to interface in metal and dielectric. **c** Surface plasmon dispersion relation, with light dispersion shown in dashed line. At a given frequency ω, a momentum mismatch exists between the light and plasmon dispersion. Adapted from [6].

Surface plasmons are collective plasma oscillations of the free electrons near a metal's surface. The charge oscillations give rise to an evanescent electric field which decays in the direction normal to either side of the surface, into the dielectric and metal bulk. The evanescent field propagates into the dielectric with a typical length on the order of half the wavelength of the exciting light. The field's propagation into the metal is about an order of magnitude shorter, however, due to the metal's lossy absorbing properties [6]. The plasmon oscillations propagate along the metal/dielectric interface, decaying with a characteristic length of $1/k_{SP}$, where k_{SP} is the wave vector of the surface plasmon, defined in the x direction parallel to the surface. Plasmons in metals also decay in the x direction, with typical lengths in the tens of microns. These general characteristics are depicted in Figure 6.3a and b.

For a lossless dielectric with a real relative permittivity ε_1 and a metal with complex permittivity $\varepsilon_2 = \varepsilon_2^{'} + i\varepsilon_2^{''}$, the first order approximation dispersion relation for a surface plasmon at the interface between the two media is given by

$$k_{SP} = \frac{\omega}{c}\sqrt{\frac{\varepsilon_1 \varepsilon_2^{'}}{\varepsilon_1 + \varepsilon_2^{'}}}. \tag{6.10}$$

This dispersion relation shows that at a given frequency ω, a surface plasmon will have a slightly higher momentum than light, which has a linear dispersion relation $k_1 = \omega/(c\sqrt{\varepsilon_1})$ in medium 1. Due to this momentum mismatch with light, plasmon decay is non-radiative, with energy loss occurring via evanescent electric fields. Another consequence of the plasmon dispersion relation is that incident plane wave light cannot be used to excite plasmons

on smooth surfaces due to the momentum mismatch [6], as shown in Figure 6.3c. One way of exciting surface plasmons is to use the near field light from decaying fluorophores in the vicinity of the metal surface; the large in-plane components of the light can successfully overcome the momentum mismatch [2]. Far-field plasmonic coupling can be achived by modifying the dielectric environment in front of the metal surface, so as to scatter the light in such a way that the momentum mismatch criterion can be overcome [1, 2, 7]. Yet another approach at achieving plasmonic coupling does away with the surface altogether, by confining fields into metallic wires or particles much smaller than the characteristic wavelength. These nano-structures do not follow the plasmonic dispersion relation shown above, and thus coupling to these localized plasmons is generally easier when studying nano-scale systems [1].

Energy transfer from a fluorophore to a surface or localized plasmon is nonradiative, drastially reducing its decay lifetime, and quenching its emission (Figure 6.2a). Nonetheless, some of this energy may be recovered in a "concentrated" way by using the resulting enhanced evanescent electric field normal to the metal/dielectric surface to re-excite the fluorophore [2]. However, the distance from the metal surface must be carefully controlled: the fluorophore must be close enough to benefit from the evanescent electric field normal to the metal/dielectric interface, but not so close as to be quenched by lossy waves due to electron-hole excitation at the metal surface. This can be accomplished by using a transparent dielectric spacer to separate the metal and fluorophore, generally tens of nm thick [2]. Plasmonic effects also affect the directionality of the emitted light, and may contribute to more effective collection of emitted photons [8]. The recovery of energy transmitted to surface plasmons is generally more efficient when the plasmons exist on rough surfaces or metallic nanoparticles. These structures not only modify the surface plasmon dispersion relation, making their excitation with far-field light easier, but their high curvature results in "hot-spots" of very high electric field enhancement [1, 7].

Numerous studies have been carried out investigating the relationship between semiconducting CQDs and surface plasmons, with the most efficient coupling and radiative enhancement achieved using rough films or metallic nanoparticles, for the reasons mentioned above. A drastic decrease in fluorescence lifetime was measured for CQDs on smooth and rough gold surfaces [9, 11–14], or interspersed with gold nanoparticles [10]. This effect is observed in Figure 6.4a, showing the fluorescence decay for individual CQDs dispersed on rough and smooth Au surfaces [9]. This study, like all others mentioned herein, observed CQD emission quenching on smooth gold surfaces, resulting from coupling to lossy surface waves, and enhancement on rough gold surfaces due to plasmonic coupling. Plasmons can be launched by coupling to the excitation field [9, 13], the emission field resulting from the CQD decay [12], or both, and can result in such fast decay rates as to overwhelm the nonradiative Auger recombination process [14].

Another approach for plasmonic enhancement of CQD emission involves the use of metallic nanoparticles. The location of the plasmonic resonance in Au nanoparticles is a function

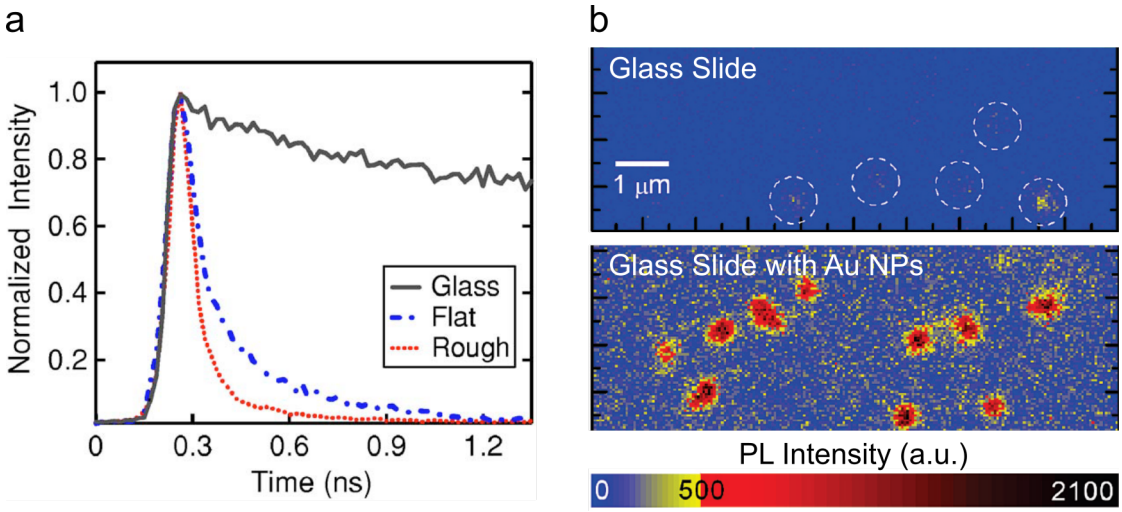

Figure 6.4: **a** Fluorescence decay curves for individual CQDs on glass surface, and rough and smooth Au surfaces. Adapted from [9]. **b** PL map of individual ECQDs on glass slide, and on glass slide interspersed with Au nanoparticles (Au NPs). Adapted from [10].

of their size; thus by tailoring this resonance to the emission of the CQDs or to the excitation wavelength, strong emission enhancement can be achieved. This approach was used by dispersing ECQDs, very similar to the ones used in this work, with Au nanoparticles on a glass slide [10], as shown in Figure 6.4. The resulting emission enhancement was a consequence of suppressed nonradiative Auger recombination [10]. Recently, an innovative synthesis method was pioneered by Ji et al [15], by encapsulating semiconducting CQDs in a silica shell and subsequently growing a Au film around the shell, thus integrating the fluorophore/dielectric/metal system in a compact structure. Plasmonic coupling to both the excitation and emissin field in these structures resulted in an enhancement factor of 3.2 [15].

6.1.5 Dipole-Graphene Interaction

The problem of energy transfer between an excited fluorophore and a graphene sheet was first treated by Swathi and Sebastian [16, 17]. Taking a quantum approach, they used Fermi's golden rule to calculate the energy transfer rate between the two state excited fluorophore and the continuous density of states around graphene's Dirac cone. The decay rate they arrived at was presented in a form useful for comparison with experiment by Chen et al [18], given by

$$\begin{aligned} \frac{\Gamma_\perp}{\Gamma_0} &= 1 + \frac{\pi}{16}\frac{\alpha}{\varepsilon^{5/2}}\left(\frac{c}{v_f}\right)^4 I(d) \\ I(d) &= \int_0^1 \exp\left(-\frac{4\pi c d}{v_F \lambda_0} t\right) \frac{t^3}{\sqrt{1-t^2}}\,\mathrm{d}t, \end{aligned} \tag{6.11}$$

where $\alpha = q^2/\hbar c$ is the fine structure constant, which characterizes graphene's absorption in the visible range, ε is the dielectric constant of the surrounding medium, d is the distance from the fluorohore to the graphene, λ_0 is the emission wavelength and $v_F = 1 \times 10^6$ m/s is

the graphene Fermi velocity. For separations greater than about 2 nm, this equation gives a d^{-4} dependence. Energy transfer between a radiating dipole and graphene in the visible wavelength range occurs through the excitation of electron-hole pairs in the graphene Dirac cone, similar to the lossy waves mechanism described for metal surfaces, which also has a d^{-4} dependence. Another important characteristic touched upon by Swathi and Sebastian was the effect of graphene doping on the energy transfer. They found that for "naturally" occurring graphene doping levels ($|E_F| < 0.5$ eV), there is very little effect on energy transfer for dipole decay in the visible energy range. This is because visible light is of much higher energy than the doping, and thus still able to efficiently excite graphene electrons into the valence band.

Gaudreau and coworkers [19] tackled a similar problem using a classical approach of a decaying dipole dissipating energy, separated from the graphene film by a lossless medium with dielectric constant ε. They arrived at an integral expression for the relative decay rate, where the dissipated power was integrated over all parallel wave vectors k_x

$$\frac{\Gamma}{\Gamma_0} = 1 + \frac{3\nu\lambda_0^3}{32\pi^3}\int_0^\infty k_x^2 e^{-2k_x d}\mathrm{Im}\{r_p\}\mathrm{d}k_x, \tag{6.12}$$

where ν is equal to 1 or 2 for parallel and perpendicular dipole orientations, λ_0 is the emitted wavelength, and r_p is the Fresnel reflection coefficient at the graphene/dielectric interface. In the 3-15 nm range, this integral yields the tidy expression

$$\frac{\Gamma}{\Gamma_0} = 1 + \frac{9\nu\alpha}{256\pi^3(\varepsilon+1)}\left(\frac{\lambda_0}{d}\right)^4, \tag{6.13}$$

where α is the fine structure constant, which characterizes graphene's absorption in the visible range, with $\alpha = q^2/\hbar c$. Both the classical and quantum approaches yield qualitatively similar results, showing decay rates with characteristic d^{-4} dependence [17, 19]. Moreover, the underlying mechanism of energy transfer through the excitation of electron-hole pairs is the same in both approaches. Another important similarity is that graphene's energy absorption can be characterized by its optical conductivity $\sigma = q^2/4\hbar$ in the visible range, resulting in a characteristic constant absorption of 2.3%.

Several studies have confirmed energy transfer between excited fluorophores, including semiconducting CQDs, and graphene, which results in emission quenching and decreases fluorescence decay lifetimes [18–20]. For fluorescent molecules, a spacing dielectric layer is required to prevent direct charge transfer between the organic molecules and the graphene. In semiconducting CQDs, organic ligands serve as the dielectric spacer, and prevent charge transfer from occuring. Direct charge transfer shows a d^{-6} dependence, requiring very small distances between the semiconducting CQD and the graphene to ensure orbital overlapping [18]. To facilitate charge transfer, CQDs must be coated with specifically designed very short ligands [21]. The thick silica shell surrounding the ECQDs used in this study prevent charge transfer from occurring between the semiconducting ECQD core and the graphene sheets.

6.2 Methods

Photoluminescence (PL) spectra and maps taken at IMDEA Nanoscience were measured using the optical setup described in Chapter 2. Continuous wave excitation for PL measuremens was carried out with a 488 nm Ar laser. Pulsed excitation at various wavelengths was carried out using a Fianium SuperChrome SC 400 supercontinuum laser, with a 40 MHz pulse rate. Light was collected in an inverted microscope setup via a 40× magnification objective with a numerical aperture (NA) of 0.65, resulting in a diffraction limited spot size below 1 µm in diameter, with typical powers between 3 and 10 µW for both excitation sources. Spectra were collected in a Peltier cooled, electron multiplied, silicon CCD detector (Andor Newton EM), passing through a 0.5 m diffraction spectrometer, using a 300 lines/mm reflective diffraction grating. PL measurements at Lancaster University were carried out on a Horiba LabRAM HR Raman scanner, with 532 nm continuous wave laser, and collected in a 100× 0.9 NA objective.

Fluorescence lifetime decays were measured with a PicoQuant τ-SPAD 250 single photon counting module based on an avalanche photodiode. A 32 bit, time correlation single photon counting acquisition card was used, with a 25 ps binning time. A constant excitation power of 3 µmW at 470 nm was used, ensuring that photon detection occured in less than 1% of excitation cycles, in order to prevent pileup effects and artificially low lifetime measurements [22]. Experimentally measured fluorescence curves $I(t)$ consist of the convolution of two signals: the intrinsic fluorescence decay of the sample $f_{dec}(t)$ and the instrument response function IRF(t) [22]. The system's IRF was measured with the same optical setup as used for measuring the samples, but replacing the samples with a reflecting mirror. Light in the range 586 ± 25 nm, replicating the emission spectrum of the ECQD film, was aimed at the mirror and collected, producing the characteristic IRF of the optical excitation and collection system (see Figure 6.6). This IRF was convoluted with the intrinsic decay function of the ECQDs to fit the measured data:

$$I(t) = \int_0^t \mathrm{IRF}(\tau) \times f_{dec}(\tau)\mathrm{d}\tau. \tag{6.14}$$

A stretched exponential was used to fit the intrinsic decay function

$$f_{dec}(t) = \exp\left[(-t/\tau_s)^{\beta}\right], \tag{6.15}$$

with a stretch parameter $0 < \beta \leq 1$ and stretch decay time τ_s as the fitting parameters. The stretch parameterβ is used to express an underlying distribution of decay rates in the system, caused for example by illuminating multiple emitting fluorophores simultaneously [23]. Finally, the parameter of interest, the decay time τ was calculated by averaging the fitted decay function over the measurement time t_{meas}

$$\tau = \int_0^{t_{meas}} f_{dec}(t)\mathrm{d}t. \tag{6.16}$$

MATLAB's lsqcurvefit function was used to fit the experimentally acquired fluorescence decay and PL data, by minimizing the least-squares error between the fitting function and the data.

Photodetection measurements were carried out on a probe station (see chapter 2), illuminating with a handheld flashlight (Lumitorch with a Edixeon Pro 26 UV LED). The output light was centered at 410 nm, with a total power of 1 W.

6.3 Optical Properties

6.3.1 Results

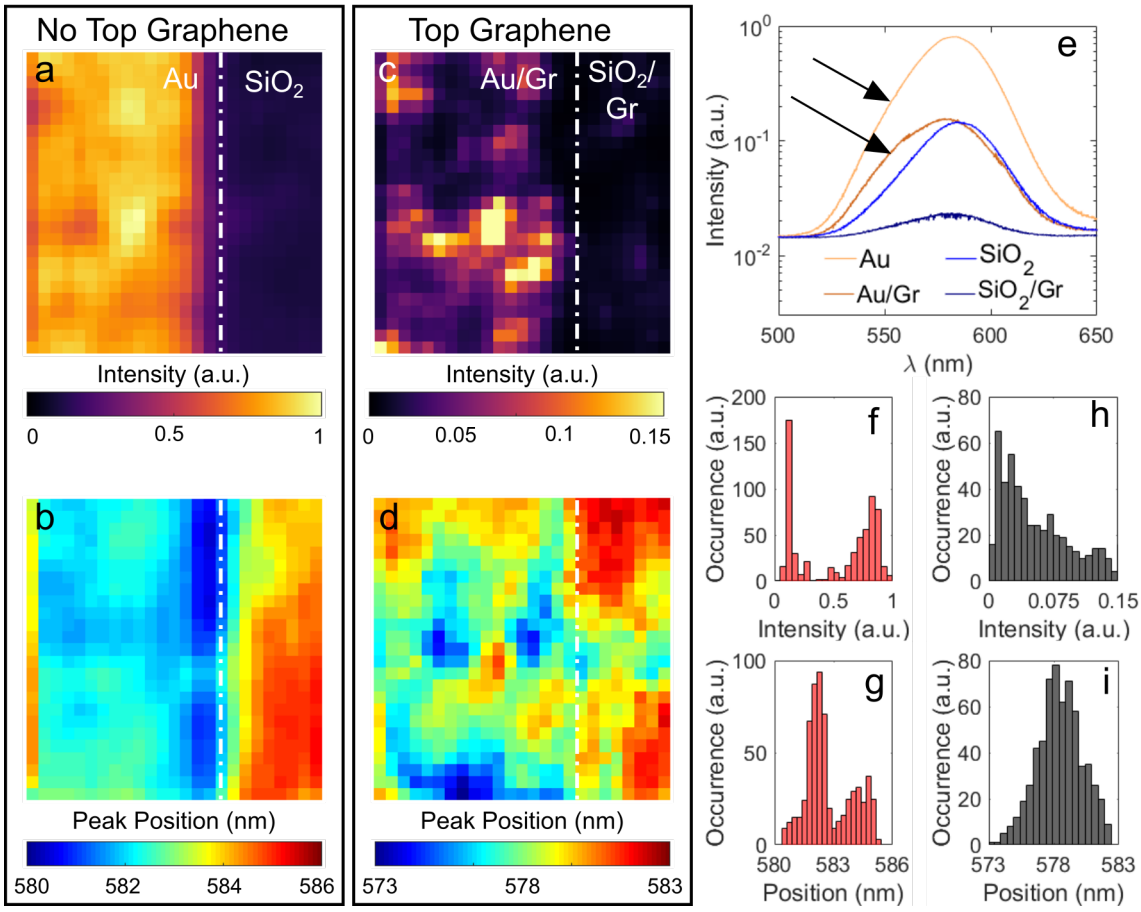

Figure 6.5: PL maps of ECQD film on the same sample, in regions without (**a** and **b**) and with (**c** and **d**) top graphene sheet present. No bottom graphene sheet was present for either map. Fitted integrated peak intensity (**a** and **c**) and peak position (**b** and **d**). Both maps 30x30 µm. **e** Typical PL spectra showing peak intensity and position differences in each region. **f-i** Histograms corresponding to data shown in **a-d**, respectively. Fitted peak intensity and position without top graphene (**f** and **g**), and with top graphene (**h** and **i**). All measurements taken with excitation wavelength 488 nm collected with a 40× 0.65 NA objective.

Figure 6.5 shows the results of PL mapping of ECQD films in two different regions of the same sample. Both maps show a Au/SiO_2 interface, with the ECQD film covered in a top graphene sheet for the map in Figure 6.5c/d. No bottom graphene sheet was present in either map. The intensity and position of the resulting peaks were fitted to a Gaussian curve at each point. The intensity map of the region without a top graphene sheet (Figure 6.5a) shows strong enhancement in the zone where the ECQD film sits atop a gold electrode. This effect is also clearly visible in the PL spectra and is quantified in the histogram (Figure 6.5e and f), which shows two clear peaks corresponding to the spectra in the gold and SiO_2 zones. An average intensity enhancement factor of 6.5±1.35 is calculated in the gold compared to the SiO_2 region. PL intensity is quenched in the region with a top graphene present, shown in the map and histogram of Figure 6.5c and h, as well as in the individual PL spectra (Figure 6.5e). A quenching factor of about 7 is calculated when comparing the SiO_2 zones in the maps with and without graphene. Emission quenching also occurs in the gold/graphene zone, although there is a much larger variation in the emission intensity compared to the SiO_2/graphene zone. As such, there is no clear distinction in the histogram distinguishing gold/graphene and SiO_2/graphene zones. This is likely due to variations in the ECQD film thickness, observed in the previous chapter. In zones with multiple stacked ECQDs, those towards the bottom will interact much less with the graphene and will thus be able to emit much more brightly.

The presence of a top graphene sheet results in a large variation in the emission peak positions, with values in the range of 573 to 583 nm, as displayed in Figure 6.5d. In addition, there is not a clear difference in peak position between the gold/graphene and SiO_2/graphene zones, as evidenced by the lack of multiple peaks in the histogram in Figure 6.5i. This is in stark contrast to the map of the region with no top graphene sheet, which shows a much smaller range of peak positions (580-586 nm, Figure 6.5b), and displays a clear blue-shifting on the gold zone. This effect is especially strong in the proximity of the gold edge, with the peak position dipping down towards 580 nm. The blue shifting within the gold zone causes two peaks to appear in the peak position historgram in Figure 6.5g. Spectra taken within each of the regions, plotted in Figure 6.5e, show a bulge or shoulder for wavelengths below the peak maximum value in the gold and gold/graphene zones, identified with arrows in the figure. This bulging at lower wavelengths is responsible for the blue-shifting of the fitted peak position within the gold region. Also visible in the spectra is the PL tail at long wavelengths, possibly resulting from the presence of surface trap states [21], which was observed in the Raman measurements at 633 nm in the previous chapter.

Measured ECQD film fluorescence decay rates and fitted curves are plotted in Figure 6.6, in regions without and with a top graphene sheet present (a and b). Both plots show measurements taken on zones with the ECQD film on top of gold and SiO_2. Table 6.1 shows the decay parameters obtained from fitting several measured curves in each zone. The longest lifetime of 4.66 ns is measured in the SiO_2 region with no top graphene sheet present. As the environment surrounding the ECQDs changes, the lifetime (decay rate)

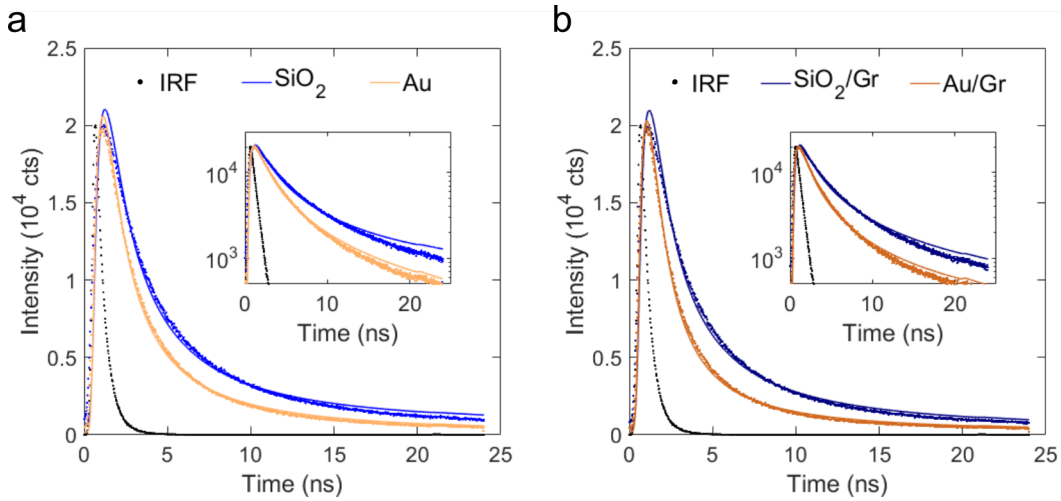

Figure 6.6: Measured fluorescence decays and fits of **a** ECQD film and **b** ECQD film with graphene sheet on top. Insets show decay and fits in logarithmic scale.

Zone	τ (ns)	Γ (ns^{-1})	Γ/Γ_0	η (%)
SiO_2	4.66 ± 0.03	0.21	1	0
Au	4.23 ± 0.18	0.24	1.10	9.0
SiO_2/Gr	4.34 ± 0.32	0.23	1.07	6.5
Au/Gr	3.29 ± 0.35	0.30	1.42	29.6

Table 6.1: Fitted fluorescence decay lifetimes, decay rates (Γ), and decay rate ratios with respect to SiO_2 decay rate (Γ_0).

decreases (increases), due to energy transfer processes, with the shortest lifetime of 3.29 ns obtained when the ECQDs are in the vicinity of both gold and graphene. Note that the highest dispersion in measured lifetime values occurs in the regions covered by a top graphene sheet, replicating the intensity and peak position variability observed in Figure 6.5c and d. The measured decay rates are significantly shorter than the 30-40 ns measured for the original ECQDs in solution [24]. This is most likely a consequence of increased non-radiative decay channels appearing in the ECQDs due to the heterostructure assembly process, which included floating on a liquid/air interface during the Langmuir-Blodgett transfer process, a 4 hour 80° C bake in vacuum, immersion in water to transfer the top graphene sheet, and a 15 minute baking step in ambient at 200° C to ensure the adhesion of the top graphene sheet. Taking the decay rate on SiO_2 with no top graphene sheet as Γ_0, an energy transfer efficiency can be defined as $\eta = (1 - \Gamma_0/\Gamma) \times 100\%$. When $\eta = 1$, all of the fluorophore's energy is transferred non-radiatively to the environment. The measured change in decay rates with respect to Γ_0, and consequent energy transfer efficiency, are quite modest compared to the values measured in literature for coupling between CQDs and gold films or gold nanoparticles [9–14], and fluorophores (including CQDs) and graphene [18–20].

Note that Γ_0 is defined as the decay rate when the fluorophore is in a homogeneous

medium, free of interactions with its environment. For the ECQDs on SiO_2, this is not strictly true, as the enviroment surrounding the emitting core changes from silica to air on one side, and silica to SiO_2 and silicon on the other side. As a first order approximation for analyzing the current results, however, the ECQDs are assumed to not have any interaction with their environment, due to the transparent dielectric nature of the air, silica and SiO_2, and the large distance to the silicon (300 nm). The errors introduced by these assumptions are further minimized because the main parameter of interest Γ/Γ_0 is a measure of *changes* in the overall decay rate, as opposed to absolute decay rate values. Similar assumptions have been made in previous studies of 2D material/fluorophore interations [19, 25].

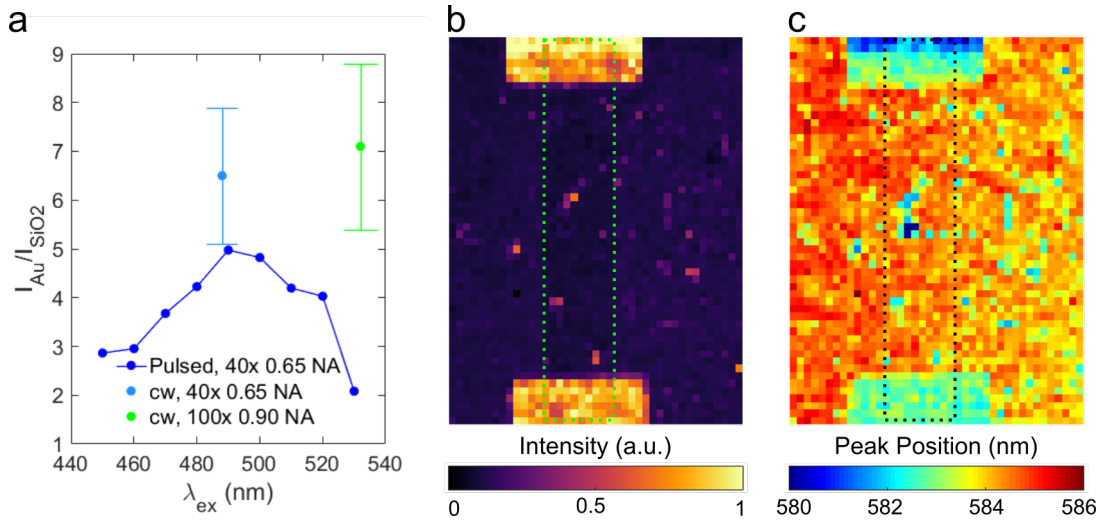

Figure 6.7: Effects of changing the excitation and collection conditions on the collected PL intensity. **a** Enhancement factor of ECQD film, measured as intensity ratio on Au and SiO_2, I_{Au}/I_{SiO_2}, versus excitation wavelength. Single points with error bars specify measurements taken under different excitation or collection conditions. Specifically, light blue point corresponds to data from map in Figure 6.5a, green point to this Figure, **b**. PL peak maps of ECQD film showing **b** integrated intensity and **c** peak position measured using 532 nm excitation wavelength, 100× objective with 0.9 NA. Gold contacts, seen in yellow in **b** and light green and blue in **c**, clearly show a strong peak enhancement and blue shifting. Graphene device below ECQD film highlighted with green and black dotted lines in **b** and **c**, respectively. Size 40×50 µm.

Equation 6.3 includes three terms to account for the detected PL intensity: the excitation rate Γ_{exc}, the quantum yield, related to the radiative decay rate and fluorescence decay lifetime through $Q = \Gamma_r/\tau$, and the collection efficiency of the optical system CE. For a given optical system, this last term will depend on the directionality of the emitted light. The relatively low energy transfer efficiencies measured indicate that the quantum yield $Q = \Gamma_r/\tau$ is not greatly affected by changing the environment surrounding the ECQDs. Therefore the other two terms, the excitation rate Γ_{exc} and the collection efficiency CE, are most likely responsible for the measured intensity changes. The qualitative importance of these terms is examined in Figure 6.7a and b, by varying the excitation wavelength and numerical aperture

of the collection objective. Figure 6.7a shows the PL intensity enhancement I_{Au}/I_{SiO_2} between the gold and SiO_2 zones as a function of excitation wavelength, measured using the 40× , 0.65 NA objective. The enhancement factor approaches a maximum value of 5 at 490 nm, within the range of values measured in the maps of Figure 6.5 for 488 nm wavelength excitation, measured using the same objective, and shown in Figure 6.7a with a light blue point with error bars. In order to probe the collection efficiency, the collection objective was changed to one with a higher numerical aperture (100×, 0.9 NA), allowing for the collection of light emitted at larger solid angles. Fitted PL intensity maps of taken under these conditions are shown in Figure 6.7b. This map was used to calculate an enhancement factor of $I_{Au}/I_{SiO_2} = 7.1 \pm 1.7$ (shown in the green point with error bars in Figure 6.7a). This is more than three times as high as the enhancement factor measured with the 40×, 0.65 NA objective at the same excitation wavelength, indicating that the collection efficiency is indeed an important factor in accounting for the detected PL intensity. Figure 6.7c shows the fitted peak position, confirming that there is a peak blue-shifting on the gold electrodes, as seen in Figure 6.5b. Note that the excitation wavelength sweep in Figure 6.7 was carried out using a pulsed laser, whereas the maps in Figure 6.5 and Figure 6.7b were taken with a continuous wave laser. We do not expect this to have much of an effect on the measured PL intensity, given the coincidence in enhancement factors measured with the two lasers near 490 nm.

6.3.2 Discussion: Enhancement on Gold

The measured energy transfer from the ECQD film to the gold was found to be quite inefficient, about 9%. The small amount of energy transferred could be due to near-field coupling of the emitted light to surface plasmons, as mentioned in Section 6.1.4, or to non-radiative lossy surface waves. Although the gold films in this study are smooth, with 1.7 nm root-mean-square roughness as measured by AFM (see Chapter 5), near-field plasmonic coupling could in theory be possible due to the silica sphere encapsulation, which separates the first layer of ECQDs from the gold film by an average of 35 nm. This spacer has a a two fold-effect: it drastically reduces lossy wave quenching, which is especially prominent below 20 nm [2, 3], and allows near field wavevectors to interact with the gold film. In the near field, light does not follow the far field dispersion relation $\omega = ck$, and thus momentum matching to surface plasmons is possible. Fluorophores separated from a smooth gold film by a dielectric spacer have been used to succesfully excite surface plasmons using near field emitted light [10], with numerous applications in biosensing [26].

The likelihood of plasmonic coupling to the excitation and emission fields can be discerned from the plot of the plasmon and light dispersion curves at the Au/ECQD interface, shown in Figure 6.8, and calculated using equation 6.10, for various ECQD relative dielectric permittivities. These calculations have assumed that the ECQD film has a uniform, homogeneous dielectric relative permittivity constant. This assumption is valid when the characteristic length of the geometric features within the film is much smaller than the

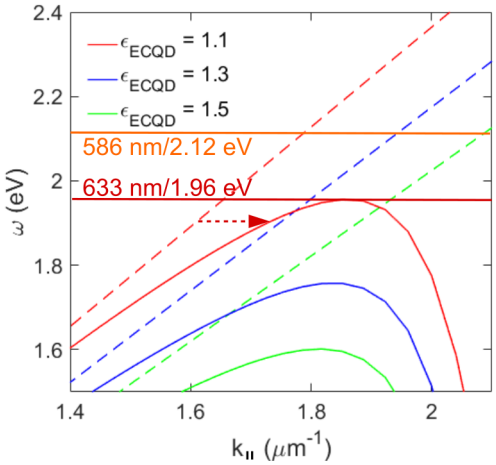

Figure 6.8: Surface plasmon dispersion at Au/ECQD interface, plotted with solid lines for various ECQD permittivities, along with light dispersion in ECQD film, plotted with dashed lines. Arrow shows the momentum mismatch that must be overcome by light for a given ECQD permittivity. This can be accomplished by light in the near field, which does not follow the far field light dispersion. The solid horizontal lines are references, relating the given energy to wavelengths of interest, with the ECQD emission spectrum center shown at 586 nm. Dielectric data for gold from [27].

excitation wavelenght, and has been confirmed by Deák et al [28] for LB deposited silica nanoparticle films. Light dispersion lines for each ε_{ECQD} are also plotted with dashed lines. This figure clearly shows the momentum mismatch between far field light and surface plasmons, as indicated by the red dashed arrow for an ECQD film with $\varepsilon_{ECQD} = 1.1$. To excite surface plasmons, the momentum mismatch must be overcome, which could in theory be possible through coupling with the near-field emission of the ECQDs [1, 7].

Figure 6.8 clearly illustrates the conditions necessary for increasing the likelihood of plasmonic coupling. First, the refractive index of the ECQD must be as low as possible. This allows for momentum matching at wavelengths longer than about 633 nm, at the tail end of the ECQD emission spectrum. This observation seems to rule out plasmonic enhancement due to scattering of the excitation fields at 532 nm or 488 nm. In general, excitation of surface plasmons on gold films at wavelengths below 600 nm is inhibited by an interband transition around 470 nm, which causes the plasmon to decay into electron hole pairs [29]. This is manifested as a peak and rapid decrease in the plasmon dispersion curves for higher $k_{\|}$ values. Transport measurements, detailed in the next section, yielded a dielectric permittivity $\varepsilon_{ECQD} = 1.28$, too high for plasmonic coupling at the wavelengths of interest. This value is an average of the packing of the ECQD spheres and the surrounding air, and thus may be slightly smaller in zones where the film is less dense. The calculated value is also directly proportional to the average film height, measured via AFM in the previous chapter; errors in this height measurement would result in errors in the calculated ε_{ECQD}. Nevertheless, the error would have to be quite large in order for plasmonic coupling

to occur with the light emitted from the ECQDs. In conclusion, excitation of gold surface plasmons seems exceedingly difficult given the wavelengths of the excitation and emitted light, and the dielectric environment in the ECQD film. Plasmonic coupling would only be possible if the "homogeneous film" assumption for calculating ε_{ECQD} failed locally, allowing for coupling between the gold film and the ECQD emission field in the vicinity of zones with low ε_{ECQD}.

Internal reflections between the gold film and the ECQD/air interface could be another possible mechanism to explain the emission enhancement on the gold films. Since the ECQD film has a higher refractive index than air, it can act as an anti-reflective coating, as shown by Deák et al [28]. For an LB deposited monolayer film of 80 nm diameter silica nanoparticles, they measured maximum internal reflection at normal light incidence for a wavelength of about 500 nm, achieving a transmittance of nearly 98% for an LB deposited film of silica nanoparticles on glass [28]. Enhanced reflection at the Au/ECQD interface, not present at the SiO_2/ECQD interface, could thus lead to multiple internal reflections between the gold/ECQD and ECQD/air interfaces, increasing the number of excitation events, without affecting the fluorescence decay lifetime. This would also help to explain the Raman spectroscopy results of the previous chapter, which showed increased peak intensity for graphene under an ECQD film.

Apart from affecting the nature of ECQD excitation, both plasmonic coupling and internal light reflections can affect the collection efficiency. These phenomena are dependent on the Fresnel transmission and reflection coefficients, which themselves depend on the incident angle of light and affect the direction of light emission, directly determining the collection efficiency for a given optical collection objective.

6.3.3 Discussion: Quenching on Graphene

The strong quenching effect of the top graphene film is not yet understood. Fluorescence decay measurements indicate that the energy transfer efficiency to the graphene is very low. This is in agreement with the physical models outlined in section 6.1.5. Energy transfer to the graphene, having a d^{-4} distance dependence, is inhibited by the large distances to the ECQD fluorophores (35 nm on average for the ECQD layer in contact with the graphene). This is illustrated in Figure 6.9, which shows the ratio of increased energy transfer due to the presence of graphene for an ECQD film with an average of 1.5 monolayers (as measured by AFM in the previous chapter). These curves were calculated using the two models presented by equation 6.11 and equation 6.13. In the latter case, the authors claim their equation is valid for distances 3-15 nm, whereas in our case the distance is at least 35 nm [19]. Moreover, the equation was derived for the emitter in vacuum (or air), and the graphene on a substrate with permittivity ε. The situation in the ECQD film is reversed, with the emitter within a dielectric ε, and the graphene on an "air substrate". Despite these discrepancies, the equation can give an order of magnitude idea of the changes in fluorescence decay rates. Although the calculations given by the two models differ in value, they both show that the energy transfer

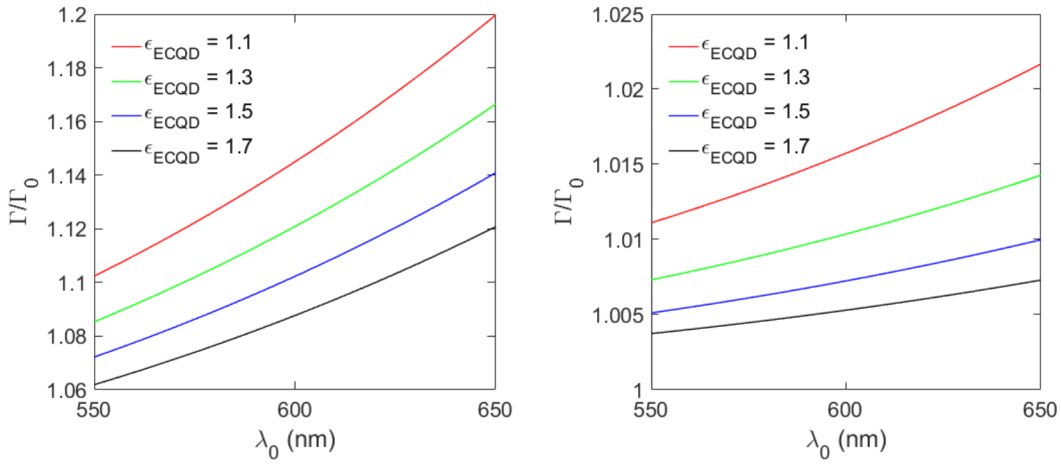

Figure 6.9: Decay rate ratios for an ECQD film in the presence of a graphene sheet, calculated using equation 6.13 in **a** and equation 6.11 in **b**. The calculations were carried out considering 1.5 monolayers of 71 nm ECQDs, as measured by AFM, considering that 2/3 of the ECQD spheres are directly in contact with the top graphene sheet ($d_1 = 35.5$ nm) and 1/3 are separated from the graphene by another ECQD ($d_1 = 106.5$ nm). In **a**, an average dipole orientation was used, calculated as $\nu = \frac{1}{3}\nu_\perp + \frac{2}{3}\nu_\parallel$.

to the graphene at such large distances is quite inefficient, as measured in the fluorescence decay experiments, and summarized in Table 6.1. This is in contrast to the measurements of other authors, taken with a much smaller separation between the graphene and fluorophore [18–20]. It is therefore difficult to explain the seven-fold quenching in emission of ECQD films on SiO_2 when a graphene sheet is placed on top of the film. With such a small energy transfer rate, it stands to reason that the quenching is somehow related to the excitation rate Γ_{exc} or the collection efficiency, as opposed to a change in the ECQD quantum yield. Another intriguing observation is that the strong quenching was only observed for a top graphene sheet. When the bottom sheet was present, no such quenching was observed, as depicted in the map in Figure 6.7b. The reasons behind this are not yet understood. The top sheet is only expected to absorb 2.3% of incoming or outgoing light, hardly enough to cause the 7-fold emission quenching seen in the measurements of Figure 6.5. It may be possible that the quenching is strengthened when the graphene is corrugated, by sitting on top of the rough ECQD films. Further studies need to be carried to probe these effects.

6.4 Electronic and Optoelectronic Properties

Figure 6.10a shows a graphene device covered in an ECQD film and a top graphene sheet electrode. The bottom graphene device was fabricated using the standard photolithography recipe, prior to LB transfer of the ECQD film. Patterning the top graphene sheet into an electrode required modifications in the fabrication process, the most important of which was the graphene etching step. The habitual plasma etching process last several minutes,

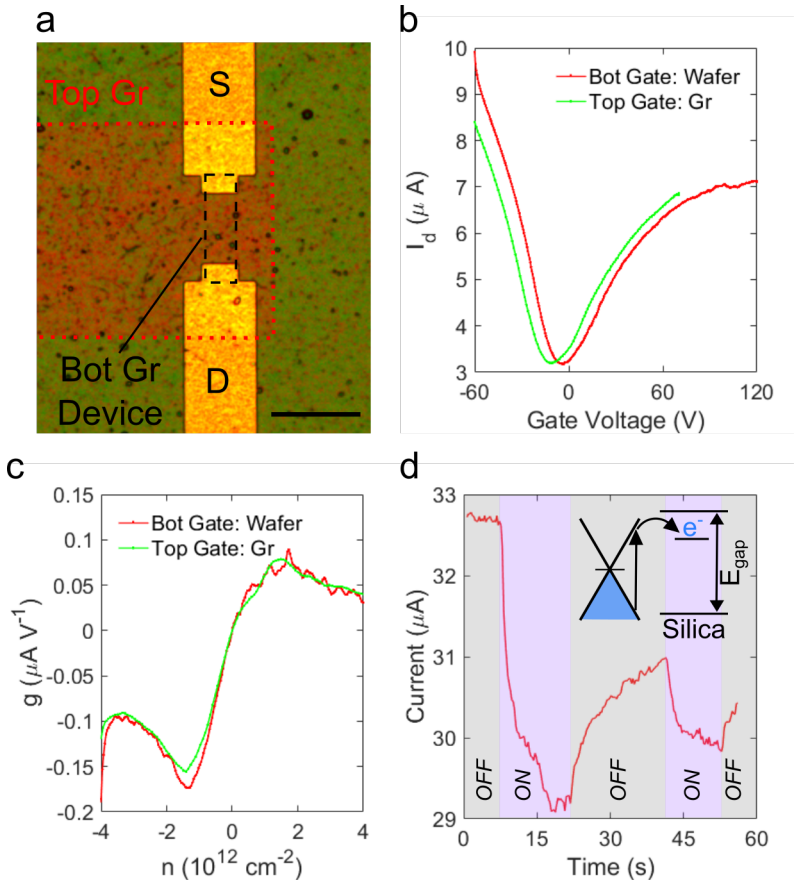

Figure 6.10: **a** Gr/ECQD/Gr device. Bottom graphene is contacted to two gold electrodes, the source (S) and drain (D), forming GFET channel. Top graphene is contacted to single gold electrode, not visible in picture. Scale bar 50 µm. **b** Transfer curves of graphene device, with resistance modulated from the bottom, by the highly doped silicon wafer, and from the top, from the graphene sheet on top of the ECQD film. **c** Transconductance of curves in **b**. **d** Photodetection in graphene device, measured for 0 gate voltage, with shaded blocks indicating excitation light being on or off. The inset shows a possible charge trapping mechanism, in which an photo-excited electron hops into a localized state deep within the ECQD silica shell bandgap.

and resulted in nearly complete quenching of the ECQD film emission. This may be due to oxygen radical diffusion into the pores of the silica, resulting in oxidation of the ECQD semiconductor core. To minimize this effect, the graphene was etched with a reactive ion etching (RIE) process, which provided two advantages over the conventional plasma etch. First, the RIE is capable of etching the graphene much more quickly, on the order of seconds as opposed to minutes with the plasma process, reducing the ECQD exposure to the plasma. Second, the etching process in RIE is dominated by the anisotropic acceleration of ions, as opposed to the isotropic diffusion of radicals. The shorter process times and relatively weaker diffusion prevented the complete quenching of the ECQD film emission. The effective power of the process was reduced further to minimize damage to the ECQD core by igniting the

plasma in pulses. The plasma within the RIE requires several seconds to reach its full power; by turning off the plasma before reaching the full power, the effective overall power is reduced. It is possible that the etching process could be further optimized by changing the plasma gas from oxygen to argon, thus reducing ECQD core oxidation quenching.

Figure 6.10b shows transfer curves of a bottom graphene sheet device, with the gate voltage swept from the bottom by the highly doped silicon wafer, and from the top by the top graphene sheet electrode. The graphene device was initially highly p-doped (V_{DP} around +80 V, not shown). ECQD film transfer drastically reduced the doping, resulting in a nearly intrinsically doped device. Figure 6.10c shows the transconductance curves for each gate. The bottom gate sweep allowed for the calculation of the hole and electron mobilities in the device, 254 and 153 $\mathrm{cm^2V^{-1}s^{-1}}$, respectively. These rather low mobility values are a consequence of the small grain size graphene used to fabricate these devices. The advantage of the small grain size is the improved adhesion to the substrate, ensuring that the bottom graphene does not peel off of the substrate during the LB process using DMSO. For the same reasons, small grain graphene was also used for the top sheet, resulting in strong adherence to the ECQD film. The top graphene electrode functions perfectly as a top gate, exhibiting a leakage current below 1 nA, comparable to the 285 nm thick SiO_2 dielectric.

The transconductance values measured with each gate can be used to solve for the capacitance of the ECQD film C_{ECQD}. The transconducance is given by

$$g_i \equiv \frac{\mathrm{d}I_{d,i}}{\mathrm{d}V_g} = \mu \frac{C_i}{q} \frac{W}{L} V_d \tag{6.17}$$

where the subscript i denotes the top ECQD or bottom SiO_2 gate, V_d and $I_{d,i}$ are the applied drain voltage and measured drain current, V_g is the applied gate voltage, W and L are the device width and length, μ is the mobility and q the elementary charge. Comparing the measured transconductance values allows one to solve for C_{ECQD}, from the relation $g_{ECQD}/g_{SiO_2} = C_{ECQD}/C_{SiO_2}$. The maximum/minimum transcondutance values were used in the electron/hole branch (the same points used to calculate the electron and hole mobility) and averaged, yielding $C_{ECQD}/C_{SiO_2} = 0.90$ in the hole branch, $C_{ECQD}/C_{SiO_2} = 0.88$ in the electron branch, and a mean of 0.89. This value can be used to solve for the relative dielectric permittivity by using the relation $C = \varepsilon/d$. Knowing that $d_{SiO_2} = 285$ nm, $\varepsilon_{SiO_2} = 3.9$, and the AFM measured average thickness $d_{ECQD} = 105.8$ nm (see previous chapter), one obtains

$$\varepsilon_{ECQD} = \varepsilon_{SiO_2} \frac{d_{ECQD}}{d_{SiO_2}} \frac{C_{ECQD}}{C_{SiO_2}} = 1.28. \tag{6.18}$$

Deák et al [28] used optical measurements to calculate the relative permittivity of LB deposited films of 78 nm diameter silica nanoparticles, obtaining a value of $\varepsilon = 1.63$.

There are several factors that could explain this difference in value. First is the nature of the silica itself. Similar processes were used to grow the silica nanoparticles used in [28] and the silica shells surrounding the ECQDs in this work. This process is based on the hydrolysis of tetraethyl orthosilicate (TEOS) in the presence of ammonia, known as

the Störber process. For the ECQD's, however, the process was slightly modified to ensure adequate nucleation on the organic ligands surrounding the alloyed CQD core [24]. Thus the silica shell in the ECQDs will have a slightly different composition and density, apart from being intermeshed with the organic ligands. The porous nature of ECQD silica shells will tend to reduce their dielectric constant [30]. Along these same lines, the porosity of the final film will also have an effect. The relative dielectric permittivity of these films is a volumetric average of the silica spheres and surrounding air. Deák et al [28] were able to obtain highly organized monolayer films, whereas the ECQD films exhibit significant variations and lack short and long range order. Therefore, reduced ECQD packing and compositional variation are expected to reduce the dielectric permittivity of the ECQD film compared to similar silica nanoparticle films.

Figure 6.10d shows photodetection in the ECQD covered graphene device. All of the optoelectronic measurements were carried out with a handheld 1W UV/Visible flashlight, with emission from an LED centered about 410 nm (details in methods). As such, no quantitative figures of merit can be deduced from the measurements. Nonetheless, some valuable qualitative observations can be made. For example, the reduction in current upon illumination observed in Figure 6.10d is indicative of a photogating effect [31]. In this process, illumination excites electron-hole pairs in the device channel. One type of carrier becomes preferentially trapped in localized states, while the other is free to contribute to the current generation process. A schematic of this process is shown in the inset of Figure 6.10d, portraying a photo-excited electron becoming trapped in a localized state within the bandgap of the ECQD silica sphere. The trapped carriers act as local gates, shifting the device's Fermi level. Depending on the type of charge carrier that is trapped, the shift in the Fermi level can increase or decrease the current [31].

Photodetection transfer curves are shown in Figure 6.11, for sweeps with the top and bottom gates, along with the measured photocurrent, defined as $I_{pc} = I_{dark} - I_{illuminated}$. The transfer curves show different photocurrent behaviors for the hole and electron conduction branches. When sweeping with the bottom gate, the photocurrent shows a minimum negative value at a gate voltage of -36 V. Near the Dirac peak, the photocurrent is nearly zero, and increases rapidly with gate voltage up to $V_g = 40$ V. Beyond this value, the photocurrent remains fairly constant, with an average value around -700 nA. The horizontal shifting in the electron conduction branch is typical of photogating induced by trapped charges [31]. In this case, the reduction in electron charge carriers is caused by trapped immobile electrons, which screen the electric field induced by the bottom gate and effectively lower the Fermi level in the graphene device. The same effect happens for the hole conduction branch, but with the polarities reversed, with trapped holes increasing the channel resistance. Photocurrent measurements made by sweeping the graphene sheet top gate produce qualitatively similar effects for the hole conduction branch. A peak in negative photocurrent (-660 nA) is measured at $V_g = -24$ V. In the electron conduction branch, the

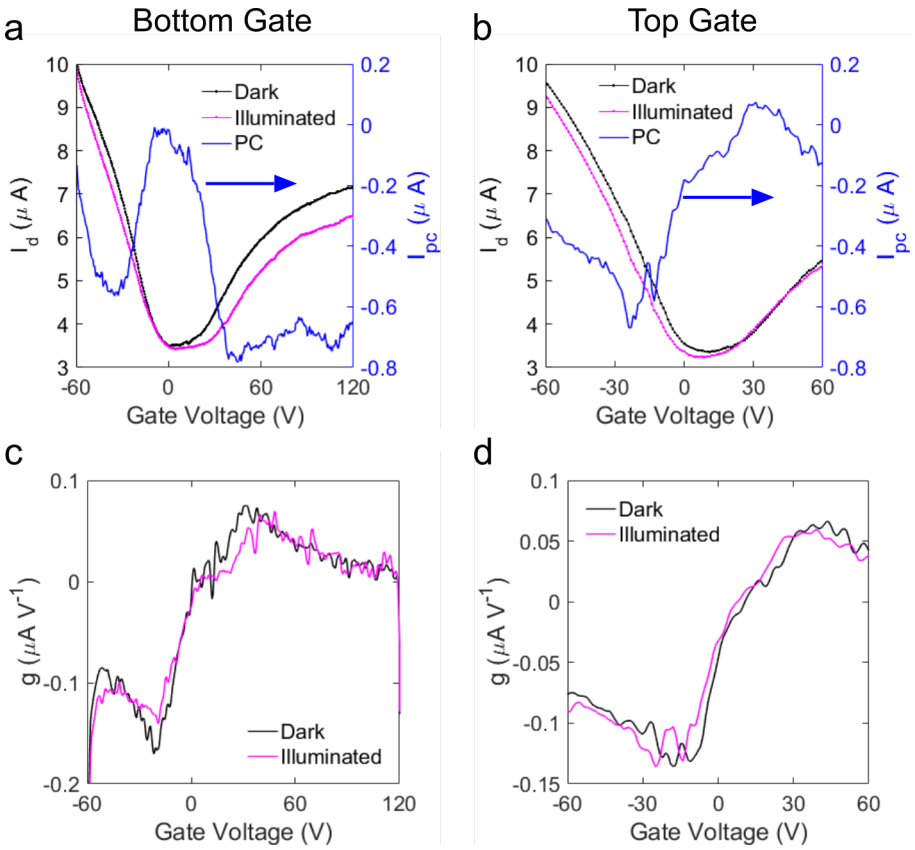

Figure 6.11: Transfer curves and photocurrent of device using top gate **a** and bottom back gates **b**, and respective transconductance curves (**c** and **d**).

photocurrent magnitude is greatly reduced, decreasing in magnitude and even obtaining a small peak positive value of 54 nA at +32 V gate voltage, before becoming negative again.

The transconductance of the curves in Figure 6.11a and b are shown in Figure 6.11c and d, respectively. For the bottom gate curves, there is little resemblance between the photocurrent and transconductance curve. For the top gate, however, there is a strong resemblance in shape and behavior. This is an indication of a gain mechanism, in which multiple charge carriers are being extracted from the device channel due to the absorption of a single photon [31]. The photoconductive gain G is the ratio of the lifetime of the electron-hole pairs, in which one carrier remains trapped τ_{trap} and the transit time of an electron across the device channel, $\tau_{transit}$. The former will depend on the amount of time a trapped carrier remains immobilized in a localized state, while the latter depends on the device length L, applied voltage V_d, and mobility μ. The gain can thus be written as

$$G = \frac{\tau_{trap}}{\tau_{transit}} = \tau_{eh}\frac{\mu V}{L^2}. \tag{6.19}$$

When a gain mechanism is present, the photocurrent will be directly proportional to the gain, and thus to the mobility: $I_{pc} \propto G \propto \mu$ [31]. Since the mobility as a function of gate voltage is proportional to the transconductance (see equation 6.17), the photocurrent

dependence on gate voltage will be proportional to the transconductance: $I_{pc}(V_g) \propto g(V_g)$. This behavior is clearly observed for the top gate transfer curve and transconductance, in Figures 6.11b and d, respectively. It is not clear why sweeping with the bottom gate does not reproduce the shape of the transconductane curves. In this case, it is possible that the lifetime of the electron-hole pairs, dependent on the trapping mechanism, is also dependent on the gate voltage. This would yield a more complicated relation for the photocurrent, $I_{pc}(V_g) \propto g(V_g)\tau_{eh}(V_g)$.

There have been numerous examples of graphene photodetectors operating due to a gain mediated trapping mechanisms [32]. One notable example involved a CQD film deposited on top of graphene. Upon illumination, electron hole pairs were excited in the CQDs. Holes were transferred to the graphene, with the electrons remaining trapped in the CQDs, and acting as local gates, producing a change in current. The holes were free to drift across the device channel many times before finally recombining, resulting in a large photoconductive gain [33]. In that heterostructure device, the CQDs provided both the excited photocarriers and the trap states. In the graphene/ECQD heterostructure devices, the electron-hole pairs participating in photocurrent generation are excited in the graphene, not the ECQDs. Electrons and holes excited within the ECQD core are insulated from the graphene by a high bandgap ZnS outer layer, organic ligands and an insulating silica shell. For carriers photoexcited in the graphene, one type of carrier is preferentially trapped and immobilized, most likely in deep states present within the silica shell bandgap of the ECQDs. Indeed, electron trapping in deep states within the SiO_2 substrate is partially responsible for the intrinsic p doping and hysteresis seen in graphene devices [34]. Without the presence of trap states, photodetection in bare graphene, without any doping modulation is exceedingly hard, due to the extremely fast (sub ps) charge relaxation and recombination times [35].

Incident light excites electron-hole pairs in the graphene, although other mechanisms may be at work also. The ECQD cores will also be excited by the incoming light, and a small amount of their energy will be transferred nonradiatively to the graphene (as seen in the previous section), inducing electron-hole pair formation. Indeed, photocurrent generation due to a resonant energy transfer mechanism was recently demonstrated for photoexcited diamond nitrogen-vacancy centers coupled to a graphene device [36]. Multiple excitations due to the anti-reflective nature of the ECQD film may also increase the density of excited charge carriers in the graphene. The relative importance of each of these excitation mechanisms, and the effect of the charge trap density and energetic position needs to be further explored in order to more fully understand the photodetection mechanism in graphene/ECQD heterostructure devices.

6.5 Future Work

The complex physics present in the graphene/ECQD heterostructures leaves many unexplained observations. What follows is a list of steps to be taken to begin filling in these gaps in knowledge, which were not completed prior to writing the manuscript due to lack of time:

- Full optical characterization of the ECQD films in the presence of graphene, including emission intensity dependence on the excitation field and effect of changing the numerical aperture, to probe the collection efficiency. Comparison of emission quenching characteristics between top and bottom graphene sheet.

- Characterization of the optical properties of the ECQD, not related to PL emission. What are the absorption and scattering properties of the ECQDs silica sphere film? How well do they work as an antireflective coating? Could this be the origin of the emission enhancement on gold? In order to discern these properties without interference from the emission in the ECQD core, adequate optical filtering would be necessary. Another option is to purposely quench the emission of the ECQDs.

- Develop a model of the dielectric environment in the Gr/ECQD heterostructures, including all layers in the stack: silicon, SiO_2, Au, ECQDs and graphene. By calculating the Fresnel transmission and reflection coefficients, a much better understanding can be gained of the physical phenomena present. This will be useful in gauging the importance of many processes, from possible electric field enhancement due to surface plasmons, to the anti-reflective properties of the ECQD film.

- More precise characterization of the photodetection properties of the Gr/ECQD devices. What is the primary electron-hole pair excitation mechanism? What is the nature of the charge traps responsible for the photoconductive gain?

6.6 Conclusion

Optical and electrical characterization of ECQD heterostrucures clearly revealed the presence of many simultaneous physical phenomena. The ECQD PL intensity was significantly enhanced or quenched in the presence of gold or a top graphene sheet, respectively. Fluorescence decay measurements showed that energy transfer processes were rather inefficient. The measured, small changes in fluorescence decay rates agree with theory, but do not agree with the experimentally measured variations in PL intensity. Low energy transfer rates result from the silica shell isolating the ECQD core from its environment, and minimizing energy transfer to nonradiative, lossy waves in the metal and graphene. Calculations of the plasmonic dispersion at the gold/ECQD interface, assuming a homogeneous dielectric relative permittivity for the ECQD film, ruled out the possibility of plasmonic coupling with the excitation field. Plasmonic coupling to the emission field may be possible at the tail end of the PL spectrum, above 633 nm; however, the mismatch in energies between the plasmons and the emitted light largely rules out this mechanism as the origin for the emission enhancement observed. An alternative explanation could arise from the anti-reflective capabilities of the ECQD film, although this process needs to be further investigated theoretically and experimentally. Quenching due to the presence of graphene is not well understood.

By carefully modifying and optimizing the fabrication process, the graphene sheet atop an ECQD was patterned into an electrode, without completely quenching the emission of the ECQD film. This top electrode functioned as a gate, demonstrating the strongly insulating properties of the ECQD film, and permitting the calculation of a relative dielectric permittivity $\varepsilon_{ECQD} = 1.3$, which was used to calculate the plasmon dispersion at the gold/ECQD interface. The bottom graphene devices were also shown to photodetect in the UV/Vis range, most likely due to a charge trapping mechanism which immobilized charge carriers within deep states in the ECQDs. The devices exhibited photoconductive gain, with the measured photocurrent proportional to the device transconducance and thus to the gate dependent mobility.

Although many processes still require a full explanation, the measurements carried out thus far offer a starting point for further explorations of ECQD heterostrucutres. One can envision many future fundamental studies, and even technological applications, based on the combinations of 2D-0D materials and structures into hybrid quantum systems.

Bibliography

[1] L. Novotny and B. Hecht. *Principles of Nano-Optics*. Cambridge University Press, 2006.

[2] E. Fort and S. Grésillon. Surface enhanced fluorescence. *Journal of Physics D: Applied Physics*, 41:013001, 2008.

[3] W. L. Barnes. Fluorescence near interfaces: The role of photonic mode density. *Journal of Modern Optics*, 45:661–699, 1998.

[4] E. M. Purcell, H. C. Torrey, and R. V. Pound. Resonance absorption by nuclear magnetic moments in a solid. *Physical Review*, 69:37–38, 1946.

[5] R.R. Chance, A. Prock, and R. Silbey. Molecular flourescence and energy transfer near interfaces. In I. Prigogine and S.A. Rice, editors, *Advances in Chemical Physics*, volume 37. Wiley, 1978.

[6] W. L. Barnes, A. Dereux, and T.W. Ebbesen. Surface plasmon subwavelength optics. *Nature*, 424:824–830, 2003.

[7] H. Raether. *Surface Plasmons on Smooth and Rough Surfaces and on Gratings*. Springer-Verlag, 1988.

[8] J. Enderlein and T. Ruckstuhl. The efficiency of surface-plasmon coupled emission for sensitive fluorescence detection. *Optics Express*, 13:8855–8865, 2005.

[9] Y. Ito, K. Matsuda, and Y. Kanemitsu. Mechanism of photoluminescence enhancement in single semiconductor nanocrystals on metal surfaces. *Physical Review B*, 75:033309, 2007.

[10] X. Ma, H. Tan, T. Kipp, and A. Mews. Fluorescence enhancement, blinking suppression, and gray states of individual semiconductor nanocrystals close to gold nanoparticles. *Nano Letters*, 10:4166–4174, 2010.

[11] K. T. Shimizu, W. K. Woo, B. R. Fisher, H. J. Eisler, and M. G. Bawendi. Surface-enhanced emission from single semiconductor nanocrystals. *Physical Review Letters*, 89:117401, 2002.

[12] D. Canneson, I. Mallek-Zouari, S. Buil, X. Quélin, C. Javaux, B. Mahler, B. Dubertret, and J.-P. Hermier. Strong purcell effect observed in single thick-shell CdSe/CdS nanocrystals coupled to localized surface plasmons. *Physical Review B*, 84:245423, 2011.

[13] K. Matsuda, Y. Ito, and Y. Kanemitsu. Photoluminescence enhancement and quenching of single CdSe/ZnS nanocrystals on metal surfaces dominated by plasmon resonant energy transfer. *Applied Physics Letters*, 92:211911, 2008.

[14] S.J. LeBlanc, M.R. McClanahan, M. Jones, and P.J. Moyer. Enhancement of multiphoton emission from single CdSe quantum dots coupled to gold films. *Nano Letters*, 13:1662–1669, 2013.

[15] B. Ji, E. Giovanlli, B. Habert, P. Spinicelli, M. Nasilowski, X. Xu, N. Lequeux, J.-P. Hugonin, F. marquier, J.-J. Greffet, and B. Dubretet. Non-blinking quantum dot with a plasmonic nanoshell resonator. *Nature Nanotechnology*, 10:170–175, 2015.

[16] R. S. Swathi and K. L. Sebastian. Resonance energy transfer from a dye molecule to graphene. *The Journal of Chemical Physics*, 129:054703, 2008.

[17] R. S. Swathi and K. L. Sebastian. Long range resonance energy transfer from a dye molecule to graphene has (distance)-4 dependence. *The Journal of Chemical Physics*, 130:086101, 2009.

[18] Z. Chen, S. Berciaud, C. Nuckolls, T.F. Heinz, and L.E. Brus. Energy transfer from individual semiconductor nanocrystals to graphene. *ACS Nano*, 4:2964–2968, 2010.

[19] L. Gaudreau, K. J. Tielrooij, G. E. D. K. Prawiroatmodjo, J. Osmond, F. J. García de Abajo, and F. H. L. Koppens. Universal distance-scaling of nonradiative energy transfer to graphene. *Nano Letters*, 13:2030–2035, 2013.

[20] A. Kasry, A.A. Ardakani, G.S. Tulevski, B. Menges, M. Copel, and L. Vyklicky. Highly efficient fluorescence quenching with graphene. *The Journal of Physical Chemistry C*, 116:2858–2862, 2012.

[21] C.R. Kagan, E. Lifshitz, E.H. Sargent, and D.V. Talapin. Building devices from colloidal quantum dots. *Science*, 353:aac5523, 2016.

[22] M. Sauer, J. Hofkens, and J. Enderlein. *Basic Principles of Fluorescence Spectroscopy*. Wiley-VCH Verlag GmbH, 2011.

[23] A. F. van Driel, I. S. Nikolaev, P. Vergeer, P. Lodahl, D. Vanmaekelbergh, and W. L. Vos. Statistical analysis of time-resolved emission from ensembles of semiconductor quantum dots: Interpretation of exponential decay models. *Phys. Rev. B*, 75:035329, 2007.

[24] M. Acebrón, J.F. Galisteo-López, D. Granados, J. López-Ogalla, J.M. Gallego, R. Otero, C. López, and B.H. Juárez. Protective ligand shells for luminescent SiO_2-coated alloyed semiconductor nanocrystals. *ACS Applied Materials & Interfaces*, 7:6935–6945, 2015.

[25] H. Zang, P.K. Routh, Y. Huang, J.-S. Chen, E. Sutter, P. Sutter, and M. Cotlet. Nonradiative energy transfer from individual CdSe/ZnS quantum dots to single-layer and few-layer tin disulfide. *ACS Nano*, 10:4790–4796, 2016.

[26] J.R. Lakowicz. Radiative decay engineering 3. surface plasmon-coupled directional emission. *Analytical Biochemistry*, 324:153 – 169, 2004.

[27] R.L. Olmon, B. Slovick, T.W. Johnson, D. Shelton, S.-H. Oh, G.D. Boreman, and M.B. Raschke. Optical dielectric function of gold. *Physical Review B*, 86:235147, 2012.

[28] A. Deák, B. Bancsi, A.L. Tóth, A.L. Kovács, and Z. Hórvölgyi. Complex Langmuir–Blodgett films from silica nanoparticles: An optical spectroscopy study. *Colloids and Surfaces A: Physicochemical and Engineering Aspects*, 278:10 – 16, 2006.

[29] M.G. Blaber, M.D. Arnold, and M.J. Ford. A review of the optical properties of alloys and intermetallics for plasmonics. *Journal of Physics: Condensed Matter*, 22:164705, 2010.

[30] M. Darbandi, G. Urban, and M. Krüger. A facile synthesis method to silica coated CdSe/ZnS nanocomposites with tuneable size and optical properties. *Journal of Colloid and Interface Science*, 351:30 – 34, 2010.

[31] M. Buscema, J.O. Island, D.J. Groenendijk, S.I. Blanter, G.A. Steele, H.S.J. van der Zant, and A. Castellanos-Gomez. Photocurrent generation with two-dimensional van der Waals semiconductors. *Chemical Society Reviews*, 44:3691–3718, 2015.

[32] F.H.L. Koppens, T. Mueller, P. Avouris., A.C. Ferrari, M.S. Vitiello, and M. Polini. Photodetectors based on graphene, other two-dimensional materials and hybrid systems. *Nature Nanotechnology*, 9:780–793, 2014.

[33] G. Konstantatos, M. Badioli, L. Gaudreau, J. Osmond, M. Bernechea, F.P.G. Garcia de Aquer, F. Gatti, and F.H.L. Koppens. Hybrid graphene-quantum dot phototransistors with ultrahigh gain. *Nature Nanotechnology*, 7:363–368, 2012.

[34] P. Joshi, H.E. Romero, A.T. Neal, V.K. Toutam, and S.A. Tadigadapa. Intrinsic doping and gate hysteresis in graphene field effect devices fabricated on SiO_2 substrates. *Journal of Physics: Condensed Matter*, 22:334214, 2010.

[35] P.A. George, J. Strait, J. Dawlaty, S. Shivaraman, M. Chandrashekhar, F. Rana, and M.G. Spencer. Ultrafast optical-pump terahertz-probe spectroscopy of the carrier relaxation and recombination dynamics in epitaxial graphene. *Nano Letters*, 8:4248–4251, 2008.

[36] A. Brenneis, L. Gaudreau, M. Seifert, H. Karl, M.S. Brandt, H. Huebl, J.A. Garrido an F.H.L. Koppens, and A.W. Holleirner. Ultrafast electronic readout of diamond nitrogen–vacancy centres coupled to graphene. *Nature Nanotechnology*, 10:135–139, 2015.

Conclusiones

Los resultados presentados en esta tesis demuestran la capacidad de integración del grafeno en dispositivos híbridos, mediante la combinación con moléculas orgánicas y puntos cuánticos coloidales encapsulados (PCCE) de dimensionalidad 0. Antes de llevar a cabo estos experimentos, varios procesos tecnológicos se optimizaron para poder producir muestras de calidad. Intentos iniciales de crecer grafeno sobre láminas de cobre produjeron un recubrimiento superficial no homogéneo. Esto se corrigió modificando la geometría dentro del horno de crecimiento, colocando la lámina en un tubo de cuarzo para reducir el efecto de convección gaseosa a su alrededor. Se obtuvieron dos recetas de crecimiento: una capaz de producir grafeno de pequeños dominios cristalográficos, dando lugar a muestras con propiedades eléctricas mediocres y fuerte adherencia a superficies, y un proceso para obtener grafeno de grandes dominios, con altas movilidades eléctricas, pero con adherencia reducida. La transferencia del grafeno a sustratos arbitrarios es dominada por la interacción entre el grafeno y el sustrato. Las superficies hidrofóbicas favorecen una fuerte adherencia, resultando en transferencias de grafeno limpias, homogéneas y de gran superficie. La fabricación de dispositivos mediante la fotolitografía fue un gran reto, debido a las propiedades contaminantes de la fotoresina. Ajustando el proceso de plasma usado para atacar química y físicamente al grafeno, se minimizaron los residuos de fotoresina. La superficie del grafeno se puede limpiar aún más con disolventes fuertes y un recocido corto en argón, obteniéndose consistentemente dispositivos con movilidades de huecos en torno a 1500 $\mathrm{cm^2V^{-1}s^{-1}}$, y en algunos casos aproximándose a los 2000 $\mathrm{cm^2V^{-1}s^{-1}}$. A lo largo de esta tesis se observó conducción suprimida de electrones en dispositivos producidos mediante fotolitografía. Esto se debe a restos de fotoresina que actúan como centros de dispersión de carga de gran alcance tipo Coulomb, e introducen una barrera a la inyección de electrones en la interfase grafeno/electrodo.

Se demostró la funcionalización química del grafeno con moléculas orgánicas, usando 7,7,8,8-tetracyano-quinodimetano (TCNQ) y etilendiamena (EDA) como dopantes tipo p y n, respectivamente. Se exploraron varias condiciones para la deposición en vapor de la TCNQ. Manteniendo el sustrato a temperatura ambiente, crecieron cristales de TCNQ a muy bajos recubrimientos. En cambio, al calentar el sustrato durante la evaporación se obtuvieron películas de TCNQ delgadas en la superficie del grafeno. Mediante espectroscopía Raman se demostró que existe transferencia de carga entre el grafeno y las primeras capas de estas películas. Medidas de transporte eléctrico corroboraron estas conclusiones, aunque también mostraron que la TCNQ produce una fuerte supresión en la conducción de electrones, además de reducir la movilidad. Suponemos que esto es una consecuencia del arrugamiento causado por la formación de pequeños cristales de TCNQ en la superficie del grafeno. La molécula

EDA, en cambio, es un dopante fuerte tipo n cuyo efecto sobre la movilidad del grafeno es muy pequeño. El dopaje es reversible dejando la muestra en ambiente por varios días o sumergiéndola en alcohol isopropílico por unas horas. El crecimiento de películas de óxido sobre el grafeno funcionalizado mediante deposición atómica por capas (DAC) resultó ser muy difícil debido al carácter inerte del grafeno, incluso con moléculas orgánicas recubriendo su superficie. Usando un método que combina una evaporación inicial de una capa metálica delgada, oxidada en el ambiente, previo crecimiento por DAC, resultó en un recubrimiento mejorado. Sin embargo, este método alteró severamente a las muestras funcionalizadas con TCNQ, como consecuencia de un aumento en las arrugas del grafeno y la desorción del TCNQ. El método combinado de evaporación térmica/DAC resultó mucho más efectivo sobre muestras funcionalizadas con EDA, ralentizando apreciablemente la desorción de dopantes. Especulamos que el futuro de la encapsulación del grafeno bajo capas de óxido pasa por desarrollar nuevos métodos de crecimiento directo por DAC, sin tener que previamente evaporar una capa térmica.

Combinar el grafeno con otros materiales de baja dimensionalidad ha sido en los últimos años un tema de gran actividad científica. En esta tesis, se estudió la integración del grafeno con PCCEs fluorescentes semiconductores mediante el método de transferencia de películas Langmuir-Blodgett. La subfase liquida de deposición resultó ser altamente importante. Mientras el agua produjo películas llenas de agujeros cuya emisión se vio eliminada, dimetilsulfóxido produjo películas compactas y densas sobre superficies grandes (>1 cm^2), manteniendo las propiedades ópticas de las PCCEs. Transferir una capa de grafeno encima de las PCCEs sin eliminar su emisión óptica resulto ser un gran reto, y se logró mediante varios pasos sucesivos de calentamiento. Medidas de microscopía de sonda local mostraron un recubrimiento de 1.5 capas de PCCEs, que las películas son mecánicamente elásticas y además eléctricamente aislantes. El ruido de fondo y la intensidad de picos de grafeno se vieron aumentados en espectros Raman tomados en zonas recubiertas por las películas, además de observarse un dopaje aumentado en el grafeno.

En el último capítulo de esta tesis se estudiaron los diferentes procesos físicos que acontecen simultáneamente en las películas de PCCE, de los cual varios aún no se entienden bien. La emisión fotoluminiscente (FL) de las películas se vio fuertemente amplificada o atenuada en la presencia de oro o de una capa de grafeno, respectivamente. Aunque estas observaciones parecen insinuar un proceso de transferencia de energía, medidas de fluorescencia resuelta en tiempo, apoyadas en cálculos rudimentarios, indican que este no es el origen de la variación en emisión. Las propiedades anti-reflectivas de las capas de silica en las PCCEs podrían estar jugando un papel activo en la modulación de la emisión. Mediante un proceso de microfacbriación optimizado, se fabricó un electrodo a partir de la capa de grafeno encima de los PCCEs. Las películas de los mismos resultaron ser aislantes eléctricos excelentes, y se usaron en medidas eléctricas de efecto campo, permitiendo el cálculo directo de la permitividad dieléctrica efectiva de las películas. Dispositivos de grafeno debajo de los PCCEs son capaces de fotodetectar en el rango UV/Vis, debido a lo que parece ser un

mecanismo de ganancia fotoconductiva, que suponemos que se debe a atrapamiento de cargas en la capa de silica de los PCCEs. Aunque muchas de las observaciones en este capítulo aún carecen de una explicación completa, se proponen varios experimentos y modelos para llegar a entender mejor este sistema.

El grafeno aún no ha llegado a realizar su potencial como material del futuro. Su integración en dispositivos híbridos, combinando sus propiedades con las de materiales, moléculas y estructuras complementarias, podría aún ofrecer un camino a aplicaciones tecnológicas.

Conclusions

The results presented in this thesis demonstrated graphene's ability to be integrated into hybrid devices, through combination with organic molecules or 0-Dimensional encapsulated colloidal quantum dots (ECQDs). Prior to carrying out these experiments, various technological processes were optimized in order to produce quality devices. Initial attempts at growing graphene on copper foil yielded inhomogeneous surface coverage. This was corrected by modifying the geometry within the growth furnace, placing the foil in a quartz tube to reduce the effect of gaseous convection around it. Further optimization yielded two growth recipes: one capable of producing small grain graphene, which suffers from poor electrical properties but exhibits strong adhesion, and a large grain graphene process, resulting in high mobility samples with weaker adhesion. Graphene transfer to arbitrary substrates is dominated by the interactions between the graphene and the substrate, with hydrophobic substrates favoring strong adhesion and resulting in large area, clean, homogeneous transfers. Device fabrication via photolithography proved to be quite challenging, due to the contaminating properties of the photoresist. By tailoring the graphene plasma etching step, photoresist residues were minimized. Post processing with strong solvents and a short argon annealing further cleaned the graphene surface, resulting in devices with hole mobilities consistently around 1500 $cm^2V^{-1}s^{-1}$, and sometimes approaching 2000 $cm^2V^{-1}s^{-1}$. Suppressed electron branch conduction was constantly observed throughout this thesis in devices fabricated via photolithography, resulting from photoresist residues acting as long range Coulomb scatterers and introducing a barrier to electron injection at the graphene/electrode interface.

Chemical functionalization of graphene with organic molecules was demonstrated using 7,7,8,8-tetracyano-quinodimethane (TCNQ) and ethylenediamine (EDA) as p and n dopants, respectively. Various conditions for vapor phase evaporation of TCNQ were explored. Maintaining the substrate at room temperature produced TCNQ crystals at very low coverage, whereas by heating the substrate during the evaporation, thin TCNQ films could be obtained on the graphene surface. Raman spectroscopy demonstrated that electron charge transfer occurs from the graphene to the first few layers of these films. Electron transport measurements corroborated these conclusions, although they also showed that the TCNQ induces strong electron branch suppression, and decreases mobility. We surmise that this is a consequence of the rippling and wrinkling of the graphene caused by the formation of TCNQ clusters on its surface. EDA, on the other hand, was found to be a strong n dopant, having a very small effect on graphene's mobility. The doping is reversible over the course of days by leaving the sample in ambient, or in a matter of a few hours through immersion in iso-propyl alcohol. Atomic layer deposition (ALD) growth of oxide films on the functionalized graphene proved to be quite difficult due to graphene's inert nature, even with organic

molecules covering its surface. A method combining an initial thermal evaporation of a thin metal film, oxidized in ambient, prior to ALD growth yielded much better film coverage. This method severely altered the TCNQ functionalized substrate, possibly a consequence of increased wrinkling in the graphene and desorption of the TCNQ. The combined thermal/ALD method proved to be much more effective on EDA functionalized samples, greatly slowing the desorption of dopants. We speculate that the future of graphene encapsulation under oxide films lies in developing new direct growth ALD methods, bypassing seeding with a thermally evaporated layer.

Combining graphene with other low dimensional materials and structures has proved to be an exciting and thriving research topic in the last few years. This thesis studied graphene's integration with fluorescent semiconducting ECQDs through the Langmuir-Blodgett film transfer technique. The liquid deposition subphase was found to be of utmost importance. Whereas a water subphase yielded inhomogeneous films full of gaps, and quenched the ECQD fluorescence, dimethyl sulfoxide (DMSO) produced compact, dense films over large areas ($>$1 cm^2), while maintaining the optical properties of the ECQDs. Transferring a graphene sheet onto ECQD films without completely quenching their optical emission proved to be quite challenging, and was accomplished through several baking steps at elevated temperatures. Scanning probe measurements revealed an average coverage of 1.5 ECQD layers, with the films exhibiting low mechanical stiffness and high electrical insulation. Enhanced background noise and peak intensity were observed in Raman spectra taken on film covered zones, along with increased graphene doping.

The final chapter in this thesis unveiled numerous physical phenomena occurring simultaneously in the ECQD films, several of which are not yet well understood. Strong photoluminescent (PL) emission enhancement and quenching in the ECQD films was measured in the vicinity of gold and a top graphene sheet, respectively. Although these observations would seem to hint at an energy transfer process, temporal fluorescence decay measurements, supported by rudimentary calculations, indicate that this is not the origin of the emission variation. The anti-reflective properties of the silica shells in the ECQDs may be playing an active role in modulating the emission. Careful optimization of the fabrication process permitted the graphene sheet atop the ECQDs to be patterned into an electrode. The ECQD films were found to be excellent electrical insulators, and were used in electric field effect measurements, allowing for the direct calculation of the films' relative dielectric permittivity. Graphene devices below the ECQD films are capable of photodetection, resulting from what appears to be a photoconductive gain mechanism, which we surmised to be due to charge carrier trapping at the silica shell of the ECQDs. Although many of the observations in this chapter still lack a full explanation, several experiments and modeling methods are proposed to better understand the system.

Graphene has yet to realize its much hyped potential as a wonder material. Integrating it into hybrid devices, combining its properties with those of complimentary materials, molecules, and structures, may yet offer a path to real world technological applications.

Appendix A

CVD Growth Recipes

Purging the furnace gas lines is advisable prior to starting a CVD growth process. After cutting the copper foil to the desired size, and prior to inserting into the growth furnace, copper foils were blown with a nitrogen gas jet to remove any particles from their surface. For all recipes, the scroll pump pressure setpoint was set to 0 mbar for the entire process.

Hydrogen Growth Process

1. Evacuate: 600 standard cubic centimeter per minute (sccm) Ar, 3 minutes
2. Heat and Anneal: 1000° C, 100 sccm H_2, 45 minutes
3. Growth: 1000° C, 200/2 sccm H_2/CH_4, 10 minutes
4. Purge: 1000° C, 100 sccm H_2, 2 minutes
5. Cool: Open heat shield/heating coil, turn off furnace heating. Flow 100 sccm H_2 until sample thermocouple reading is below 100° C before removing sample.

Argon Growth Process

1. Evacuate: 600 standard cubic centimeter per minute (sccm) Ar, 3 minutes
2. Heat and Anneal: 1000° C, 100 sccm Ar, 45 minutes
3. Growth: 1000° C, 100/50/2 sccm $Ar/H_2/CH_4$, 10 minutes
4. Purge: 1000° C, 300 sccm Ar, 1 minute
5. Cool: Open heat shield/heating coil, turn off furnace heating. Flow 300 sccm Ar until sample thermocouple reading is below 100° C before removing sample.

Argon+Anneal Growth Process

1. Evacuate: 600 standard cubic centimeter per minute (sccm) Ar, 3 minutes
2. Heat and Anneal: 1000° C, 100 sccm Ar, 3 hours
3. Growth: 1000° C, 200/200/2 sccm $Ar/H_2/CH_4$, 20 minutes
4. Purge: 1000° C, 300 sccm Ar, 1 minutes

5. Cool: Open heat shield/heating coil, turn off furnace heating. Flow 300 sccm Ar until sample thermocouple reading is below 100° C before removing sample.

Appendix B

Graphene Transfer

This appendix outlines how to transfer graphene from a copper foil substrate onto an arbitraty substrate. The recipe has been optimized for transfer onto Si/SiO_2 wafers. During all process steps involving the copper foil, it is recommended that it be kept as flat as possible. This can be accomplished by firmly pressing the copper foil between two microscope glass slides. Maintaining a flat substrate ensures that the graphene/PMMA stack is also flat, improving graphene/substrate adhesion.

Hydrogen Growth Process

1. Kapton Frame: Fasten the copper foil, graphene side up, to a glass slide. This is accomplished by using Kapton tape, to adhere the edges of the copper foil to the glass slide, as shown in Figure 2.3.

2. PMMA Spin: Spin the sample at 2500 rpm for 1 minute with 950 PMMA A4 (other types of PMMA can be utilized, but were not tested during this thesis). Allow the PMMA to dry in ambient, overnight.

3. Backside Graphene Etch: Remove the Kapton frame, flip the copper foil upside down, and secure it to a glass slide making another Kapton frame. This time, the non-PMMA copper face should face up. Etch the graphene from this face using the following RIE parameters: 15 sccm O_2, 100 mT, 75 W, 30 seconds.

4. Copper Etch: Prepare an etching solution of 0.1 g/mL ammonium persulfate (APS) in deionized water. A large enough volume should be prepared so as to adequately etch the copper without saturating the solution (usually between 50 and 100 mL for a sample of a few cm. Float the copper foil, PMMA side up, on the surface of the solution.

5. Cleaning: After the copper has fully etched, usually between 2 and 3 hours, the graphene/PMMA stack can be removed from the solution. Using a syringe to gently guide the graphene/PMMA stack on the liquid surface, scoop up with a clean glass slide, and carefully transfer the stack to the surface of a deionized water bath. After leaving for about 5 minutes, repeat this process 3 more times with successive DI water baths to ensure a clean graphene/PMMA stack free of copper etchant residues.

6. Transfer to Substrate: Scoop the graphene/PMMA stack from the final DI water bath with the desired substrate. The substrate should be clean, and if possible, hydrophobic, to improve adhesion.

7. Dry: Allow the water between the graphene and the substrate to dry. This can be accomplished by placing the sample in vacuum overnight or longer. Longer drying times are required for graphene with larger grain sizes. After drying, an optional 10 minute bake on a hotplate at 200 ° C can be carried out to further improve adhesion.

8. PMMA Removal: Remove the PMMA by placing in two successive acetone baths, 5 minutes each. The acetone baths can be optionally heated for increased efficiency. After taking out of the last acetone bath, rinse in isopropyl alcohol and blow dry with nitrogen.

Acknowledgements

Ante todo gracias a mis padres y a mi hermana por siempre apoyarme en todo, y por empujarme a continuar por mi camino hasta el final. Sé que no ha sido fácil tenerme tan lejos de casa, pero incluso en los momentos más duros siempre me han animado a que me quedase en España y terminase lo que había empezado. Gracias a Eva, bueno, por absolutamente todo. Más que nada por aguantarme todos estos años, no cabe duda que sin ti esto no se hubiese terminado, y probablemente ni siquiera estaría en España todavía.

Gracias a mis compañeros de DC Wafers, sobre todo a los compañeros del departamento de I+D, Teresa y David. Me acogieron con los brazos abiertos al llegar a León hace ya más de 8 años, e hicieron que el aterrizaje fuese mucho más fácil. A los colegas del máster, Gonzalo y Sandra, que hicieron posibles aguantar y acabar (sin malas notas) todo lo relacionado con fluidos, motores, aerodinámica, y por supuesto, las plasmas, que por fin más o menos llego a entender qué son, aunque no mucho. A Ernesto Dieguez, por echarme una mano cuando la experiencia en DC Wafers se termino, y por ayudarme a conseguir la beca que hizo posible quedarme haciendo investigación en España. A los compañeros del CGL, especialmente a Jerome: it was great having a fellow American around, especially one from Chicago, who kept it so real. You were the guy who first started teaching me to do experimental work and get my hands dirty, back when I used to only do simulation.

A la gente de IMDEA. A mis directores, Amadeo y Dani, gracias por tomar un riesgo con un chaval que no es físico, que se puso a hacer cosas raras (y caras) en la sala blanca. Gracias a Manuel, sin ti nada hubiese sido posible, sin ti no existiría la sala, sin ti no existirían mis muestras, sin ti no existiría mi tesis. Gracias a Ramón, por ser un "partner in crime" inigualable, por los días que casi morimos electrocutados o envenenados en el C3, por todos los minis y los "pints" en Spain y UK, y todas las veces que me llevaste a casa en tu coche. Y bueno, algo has conseguido enseñarme de ciencia, de óptica, de Arduino, de política, de música, de la vida en general. Y gracias por tener la idea, "y que pasa si echamos las nanopartículas de Mary encima de tu grafeno?". A Fernando, mejor monito, muy difícil. Hemos vivido muchos momentos juntos, buenos y menos buenos, y me has enseñado muchísimo. De ciencia, cultura general, vida, etc. Toda ocasión en cual te he dado un consejo o echado una mano, es un momento en que yo he aprendido algo. Y bueno, nos hemos divertido mucho en el camino. Dale duro, que puedes. A María, tus partículas son increíbles y han llevado mi trabajo y mi tesis a otro nivel. Gracias por las muestras y la ayuda y los consejos. Ya sé yo cuanto te has esforzado y cuanto has currado, pero ten presente que por ti ha sido posible hacer un trabajo muy bonito, que ha dado mucho juego. A todos los demás colegas de IMDEA, abrazos y besos, que sin la alegría que aportaron, no hubiese sido posible.

To the people in Lancaster, thank you for making my stay so pleasant. To Professor Robert Young, thanks for welcoming me into your lab warmly and letting me use your equipment, not to mention allowing me to spend your money freely. I hope it was worth it in the end. To Dr. Ben Robinson, for providing the LB trough that took my research to another level. To Jonny, thanks for helping me along the way those summer days last year in the lab; we were able to advance that much more quickly working together. Not to mention we had a good time along the way. To the rest of the Lancasterarans, you made my stay there way more fun than I expected, Revenge of the South and equalité/diversité forever.

Finally, shouts to the dC and to Mutts for always always always keeping it one hunnid.